

Universal Magnetic Oscillations of dc Conductivity in the Incoherent Regime of Correlated Systems

Jakša Vučičević¹ and Rok Žitko^{2,3}

¹*Scientific Computing Laboratory, Center for the Study of Complex Systems, Institute of Physics Belgrade, University of Belgrade, Pregrevica 118, 11080 Belgrade, Serbia*

²*Jožef Stefan Institute, Jamova 39, SI-1000 Ljubljana, Slovenia*

³*Faculty of Mathematics and Physics, University of Ljubljana, Jadranska 19, SI-1000 Ljubljana, Slovenia*

 (Received 19 May 2021; revised 13 August 2021; accepted 21 September 2021; published 2 November 2021)

Using the dynamical mean field theory we investigate the magnetic field dependence of dc conductivity in the Hubbard model on the square lattice, fully taking into account the orbital effects of the field introduced via the Peierls substitution. In addition to the conventional Shubnikov–de Haas quantum oscillations, associated with the coherent cyclotron motion of quasiparticles and the presence of a well-defined Fermi surface, we find an additional oscillatory component with a higher frequency that corresponds to the total area of the Brillouin zone. These paradigm-breaking oscillations appear at elevated temperature. This finding is in excellent qualitative agreement with the recent experiments on graphene superlattices. We elucidate the key roles of the off-diagonal elements of the current vertex and the incoherence of electronic states, and explain the trends with respect to temperature and doping.

DOI: 10.1103/PhysRevLett.127.196601

Quantum oscillations (QOs) are a fundamental phenomenon in solid state physics. The Lorentz force affects electrons in such a way that all the system properties vary periodically with the inverse of the magnetic field [1]. Conventionally, QOs are observable at low temperatures T and in absence of strong incoherence, and provide detailed information about the topology and shape of the Fermi surface [1,2]. Yet, QOs are surprisingly ubiquitous. They also appear in non-Fermi liquids [3–5] and even in gapped systems such as Kondo insulators [6]. They were observed in graphite [7,8], graphene [9,10], organics [11], cuprates [12–14], perovskite heterostructures [15,16], iron-pnictide superconductors [17], and moiré systems [18].

In moiré systems, huge superlattice spacing allows access to regime of large flux per unit cell Φ . Precisely in this regime, recent experiments [19–22] have uncovered a new, peculiar type of QOs of conductivity: peaks at Φ equal to simple fractions of the flux quantum, i.e., $\Phi = \Phi_0 p/q$ with p, q coprime integers, and p and q small [21]. These Brown-Zak (BZ) oscillations are clearly distinct from the conventional Shubnikov–de Haas (SdH) oscillations: BZ QOs appear at elevated temperatures [20], and their frequency does not depend on the electron density n (in 2D, SdH QOs have a frequency proportional to n). Some understanding of this phenomenon was reached by noting that the conductivity is high whenever the non-interacting density of states consists of a small number (q) of wide energy bands (magnetic “minibands”) [20,21]. States in wider bands should have a higher velocity, and therefore conduct better. However, this heuristic picture cannot explain the totality of experimental observations. In

this Letter we present a microscopic theory of conductivity in the Hubbard model and unexpectedly recover a phenomenology strikingly similar to that observed in the experiments of Refs. [20] and [21]. Our analysis elucidates the essential role of incoherence for the BZ oscillations, and explains the temperature, doping and interaction trends in a systematic manner.

We employ the recently developed extension of the dynamical mean field theory (DMFT) [23] to finite magnetic fields [24–26]. In absence of the magnetic field, the DMFT solution of the Hubbard model was previously shown to describe the transport properties of various materials [27–31] and cold atoms in optical lattices [32,33]. The DMFT approximates the self-energy by a local quantity, and becomes exact in the limit of infinite coordination number. In a separate accompanying publication Ref. [26], we prove that the vertex corrections for the longitudinal conductivity cancel at the level of DMFT, regardless of the magnetic field (see also Refs. [34] and [25]); this makes it possible to calculate conductivity by the Kubo bubble without any additional approximations. Our approach fully takes into account local correlations due to electron-electron ($e-e$) interaction, and is formally applicable at any T , coupling strength U and field B .

Our conductivity results exhibit oscillations that clearly correspond to the BZ QOs observed in experiment. The oscillations have a frequency $p/q = 1$ (corresponding to maxima at $p/q = 1/q$) and appear at relatively high T where the SdH oscillations are getting thermally washed out. BZ either coexist with the SdH oscillations or appear as the sole oscillatory component. As T is lowered, higher

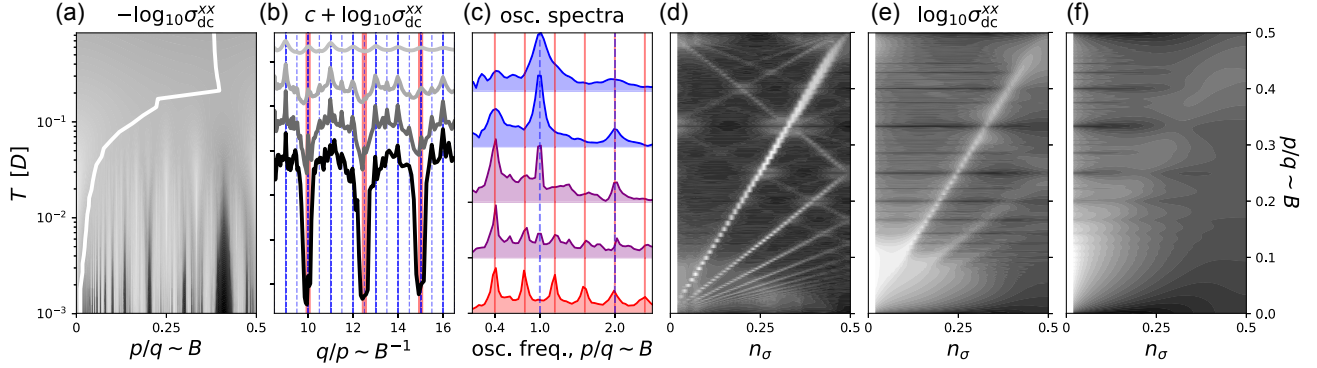


FIG. 1. DMFT results for conductivity in the Hubbard model for $U = 1D$. (a) Conductivity as a function of temperature and field at band filling $n_\sigma = 0.4$. Color code is logarithmic: black means $\log_{10} \sigma_{dc}^{xx} \approx -7.95$, white means $\log_{10} \sigma_{dc}^{xx} \approx 2.12$. White line: onset points of the nonmonotonic behavior of $\sigma_{dc}^{xx}(B)|_T$. (b) Conductivity as a function of inverse magnetic field. Bottom to top: $T = 0.0012, 0.0049, 0.0109, 0.024D$; lines are plotted on the log scale, and offset for the sake of clarity. (c) Frequency spectrum of conductivity in the range $p/q \in [0.03, 0.15]$ at different temperatures. Bottom to top: $T = 0.001, 0.009, 0.016, 0.029, 0.064D$. Each spectrum is normalized to 1 and shifted for the sake of clarity. (b),(c) Vertical lines: peaks due to SdH oscillations (red), and BZ oscillations (blue). (d)–(f) Conductivity with respect to band filling and field at $T = 0.005, 0.03, 0.1D$, respectively. Color code: white means $-8.22, -3.57, -3.12$, black means $2.14, 1.77, 1.03$, respectively.

harmonics of BZ oscillations become more pronounced (peaks become sharper, and additional maxima at $p/q = 2/q, 3/q, \dots$ appear). Ultimately, at very low T , regular BZ oscillations give way to fractal behavior which does not yield any pronounced peaks in the Fourier spectrum. It turns out that the essential ingredient for the regular (sinusoidal) BZ oscillations are the incoherent electronic states. Incoherence allows for conduction processes that involve tunneling between two eigenstates of the Hamiltonian, and it is precisely the contribution of those processes that oscillates at frequency $p/q = 1$. Our numerical data suggest that in strongly correlated regimes, regular BZ oscillations should appear at very low temperature.

Model and method.—We consider the Hubbard model on the square lattice with nearest-neighbor hopping t , coupling U , and band filling per spin n_σ , with $n = \sum_\sigma n_\sigma$. We use $D = 4t$ as the unit of energy. The field is included through Peierls phases for rational flux values $\Phi/\Phi_0 = p/q$ to obtain commensurate magnetic cell [35]. We do not include the Zeeman term [36,37], as it does not affect the QO frequencies, only their amplitudes [1]. We solve the problem within the DMFT with numerical renormalization group solver. Full details of our calculations are given in Ref. [26].

Results.—Figure 1(a) shows the conductivity for moderate doping and interaction ($n_\sigma = 0.4$, $U = 1$) over a broad range of temperature and field (flux). At low T , we clearly see prominent oscillations. The onset of nonmonotonic behavior is marked with the white line: it indicates the value of B where the first extremum in σ_{dc}^{xx} is encountered for a given T . In Fig. 1(b) we close in on a narrow field range and plot σ_{dc}^{xx} as a function of $1/B$ at several T . At low T , we see large dips in conductivity for $p/q = n_\sigma/i$ (red lines; i is integer), corresponding to occurrences of a large

gap in the density of states at the Fermi level. These are the SdH oscillations with a frequency related to the area of the Fermi sea A_{FS} by the Onsager relation $F = \Phi_0/(2\pi)^2 A_{FS}$, $A_{FS} = (2\pi)^2 n_\sigma$. In between the sharp SdH dips, one can observe a weak but highly nonmonotonic behavior of σ_{dc}^{xx} with high-frequency oscillatory features exceeding the resolution of our calculations. With increasing T , the amplitude of the SdH oscillations is reduced in line with the Lifshitz-Kosevich theory [2,26], and the behavior in between the SdH dips becomes simpler: one gets spikes coinciding with small- p moderate- q values of flux (denoted with blue lines: full line is $p = 1$, dashed line is $p = 2$). Ultimately, only regular sinusoidal oscillations of period 1 remain, with maxima at $p/q = 1/q$. Increasing T further erases all nonmonotonic behavior.

Figure 1(c) shows the oscillation spectra obtained by Fourier transforming $\sigma_{dc}^{xx}(B^{-1} \sim q/p)$ on the range $p/q \in [0.03, 0.15]$. At the lowest temperature we see strong peaks at $p/q = n_\sigma$ and its higher harmonics, corresponding to (sharp) SdH oscillations. The fractal behavior in between the SdH dips seen in Fig. 1(b) does not produce a clear oscillatory signal [26]. As T is increased, the peaks at $p/q = 1$ and $p/q = 2$ appear, while at the highest T one is left only with the peak at $p/q = 1$.

In Figs. 1(d)–1(f) we plot the conductivity in the (n_σ, B) plane. At low T , the SdH oscillation fans out from the $(0,0)$ point, clearly indicating the n_σ dependence of the oscillation frequency. At a higher T , SdH oscillations become weaker; horizontal (i.e., n_σ -independent) stripes corresponding to fractal BZ oscillations become visible, and are particularly pronounced at small p values. At the highest T shown, only the BZ oscillations remain.

We summarize our observations by presenting in Figs. 2(a) and 2(b) the two relevant Hubbard model phase

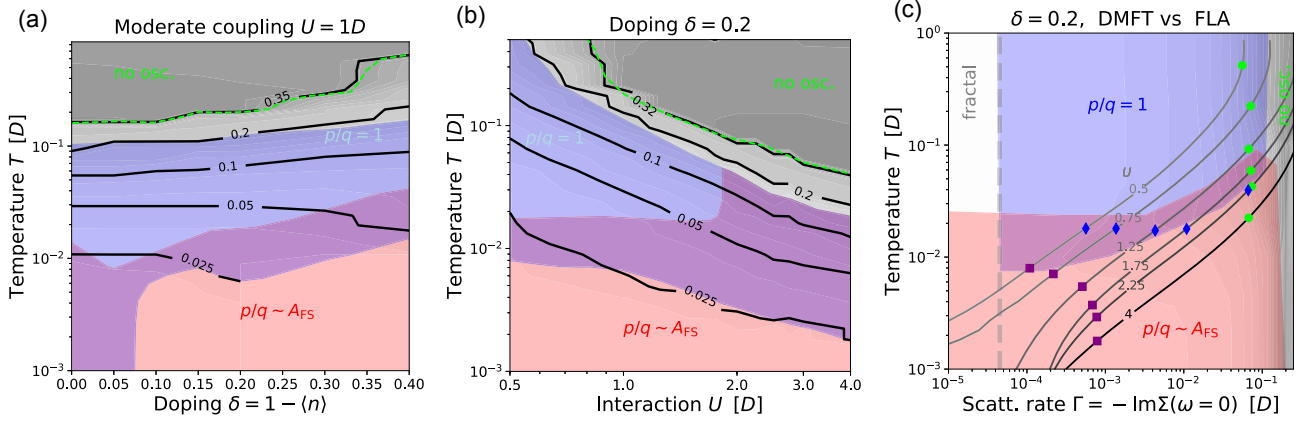


FIG. 2. Phase diagrams showing the type of QOs observed in the range of field $p/q \in [0.03, 0.15]$. (a) DMFT results in (δ, T) plane, (b) DMFT results in (U, T) plane, (c) FLA results in (Γ, T) plane. Red: SdH only. Purple: both SdH and BZ, but SdH dominant. Blue: BZ dominant ($p/q = 1$ peak stronger than $p/q \approx n_\sigma$ peak). Black shading and contours in (a),(b) denote the value of the field where nonmonotonic behavior starts in $1/\sigma_{dc}^{xy}(B)|_T$ (analogous to the white line in Fig. 1). Above the lime dashed line, no oscillations are detectable at any field strength. In (c), lines and symbols correspond to DMFT results, shading to FLA results. Lines are $\Gamma(T)$ for various values of U . Purple squares indicate where the BZ oscillations start with increasing T , blue diamonds where the BZ becomes dominant, and lime circles where all QOs cease [corresponding to the top edge of blue and purple regions in (b)].

diagrams, showing the dominant type of (regular) oscillations, based on the Fourier spectrum of $\sigma_{dc}^{xy}(q/p)$ in the field range $p/q \in [0.03, 0.15]$. We also indicate the onset field for the nonmonotonic behavior (gray scale color coding and the black contours). Clearly, the onset field depends strongly on U and n ; the nonmonotonic behavior is stronger and requires less strong fields in more coherent regimes (lower U and/or higher doping away from half-filling $\delta = 1 - n$). Another notable trend is that the BZ oscillations start at a lower temperature in less coherent regimes (lower δ at fixed U ; stronger U at fixed δ).

To elucidate the role of incoherence we perform calculations within the finite-lifetime approximation (FLA) [26], where a lifetime of electronic states is set by hand by fixing the (local) self-energy to $\Sigma(\omega) = -i\Gamma$. We determine the phase diagram of FLA with respect to the two parameters of this toy model, the scattering rate Γ , and temperature T [Fig. 2(c)]. There appears to be a well-defined upper cutoff value of Γ for the observation of any QOs. For the observation of SdH oscillations, there is a relatively well-defined upper cutoff T . The region of dominant regular BZ oscillations is additionally limited by lower cutoff Γ and T . Below $\Gamma \approx 5 \times 10^{-5}$, fractal behavior is observed, with or without the SdH oscillations, depending on temperature. At moderate Γ , increasing the temperature alone does not wash out the BZ oscillations, and they persist up to infinite temperature.

We superimpose on the FLA phase diagram the DMFT results by identifying $\Gamma = -\text{Im}\Sigma(\omega = 0)$. In DMFT the self-energy has frequency dependence and depends on both U and T . The gray scale lines represent the DMFT result for $\Gamma(T)$ for different U values. The upper cutoff Γ for QOs (lime points) holds in good agreement with FLA results, as

well as the upper cutoff T for SdH oscillations (blue diamonds). At low U , the lower cutoff T for BZ oscillations is also in agreement with FLA. However, at high U , the discrepancy from FLA is significant: the sinusoidal BZ oscillations appear at much lower T than one would expect based on a simple FLA toy model where Σ has no frequency dependence. At very strong U , there rather seems to be a well-defined lower cutoff Γ for regular BZ QOs extending to very low T (this lower Γ cutoff being a bit higher than the one at high T). The observation of BZ oscillations at very low T is therefore a clear indication of strong electronic correlations that go beyond simple incoherence effects.

Discussion.—The trends related to incoherence and temperature can be understood from the linear-response transport theory underlying our calculations. The Kubo bubble for conductivity is illustrated in Fig. 3(a). At the level of the DMFT where the self-energy does not depend on the momentum, the product of two velocities $v_{\mathbf{k},m,m'} v_{\mathbf{k},m',m}$ can be rewritten as a single factor with two kinetic-energy arguments, $v(\epsilon, \epsilon')$. Depending on temperature, effective scattering rate, and chemical potential, different (ϵ, ϵ') domains play a role [26]. In particular, only (ϵ, ϵ') such that $|\epsilon - \epsilon'| < \Gamma$ and $\epsilon^{(l)} - \mu < T$ give significant contributions. At low T , we observe that the SdH effect is already contained in $v(\epsilon, \epsilon')$. The oscillation spectrum for $v(\epsilon, \epsilon' \approx \epsilon \approx \mu)$, exhibits a peak that moves with μ and coincides with n_σ . As the thermal window becomes larger, a wider range of $v(\epsilon, \epsilon' \approx \epsilon)$ enter the calculation, yet oscillate with different frequencies, depending on ϵ . This leads to dephasing and washing out of the SdH oscillations. By contrast, the BZ oscillation is mild at any given ϵ , but it *always* has the same frequency

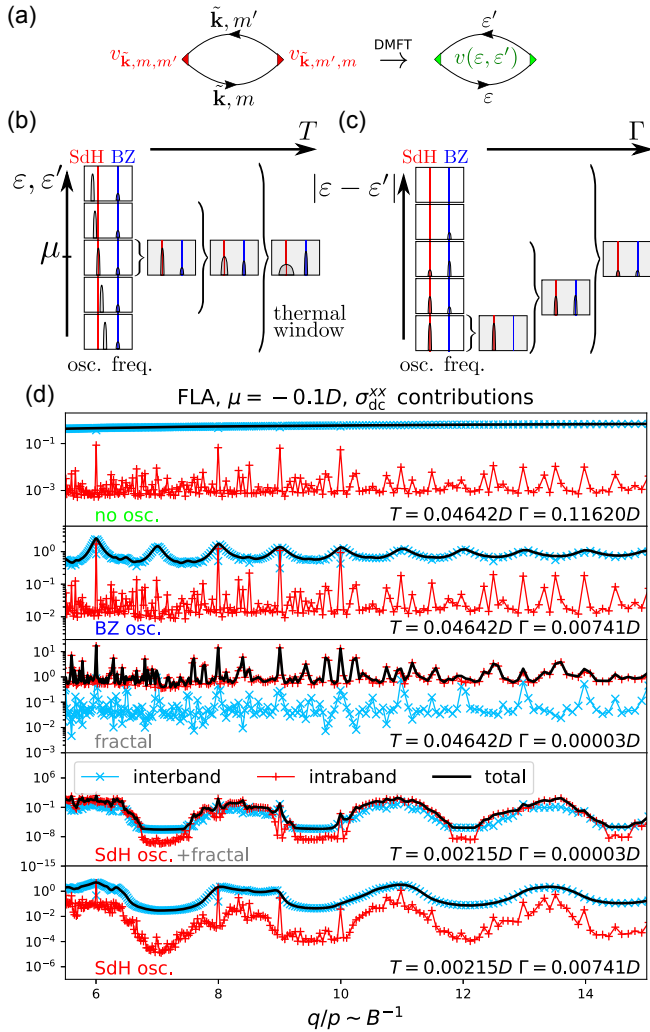


FIG. 3. (a) Diagrammatic representation of the Kubo bubble. Left: in general; right: at the level of the DMFT. (\vec{k}, m) denotes eigenstates of the noninteracting Hamiltonian (see [26] for details). Red or lime triangles are the velocity vertices, in DMFT rewritten as a single factor depending on two kinetic energies, $v(\epsilon, \epsilon')$. (b),(c) White panels: oscillation spectra of $v(\epsilon, \epsilon')$ at a given (ϵ, ϵ') domain. Gray panels: oscillation spectra of v integrated over the relevant (ϵ, ϵ') domain, depending on model parameters (T and Γ), as indicated by the large curly bracket; (b) trend with respect to temperature. (c) Trend with respect to the scattering rate. (d) Field dependence of conductivity and the contributions of interband ($\epsilon \neq \epsilon'$) and intraband ($\epsilon \approx \epsilon'$) processes in FLA in four different parameter regimes.

($p/q = 1$), thus its contribution accumulates with increasing T and can become the dominant effect, as illustrated in Fig. 3(b). The domain of v that turns out to oscillate with the BZ frequency is found at moderate $|\epsilon - \epsilon'|$. Therefore, as the scattering rate Γ is increased, those values enter the calculation and the BZ oscillations become visible in $\sigma_{dc}^{xx}(q/p)$. The values of $v(\epsilon, \epsilon')$ at large $|\epsilon - \epsilon'|$ do not oscillate with any particular frequency. As those get included at large Γ , all oscillations are ultimately overcome

by the nonoscillatory contributions, as illustrated in Fig. 3(c). The velocity v is the only source of BZ oscillations in the Kubo bubble, as Green's function and the self-energy do not have an oscillatory component at the frequency of BZ oscillations [26].

In previous works [20,21], the BZ oscillations were connected with the velocity of the magnetic minibands, calculated as $v = \partial \epsilon_{\vec{k},m} / \partial \vec{k}_x$. Nevertheless, it is important to note that the eigenstates of the noninteracting Hamiltonian do not have a well-defined velocity in the presence of the field. Rather, the velocity $v_{\vec{k},m,m'}$ is a matrix in the miniband space m, m' . In previous works this was not taken into account and the results were interpreted in terms of only the *intra*band processes (diagonal elements of v). This would be well justified only in the limit of coherent, long-lived quasiparticle states. However, increasing T even at weak coupling leads to decoherence of electron states, which activates the contribution of off-diagonal velocity components and even makes them fully dominant [26]. This corresponds to $m \neq m'$ (or $\epsilon \neq \epsilon'$) terms in the Kubo bubble in Fig. 3(a). For these *inter*band processes, the amplitude is determined by the probability of *tunneling* between two minibands upon measurement of velocity. We illustrate the relative contributions of interband and intra-band processes to overall dc conductivity in Fig. 3(d) in five different regions of parameters of the FLA toy model. These plots reveal that the diagonal components of the velocity cannot account for the regular sinusoidal BZ oscillations, but only for the fractal behavior that is observed at low Γ . It is interesting to note that even at very high Γ , the intraband processes still exhibit strong fractal behavior, while the overall conductivity is already devoid of any apparent QOs. This indicates that the regular BZ oscillations are not a simple “smoothing” of the fractal behavior due to widened peaks in the (fractal) spectral function. Rather, this is a separate phenomenon, ultimately due to oscillations in the tunneling amplitudes $v_{\vec{k},m,m' \neq m}$.

Relation to experiment.—Both the fractal behavior (peaks in σ_{dc}^{xx} up to $p/q = 4/q$) and the regular BZ oscillations have been observed in experiment [20,21]. The T -trend observed in Figs. 1(d)–1(f) is in qualitative agreement with the experimental findings of Ref. [20]. Note that the lattice in this moiré system is different from that in our model, and that the dominant interaction in graphene at high T is likely of the electron-phonon (e -ph) type, while our Hamiltonian only includes e - e repulsion. The agreement despite such differences indicates a significant level of universality in these phenomena. Notwithstanding, the doping trend at the highest temperature is in apparent contrast to the measurements in Ref. [20]. In our Fig. 1(f), BZ oscillations are regular (sinusoidal) close to half-filling; closer to the empty band limit a stronger fractal behavior remains in place. In the corresponding high- T experimental result in Ref. [20] [Figs. 2(b) and 2(c)], only the regular oscillations are


observed, and no oscillations at all are observed close to the “neutrality point” (corresponding to the empty band limit in our calculations). This discrepancy appears to be due to the difference in the scattering mechanism: the e - e scattering rate goes to zero as the band empties, but the e -ph scattering rate does not. The FLA calculation [26] where Γ is fixed regardless of the doping clearly reproduces the doping trend observed in the experiment. Similarly, at low temperature in the Hubbard model, one observes both the SdH oscillations and fractal behavior [Fig. 1(b)]. In experiment, there are cases where only SdH oscillations are observed at low temperature. This discrepancy is, again, likely due to the difference in scattering mechanisms. In the Hubbard model the scattering rate goes down with temperature [Fig. 2(c)]. If the scattering rate is kept fixed at a moderate value (as in FLA), at low T one only observes the SdH effect [see bottom panel in Fig. 3(d)].

Conclusion.—We have studied the magnetic quantum oscillations of longitudinal dc conductivity in the 2D Hubbard model. We observe three types of nonmonotonic behavior in σ_{dc}^{xx} : (1) Shubnikov–de Haas oscillations with frequency $p/q = n_\sigma$ (and higher harmonics), at low temperature; (2) fractal behavior of conductivity with peaks at $\Phi/\Phi_0 = 1/q, 2/q, 3/q, \dots$, in the coherent regimes; (3) sinusoidal $p/q = 1$ -frequency oscillations, in moderately incoherent regimes (the Brown-Zak oscillations, BZ). Our findings are in striking agreement with recent experiments on graphene superlattices. The discrepancies from experiment can be traced back to a difference in interactions present in the system. The oscillation phenomenology crucially depends on the scattering rate, and can thus be used in experiment as a characterization tool for scattering mechanisms. The fractal behavior is ultimately a manifestation of the Hofstadter butterfly, and is an indication of a low scattering rate; in contrast, the BZ oscillations indicate a higher scattering rate, and when observed at very low temperature are an indication of a strong e - e coupling. Our results present clear predictions for future experiments where the dependence on coupling strength and doping might be investigated.

Computations were performed on the PARADOX supercomputing facility (Scientific Computing Laboratory, Center for the Study of Complex Systems, Institute of Physics Belgrade). J. V. acknowledges funding provided by the Institute of Physics Belgrade, through the grant by the Ministry of Education, Science, and Technological Development of the Republic of Serbia, as well as by the Science Fund of the Republic of Serbia, under the Key2SM project (PROMIS program, Grant No. 6066160). R. Ž. is supported by the Slovenian Research Agency (ARRS) under Program P1-0044 and Projects No. J1-1696 and No. J1-2458.

- [1] D. Schoenberg, *Magnetic Oscillations in Metals* (Cambridge University Press, Cambridge, England, 1984).
- [2] I. M. Lifshitz and A. M. Kosevich, Zh. Éksp. Teor. Fiz. **29**, 730 (1956) [Sov. Phys. JETP **2**, 636 (1956)].
- [3] F. Denef, S. A. Hartnoll, and S. Sachdev, Phys. Rev. D **80**, 126016 (2009).
- [4] S. A. Hartnoll and D. M. Hofman, Phys. Rev. B **81**, 155125 (2010).
- [5] D. V. Else, R. Thomgren, and T. Senthil, Phys. Rev. X **11**, 021005 (2021).
- [6] J. Knolle and N. R. Cooper, Phys. Rev. Lett. **115**, 146401 (2015).
- [7] D. E. Soule, J. W. McClure, and L. B. Smith, Phys. Rev. **134**, A453 (1964).
- [8] S. B. Hubbard, T. J. Kershaw, A. Usher, A. K. Savchenko, and A. Shytov, Phys. Rev. B **83**, 035122 (2011).
- [9] K. S. Novoselov, A. K. Geim, S. V. Morozov, D. Jiang, M. I. Katsnelson, I. V. Grigorieva, S. V. Dubonos, and A. A. Firsov, Nature (London) **438**, 197 (2005).
- [10] Y. Zhang, Y.-W. Tan, H. L. Stormer, and P. Kim, Nature (London) **438**, 201 (2005).
- [11] M. V. Kartsovniuk and V. G. Peschansky, Low Temp. Phys. **31**, 185 (2005).
- [12] N. Doiron-Leyraud, C. Proust, D. LeBoeuf, J. Levallois, J.-B. Bonnemaïson, R. Liang, D. A. Bonn, W. N. Hardy, and L. Taillefer, Nature (London) **447**, 565 (2007).
- [13] S. E. Sebastian, N. Harrison, E. Palm, T. P. Murphy, C. H. Mielke, R. Liang, D. A. Bonn, W. N. Hardy, and G. G. Lonzarich, Nature (London) **454**, 200 (2008).
- [14] S. E. Sebastian and C. Proust, Annu. Rev. Condens. Matter Phys. **6**, 411 (2015).
- [15] A. D. Caviglia, S. Gariglio, C. Cancellieri, B. Sacépé, A. Fête, N. Reyren, M. Gabay, A. F. Morpurgo, and J.-M. Triscone, Phys. Rev. Lett. **105**, 236802 (2010).
- [16] P. Moetakef, D. G. Ouellette, J. R. Williams, S. J. Allen, L. Balents, D. Goldhaber-Gordon, and S. Stemmer, Appl. Phys. Lett. **101**, 151604 (2012).
- [17] A. Carrington, Rep. Prog. Phys. **74**, 124507 (2011).
- [18] Y. Cao, J. Y. Luo, V. Fatemi, S. Fang, J. D. Sanchez-Yamagishi, K. Watanabe, T. Taniguchi, E. Kaxiras, and P. Jarillo-Herrero, Phys. Rev. Lett. **117**, 116804 (2016).
- [19] B. Hunt, J. D. Sanchez-Yamagishi, A. F. Young, M. Yankowitz, B. J. LeRoy, K. Watanabe, T. Taniguchi, P. Moon, M. Koshino, P. Jarillo-Herrero, and R. C. Ashoori, Science **340**, 1427 (2013).
- [20] R. K. Kumar, X. Chen, G. H. Auton, A. Mishchenko, D. A. Bandurin, S. V. Morozov, Y. Cao, E. Khestanova, M. B. Shalom, A. V. Kretinin, K. S. Novoselov, L. Eaves, I. V. Grigorieva, L. A. Ponomarenko, V. I. Fal’ko, and A. K. Geim, Science **357**, 181 (2017).
- [21] R. K. Kumar, A. Mishchenko, X. Chen, S. Pezzini, G. H. Auton, L. A. Ponomarenko, U. Zeitler, L. Eaves, V. I. Fal’ko, and A. K. Geim, Proc. Natl. Acad. Sci. U.S.A. **115**, 5135 (2018).
- [22] J. Barrier, P. Kumaravadeivel, R. K. Kumar, L. A. Ponomarenko, N. Xin, M. Holwill, C. Mullan, M. Kim, R. V. Gorbachev, M. D. Thompson, J. R. Prance, T. Taniguchi, K. Watanabe, I. V. Grigorieva, K. S. Novoselov,

- A. Mishchenko, V.I. Fal'ko, A.K. Geim, and A.I. Berdyugin, *Nat. Commun.* **11**, 5756 (2020).
- [23] A. Georges, G. Kotliar, W. Krauth, and M.J. Rozenberg, *Rev. Mod. Phys.* **68**, 13 (1996).
- [24] S. Acheche, L.-F. Arsenault, and A.-M.S. Tremblay, *Phys. Rev. B* **96**, 235135 (2017).
- [25] A. A. Markov, G. Rohringer, and A. N. Rubtsov, *Phys. Rev. B* **100**, 115102 (2019).
- [26] J. Vučičević and R. Žitko, companion paper, *Phys. Rev. B* **104**, 205101 (2021).
- [27] P. Limelette, P. Wzietek, S. Florens, A. Georges, T. A. Costi, C. Pasquier, D. Jérôme, C. Mézière, and P. Batail, *Phys. Rev. Lett.* **91**, 016401 (2003).
- [28] H. Terletska, J. Vučičević, D. Tanasković, and V. Dobrosavljević, *Phys. Rev. Lett.* **107**, 026401 (2011).
- [29] J. Vučičević, H. Terletska, D. Tanasković, and V. Dobrosavljević, *Phys. Rev. B* **88**, 075143 (2013).
- [30] T. Furukawa, K. Miyagawa, H. Taniguchi, R. Kato, and K. Kanoda, *Nat. Phys.* **11**, 221 (2015).
- [31] J. Vučičević, D. Tanasković, M.J. Rozenberg, and V. Dobrosavljević, *Phys. Rev. Lett.* **114**, 246402 (2015).
- [32] J. Vučičević, J. Kokalj, R. Žitko, N. Wentzell, D. Tanasković, and J. Mravlje, *Phys. Rev. Lett.* **123**, 036601 (2019).
- [33] P. T. Brown, D. Mitra, E. Guardado-Sanchez, R. Nourafkan, A. Reymbaut, C.-D. Hébert, S. Bergeron, A.-M.S. Tremblay, J. Kokalj, D.A. Huse, P. Schauf, and W.S. Bakr, *Science* **363**, 379 (2019).
- [34] A. Khurana, *Phys. Rev. Lett.* **64**, 1990 (1990).
- [35] D. R. Hofstadter, *Phys. Rev. B* **14**, 2239 (1976).
- [36] L. Laloux, A. Georges, and W. Krauth, *Phys. Rev. B* **50**, 3092 (1994).
- [37] J. Bauer and A.C. Hewson, *Phys. Rev. B* **76**, 035118 (2007).

Electrical conductivity in the Hubbard model: Orbital effects of magnetic fieldJ. Vučičević¹ and R. Žitko^{2,3}¹*Scientific Computing Laboratory, Center for the Study of Complex Systems, Institute of Physics Belgrade, University of Belgrade, Pregrevica 118, 11080 Belgrade, Serbia*²*Jožef Stefan Institute, Jamova 39, SI-1000 Ljubljana, Slovenia*³*Faculty of Mathematics and Physics, University of Ljubljana, Jadranska 19, SI-1000 Ljubljana, Slovenia* (Received 19 May 2021; revised 13 August 2021; accepted 17 August 2021; published 2 November 2021)

Calculation of conductivity in the Hubbard model is a challenging task. Recent years have seen much progress in this respect and numerically exact solutions are now possible in certain regimes. In this paper we discuss the calculation of conductivity for the square-lattice Hubbard model in the presence of a perpendicular magnetic field, focusing on orbital effects. We present the relevant formalism in all detail and in full generality, and then discuss the simplifications that arise at the level of the dynamical mean field theory (DMFT). We prove that the Kubo bubble preserves gauge and translational invariance, and that in the DMFT the vertex corrections cancel regardless of the magnetic field. We present the DMFT results for the spectral function and both the longitudinal and Hall conductivities in several regimes of parameters. We analyze thoroughly the quantum oscillations of the longitudinal conductivity and identify a high-frequency oscillation component, arising as a combined effect of scattering and temperature, in line with recent experimental observations in moiré systems.

DOI: [10.1103/PhysRevB.104.205101](https://doi.org/10.1103/PhysRevB.104.205101)**I. INTRODUCTION**

Strong correlations in electronic systems have a profound effect on conductivity, and lead to a range of unconventional behaviors which are at the center of interest in condensed matter theory. One such behavior is the linear temperature dependence of resistivity, observed in the cuprate superconductors [1–3]. The linear resistivity has been reproduced by numerical simulation of the Hubbard model [4–13], as well as with ultra-cold-atom simulations [14]. It is viewed as an effect of proximity to the Mott transition [8,15,16] or quantum critical points [6,17–19], as well as a generic high-temperature feature of correlated materials which are well approximated by a single-band model [9].

External magnetic fields are also known to affect the transport properties of electronic systems [20], sometimes drastically: in the context of the two-dimensional electron gas, magnetic field leads to the well-known quantum Hall effect (QHE), where conductivity displays intricate dependence on the magnetic field [21–24]. The effect of the Coulomb interaction is here essential for the understanding of the fractional QHE [25,26]. In conventional metals, resistivity is an oscillatory function of the magnetic field, which is the well-known Shubnikov–de Haas effect (SdH) [27,28]. However, the SdH effect is often observed even in states which are assumed to be correlated and are not yet fully understood [29–31]. In such cases, an effective Fermi-liquid description of the material is often invoked to analyze the experimental data, and to map out the geometry of the Fermi surface. It is, therefore, of great importance to understand the interplay of strong coupling and magnetic fields in lattice systems. The study of magnetoresistance in correlated lattice models has been so far limited

to perturbative approaches, either for weak fields [32–34] or weak interactions [22,35,36]. To the best of our knowledge, the only nonperturbative calculations of magnetotransport were limited to the transversal conductivity [37–39]. Nonperturbative calculations were also performed for the effective Fermi-liquid parameters (quasiparticle weight, scattering rate, and density of states at the Fermi level) [38,40,41], which can be considered relevant for longitudinal conductivity.

In this paper we study the effect of magnetic field on both the longitudinal and transversal conductivity in the square-lattice Hubbard model in several parameter regimes: from weak to strong coupling, low to high temperature, and in the full range of the magnetic field.

We first lay out the general formalism for the calculation of conductivity in the presence of the magnetic field and then describe the simplifications that arise at the level of the dynamical mean field theory (DMFT), as previously implemented in Refs. [38,41]. Most importantly, we show that the Kubo bubble is gauge invariant and that the vertex corrections to the current-current correlation function cancel, analogously to the zero-field case. The latter is done by rederiving the well-known zero-field proof from Ref. [42] in real space, and then generalizing it to the case of external magnetic fields. Cancellation of vertex corrections at the level of DMFT was previously shown only for the transversal conductivity [38], and here we give a different, fully general proof.

We perform extensive DMFT calculations to cover a large part of the phase diagram. Our numerical results show that the oscillatory behavior of conductivity is restricted to a finite range of temperature which is mainly determined by the amount of dynamic correlations (which are promoted by interactions, yet hindered by doping). The amplitude of

oscillations decays exponentially with temperature, as expected from the Lifshitz-Kosevich theory [43]. Above a certain characteristic temperature, no nonmonotonic behavior can be induced no matter how strong the magnetic field is. We also observe that in a big range of magnetic fields and interaction strengths, the conductivity follows a scaling law, with the temperature scale set by the coupling strength. Most importantly, the T -linear dependence of resistivity in the high-temperature regime is not qualitatively modified by the magnetic field.

We investigate transverse conductivity in the noninteracting limit, and observe exponential decay of σ^{xy} with temperature, and a power-law divergence as $B_z \rightarrow 0$. The analytic behavior at $B_z = 0$ is restored by interactions, which led to a smooth decay of σ^{xy} as the magnetic field is gradually turned off.

Finally, we investigate the oscillatory behavior of conductivity in weak-to-moderate magnetic fields. In all the cases we studied, the longitudinal conductivity turns out to be dominated by the current-vertex factors, rather than the local density of states at the Fermi level or the effective scattering rate. This leads to an important simplification: one can reliably calculate conductivity at an arbitrary field by using the zero-field DMFT calculation for the self-energy. We further observe that at high temperature, moderate-to-high interactions, and moderate fields, the oscillation occurs at two separate frequencies: one that corresponds to the area of the Fermi sea, as in the Shubnikov–de Haas effect, and the other which corresponds to the full area of the two-dimensional Brillouin zone (BZ), and is therefore of higher frequency and independent of the doping level. This finding is in excellent qualitative agreement with the recent experimental observations in graphene superlattices [44–47]. The full discussion of the observed phenomenology of quantum oscillations of conductivity in the Hubbard model is presented in a separate publication, Ref. [48], while here we present the raw data and describe the basic mechanism behind the onset of the high-frequency oscillations.

The paper is organized as follows. We first describe the formalism: the Hamiltonian, the gauge choice, reciprocal-space formulation, gauge-invariant Green's function, current operators and the correlation function, DMFT approach, calculation of the conductivity tensor, and vertex factors. We then present and discuss the results. For the benefit of the reader and for easy rederivation and validation of the results presented in this work, we provide very detailed proofs of all steps in the derivations in the Appendices. For reasons of clarity and to facilitate dimensional analysis we maintain all constants (e , \hbar , k_B , and lattice constants a in c) in the equations.

II. FORMALISM

A. Model

We study the Hubbard model on the square lattice with lattice constant a , defined by the Hamiltonian

$$H = H_0 + H_{\text{int}}, \quad (1)$$

where the noninteracting part H_0 is the tight-binding (TB) model that we discuss in the following sections, while the interacting part H_{int} is the local density-density coupling, i.e.,

the Hubbard interaction

$$H_{\text{int}} = U \sum_i n_{i,\uparrow} n_{i,\downarrow}, \quad (2)$$

where i indexes the lattice sites, $n_{i,\sigma}$ are the density operators, and U is the coupling constant. The electron spin is denoted $\sigma = \uparrow, \downarrow$.

1. Orbital space

The lattice sites are assumed to lie in the $z = 0$ plane; where convenient, we will treat the system as a three-dimensional stack of such planes separated by the lattice constant c in the perpendicular direction.

The effect of the external magnetic field \mathbf{B} in the TB model is twofold: it couples to the electrons' spin degree of freedom (Zeeman term), as well as the momentum. The latter is approximated on the lattice by means of the Peierls substitution [49,50]. The resulting Hamiltonian is

$$H_0 = -\mu \sum_{i,\sigma} n_{i,\sigma} + g\mu_B \sum_i \mathbf{B}(\mathbf{r}_i) \cdot \mathbf{S}_i - \sum_{i,j,\sigma} t_{ij} e^{if_{ij}} c_{i,\sigma}^\dagger c_{j,\sigma}, \quad (3)$$

where μ is the chemical potential, g is the gyromagnetic factor, μ_B is the Bohr magneton, the position vector of site i is \mathbf{r}_i , and the operator of the electron SU(2) spin is

$$S_i^\eta = \frac{1}{2} (c_{i,\uparrow}^\dagger, c_{i,\downarrow}^\dagger) \hat{\sigma}^\eta \begin{pmatrix} c_{i,\uparrow} \\ c_{i,\downarrow} \end{pmatrix}, \quad (4)$$

where $\hat{\sigma}^\eta$ are the Pauli matrices, and η enumerates the spatial directions x, y, z . The t_{ij} is the hopping amplitude between the sites i and j . The Peierls substitution introduces a phase shift f_{ij} that is picked up by an electron on the path from site i to site j :

$$f_{ij} = \frac{e}{\hbar} \int_{\mathbf{r}_i}^{\mathbf{r}_j} \mathbf{A}(\mathbf{r}) \cdot d\mathbf{r}. \quad (5)$$

Here \mathbf{A} is the vector potential, e the elementary charge, and \hbar the reduced Planck's constant. In matrix notation in site space, the effect of the gauge field corresponds to element-wise multiplication of the bare Hamiltonian:

$$\mathbf{H}_0[\mathbf{A}] = \mathbf{H}_0[\mathbf{A} = 0] \circ e^{i\mathbf{f}}, \quad (6)$$

where $e^{i\mathbf{f}}$ is simply a matrix constructed out of $e^{if_{ij}}$ elements.

We are interested in the effects of a uniform magnetic field perpendicular to the two-dimensional (2D) lattice: $\mathbf{B} = (0, 0, B_z)$. The vector potential \mathbf{A} is not uniquely determined by \mathbf{B} . There are two obvious choices: the Landau gauge

$$\mathbf{A}(\mathbf{r}) = (0, xB_z, 0), \quad (7)$$

and the symmetric gauge

$$\mathbf{A}(\mathbf{r}) = \left(-\frac{y}{2} B_z, \frac{x}{2} B_z, 0 \right). \quad (8)$$

Throughout this paper, we work in the Landau gauge.

In the rest of the paper, we define lattice site coordinates x_i and y_i as integers, and define $\mathbf{r}_i = (x_i, y_i, 0)$. The physical position vector of the lattice site i is then $a\mathbf{r}_i$ and we give spatial indices in terms of \mathbf{r} as, e.g., $\mathbf{A}_{\mathbf{r}} \equiv \mathbf{A}(a\mathbf{r})$.

Plugging the Landau gauge field \mathbf{A} [Eq. (7)] in the expression for the Peierls phase [Eq. (5)] one obtains [41,48] (see Appendix A for proof)

$$\begin{aligned} f_{ij} &\equiv f_{\mathbf{r}_i, \mathbf{r}_j} \\ &= \frac{e}{\hbar} (B_z a^2) \frac{(y_j - y_i)(x_i + x_j)}{2} \\ &= 2\pi \frac{\Phi}{\Phi_0} \frac{(y_j - y_i)(x_i + x_j)}{2}, \end{aligned} \quad (9)$$

where $\Phi_0 = h/e$ is the unit flux, and $\Phi = B_z a^2$ is the flux per lattice plaquette.

To be able to define a finite-sized (commensurate) magnetic unit cell, the values of B_z must satisfy

$$\frac{e}{\hbar} (B_z a^2) = 2\pi \frac{p}{q}, \quad (10)$$

where p and q are coprime integers. q is then the size of the unit cell in the x direction (for proof see Appendix B). In the other direction the size of the unit cell is 1, as the translational invariance is not broken along the y axis; this is obvious as f_{ij} depends only on the difference $y_i - y_j$.

The effect of B_z on the kinetic energy term is periodic. As B_z enters the kinetic energy through $e^{2\pi i \frac{p}{q} (y_j - y_i)(x_i + x_j)/2}$, if $(y_j - y_i)(x_i + x_j)/2$ is an integer for all (i, j) connected by hopping (as is the case with nearest-neighbor hopping), increasing p/q by an integer makes no difference. Therefore, the effect of $\frac{p}{q}$ is the same as that of $\frac{p+mq}{q}$, with m integer. The inversion symmetry of the lattice implies that the effect of $\frac{p}{q}$ is the same as that of $\frac{q-p}{q}$. When it comes to the kinetic energy term, all physically discernible magnetic fields [that satisfy Eq. (10)] can be mapped onto the range $0 \leq p/q \leq \frac{1}{2}$. The field $p/q = 1$ is then a characteristic value of the field, the lowest one (other than zero) that does not couple with electron motion.

In numerics, we will consider a finite $L \times L$ cyclic lattice, which must fit an integer number of magnetic unit cells of size $q \times 1$. We can rewrite the condition (10) as

$$\frac{e}{\hbar} (B_z a^2) = 2\pi \frac{p}{q} = 2\pi \frac{n}{L} \quad (11)$$

with the size of magnetic unit cell being L or smaller, as given by $L/\text{gcd}(L, n)$, where ‘‘gcd’’ denotes the greatest common divisor, and n is an arbitrary integer. In fact, the relation between the finite and infinite lattice is simply

$$q = L/\text{gcd}(L, n), \quad p = n/\text{gcd}(L, n).$$

The size of the lattice L determines the resolution of p/q that one can achieve in scanning the strength of the field in the model.

Under the assumption of only the nearest-neighbor hopping, we now rewrite the full Hamiltonian as

$$\begin{aligned} H_0 &= -\mu \sum_{i,\sigma} n_{i,\sigma} + \frac{1}{2} g \mu_B B_z \sum_{i,\sigma=\uparrow,\downarrow} (-1)^{\delta_{\sigma,\downarrow}} n_{i,\sigma} \\ &\quad - t \sum_{i,\mathbf{u} \in \{\mathbf{e}_x, \mathbf{e}_y\}, \sigma} e^{i \frac{ea^2}{\hbar} x_i B_z \mathbf{u} \cdot \mathbf{e}_y} c_{\mathbf{r}_i, \sigma}^\dagger c_{\mathbf{r}_i + \mathbf{u}, \sigma} + \text{H.c.} \end{aligned} \quad (12)$$

Numeric scales. The importance of the Zeeman splitting depends on the ratio of the Zeeman energy over the bandwidth. Both g and the bandwidth are material specific. A quick

estimate for cuprate compounds, under the assumption of $g = 2$ and half-bandwidth of around 10^5 K, gives that B_z of about 50 T corresponds to a Zeeman energy of about $\approx 3 \times 10^{-3} D$, where $D = 4t$ is the half-bandwidth. While the effect of Zeeman splitting is interesting to study on its own, throughout this paper we restrict to only the gauge-field effects and set $g = 0$.

The effect of the gauge field is determined by the lattice spacing. Assuming $a \sim 5 \times 10^{-10}$ m which is relevant for cuprates, we see that the characteristic $p/q = \frac{1}{2}$ field corresponds to $B_z = \frac{\pi \hbar}{ea^2} \approx 8 \times 10^3$ T. At $B_z = 50$ T, we therefore have $p/q \approx \frac{1}{300}$, and we need at least the lattice size $L = 300$ to describe this regime. Clearly, the bigger the lattice spacing, the bigger the phase picked up upon traveling between the lattice sites, and the bigger the effect of the coupling to the gauge field. The regime of large p/q is therefore relevant for systems with a larger lattice spacing (as in moiré heterostructures [51]), or where high gauge fields can be introduced artificially (as in optical lattices [52,53]).

2. Momentum space

Rewriting the kinetic energy in momentum space leads to the Harper equation [54,55]. By applying to the kinetic energy term the Fourier transformation of the creation and annihilation operators,

$$c_i^\dagger = \frac{1}{\sqrt{N}} \sum_{\mathbf{k}} e^{-i\mathbf{k} \cdot \mathbf{r}_i} c_{\mathbf{k}}^\dagger, \quad c_i = \frac{1}{\sqrt{N}} \sum_{\mathbf{k}} e^{i\mathbf{k} \cdot \mathbf{r}_i} c_{\mathbf{k}}, \quad (13)$$

where $N = L^2$ is the number of sites in the lattice, one obtains

$$\begin{aligned} H_{\text{kin}} &= -t \sum_{i,\mathbf{u} \in \{\mathbf{e}_x, \mathbf{e}_y\}, \sigma} e^{i2\pi \frac{n}{L} x_i \mathbf{u} \cdot \mathbf{e}_y} c_{\mathbf{r}_i, \sigma}^\dagger c_{\mathbf{r}_i + \mathbf{u}, \sigma} + \text{H.c.} \\ &= -2t \sum_{\mathbf{k}, \sigma} \cos k_x n_{\mathbf{k}, \sigma} - t \sum_{\mathbf{k}, \sigma} e^{i k_y} c_{\mathbf{k}, \sigma}^\dagger c_{\mathbf{k} - 2\pi \frac{n}{L} \mathbf{e}_x, \sigma} + \text{H.c.} \end{aligned} \quad (14)$$

For a detailed proof see Appendix C.

There is a coupling between the different \mathbf{k} states which results in a reduction of the Brillouin zone (BZ) by a factor of $q = L/\text{gcd}(L, n)$, where q is the size of the magnetic unit cell. We define $\tilde{\mathbf{k}}$ as \mathbf{k} within the reduced BZ (RBZ). Now, $\tilde{k}_x \in [0, 2\pi/q)$, while $\tilde{k}_y \in [0, 2\pi)$. $\tilde{\mathbf{k}}$ is a good quantum number, but there is now an additional degree of freedom that we denote l such that $l \in [0, q)$. A single-particle state is fully determined by a triplet $(\tilde{\mathbf{k}}, l, \sigma)$, with $c_{\tilde{\mathbf{k}}, l, \sigma} \equiv c_{\mathbf{k} = \tilde{\mathbf{k}} + l \frac{2\pi}{q} \mathbf{e}_x, \sigma}$.

On a finite cyclic lattice, the momentum space is discrete, with a step of the size $2\pi/L$. If $\text{gcd}(L, n) = 1$ there is only one \tilde{k}_x value in the RBZ (equal to 0), and for each momentum there are $q = L$ different values of l .

The Hamiltonian has a block-diagonal structure. For a given $(\tilde{\mathbf{k}}, \sigma)$, the Hamiltonian in the space of l is given by the Harper equation

$$\begin{aligned} [H_{0, \tilde{\mathbf{k}}, \sigma}]_{l, l'} &= \left(-\mu_\sigma - 2t \cos \left(\tilde{k}_x + l \frac{2\pi}{q} \right) \right) \delta_{l, l'} \\ &\quad - t (e^{i \tilde{k}_y} \delta_{l, l' \oplus p} + e^{-i \tilde{k}_y} \delta_{l', l \oplus p}), \end{aligned} \quad (15)$$

where \oplus denotes the cyclic addition modulo q defined as

$$l \oplus l' \equiv l + l' - q \text{div}(l + l', q), \quad (16)$$

and $p = n/\text{gcd}(L, n)$. We also introduced $\mu_\sigma = \mu - (-1)^{\delta_{\sigma,\downarrow}} g\mu_B B_z/2$.

Each block of the Hamiltonian can be diagonalized to yield the eigenenergies $\varepsilon_{\tilde{\mathbf{k}},\sigma,m}$, with $m \in [0, q)$. The basis change matrix elements are defined by

$$c_{\tilde{\mathbf{k}},l,\sigma}^\dagger = \sum_m [\alpha_{\tilde{\mathbf{k}},\sigma}]_{l,m} c_{\tilde{\mathbf{k}},m,\sigma}^\dagger. \quad (17)$$

Note that throughout this work, we distinguish between different operators ($c_{i,\sigma} \equiv c_{\mathbf{r}_i,\sigma}$, $c_{\mathbf{k},\sigma}$, $c_{\tilde{\mathbf{k}},l,\sigma}$, $c_{\tilde{\mathbf{k}},m,\sigma}$, etc.) only by the choice of the symbols in the subscript (e.g., $c_{\tilde{\mathbf{k}},l,\sigma}$ is not equal $c_{\tilde{\mathbf{k}},m,\sigma}$ even if $l = m$), and similarly for other functions.

The blocks of the Hamiltonian have several symmetries. One can invert the x axis

$$[H_{0,(\tilde{k}_x,\tilde{k}_y),\sigma}]_{l,l'} = [H_{0,(-\tilde{k}_x,\tilde{k}_y),\sigma}]_{q-l,q-l'}^*, \quad (18)$$

which means that

$$[\alpha_{(\tilde{k}_x,\tilde{k}_y),\sigma}]_{l,m} = [\alpha_{(-\tilde{k}_x,\tilde{k}_y),\sigma}]_{q-l,m}^* \quad (19)$$

and that the eigenenergies remain the same upon inverting the x axis.

One can also invert the y axis

$$[H_{0,(\tilde{k}_x,\tilde{k}_y),\sigma}]_{l,l'} = [H_{0,(\tilde{k}_x,-\tilde{k}_y),\sigma}]_{l,l'}^*. \quad (20)$$

Again, inverting k_y does not affect the eigenenergies, but merely flips the chirality of the eigenstates

$$[\alpha_{(\tilde{k}_x,\tilde{k}_y),\sigma}]_{l,m} = [\alpha_{(\tilde{k}_x,-\tilde{k}_y),\sigma}]_{l,m}^* \quad (21)$$

Inverting both axes at the same time therefore means

$$[H_{0,(\tilde{k}_x,\tilde{k}_y),\sigma}]_{l,l'} = [H_{0,(-\tilde{k}_x,-\tilde{k}_y),\sigma}]_{q-l,q-l'} \quad (22)$$

and

$$[\alpha_{\tilde{\mathbf{k}},\sigma}]_{l,m} = [\alpha_{-\tilde{\mathbf{k}},\sigma}]_{q-l,m}. \quad (23)$$

There is an additional periodicity along the y axis

$$\varepsilon_{\tilde{\mathbf{k}},\sigma,m} = \varepsilon_{\tilde{\mathbf{k}}+(2\pi C/q)\mathbf{e}_y,\sigma,m} \quad (24)$$

and

$$[\alpha_{\tilde{\mathbf{k}},\sigma}]_{lp \bmod q, m} = e^{iC\frac{2\pi}{q}l} [\alpha_{\tilde{\mathbf{k}}+(2\pi C/q)\mathbf{e}_y,\sigma}]_{lp \bmod q, m} \quad (25)$$

with C integer. This symmetry is important on a finite lattice, where k_y takes values of the form $C2\pi/L$. If $L = q$ [i.e., $\text{gcd}(n, L) = 1$], this means that the density of states and other relevant quantities can be obtained by considering only the block $\tilde{\mathbf{k}} = (0, 0)$. Otherwise, k_y values up to $2\pi/q$ need to be considered. For a proof see Appendix D.

B. Gauge-invariant Green's function

A uniform magnetic field does not break physical translational invariance. However, at the formal level, the inclusion of the appropriate vector potential means that all correlators connecting two or more points in space depend not only on the relative positions, but also on the absolute positions. The spatial dependence of correlators can depend on the gauge choice. Nevertheless, physical observables preserve both translational and gauge invariance.

The quantity of primary interest is the Green's function. It is defined as a function of imaginary time

$$G_{ij,\sigma}(\tau) = -\langle T_\tau c_{i,\sigma}(\tau) c_{j,\sigma}^\dagger(0) \rangle. \quad (26)$$

As a function of complex frequency z , and as a matrix in the site space, one can always write

$$\mathbf{G}_\sigma(z) = [\hbar z \mathbf{I} - \mathbf{H}_0 - \boldsymbol{\Sigma}(z)]^{-1}, \quad (27)$$

where $\boldsymbol{\Sigma}(z)$ is the self-energy. The diagonal elements of the Green's function with $z = \omega + i0^+$ determine the local spectral function which is a physical observable. As such, the local Green's function is uniform in space. Nevertheless, the off-diagonal elements do not exhibit translational invariance $G_{ij} = G_{\mathbf{r}_i - \mathbf{r}_j}$, but rather this equality is satisfied only up to a phase.

It can be shown that the quantity

$$\tilde{G}_{ij,\sigma}(z) \equiv e^{-if_{ij}} G_{ij,\sigma}(z) \quad (28)$$

is gauge invariant, and *preserves the full symmetry of the lattice*. We reproduce here a proof from Ref. [56] which is valid in the noninteracting case, but is completely analogous in the case of a fully local and spatially uniform self-energy. In orbital space we have

$$\begin{aligned} \mathbf{G} &= [\mathbf{I}\hbar z - \mathbf{H}_0[\mathbf{A}] - \mathbf{I}\boldsymbol{\Sigma}(z)]^{-1}, \\ \mathbf{G}^{-1} &= [\mathbf{I}\hbar z - \mathbf{H}_0 \circ e^{i\mathbf{f}} - \mathbf{I}\boldsymbol{\Sigma}(z)], \\ \mathbf{I} &= [\mathbf{I}\hbar z - \mathbf{H}_0 \circ e^{i\mathbf{f}} - \mathbf{I}\boldsymbol{\Sigma}(z)]\mathbf{G}. \end{aligned} \quad (29)$$

It is also easy to verify that $\mathbf{I} \circ e^{i\mathbf{f}} = \mathbf{I}$ so we can further write

$$\begin{aligned} \mathbf{I} \circ e^{i\mathbf{f}} &= ([\mathbf{I}\hbar z - \mathbf{H}_0 - \mathbf{I}\boldsymbol{\Sigma}(z)] \circ e^{i\mathbf{f}})\mathbf{G}, \\ \mathbf{I} \circ e^{i\mathbf{f}} &= ([\mathbf{I}\hbar z - \mathbf{H}_0 - \mathbf{I}\boldsymbol{\Sigma}(z)] \circ e^{i\mathbf{f}})(\tilde{\mathbf{G}} \circ e^{i\mathbf{f}}). \end{aligned} \quad (30)$$

We now write the scalar form

$$\begin{aligned} \delta_{ij} e^{if_{ij}} &= \sum_k [\mathbf{I}\hbar z - \mathbf{H}_0 - \mathbf{I}\boldsymbol{\Sigma}(z)]_{ik} e^{if_{ik}} \tilde{G}_{kj} e^{if_{kj}}, \\ \delta_{ij} &= \sum_k [\mathbf{I}\hbar z - \mathbf{H}_0 - \mathbf{I}\boldsymbol{\Sigma}(z)]_{ik} \tilde{G}_{kj} e^{if_{ik}} e^{if_{kj}} e^{-if_{ij}}, \\ \delta_{ij} &= \sum_k [\mathbf{I}\hbar z - \mathbf{H}_0 - \mathbf{I}\boldsymbol{\Sigma}(z)]_{ik} \tilde{G}_{kj} e^{if_{ik}} e^{if_{kj}} e^{if_{ji}}. \end{aligned} \quad (31)$$

The expression $e^{if_{ik}} e^{if_{kj}} e^{if_{ji}}$ is simply the magnetic flux passing through the triangle defined by the lattice sites i , j , and k . This quantity is gauge invariant. As Eq. (31) is a defining relation for \tilde{G}_{ij} , it means that \tilde{G}_{ij} is gauge invariant. Furthermore, the quantity $[\mathbf{I}\hbar z - \mathbf{H}_0 - \mathbf{I}\boldsymbol{\Sigma}(z)]_{ik}$ has full lattice symmetry, thus \tilde{G}_{ij} does as well.

However, it is interesting to consider the case of a general (possibly nonlocal and nonuniform) self-energy $\boldsymbol{\Sigma}$. In that case, the step performed between Eqs. (29) and (30) reads as

$$[\mathbf{I}\hbar z - \mathbf{H}_0 \circ e^{i\mathbf{f}} - \boldsymbol{\Sigma}(z)] = [\mathbf{I}\hbar z - \mathbf{H}_0 - \boldsymbol{\Sigma}(z) \circ e^{-i\mathbf{f}}] \circ e^{i\mathbf{f}}. \quad (32)$$

The proof can proceed from there completely analogously, but only if the quantity $\tilde{\boldsymbol{\Sigma}}(z) \equiv \boldsymbol{\Sigma}(z) \circ e^{-i\mathbf{f}}$ is gauge invariant and preserves the full lattice symmetry.

A proof for the gauge invariance and lattice symmetry of $\tilde{\boldsymbol{\Sigma}}$ can be given in terms of Feynman diagrams for a special case of local density-density interactions, as follows.

Each diagram's contribution is a product of a certain number of fermionic loops. In case of local density-density interactions, a single Green's function loop is just the density, and this quantity is gauge invariant. Then, we have a loop of arbitrary size N :

$$G_{0,i_1i_2}G_{0,i_2i_3}\dots G_{0,i_Ni_1} = \bar{G}_{0,i_1i_2}\bar{G}_{0,i_2i_3}\dots\bar{G}_{0,i_Ni_1} \times e^{if_{i_1i_2}}e^{if_{i_2i_3}}\dots e^{if_{i_Ni_1}}, \quad (33)$$

which is gauge invariant for the same reason as we had above [note that for the bare propagator \bar{G}_0 , gauge invariance and symmetries have already been proven by Eq. (31)]. The closed fermionic loops are multiplied with the fermionic line connecting the terminals of the self-energy. Say, in case of Σ_{i_1,i_N} ,

$$G_{0,i_1i_2}G_{0,i_2i_3}\dots G_{0,i_N-1i_N} = \bar{G}_{0,i_1i_2}\bar{G}_{0,i_2i_3}\dots\bar{G}_{0,i_N-1i_N} \times e^{if_{i_1i_2}}e^{if_{i_2i_3}}\dots e^{if_{i_N-1i_N}}. \quad (34)$$

Clearly, if we multiply now both sides with $e^{-if_{i_1,i_N}}$, we get on one side $\bar{\Sigma}_{i_1,i_N}$, and on the other

$$\begin{aligned} \bar{G}_{0,i_1i_2}\bar{G}_{0,i_2i_3}\dots\bar{G}_{0,i_N-1i_N}e^{if_{i_1i_2}}e^{if_{i_2i_3}}\dots e^{if_{i_N-1i_N}}e^{-if_{i_1,i_N}} \\ = \bar{G}_{0,i_1i_2}\bar{G}_{0,i_2i_3}\dots\bar{G}_{0,i_N-1i_N}e^{if_{i_1i_2}}e^{if_{i_2i_3}}\dots e^{if_{i_N-1i_N}}e^{if_{i_N,i_1}} \end{aligned} \quad (35)$$

and again the right-hand side is gauge invariant. This proves that the contribution to $\bar{\Sigma}_{ij}$ of each Feynman diagram individually is gauge invariant. Moreover, $\bar{\Sigma}$ is expressed solely in terms of objects with full lattice symmetry, thus, it must itself exhibit full lattice symmetry.

Efficient calculation of \bar{G}

A straightforward calculation of \bar{G} performed in site space would involve an inverse of the $N \times N$ matrix

$$\bar{G}(z) = e^{-if} \circ [\hbar z \mathbf{I} - \mathbf{H}_0[\mathbf{A}] - \Sigma(z)]^{-1}. \quad (36)$$

[Note that here the Peierls phase needs to be taken as Eq. (A2), see Appendix A]. This operation scales as $O(N^3)$ and the size of the lattice one can treat this way is limited to $N \sim 1000$. A more efficient approach can be formulated, and especially so in the noninteracting case, and the case when the self-energy is fully local, i.e., whenever the Green's function is fully diagonal in the eigenbasis of \mathbf{H}_0 , i.e., $G_{(\bar{\mathbf{k}},m),(\bar{\mathbf{k}}',m')}$ = $\delta_{\bar{\mathbf{k}},\bar{\mathbf{k}}'}\delta_{mm'}G_{\bar{\mathbf{k}},m}$. This is precisely the case relevant for our DMFT calculations. We will make use of the basis change matrix elements to go from eigenbasis $|\bar{\mathbf{k}}, m, \sigma\rangle$ to orbital basis $|i, \sigma\rangle$:

$$\begin{aligned} |i, \sigma\rangle &= \frac{1}{\sqrt{N}} \sum_{\mathbf{k}} e^{-i\mathbf{k}\cdot\mathbf{r}_i} |\mathbf{k}, \sigma\rangle \\ &= \frac{1}{\sqrt{N}} \sum_{\bar{\mathbf{k}}, l} e^{-i(\bar{\mathbf{k}}+l\frac{2\pi}{q}\mathbf{e}_x)\cdot\mathbf{r}_i} |\bar{\mathbf{k}}, l, \sigma\rangle \\ &= \frac{1}{\sqrt{N}} \sum_{\bar{\mathbf{k}}, l} e^{-i(\bar{\mathbf{k}}+l\frac{2\pi}{q}\mathbf{e}_x)\cdot\mathbf{r}_i} \sum_m [\alpha_{\bar{\mathbf{k}},\sigma}]_{l,m} |\bar{\mathbf{k}}, m, \sigma\rangle. \end{aligned} \quad (37)$$

Therefore,

$$G_{\mathbf{r},\mathbf{r}',\sigma}(z) = \frac{1}{N} \sum_{\bar{\mathbf{k}}, m} W_{\bar{\mathbf{k}},m,\mathbf{r},\sigma}^* W_{\bar{\mathbf{k}},m,\mathbf{r}',\sigma} G_{\bar{\mathbf{k}},m,\sigma}(z) \quad (38)$$

with

$$W_{\bar{\mathbf{k}},m,\mathbf{r},\sigma} = \sum_l e^{-i(\bar{\mathbf{k}}+l\frac{2\pi}{q}\mathbf{e}_x)\cdot\mathbf{r}} [\alpha_{\bar{\mathbf{k}},\sigma}]_{l,m}. \quad (39)$$

Calculation of $[\alpha_{\bar{\mathbf{k}},\sigma}]$ scales as $O(q^3)$. As there is N/q different $\bar{\mathbf{k}}$ to consider, the first step scales as $O(Nq^2)$, with $q \leq L$, i.e., at most $O(N^2)$. Then the calculation of $W_{\bar{\mathbf{k}},m,\mathbf{r},\sigma}$ scales as $O(q)$ but there is N different $\bar{\mathbf{k}}$, m to consider, and we need N different \mathbf{r} , which is in total $O(N^2q)$, i.e., at most $O(N^2L)$, which is the bottleneck in the calculation. The calculation of each $G_{\mathbf{r},\mathbf{r}',\sigma}(z)$ then scales as $O(N)$, but only if G is diagonal in $\bar{\mathbf{k}}, m$; if it is only diagonal in $\bar{\mathbf{k}}$ but not in m , this scales as $O(Nq)$. As $\bar{G}_{\mathbf{r},\mathbf{r}'} = \bar{G}_{\mathbf{r}-\mathbf{r}'}$, we only need to calculate N different elements of the \mathbf{G} matrix rather than all N^2 of them:

$$\bar{G}_{\mathbf{r}} = e^{-if_{\mathbf{r},\mathbf{r}'=0}} G_{\mathbf{r},\mathbf{r}'=0}. \quad (40)$$

In total, this scales as $O(N^2)$. Again, if G is diagonal in $\bar{\mathbf{k}}$ (as we expect it to be in the absence of translational symmetry breaking), but not in m , then the scaling is $O(N^2q)$, which is still better than the direct matrix inverse. When there is no translational symmetry (e.g., there is disorder), then the scaling is $O(N^4)$, which is worse than the direct matrix inverse. In that case \bar{G} is still gauge invariant, but is not translationally invariant, and all N^2 \mathbf{r}, \mathbf{r}' components need to be calculated.

Finally, we are interested in the spatial Fourier transform

$$\bar{G}_{\bar{\mathbf{k}}} = \sum_{\mathbf{r}} e^{i\bar{\mathbf{k}}\cdot\mathbf{r}} \bar{G}_{\mathbf{r}}, \quad (41)$$

which will be discussed in Sec. III A 2.

We note that other approaches might be possible for the efficient calculation of \bar{G} , e.g., the recursive scheme from Ref. [57].

C. Current density operator and the current-current correlation function

1. Orbital space

We will be interested in the direct current conductivity with respect to an infinitesimal uniform electric field. Such electric field $\mathbf{E} = \partial_t \mathbf{A}^{\text{ext}}$ can be introduced with an additional vector potential \mathbf{A}^{ext} pointing uniformly in a given direction, and growing linearly with time. For the purposes of a linear-response calculation, the current couples to such vector potential instantaneously through $-\int \mathbf{j}(\mathbf{r}) \cdot \mathbf{A}^{\text{ext}}(\mathbf{r}) d^3\mathbf{r} = -v_{\text{cell}} \sum_i \mathbf{j}_{\mathbf{r}_i} \cdot \mathbf{A}_{\mathbf{r}_i}^{\text{ext}}$, where $v_{\text{cell}} = a^2c$ is the volume of the unit cell. The additional Peierls phase coming from a \mathbf{A}^{ext} can therefore be safely rewritten within the slowly varying field approximation

$$\frac{e}{\hbar} \int_{\mathbf{a}\mathbf{r}_i}^{\mathbf{a}\mathbf{r}_j} \mathbf{A}^{\text{ext}}(\mathbf{r}) \cdot d\mathbf{r} \approx \frac{ea}{\hbar} \mathbf{A}^{\text{ext}} \cdot (\mathbf{r}_j - \mathbf{r}_i). \quad (42)$$

In the case when we have just the nearest-neighbor hoppings [as in Eq. (12)], the kinetic term in the Hamiltonian can be rewritten as

$$H_{\text{kin}} = -t \sum_{i,\mathbf{u} \in \{\mathbf{e}_x, \mathbf{e}_y\}, \sigma} e^{i(f_{\mathbf{r}_i, \mathbf{r}_i+\mathbf{u}} + \frac{ea}{\hbar} \mathbf{A}_{\mathbf{r}_i}^{\text{ext}} \cdot \mathbf{u})} c_{\mathbf{r}_i, \sigma}^\dagger c_{\mathbf{r}_i+\mathbf{u}, \sigma} + \text{H.c.} \quad (43)$$

without any additional approximation.

We can now derive the expression for the current *density* operator (with units of A/m²) in the absence of electric field, by employing

$$\mathbf{j}_{\mathbf{r}} = -\frac{1}{v_{\text{cell}}} \frac{\partial H}{\partial \mathbf{A}_{\mathbf{r}}^{\text{ext}}} \Big|_{\mathbf{A}^{\text{ext}} \rightarrow 0} \quad (44)$$

$$= it \frac{1}{ac} \frac{e}{\hbar} \sum_{\mathbf{u} \in \{\mathbf{e}_x, \mathbf{e}_y\}, \sigma} \mathbf{u} e^{i f_{\mathbf{r}_i, \mathbf{r}_i + \mathbf{u}}} c_{\mathbf{r}_i, \sigma}^\dagger c_{\mathbf{r}_i + \mathbf{u}, \sigma} + \text{H.c.} \quad (45)$$

The vector component η can be written as

$$j_{\mathbf{r}}^\eta = it \frac{1}{ac} \frac{e}{\hbar} \sum_{\sigma} \gamma^\eta(\mathbf{r}) c_{\mathbf{r}, \sigma}^\dagger c_{\mathbf{r} + \mathbf{e}_\eta, \sigma} + \text{H.c.} \quad (46)$$

with $\boldsymbol{\gamma}(\mathbf{r}) = (1, e^{i \frac{ea^2}{\hbar} B_z x})$.

The current is an observable and it should be zero even in the presence of a magnetic field. Commonly, one separates the current into the paramagnetic and diamagnetic parts. In magnetic field they may be nonzero even in thermal equilibrium, but they must cancel. See Appendix E for details.

For the sake of generality, we define the current-current correlation function without assuming zero persistent currents:

$$\begin{aligned} \Lambda_{\mathbf{r}, \mathbf{r}'}^{\eta \eta'}(\tau) &= \langle j_{\mathbf{r}}^\eta(\tau) j_{\mathbf{r}'}^{\eta'}(0) \rangle - \langle j_{\mathbf{r}}^\eta \rangle \langle j_{\mathbf{r}'}^{\eta'} \rangle \\ &= -t^2 \frac{1}{a^2 c^2} \frac{e^2}{\hbar^2} \sum_{\sigma, \sigma'} \sum_{b, b' \in \{0, 1\}} (-1)^{b+b'} C^b [\gamma_\eta(\mathbf{r})] C^{b'} [\gamma_{\eta'}(\mathbf{r}')] \\ &\quad \times \langle c_{\mathbf{r} + b \mathbf{e}_\eta, \sigma}^\dagger(\tau^+) c_{\mathbf{r} + (1-b) \mathbf{e}_\eta, \sigma}(\tau) c_{\mathbf{r}' + b' \mathbf{e}_{\eta'}, \sigma'}^\dagger(0^+) c_{\mathbf{r}' + (1-b') \mathbf{e}_{\eta'}, \sigma'}(0) \rangle - \langle j_{\mathbf{r}}^\eta \rangle \langle j_{\mathbf{r}'}^{\eta'} \rangle, \end{aligned} \quad (47)$$

where $C[\dots]$ is the operator of complex conjugation, and $C^0 = 1$.

We are interested in calculating the Kubo bubble, i.e., the disconnected part. The disconnected part will have a static and a dynamic term. The static one cancels the persistent current part, and the dynamic term can be expressed in terms of the Green's function as

$$\begin{aligned} \Lambda_{\mathbf{r}, \mathbf{r}'}^{\eta \eta', \text{disc}}(\tau) &= t^2 \frac{1}{a^2 c^2} \frac{e^2}{\hbar^2} \sum_{\sigma} \sum_{b, b' \in \{0, 1\}} (-1)^{b+b'} C^b [\gamma_\eta(\mathbf{r})] C^{b'} [\gamma_{\eta'}(\mathbf{r}')] \\ &\quad \times G_{\mathbf{r}' + (1-b') \mathbf{e}_{\eta'}, \mathbf{r} + b \mathbf{e}_\eta, \sigma}(-\tau) G_{\mathbf{r} + (1-b) \mathbf{e}_\eta, \mathbf{r}' + b' \mathbf{e}_{\eta'}, \sigma}(\tau). \end{aligned} \quad (48)$$

We can now rewrite this expression in terms of \tilde{G} . In the case of the longitudinal component

$$\begin{aligned} \Lambda_{\mathbf{r}, \mathbf{r}'}^{xx, \text{disc}}(\tau) &= t^2 \frac{1}{a^2 c^2} \frac{e^2}{\hbar^2} \sum_{\sigma} \left[\tilde{G}_{\mathbf{r}' - \mathbf{r} + \mathbf{e}_x, \sigma}(-\tau) \tilde{G}_{\mathbf{r} - \mathbf{r}' + \mathbf{e}_x, \sigma}(\tau) \right. \\ &\quad + \tilde{G}_{\mathbf{r}' - \mathbf{r} - \mathbf{e}_x, \sigma}(-\tau) \tilde{G}_{\mathbf{r} - \mathbf{r}' - \mathbf{e}_x, \sigma}(\tau) \\ &\quad \left. - 2 \cos\left(\frac{ea^2 B_z}{\hbar}(y - y')\right) \tilde{G}_{\mathbf{r}' - \mathbf{r}, \sigma}(-\tau) \tilde{G}_{\mathbf{r} - \mathbf{r}', \sigma}(\tau) \right]. \end{aligned} \quad (49)$$

We see that the expression only depends on the distance which means that it preserves translational symmetry, and is only expressed in terms of gauge-invariant quantities. We have checked explicitly that exactly the same expression is also obtained in the symmetric gauge. Furthermore, this expression has all the expected spatial symmetries. A completely

analogous calculation for $\Lambda_{\mathbf{r}, \mathbf{r}'}^{yy, \text{disc}}(\tau)$ yields the expression with $x, y \rightarrow y, x$. A general proof of the gauge invariance of $\Lambda_{\mathbf{r}, \mathbf{r}'}^{\eta, \eta', \text{disc}}(\tau)$ is given in Appendix F.

2. Momentum space

As we have shown that the current-current correlation function satisfies all the desired spatial symmetries, we can proceed to discuss the uniform current-current correlation function in a straightforward manner by performing the spatial Fourier transform. We have

$$\Lambda_{\mathbf{q}=0}^{\eta \eta'}(\tau) = v_{\text{cell}} \sum_{\mathbf{r}} \Lambda_{\mathbf{r}, \mathbf{r}=0}(\tau). \quad (50)$$

This is followed by the Fourier transform in imaginary time to finally obtain

$$\Lambda_{\mathbf{q}=0}^{\eta \eta'}(i\nu) = v_{\text{cell}} \sum_{\mathbf{r}} \frac{1}{2\hbar} \int_{-\beta\hbar}^{\beta\hbar} d\tau e^{i\nu\tau} \Lambda_{\mathbf{r}, \mathbf{r}=0}(\tau). \quad (51)$$

We can rewrite this expression more conveniently using the uniform current operator as

$$\Lambda_{\mathbf{q}=0}^{\eta \eta'}(i\nu) = \frac{V}{2\hbar} \int_{-\beta\hbar}^{\beta\hbar} d\tau \langle j_{\mathbf{q}=0}^\eta(\tau) j_{\mathbf{q}=0}^{\eta'}(0) \rangle, \quad (52)$$

where V is the total volume $V = N v_{\text{cell}}$ and

$$j_{\mathbf{q}=0}^\eta = \frac{1}{N} \sum_{\mathbf{r}} j_{\mathbf{r}}^\eta. \quad (53)$$

Note that we have here defined the uniform current operator as the average current (density) operator, rather than the spatial Fourier transform of the current operator. Using the creation

and annihilation operators in the eigenbasis of the noninteracting Hamiltonian, we can write

$$j_{\mathbf{q}=0}^{\eta} = \frac{it}{N} \frac{1}{ac} \frac{e}{\hbar} \sum_{\sigma} \sum_{\tilde{\mathbf{k}}, m, m'} v_{\tilde{\mathbf{k}}, m, m', \sigma}^{\eta} c_{\tilde{\mathbf{k}}, m, \sigma}^{\dagger} c_{\tilde{\mathbf{k}}, m', \sigma} \quad (54)$$

with

$$v_{\tilde{\mathbf{k}}, m, m', \sigma}^x = \sum_l [\alpha_{\tilde{\mathbf{k}}, \sigma}]_{l, m} [\alpha_{\tilde{\mathbf{k}}, \sigma}^*]_{l, m'}^* [e^{i\tilde{k}_x} e^{il\frac{2\pi}{q}} - e^{-i\tilde{k}_x} e^{-il\frac{2\pi}{q}}] \quad (55)$$

and

$$v_{\tilde{\mathbf{k}}, m, m', \sigma}^y = \sum_l [\alpha_{\tilde{\mathbf{k}}, \sigma}]_{l, m} [e^{i\tilde{k}_y} [\alpha_{\tilde{\mathbf{k}}, \sigma}]_{l \oplus p, m'}^* - e^{-i\tilde{k}_y} [\alpha_{\tilde{\mathbf{k}}, \sigma}]_{l \oplus p, m'}^*]. \quad (56)$$

The proof for the above expressions is given in Appendix G. Assuming no persistent currents, the uniform current-current correlation function is therefore

$$\begin{aligned} \Lambda_{\mathbf{q}=0}^{\eta\eta'}(i\nu) &= -\frac{t^2 e^2}{c\hbar^2} \frac{1}{N} \sum_{\sigma_1, \sigma_2} \frac{1}{2\hbar} \int_{-\beta\hbar}^{\beta\hbar} d\tau e^{i\nu\tau} \\ &\times \sum_{\tilde{\mathbf{k}}_1, m_1, m'_1} \sum_{\tilde{\mathbf{k}}_2, m_2, m'_2} v_{\tilde{\mathbf{k}}_1, m_1, m'_1, \sigma_1}^{\eta} v_{\tilde{\mathbf{k}}_2, m_2, m'_2, \sigma_2}^{\eta'} \\ &\times \langle c_{\tilde{\mathbf{k}}_1, m_1, \sigma_1}^{\dagger}(\tau^+) c_{\tilde{\mathbf{k}}_1, m'_1, \sigma_1}(\tau) c_{\tilde{\mathbf{k}}_2, m_2, \sigma_2}^{\dagger}(0^+) c_{\tilde{\mathbf{k}}_2, m'_2, \sigma_2}(0) \rangle. \end{aligned} \quad (57)$$

The disconnected part written as a function of bosonic Matsubara frequency reads as (see Appendix H for proof)

$$\begin{aligned} \Lambda_{\mathbf{q}=0}^{\eta\eta', \text{disc}}(i\nu) &= \frac{t^2 e^2}{c\hbar^2} \frac{1}{N} \sum_{\sigma} \sum_{\tilde{\mathbf{k}}, m_1, m'_1, m_2, m'_2} \\ &\times v_{\tilde{\mathbf{k}}, m_1, m'_1, \sigma}^{\eta} v_{\tilde{\mathbf{k}}, m_2, m'_2, \sigma}^{\eta'} \\ &\times \frac{1}{\beta} \sum_{i\omega} G_{\tilde{\mathbf{k}}, m'_2, m_1 \sigma}(i\omega) G_{\tilde{\mathbf{k}}, m'_1, m_2, \sigma}(i\omega + i\nu). \end{aligned} \quad (58)$$

D. Method

1. DMFT

In dynamical mean field theory (DMFT), the lattice problem is mapped onto a set of self-consistent local impurity problems on each lattice site i , defined by the action [58–61]

$$\begin{aligned} S_i^{\text{imp}} &= \sum_{\sigma} \int d\tau d\tau' c_{i, \sigma}^{\dagger}(\tau) [-\mathcal{G}_{0, i}^{-1}](\tau - \tau') c_{i, \sigma}(\tau') \\ &+ U \int d\tau c_{i, \uparrow}^{\dagger}(\tau) c_{i, \uparrow}(\tau) c_{i, \downarrow}^{\dagger}(\tau) c_{i, \downarrow}(\tau). \end{aligned} \quad (59)$$

The bare propagator $\mathcal{G}_{0, i}$ in the impurity problem i is determined self-consistently, so that the Green's function in each impurity problem is equal to the local Green's function on the site of the impurity problem, assuming that the self-energy on the lattice is local and on each site equal to the self-energy

of the corresponding impurity problem. This self-consistency condition can be written as

$$\mathcal{G}_{0, i}(z) = 1 / ([G^{-1}]_{ii}(z) + \Sigma_i^{\text{imp}}(z)), \quad (60)$$

where $\Sigma_i^{\text{imp}}(z)$ is the self-energy calculated in the impurity problem at site i , and the lattice Green's function is calculated as a matrix in the site space as

$$\mathbf{G}(z) = [\mathbf{I}\hbar z - \mathbf{H}_0[\mathbf{A}] - \text{diag}(\Sigma^{\text{imp}}(z))]^{-1}, \quad (61)$$

where $\text{diag}(\Sigma^{\text{imp}})$ is a diagonal matrix, with $\Sigma_i^{\text{imp}}(z)$ entries on the diagonal. This construction is general and can be used in the presence of translational symmetry breaking fields, disorder, and even used to probe spatially ordered phases. The DMFT approximation notably becomes exact in the limit of infinite coordination number, where the self-energy can be shown to be fully local [58], at least in the absence of magnetic fields.

We see that in the calculation of the bare propagator for the impurity problems, only the local Green's function plays a role, and this quantity is gauge invariant and spatially uniform. Therefore, even in the presence of the uniform magnetic field, all impurity problems are equivalent, and we may solve only one impurity problem and calculate the lattice Green's function as

$$\mathbf{G}(z) = [\mathbf{I}\hbar z - \mathbf{H}_0[\mathbf{A}] - \mathbf{I}\Sigma^{\text{imp}}(z)]^{-1}. \quad (62)$$

This leads to further simplifications. First, a local and spatially uniform self-energy is diagonal in the noninteracting eigenbasis ($\Sigma_{\sigma, ij} = \delta_{ij} \Sigma_{\sigma} \implies \langle \mathbf{k}, \sigma, m | \Sigma | \mathbf{k}', \sigma, m' \rangle = \delta_{\mathbf{k}, \mathbf{k}'} \delta_{m, m'} \Sigma_{\sigma}$, see Appendix I for proof) which means that the lattice Green's function is diagonal as well:

$$G_{\tilde{\mathbf{k}}, m, m', \sigma}(z) = \delta_{mm'} G_{\tilde{\mathbf{k}}, mm, \sigma}(z), \quad (63)$$

thus, we can drop the second eigenstate index and simply calculate the lattice Green's function as

$$G_{\tilde{\mathbf{k}}, m, \sigma}(z) = \frac{1}{\hbar z - \varepsilon_{\tilde{\mathbf{k}}, m, \sigma} - \Sigma_{\sigma}(z)}. \quad (64)$$

The local Green's function can then be obtained at low numerical cost from the knowledge of the local density of states $\rho_0(\varepsilon)$ as (see Appendix J for proof)

$$G_{ii, \sigma}(z) = \int d\varepsilon \frac{\rho_0(\varepsilon)}{\hbar z - \varepsilon - \Sigma_{\sigma}(z)}. \quad (65)$$

Therefore, the DMFT calculation for the Hubbard model in the magnetic field proceeds as the standard DMFT, and all the effects of the gauge field are contained in the noninteracting density of states [41]. In all our calculations we employ the numerical renormalization group (NRG) impurity solver [62–65] which works directly in real-frequency space, so no analytical continuation is needed to perform calculations of conductivity. The NRG solver has been previously thoroughly cross checked in Refs. [7, 11, 13].

2. Calculation of conductivity in DMFT

The fact that the Green's function is diagonal in the noninteracting eigenbasis leads to a simplification in the Kubo bubble [Eq. (57)]. One is left with only two summations over

eigenstates m :

$$\begin{aligned} \Lambda_{\mathbf{q}=0}^{\eta\eta',\text{disc}}(i\nu) &= \frac{t^2 e^2}{c\hbar^2} \frac{1}{N} \sum_{\sigma} \sum_{\mathbf{k},m,m'} \frac{1}{\beta} \sum_{i\omega} \\ &\times v_{\mathbf{k},m,m',\sigma}^{\eta} v_{\mathbf{k},m',m,\sigma}^{\eta'} G_{\mathbf{k},m,\sigma}(i\omega + i\nu) G_{\mathbf{k},m',\sigma}(i\omega). \end{aligned} \quad (66)$$

Furthermore, because the self-energy is local, the Green's function only depends on the energy of the eigenstate, so we can define $G(\varepsilon_{\mathbf{k},m,\sigma}, i\omega) \equiv G_{\mathbf{k},m,\sigma}(i\omega)$ and rewrite

$$\begin{aligned} \Lambda_{\mathbf{q}=0}^{\eta\eta',\text{disc}}(i\nu) &= \frac{t^2 e^2}{c\hbar^2} \sum_{\sigma} \frac{1}{\beta} \sum_{i\omega} \int d\varepsilon \int d\varepsilon' \\ &\times v_{\sigma}^{\eta,\eta'}(\varepsilon, \varepsilon') G(\varepsilon, i\omega + i\nu) G(\varepsilon', i\omega) \end{aligned} \quad (67)$$

with

$$\begin{aligned} v_{\sigma}^{\eta,\eta'}(\varepsilon, \varepsilon') &\equiv \frac{1}{N} \sum_{\mathbf{k},m,m'} \delta(\varepsilon - \varepsilon_{\mathbf{k},m,\sigma}) \\ &\times \delta(\varepsilon' - \varepsilon_{\mathbf{k},m',\sigma}) v_{\mathbf{k},m,m',\sigma}^{\eta} v_{\mathbf{k},m',m,\sigma}^{\eta'}. \end{aligned} \quad (68)$$

In Landau gauge, one has the symmetry $v_{\mathbf{k},m,m',\sigma}^x = -(v_{\mathbf{k},m',m,\sigma}^x)^*$ (see Appendix G), and therefore $v_{\mathbf{k},m,m',\sigma}^x v_{\mathbf{k},m',m,\sigma}^x = -|v_{\mathbf{k},m',m,\sigma}^x|^2$, which means $v_{\sigma}^{xx}(\varepsilon, \varepsilon')$ is purely real. On the contrary, as already noted in Ref. [38], $v_{\sigma}^{xy}(\varepsilon, \varepsilon')$ is purely imaginary.

The *sheet conductance* is related to the current-current correlation function through

$$\sigma^{\eta\eta'}(\nu) = c \frac{\Lambda^{\eta\eta'}(\nu) - \Lambda^{\eta\eta'}(\nu=0)}{i\nu}. \quad (69)$$

The z -axis lattice constant c cancels out c from $v_{\text{cell}} = a^2 c$ and its value is irrelevant. In the following we will discard the difference between the sheet conductance and the conductivity, and refer to σ as conductivity, even though it is actually sheet conductance and the units of the two quantities are different $[(\Omega m)^{-1}$ vs Ω^{-1} , respectively]; this is common practice in the field.

After several lines of algebra aimed at the analytical continuation to the real-axis frequency (see Appendix K), we obtain

$$\begin{aligned} \text{Re}\sigma_{\mathbf{q}=0}^{xx,\text{disc}}(\nu=0) &= t^2 \frac{e^2}{\hbar} \frac{1}{\pi} \sum_{\sigma} \int d\varepsilon \int d\varepsilon' v_{\sigma}^{xx}(\varepsilon, \varepsilon') \int d\omega \\ &\times \text{Im}G(\varepsilon, \omega) \text{Im}G(\varepsilon', \omega) n'_{\text{F}}(\omega), \end{aligned} \quad (70)$$

where $n'_{\text{F}}(\omega) = -\beta\hbar e^{\beta\hbar\omega} / (1 + e^{\beta\hbar\omega})^2$ is the derivative of the Fermi function.

For Hall conductivity one obtains [38]

$$\begin{aligned} \text{Re}\sigma_{\mathbf{q}=0}^{xy,\text{disc}}(\nu=0) &= -t^2 \frac{e^2}{\hbar} \frac{1}{\pi^2} \sum_{\sigma} \int d\varepsilon \int d\varepsilon' \text{Im}v_{\sigma}^{xy}(\varepsilon, \varepsilon') \int d\omega \int d\omega' \\ &\times \text{Im}G(\varepsilon, \omega) \text{Im}G(\varepsilon', \omega') \frac{n_{\text{F}}(\omega) - n_{\text{F}}(\omega')}{(\omega - \omega')^2}. \end{aligned} \quad (71)$$

An additional simplification is possible in the case of Hall conductivity when $U = 0$. In that case we have [22]

$$\begin{aligned} \text{Re}\sigma_{\mathbf{q}=0}^{xy,\text{disc}}(\nu=0; U=0) &= -t^2 \frac{e^2}{\hbar} \sum_{\sigma} \int d\varepsilon \int d\varepsilon' \text{Im}v_{\sigma}^{xy}(\varepsilon, \varepsilon') \frac{n_{\text{F}}(\varepsilon) - n_{\text{F}}(\varepsilon')}{(\varepsilon - \varepsilon')^2}. \end{aligned} \quad (72)$$

Finally, the resistivity is obtained as a matrix inverse

$$\begin{pmatrix} \rho^{xx} & \rho^{xy} \\ \rho^{yx} & \rho^{yy} \end{pmatrix} = \begin{pmatrix} \sigma^{xx} & \sigma^{xy} \\ \sigma^{yx} & \sigma^{yy} \end{pmatrix}^{-1}. \quad (73)$$

3. Vertex corrections in DMFT

Finally, to calculate the full current-current correlation function, one should in principle also compute the vertex corrections. At the level of the DMFT, in the absence of an external magnetic field, the vertex corrections cancel due to the well-known argument due to Khurana [42]. As we show in the following, a generalized Khurana argument holds even in the presence of the magnetic field. In the following we first derive the Khurana argument in real space, and then generalize it to the case of nonzero magnetic fields.

We start first by writing the vertex corrections in orbital space, in the most general way:

$$\begin{aligned} \Lambda_{\mathbf{q}=0}^{\eta\eta',\text{conn}}(\tau - \tau') &= t^2 \frac{e^2}{a^2 c^2 \hbar^2} \sum_{\sigma, \sigma'} \sum_{b, b' \in \{0,1\}} (-1)^{b+b'} \\ &\times \frac{1}{N^2} \sum_{\mathbf{r}, \mathbf{r}'} C^b[\gamma_{\eta}(\mathbf{r})] C^{b'}[\gamma_{\eta'}(\mathbf{r}')] \\ &\times \sum_{\mathbf{r}_1, \mathbf{r}_2, \mathbf{r}_3, \mathbf{r}_4} \int d\tau_1 d\tau_2 d\tau_3 d\tau_4 \\ &\times G_{\mathbf{r}_1, \mathbf{r} + b\mathbf{e}_{\eta}, \sigma}(\tau_1 - \tau) G_{\mathbf{r} + (1-b)\mathbf{e}_{\eta}, \mathbf{r}_2, \sigma}(\tau - \tau_2) \\ &\times F((\mathbf{r}_1, \tau_1), (\mathbf{r}_2, \tau_2), (\mathbf{r}_3, \tau_3), (\mathbf{r}_4, \tau_4)) \\ &\times G_{\mathbf{r}' + (1-b')\mathbf{e}_{\eta'}, \mathbf{r}_3, \sigma'}(\tau' - \tau_3) G_{\mathbf{r}_4, \mathbf{r}' + b'\mathbf{e}_{\eta'}, \sigma'}(\tau_4 - \tau'), \end{aligned} \quad (74)$$

as illustrated in Fig. 1(a). In the absence of external magnetic field or spontaneous symmetry breaking, $G_{\mathbf{r}, \mathbf{r}'}$ has full lattice symmetry and depends only on the difference $G_{\mathbf{r} - \mathbf{r}'}$. However, there is no symmetry operation which guarantees cancellation of all terms. There is only one symmetry operation that leaves the Green's functions intact and flips the overall sign, but it does change the full vertex. It can be formulated either for internal variables $\mathbf{r}_1, \mathbf{r}_2, b$ or for $\mathbf{r}_3, \mathbf{r}_4, b'$, and we illustrate the latter case in Fig. 1(b). The transformation can be formulated as follows:

$$\begin{aligned} \mathbf{r}' &\rightarrow -\mathbf{r}' + \mathbf{r}_3 + \mathbf{r}_4 - \mathbf{e}_{\eta'}, & b' &\rightarrow 1 - b', \\ (\mathbf{r}_3, \tau_3) &\leftrightarrow (\mathbf{r}_4, \tau_4). \end{aligned} \quad (75)$$

The flip of b' changes the overall sign, but the exchange of terminals of the full vertex function changes its value in no obvious way, and there is no cancellation in the general case.

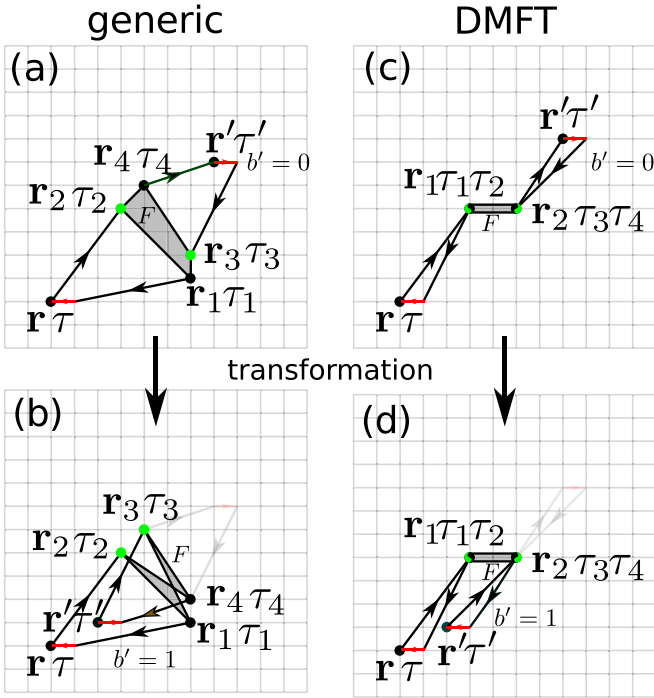


FIG. 1. Real-space diagrammatic representation of a contribution to the connected part of the current-current correlation function. F is the full vertex, red segments indicate a term in the current operator connecting two nearest-neighbor sites in the x direction; swapping the direction of the red arrow changes its sign. Top panels: for generic case [left, Eq. (74)] and DMFT [right, Eq. (76)]. Bottom panels: after the transformation in Eqs. (75) (left) and (77) (right).

However, in DMFT there is an additional simplification that the full vertex F depends on only two spatial indices:

$$\begin{aligned}
 & \Lambda_{\mathbf{q}=0}^{\eta\eta',\text{conn}}(\tau - \tau') \\
 &= t^2 \frac{e^2}{a^2 c^2 \hbar^2} \sum_{\sigma, \sigma'} \sum_{b, b' \in \{0,1\}} (-1)^{b+b'} \\
 & \times \frac{1}{N^2} \sum_{\mathbf{r}, \mathbf{r}'} C^b[\gamma_\eta(\mathbf{r})] C^{b'}[\gamma_{\eta'}(\mathbf{r}')] \sum_{\mathbf{r}_1, \mathbf{r}_2} \int d\tau_1 d\tau_2 d\tau_3 d\tau_4 \\
 & \times G_{\mathbf{r}_1, \mathbf{r}+b\mathbf{e}_\eta, \sigma}(\tau_1 - \tau) G_{\mathbf{r}+(1-b)\mathbf{e}_\eta, \mathbf{r}_1, \sigma}(\tau - \tau_2) \\
 & \times F((\mathbf{r}_1, \tau_1), (\mathbf{r}_1, \tau_2), (\mathbf{r}_2, \tau_3), (\mathbf{r}_2, \tau_4)) \\
 & \times G_{\mathbf{r}'+(1-b')\mathbf{e}_{\eta'}, \mathbf{r}_2, \sigma'}(\tau' - \tau_3) G_{\mathbf{r}_2, \mathbf{r}'+b'\mathbf{e}_{\eta'}, \sigma'}(\tau_4 - \tau').
 \end{aligned} \tag{76}$$

In that case, a transformation

$$\mathbf{r}' \rightarrow -\mathbf{r}' - \mathbf{e}_{\eta'} + 2\mathbf{r}_2, \quad b' \rightarrow 1 - b' \tag{77}$$

keeps both the Green's functions and the full vertex intact, while changing the overall sign. Then the two symmetry-connected terms together read as (up to a prefactor)

$$\begin{aligned}
 & G_{\mathbf{r}'+(1-b')\mathbf{e}_{\eta'}, \mathbf{r}_2, \sigma'}(\tau' - \tau_3) G_{\mathbf{r}_2, \mathbf{r}'+b'\mathbf{e}_{\eta'}, \sigma'}(\tau_4 - \tau') \\
 & - G_{-\mathbf{r}'+2\mathbf{r}_2-(1-b')\mathbf{e}_{\eta'}, \mathbf{r}_2, \sigma'}(\tau' - \tau_3) \\
 & \times G_{\mathbf{r}_2, -\mathbf{r}'+2\mathbf{r}_2-b'\mathbf{e}_{\eta'}, \sigma'}(\tau_4 - \tau').
 \end{aligned} \tag{78}$$

When the lattice preserves inversion symmetry, one has $G_{\mathbf{r}, \mathbf{r}'} = G_{\mathbf{r}-\mathbf{r}'} = G_{\mathbf{r}'-\mathbf{r}}$, and the above two terms always cancel. This is the real-space version of the Khurana argument.

However, when there is magnetic field, there are additional complications. Nevertheless, the full vertex is a gauge-invariant quantity, as the irreducible vertex in the particle-hole channel Γ^{ph} is fully local and therefore gauge invariant and spatially uniform $\Gamma_{ijkl}^{\text{ph}} = \delta_{ij}\delta_{jk}\delta_{kl}\Gamma^{\text{ph}}$. This comes as DMFT is the local approximation of the Luttinger-Ward functional [58,66], and $\Gamma_{ijkl}^{\text{ph}} = \frac{\partial^2 \Phi[\mathbf{G}]}{\partial G_{ij} \partial G_{kl}} |_{\mathbf{G}=\mathbf{G}_{\text{exact}}} \approx \frac{\partial^2 \Phi^{\text{DMFT}}[\{G_{ii}\}]}{\partial G_{ij} \partial G_{kl}} |_{\mathbf{G}=\mathbf{G}_{\text{DMFT}}}$. Therefore, we have

$$\begin{aligned}
 F_{ii,jj} &= \delta_{ij}\Gamma^{\text{ph}} + \Gamma^{\text{ph}} G_{ij} G_{ji} \Gamma^{\text{ph}} \\
 & + \sum_l \Gamma^{\text{ph}} G_{il} G_{li} \Gamma^{\text{ph}} G_{lj} G_{jl} \Gamma^{\text{ph}} + \dots \\
 &= \delta_{ij}\Gamma^{\text{ph}} + \Gamma^{\text{ph}} \bar{G}_{ij} \bar{G}_{ji} \Gamma^{\text{ph}} \\
 & + \sum_l \Gamma^{\text{ph}} \bar{G}_{il} \bar{G}_{li} \Gamma^{\text{ph}} \bar{G}_{lj} \bar{G}_{jl} \Gamma^{\text{ph}} + \dots
 \end{aligned} \tag{79}$$

and F is clearly expressed entirely with gauge-invariant quantities. Here we have omitted spin and temporal arguments and the corresponding sums and integrals for the sake of brevity, as they do not play a role in the proof.

In the presence of the magnetic field, the Green's function does not satisfy $G_{\mathbf{r}, \mathbf{r}'} = G_{\mathbf{r}-\mathbf{r}'} = G_{\mathbf{r}'-\mathbf{r}}$ and it is not *a priori* clear that the terms in Eq. (78) cancel. We can, however, rewrite them in terms of \bar{G} :

$$\begin{aligned}
 & e^{i\mathbf{f}_{\mathbf{r}'+(1-b')\mathbf{e}_{\eta'}, \mathbf{r}_2} \cdot \mathbf{r}'} \bar{G}_{\mathbf{r}'+(1-b')\mathbf{e}_{\eta'}, \mathbf{r}_2, \sigma'}(\tau' - \tau_3) \\
 & \times e^{i\mathbf{f}_{\mathbf{r}_2, \mathbf{r}'+b'\mathbf{e}_{\eta'}} \cdot \mathbf{r}_2} \bar{G}_{\mathbf{r}_2, \mathbf{r}'+b'\mathbf{e}_{\eta'}, \sigma'}(\tau_4 - \tau') \\
 & - e^{i\mathbf{f}_{-\mathbf{r}'+2\mathbf{r}_2-(1-b')\mathbf{e}_{\eta'}, \mathbf{r}_2} \cdot \mathbf{r}_2} \bar{G}_{-\mathbf{r}'+2\mathbf{r}_2-(1-b')\mathbf{e}_{\eta'}, \mathbf{r}_2, \sigma'}(\tau' - \tau_3) \\
 & \times e^{i\mathbf{f}_{\mathbf{r}_2, -\mathbf{r}'+2\mathbf{r}_2-b'\mathbf{e}_{\eta'}} \cdot \mathbf{r}_2} \bar{G}_{\mathbf{r}_2, -\mathbf{r}'+2\mathbf{r}_2-b'\mathbf{e}_{\eta'}, \sigma'}(\tau_4 - \tau').
 \end{aligned} \tag{80}$$

As \bar{G} satisfies $\bar{G}_{\mathbf{r}, \mathbf{r}'} = \bar{G}_{\mathbf{r}-\mathbf{r}'} = \bar{G}_{\mathbf{r}'-\mathbf{r}}$, the products of \bar{G} are the same in both terms, thus, what determines whether there is cancellation or not is

$$e^{i\mathbf{f}_{\mathbf{r}'+(1-b')\mathbf{e}_{\eta'}, \mathbf{r}_2} \cdot \mathbf{r}'} e^{i\mathbf{f}_{\mathbf{r}_2, \mathbf{r}'+b'\mathbf{e}_{\eta'}} \cdot \mathbf{r}_2} - e^{i\mathbf{f}_{-\mathbf{r}'+2\mathbf{r}_2-(1-b')\mathbf{e}_{\eta'}, \mathbf{r}_2} \cdot \mathbf{r}_2} e^{i\mathbf{f}_{\mathbf{r}_2, -\mathbf{r}'+2\mathbf{r}_2-b'\mathbf{e}_{\eta'}} \cdot \mathbf{r}_2}. \tag{81}$$

In Landau gauge and for, say, $\eta' = x$, we get

$$\begin{aligned}
 & e^{i\frac{ea^2 B_z}{2\hbar} (y_2 - y') [x' + x_2 + (1-b)']} e^{i\frac{ea^2 B_z}{2\hbar} (y' - y_2) (x' + x_2 + b')} \\
 & - e^{i\frac{ea^2 B_z}{2\hbar} (-y_2 + y') [3x_2 - x' - (1-b)']} e^{i\frac{ea^2 B_z}{2\hbar} (-y' + y_2) (-x' - b' + 3x_2)} \\
 & = e^{i\frac{ea^2 B_z}{2\hbar} (y_2 - y') (1-2b')} - e^{i\frac{ea^2 B_z}{2\hbar} B_z (-y_2 + y') (-1+2b')} \\
 & = 0.
 \end{aligned} \tag{82}$$

This means that the vertex corrections cancel. This proof is immediately valid for both Λ^{xx} and Λ^{yx} . Having in mind a completely analogous transformation of \mathbf{r} and b , this proof holds also for Λ^{xy} (a different proof was given for Λ^{xy} in Ref. [38]). However, we also want to check what happens with $\eta' = y$, which is relevant for Λ^{yy} . In that case, the

transformation affects also $C^{b'}$ [$\gamma_y(\mathbf{r}')$] so we need to take that into account:

$$\begin{aligned}
& e^{i(1-2b')\frac{ea^2B_z}{\hbar}x'} e^{if_{r'+(1-b')e_{y'}}r_2} e^{if_{r_2,r'+b'e_{y'}}} - e^{-i(1-2b')\frac{ea^2B_z}{\hbar}(-x'+2x_2)} e^{if_{-r'+2r_2-(1-b')e_{y'}}r_2} e^{if_{r_2,-r'+2r_2-b'e_{y'}}} \\
&= e^{i(1-2b')\frac{ea^2B_z}{\hbar}x'} e^{i\frac{ea^2B_z}{2\hbar}[y_2-y'+(1-b')(x_2+x')]} e^{i\frac{ea^2B_z}{2\hbar}(y'+b'-y_2)(x_2+x')} - e^{-i(1-2b')\frac{ea^2B_z}{\hbar}(-x'+2x_2)} \\
&\quad \times e^{i\frac{ea^2B_z}{2\hbar}[y'-y_2+(1-b')(3x_2-x')]} e^{i\frac{ea^2B_z}{2\hbar}(-y'+y_2-b')(-x'+3x_2)} \\
&= e^{i(1-2b')\frac{ea^2B_z}{\hbar}x'} e^{i\frac{ea^2B_z}{2\hbar}(-1+2b')(x_2+x')} - e^{-i(1-2b')\frac{ea^2B_z}{\hbar}(-x'+2x_2)} e^{i\frac{ea^2B_z}{2\hbar}[(1-2b')(3x_2-x')]} \\
&= e^{i\frac{ea^2B_z}{2\hbar}[2(1-2b')x'-(-1-2b')(x_2+x')]} - e^{i\frac{ea^2B_z}{2\hbar}[2(1-2b')x'-4(1-2b')x_2+(1-2b')(3x_2-x')]} \\
&= e^{i\frac{ea^2B_z}{2\hbar}(x'-2b'x'-x_2+2b'x_2)} - e^{i\frac{ea^2B_z}{2\hbar}(x'-2b'x'-x_2+2b'x_2)} \\
&= 0.
\end{aligned} \tag{83}$$

Indeed, the vertex corrections for Λ^{yy} cancel as well. As we have shown that the Kubo bubble is gauge invariant (see Appendix F), and having that the full correlation function needs to be gauge invariant as it relates to observables, the proof given here is fully general, even though it is formulated in Landau gauge. The proof also does not depend on whether there is Zeeman term in the Hamiltonian or not.

III. RESULTS

A. Density of states and spectral function

1. Noninteracting density of states

In the DMFT, the magnetic field enters through the noninteracting density of states $\rho_0(\omega)$. The magnetic field dependence of $\rho_0(\omega)$ (the famous Hofstadter butterfly [55]) is shown in Fig. 2. This result was obtained with lattice size $L = 1999$, and about 4000 energy bins, which sets the resolution and the minimal size of an energy gap that one can observe.

2. Translation-invariant spectral function

As we have already proven, on a finite lattice $L \times L$ and $L = q$, there is no dependence of the Hamiltonian on

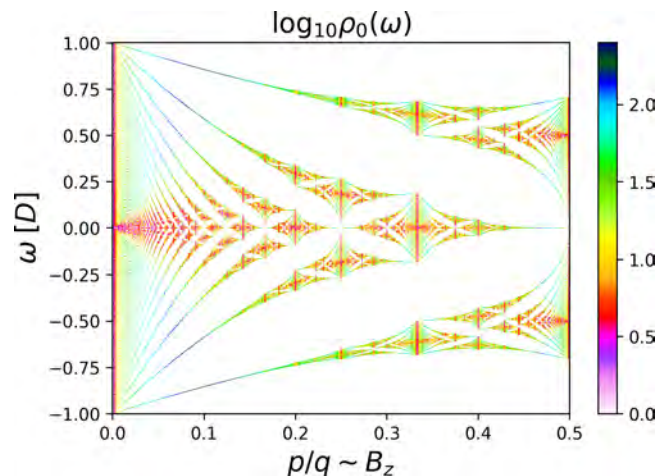


FIG. 2. Noninteracting density of states, as a function of frequency and magnetic field (the Hofstadter butterfly [55]).

k_y . A straightforward basis change of the Green's function to the original \mathbf{k} states in the full BZ yields a meaningless result for the spectral function with no k_y dependence whatsoever. Moreover, this result is gauge dependent, as the choice of a slightly different gauge $\mathbf{A} \sim (-y, 0)$ would yield a spectral function result with no k_x dependence instead.

One is therefore interested in the translationally invariant \tilde{G} , as it has all the lattice symmetries, and can ultimately be Fourier transformed into momentum space. We show this result in the noninteracting case in Fig. 3. We have used a small broadening $\Sigma(z) = -i \text{sgn}(\text{Im}z)\eta$, $\eta = 0.02$, to regularize the results. We observe that the result for the imaginary part of \tilde{G} is not necessarily negative, which is a signature of a breaking of causality, and thus the result is not a proper physical spectral function. As expected, the nonphysical features subside as the magnetic field is taken to zero. Note also that $\tilde{G}_{\text{loc}} = G_{\text{loc}}$, so the causality of the resulting local Green's function is restored upon the summation over momenta.

3. Local spectra from DMFT

In Fig. 4 we present the DMFT(NRG) results for $\text{Im}G_{\text{loc}}(\omega)$, at different values of magnetic field, and fixed $U = 2.5D$, $n = 0.85$, and $T = 0.025D$, which corresponds to the regime of the doped Mott insulator. On the left panel we show the full frequency range, while on the right panel we focus on the quasiparticle part of the spectrum. Increasing the magnetic field appears to affect an ever growing range of frequencies around $\omega = 0$, but up to the highest fields the effect is restricted to the quasiparticle peak and no significant change is observed in the Hubbard bands, apart from the lower Hubbard band getting flatter. No apparent change at all is observed below $p/q = 0.1$ for these values of model parameters.

B. Conductivity

1. Longitudinal dc conductivity $\sigma^{xx}(v = 0)$

We start by inspecting the effect of the magnetic-field dependence of the self-energy on the conductivity. In the upper panel of Fig. 5 we show $1/\sigma^{xx}(v = 0)$ calculated with the self-energy obtained from the DMFT(NRG) calculation for

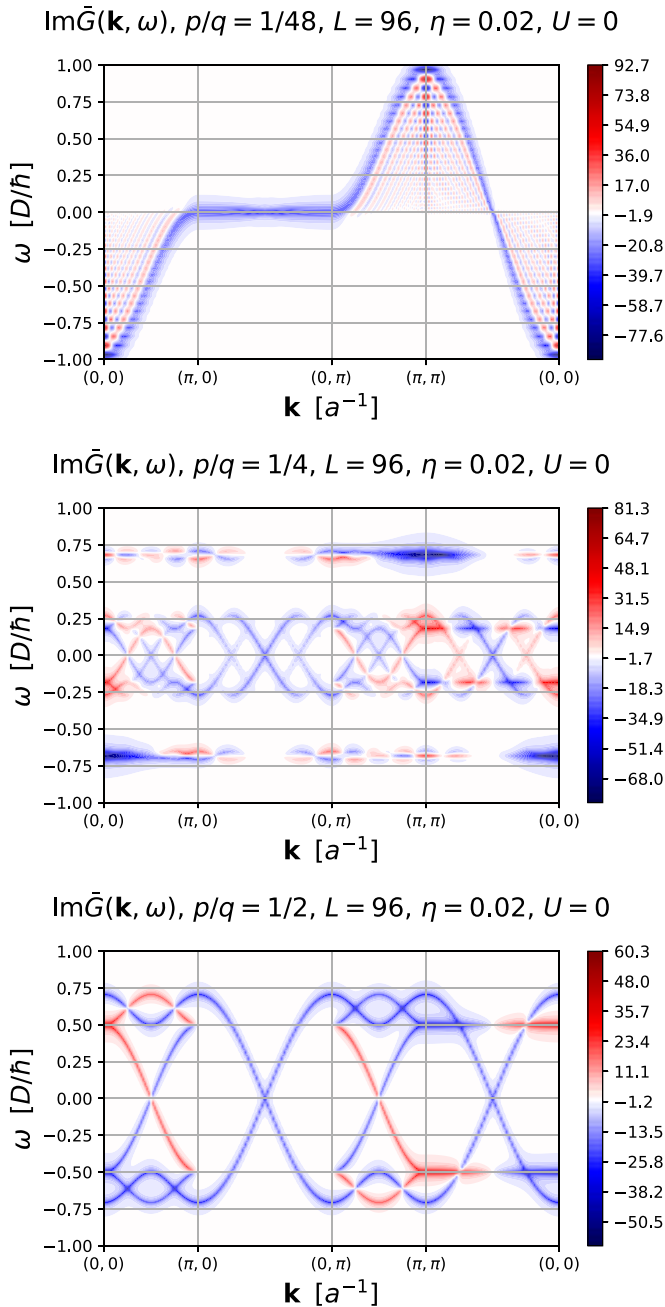


FIG. 3. Spectrum of the translation-invariant Green's function $\text{Im}\bar{G}_{\mathbf{k}}(\omega)$. The examples are given for $U = 0$ with a broadening $\eta = 0.02D$, and at three different values of p/q , as indicated in panel titles. The spectrum is not negative definite, and is therefore not indicative of the physical spectral function.

the given B_z (black curve), and compare it to the one obtained with the self-energy obtained in the $B_z = 0$ calculation; in that case the magnetic-field enters the calculation only through the current vertex $v_{\mathbf{k},m,m',\sigma}^{xx}$. Here, we can choose to fix the chemical potential to the one corresponding to the $B_z = 0$ calculation, which will lead to some density variation as the magnetic field is increased (red curve); otherwise, we can correct the chemical potential for each given B_z so that the overall occupancy is fixed (lime curve).

We see that there is excellent agreement between all three curves. The parts of the black curve that are missing are due to our inability to properly converge the DMFT(NRG) calculation at those values of B_z . As finite- B_z DMFT(NRG) calculations are difficult and require significant computational time, it is a very important observation that we can obtain solid finite B_z results by using the self-energy from the $B_z = 0$ calculation. This way, the bottleneck of our calculation becomes the calculation of the conductivity, rather than the DMFT solver. In the regime of the main interest, this does not present a significant additional approximation. Therefore, in the remainder of the paper we fix $\Sigma = \Sigma(B_z = 0)$ and correct μ at each B_z so that the overall density is fixed, unless stated otherwise.

In the bottom panel of Fig. 5 we present the density of states at the Fermi level [$\sim \text{Im}G(\omega = 0)$], as well as the effective scattering rate [$\sim \text{Im}\Sigma(\omega = 0)$]. The oscillations in these two quantities as functions of the magnetic field appear synchronous. However, the oscillations in the conductivity follow a completely different pattern. The oscillations in the density of states and the scattering rate can be readily connected with the Shubnikov-de Haas effect, where the period of oscillations in the space of inverse magnetic field is inversely proportional to the surface area of the Fermi sea (roughly the density $\langle n_\sigma \rangle$), while the oscillations of the conductivity appear to correspond to the full area of the BZ. This mismatch in the oscillation frequencies of the spectral and transport properties is, however, restricted to only certain parameter regimes. The high-frequency oscillations have been previously identified in the experiment [44–47] and dubbed the Brown-Zak (B-Z) oscillations. We discuss this phenomenon in more detail in Sec. III B 3, and in Ref. [48] which is devoted to this very topic. In Appendix L we check that no $p/q = 1$ oscillations are present in thermodynamic potentials.

We also cross-check the results of our finite B_z calculation against the reference $B_z = 0$ results, in the limit of low field. As the results are obtained numerically in rather different ways, this is a stringent test of our formalism and implementations. In Fig. 6 we show the DMFT results at $U = 2.5D$, at four different levels of doping ($n = 1$ is half-filling), at $B_z = 0$ and at three smallest possible fields in a finite B_z calculation with $L = q = 1999$. At high temperatures, small field does not significantly affect the result, and finite-field results are on top of the zero-field result, thus validating our numerics. At low temperature, the effect of the field becomes observable, but the results do tend towards the $B_z = 0$ result as the field is decreased.

Next, we inspect the effect of the magnetic field on the temperature dependence of $\sigma_{xx}^{-1}(\nu = 0)$ on Fig. 7. At low temperature, the behavior drastically depends on the precise choice of the magnetic field. At high temperature the behavior is weakly modified, and one still observes roughly linear dependence. At very high fields, the values appear increased by a constant prefactor, which means that the slope of the linear dependence is also increased. This can be more easily confirmed by looking at the linear scale plots in Fig. 8. The effect of the magnetic field appears somewhat insensitive to the strength of the interaction, and the overall trend appears similar in all three panels on the left side of Fig. 7. We are able to roughly collapse the curves at three different values of U by

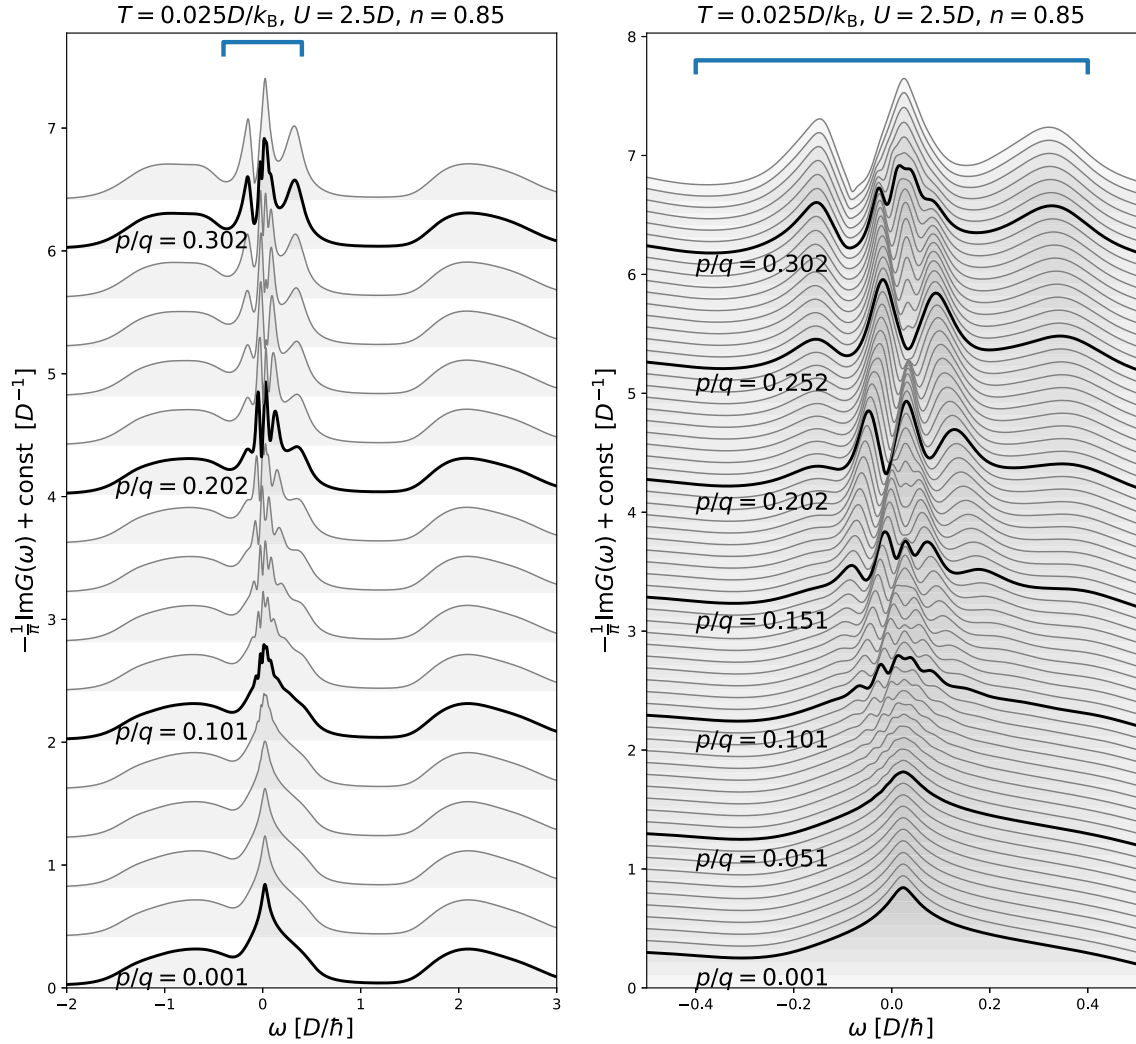


FIG. 4. Local density of states as a function of magnetic field. Left: full frequency range. Right: quasiparticle part of the spectrum. The result is obtained with the DMFT(NRG). The parameters are $U = 2.5D$, $\langle n_\sigma \rangle = 0.425$, $T = 0.025D/k_B$. The calculation was performed with $L = q = 997$.

simply rescaling the temperature $T \rightarrow T/T^*(U)$, with $T^*(U)$ roughly a linear function of U . The scaling appears particularly valid between $U = 2.5$ and $U = 4$, while the $U = 1$ curves somewhat deviate.

Finally, in Fig. 9 we present the magnetic-field dependence of the conductivity, at a fixed temperature and doping. At low temperature one observes increasingly strong oscillations as magnetic field is increased. At low fields, the oscillations are relatively small and regular, which corresponds to the SdH regime, while at strong fields the oscillations cover multiple orders of magnitude, and exhibit no simple pattern as a function of the magnetic field. (This is the quantum limit dominated by the lowest Landau levels).

2. Hall conductivity and resistivity

In Fig. 10 we show results for direct current σ^{xy} , $1/\sigma^{xx}$ as well as ρ^{xy} and ρ^{xx} . We see that σ^{xy} exhibits a nonmonotonic dependence on the magnetic field, and also some oscillation, similar to σ^{xx} . The difference appears to be that when σ^{xx} has

a local maximum, σ^{xy} has a local extremum in the value of its first derivative. The results presented in this plot correspond to the high-frequency oscillation regime, where the maxima in σ^{xx} coincide with $p/q = 1/q$. This behavior is in line with the experimental observations in Ref. [45]. We also see that, as expected, σ^{xy} tends to zero as magnetic field is decreased. The effect of σ^{xy} on ρ^{xx} is not negligible, and one clearly has $\rho^{xx} \neq 1/\sigma^{xx}$. Nevertheless, the oscillatory behavior of ρ^{xx} appears very similar to that of $1/\sigma^{xx}$ and in phase with it.

We further study the behavior of σ^{xy} in the limit of $U = 0$ where the calculation can be performed at low numerical cost. The results are presented in Fig. 11. First we look at the temperature dependence (upper panel). We see that σ^{xy} falls off exponentially with increasing temperature. At $T = 0$ the result corresponds to the Chern number of the topological insulator, whenever the chemical potential falls in an energy gap. We see that decreasing field produces gaps with ever larger Chern numbers. On the middle panel we look at this dependence more closely, and see that at a given chemical potential, the Chern number grows in a power-law fashion

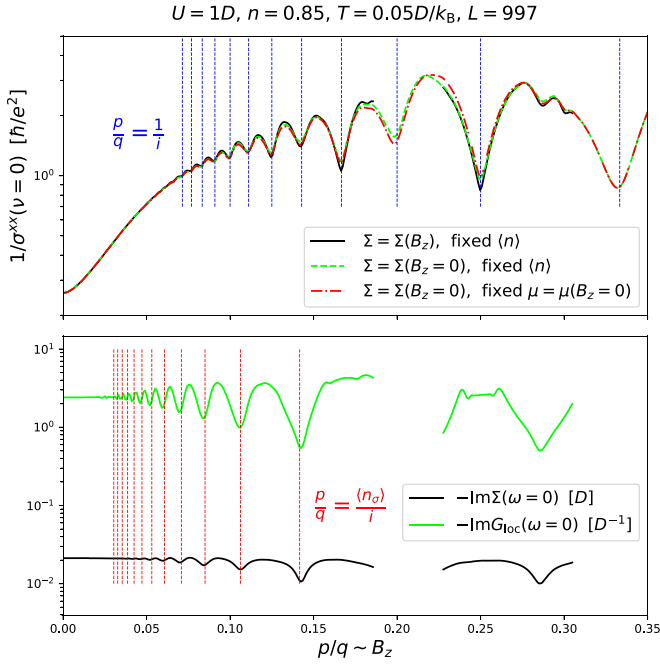


FIG. 5. Upper panel: conductivity obtained with the full DMFT(NRG) calculation (black line), and the simplified calculation where the self-energy is taken from the zero-field DMFT(NRG) calculation, and the chemical potential is either corrected to fix the overall density (lime line) or not (red line). Vertical lines indicate $p/q = 1/i$ with i integer, which coincides with the dips in the inverse conductivity. Lower panel: dependence on the magnetic field of the density of states at the Fermi level (lime line) and the scattering rate (black line). Vertical lines indicate $p/q = \langle n_\sigma \rangle / i$, which roughly coincides with the dips in both the scattering rate and the density of states at the Fermi level.

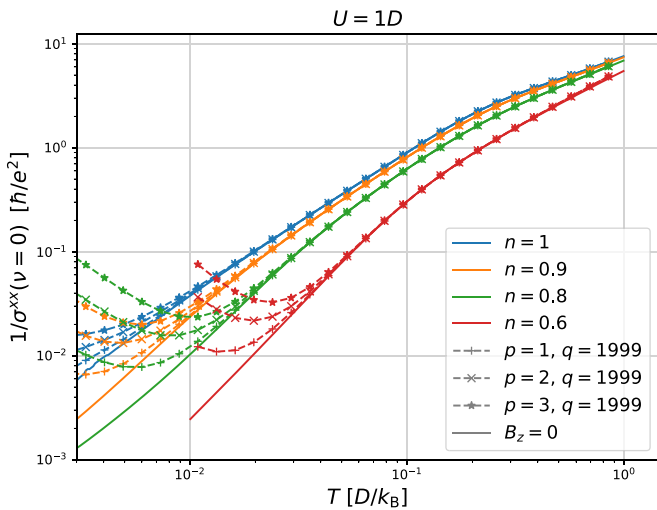


FIG. 6. Cross-check between the zero-field formalism and the finite-field formalism at weak fields. Solid lines are the $B_z = 0$ DMFT(NRG) result, obtained within the zero-field formalism, at different values of density. We keep $U = 2.5D$ fixed. Dashed lines with symbols are obtained within finite B_z formalism, at three lowest values of the field, at $L = q = 1999$.

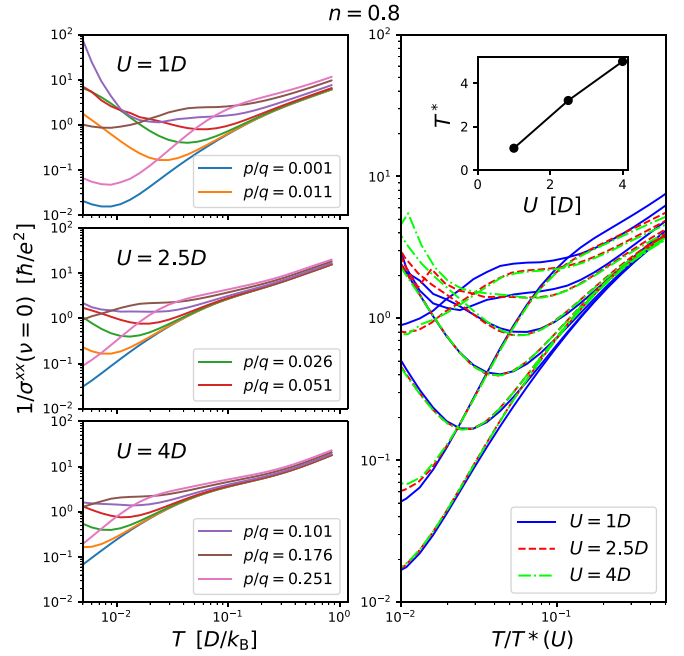


FIG. 7. Left panels: the T dependence of the inverse conductivity at different values of the field and fixed coupling and density. Right panel: the same results with rescaled temperature $T \rightarrow T/T^*(U)$. $T^*(U)$ is given in the inset.

with $1/B_z$. It is clear that this law does not have a well-defined limiting behavior at $B_z = 0$, as in the absence of magnetic field there are no gaps and strictly $\sigma^{xy} = 0$. This is an indication of the fractal structure of the density of states at low fields: the gaps become smaller and smaller, but more and more numerous, and fully disappear only strictly at $B_z = 0$. However, this ill-defined behavior is corrected at finite values of the interaction (Fig. 10), and one observes a downturn of σ^{xy} at a finite value of the field, and σ^{xy} tends to zero smoothly as $B_z \rightarrow 0$.

Finally, we study the dependence of σ^{xy} on the chemical potential, at several different values of the field and $T = 0$, in the bottom panel of Fig. 11. One has $\sigma^{xy}(\mu) = -\sigma^{xy}(-\mu)$. The plateaus in the value of Hall conductivity are indications of gaps in the density of states and are always found at integer values. We benchmark our implementation with the data in Ref. [38] in Appendix M.

3. Quantum oscillations of $1/\sigma^{xx}$

As already noted in Sec. III B 1, the conductivity displays oscillatory behavior as a function of magnetic field. We start by inspecting the region of the phase diagram where notable oscillatory behavior is present. We define a characteristic $(p/q)^*(T; n, U)$ (denoted by shaded circles in Fig. 9) as the value of magnetic field at which the first extremum in $1/\sigma^{xx}(B_z \sim p/q)$ occurs ($1/\sigma^{xx}$ initially grows, so the first extremum is always a maximum). Oscillations in the slope of $1/\sigma^{xx}(B_z \sim p/q)$ might survive even below this characteristic value of the field [or inversely at temperatures higher than $T((p/q)^*)$]; the amplitude of oscillations dies out with temperature exponentially, as in Lifshitz-Kosevich law [43] (see Fig. 12; the oscillatory part of $1/\sigma^{xx}(p/q)$ is extracted

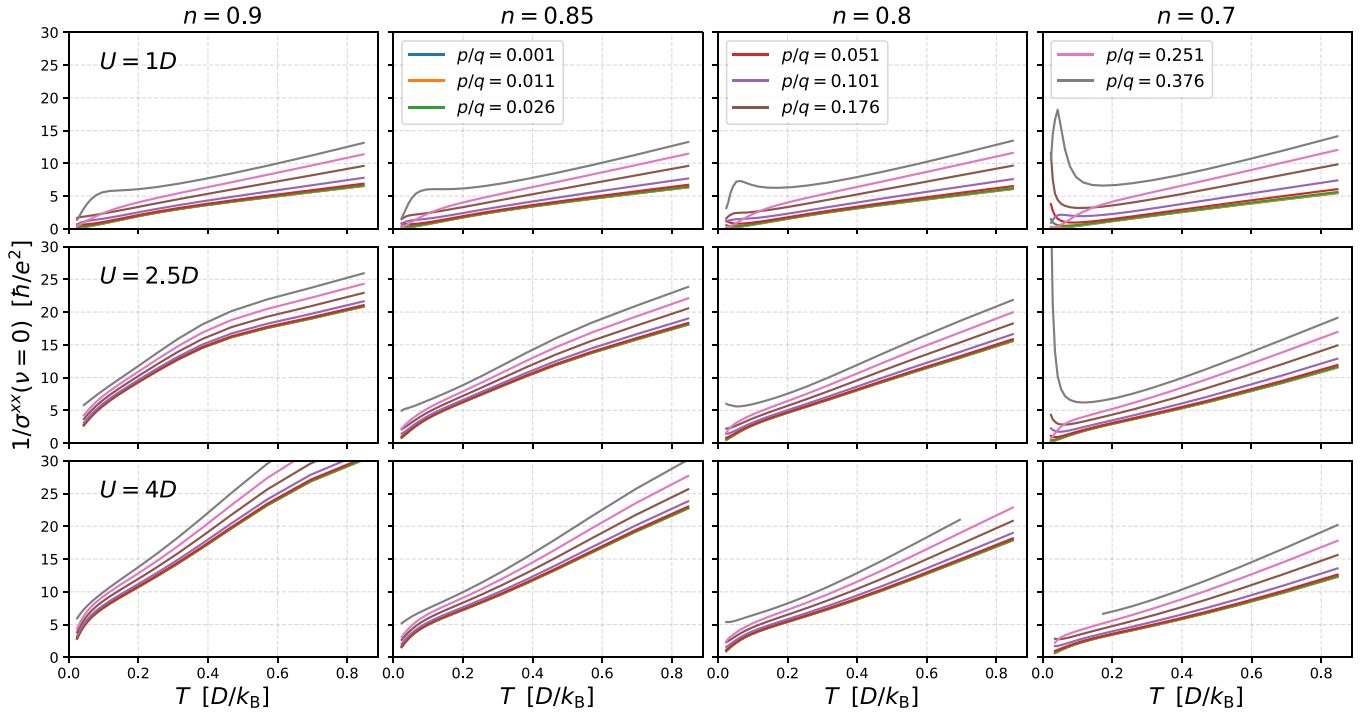


FIG. 8. Inverse conductivity on the linear scale. Columns are different dopings, rows are different values of interaction. Different curves are different values of the field.

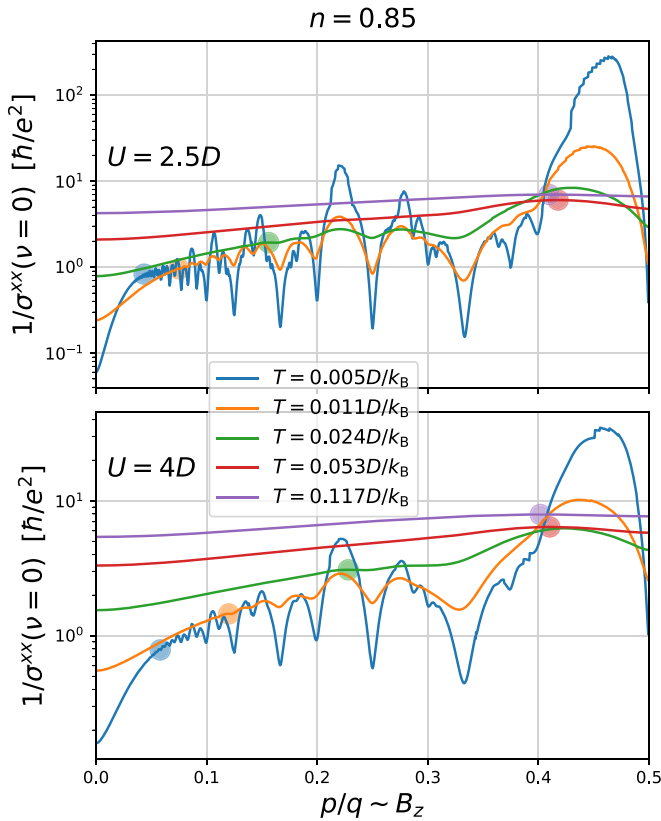


FIG. 9. Magnetic-field dependence of the inverse conductivity at two values of coupling constant, and various temperatures. Shaded circles correspond to the first extremum $(p/q)^*$ (see text).

by subtracting from the full result the average value in the range $[p/q - f(p/q), p/q + f(p/q)]$, where $f \sim p^{0.7}$. The quantity $T((p/q)^*)$ is presented in Fig. 13. We denote the doping with $\delta = 1 - n$.

We see that there is always roughly a plateau in $T((p/q)^*)$, followed by a kink and a near saturation of $(p/q)^*(T)$ at high temperature. This is because above a certain temperature, no oscillations are present at any value of magnetic field,

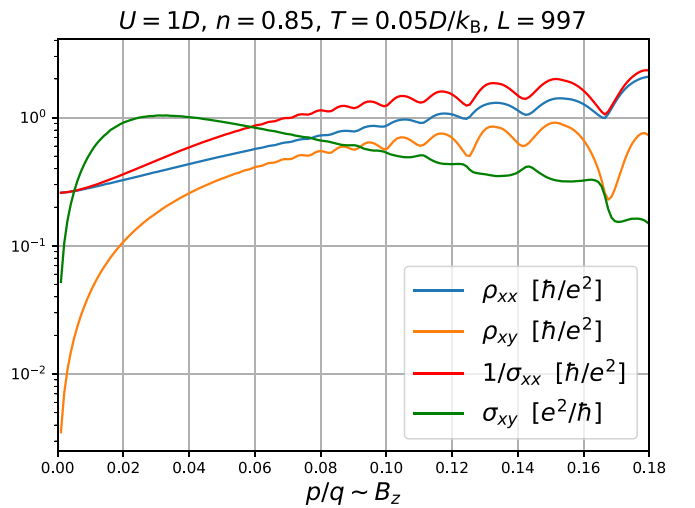


FIG. 10. Different components of the conductivity and resistivity tensors, showing the effect of the Hall component on the relation between the longitudinal resistivity ρ^{xx} and the inverse longitudinal conductivity $1/\sigma^{xx}$.

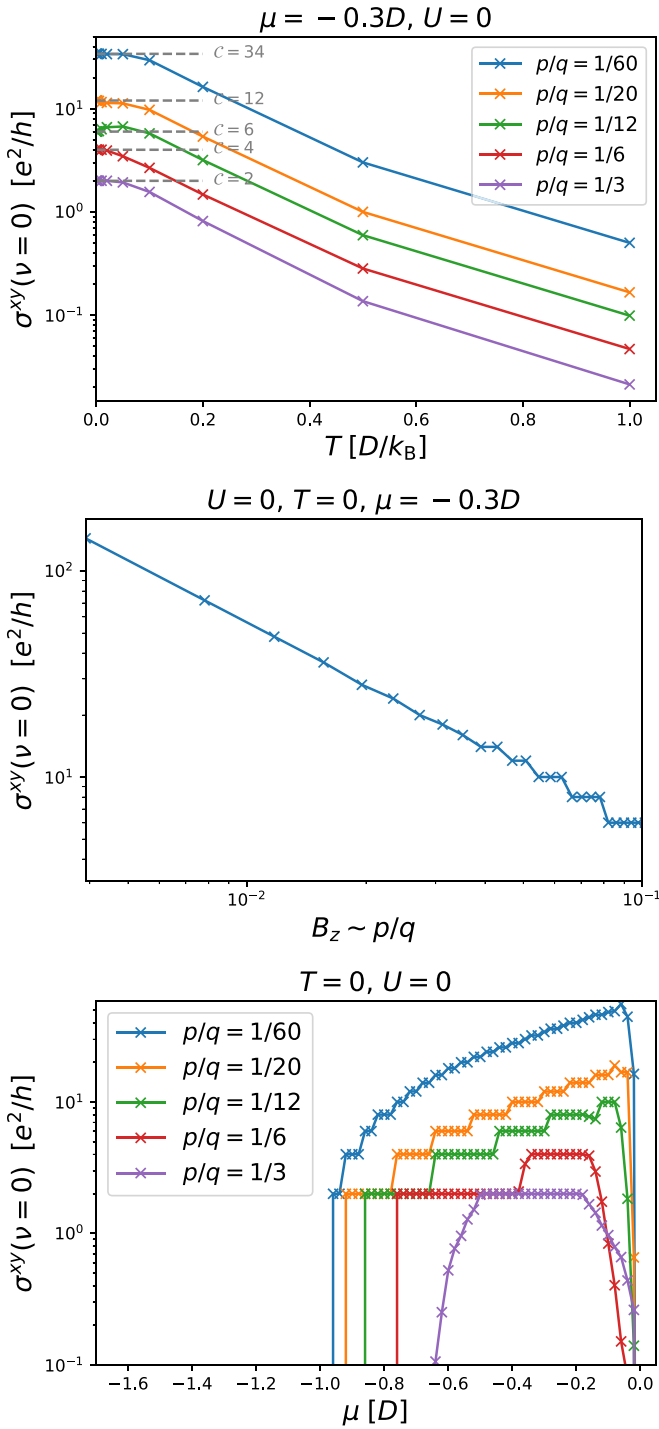


FIG. 11. Hall conductivity at $U = 0$. Top: temperature dependence of the Hall conductivity for a selection of magnetic fields. Gray lines indicate the value at $T = 0$, which is the Chern number for the corresponding topological insulator. Center: field dependence of the Hall conductivity at zero temperature. Bottom: chemical potential dependence of the Hall conductivity for a selection of magnetic fields.

and there remains at most a single maximum below $p/q = 0.5$. The maximum can persist at a roughly fixed p/q up to some temperature, and then ultimately moves to $p/q = \frac{1}{2}$. The shape of $(p/q)^*(T)$ appears nearly universal for all δ, U . We

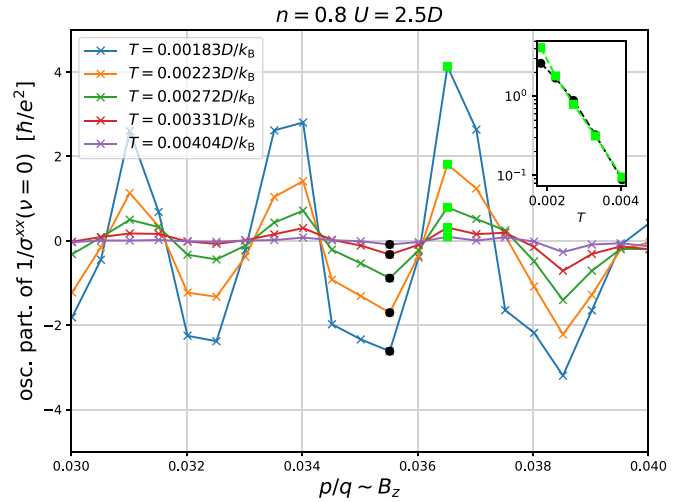


FIG. 12. Zoom-in on the oscillatory part of the magnetic-field dependence of inverse conductivity, in a range of weak fields. Different curves are different temperatures. Lime and black points denote the apparent antinodes of the wave, i.e., the amplitude of oscillation, up to a sign. Inset: dependence of the amplitude of oscillation vs temperature, on the logarithm scale, revealing exponential decay with T .

are able to roughly collapse all the curves on the left panel in Fig. 13 by rescaling the temperature as $T \rightarrow T \times U^{c(\delta)}$ (right panel), with $c(\delta)$ given in the inset. It is clear that the bigger the doping and the lower the interaction, the oscillations will persist up to a higher temperature, and start at a lower value of the field. It is interesting that roughly $(p/q)^* \sim T^{2/3}$ in the regime where multiple oscillation periods are observed.

The oscillations have a fixed period when σ^{xx} is plotted as a function of inverse magnetic field. When this period is inversely proportional to the surface area of the Fermi sea, this corresponds to the well-known Shubnikov–de Haas effect. However, in our results, we observe in some regimes of parameters an additional oscillation frequency. This is documented in Fig. 14 where we present the Fourier transform of $(\sigma^{xx})^{-1}(B_z^{-1} = q/p)$. The presented part of each oscillation spectrum is normalized to 1. In the left panel we show the temperature dependence of the oscillation spectrum as a function of temperature, at fixed doping and coupling constant. At low temperature one observes peaks at roughly integer multiples of the density $\langle n_\sigma \rangle$ which corresponds to the SdH effect. However, at intermediate temperature, there is an additional frequency corresponding to the full area of the BZ, and its higher harmonics [48]. At even higher temperature, before the oscillatory behavior is erased by thermal effects, the $p/q = 1$ peak in the spectrum becomes dominant. In the right panel we inspect the effect of doping on the oscillation spectrum, at a fixed temperature. The SdH peak is present at all dopings, and is always found at $p/q \approx \langle n_\sigma \rangle$. The doping appears to reduce the $p/q = 1$ peak, which is no longer the dominant peak at $\delta > 0.2$. At very low doping, it is not possible to distinguish between the $p/q = 1$ peak and the second harmonic of the SdH peak, as $\langle n_\sigma \rangle$ approaches 0.5. However, it is unexpected in the SdH effect that the second harmonic is stronger than the first harmonic (fundamental), which indicates a presence of a

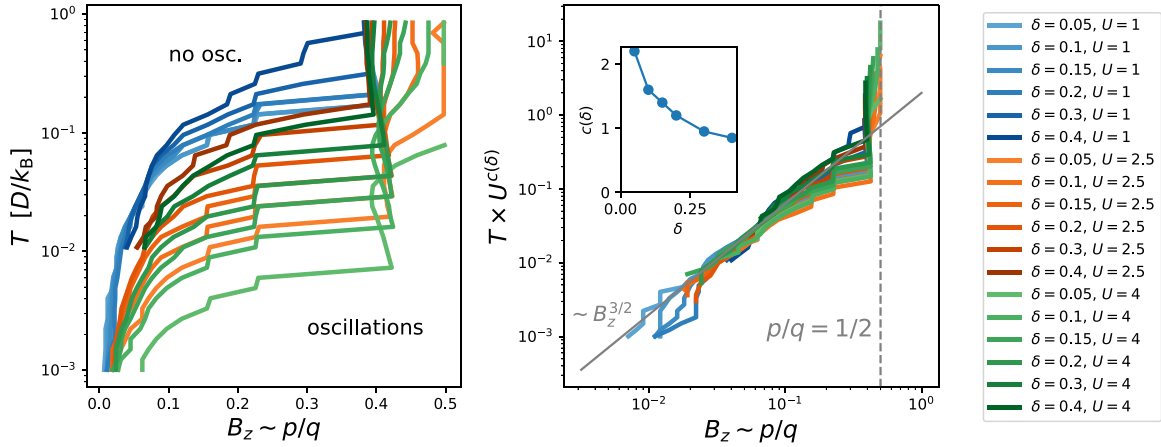


FIG. 13. The (B_z, T) phase diagram for the quantum oscillations. The diagram indicates the minimal magnetic field for observing significant quantum oscillations (nonmonotonic behavior) at a given temperature. Left: results for a set of model parameters. Right: rescaled results showing reasonable overlap.

separate mechanism which contributes to the amplitude of the peak at $p/q = 1$. In the next section, we are able to trace the origin of these high-frequency oscillations; the full description of the observed phenomenology and its relationship to experiments is presented in a separate publication (Ref. [48]).

4. Oscillations of the current vertex

At the level of the DMFT, the magnetic field enters the calculation of conductivity through the self-energy and the current vertex v . As we have concluded in Sec. III B 1, the dependence of conductivity on the self-energy is of secondary importance, and cannot possibly account for the observed $p/q = 1$ frequency oscillations, as the self-energy oscillates with the frequency $p/q = \langle n_\sigma \rangle$. The $p/q = 1$ oscillations then must come from the current vertex. This was already suggested in previous experimental works [45,46], where the

$p/q = 1$ frequency oscillations have been linked to periodic changes in the velocity of magnetic minibands, featuring spikes at $p/q = 1/q$.

We first discuss which part of $v^{xx}(\varepsilon, \varepsilon')$ plays a role at a given choice of parameters. First, by inspecting Eq. (70) we see that the ω integrand will generally have two peaks, centered around $\omega^*/\omega^{*'}$ such that $\omega^{*(l)} + \mu - \varepsilon^{(l)} - \text{Re}\Sigma(\omega^{*(l)}) = 0$. The width of those peaks is roughly proportional to $\text{Im}\Sigma(\omega^{*(l)})$. When the two peaks are further apart than is their width, the contribution of the integral will be very small. Additionally, if they fall outside of the thermal window, they will not contribute. Assuming in a most simple way $\omega^{*(l)} = \mu - \varepsilon^{(l)}$, and that the contribution is negligible if $|\varepsilon - \varepsilon'| > \Gamma$, with Γ playing the role of the width of the peaks [say roughly $\Gamma \approx -\text{Im}\Sigma(\omega = 0)$], and taking that the thermal window is a hard cutoff $|\omega^{*(l)}| < T$, we can isolate the relevant values of $v^{xx}(\varepsilon, \varepsilon')$, which determine the value of the overall

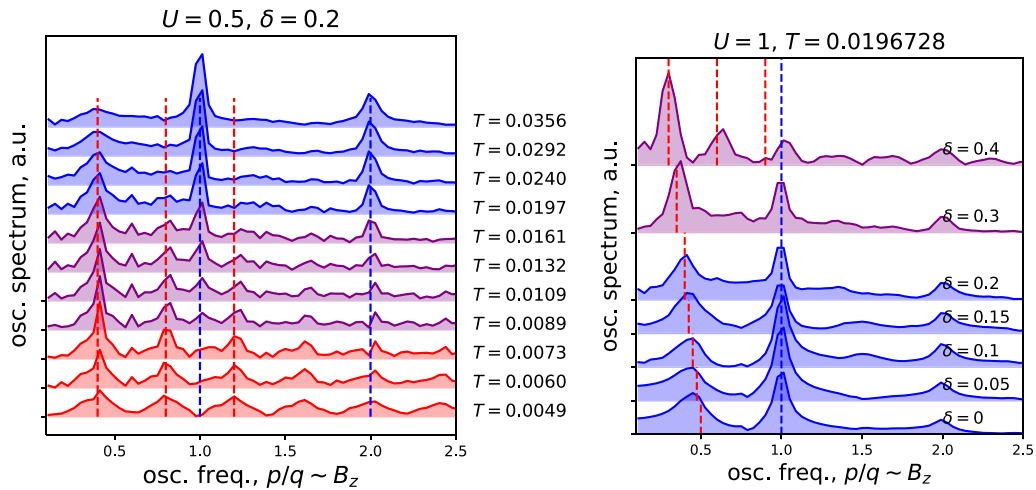


FIG. 14. Fourier spectra of the oscillatory component of the inverse dc conductivity. All spectra are normalized to 1. Left: temperature dependence at fixed electron density. Right: density dependence at fixed temperature. Both panels: vertical red dashed lines correspond to SdH frequency $p/q = \langle n_\sigma \rangle$ and its higher harmonics; vertical blue dashed lines correspond to $p/q = 1$ oscillation frequency and its higher harmonics.

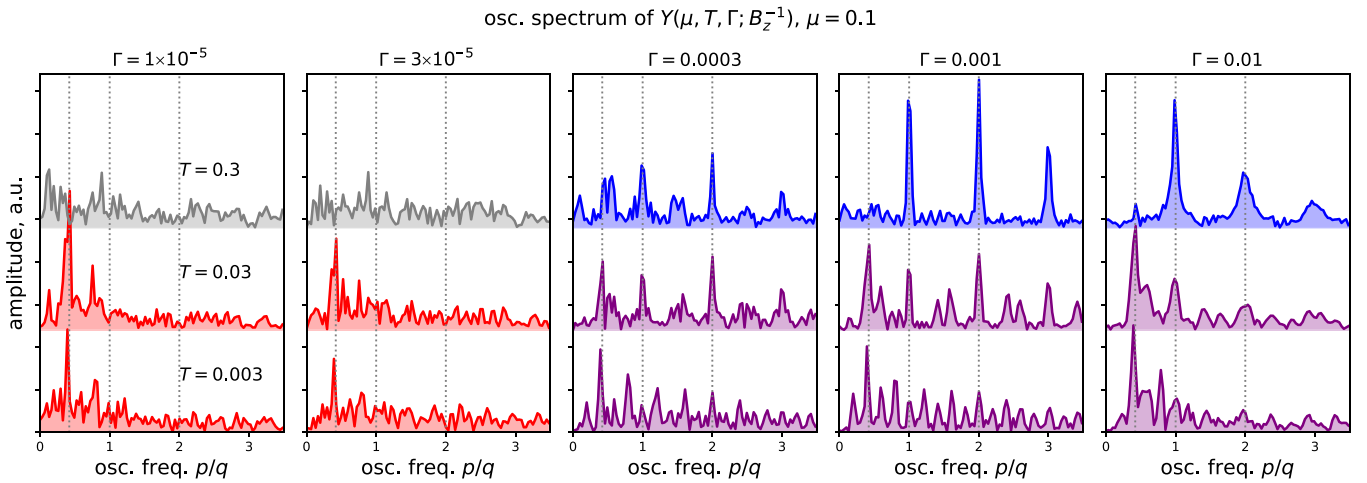


FIG. 15. Oscillation spectra of the current vertex (as quantified by Y) at various Γ, T . Spectra are colored gray where no pronounced peaks are observed, red where the standard SdH $p/q = \langle n_\sigma \rangle$ peaks and its higher harmonics are observed, purple where we also observe the $p/q = 1$ peaks, but the SdH peaks are dominant, and blue where $p/q = 1$ peak is stronger than $p/q = \langle n_\sigma \rangle$ peak.

integral. We define a quantity

$$Y(\mu, T, \Gamma; B_z) = \int d\varepsilon \int d\varepsilon' v^{xx}(\varepsilon, \varepsilon'; B_z) \theta(\Gamma - |\varepsilon - \varepsilon'|) \times [\theta(T - |\varepsilon - \mu|) + \theta(T - |\varepsilon' - \mu|)] \quad (84)$$

and inspect its oscillation spectrum as a function of B_z^{-1} . The results are presented in Fig. 15. We see that at low T and low Γ , the oscillations resemble the SdH effect. However, increasing Γ leads to an onset of $p/q = 1$ oscillations, which, with an increase of T , eventually become dominant. To better understand this behavior, in Fig. 16 we show the spectrum as a function of μ , at a fixed low temperature. We see how $p/q = \langle n_\sigma \rangle$ peak and its harmonics move with changing μ , as expected. On the contrary, the $p/q = 1, 2, 3 \dots$ peaks (when present in the spectrum), do not move with changing μ . The main insight is that roughly $Y(\mu, T + \delta T) \approx Y(\mu, T, \dots) + Y(\mu + \delta\mu, T, \dots) + Y(\mu - \delta\mu, T, \dots)$. At high temperature,

the contributions from different μ will interfere destructively, and the $p/q = \langle n_\sigma \rangle$ peak will wash out. On the other hand, the $p/q = 1$ will accumulate, and become the dominant peak, which is precisely what we find.

5. Conductivity in the finite-lifetime approximation (FLA)

In the previous sections we have concluded that the high-frequency (Brown-Zak, B-Z) oscillations of conductivity originate from the current vertex. Therefore, it is expected that B-Z oscillations are observed even in the most simple models that feature no variability in the self-energy whatsoever. In this section we calculate conductivity in the finite-lifetime approximation (FLA), where the self-energy is assumed to be a local, frequency-independent, and purely imaginary quantity, i.e.,

$$\Sigma_{ij}^{\text{FLA}}(\omega + i0^+) = -i\Gamma\delta_{ij}, \quad (85)$$

where Γ is the scattering rate. At a fixed $\mu = -0.1D$, we construct the Green's function, and evaluate the Kubo

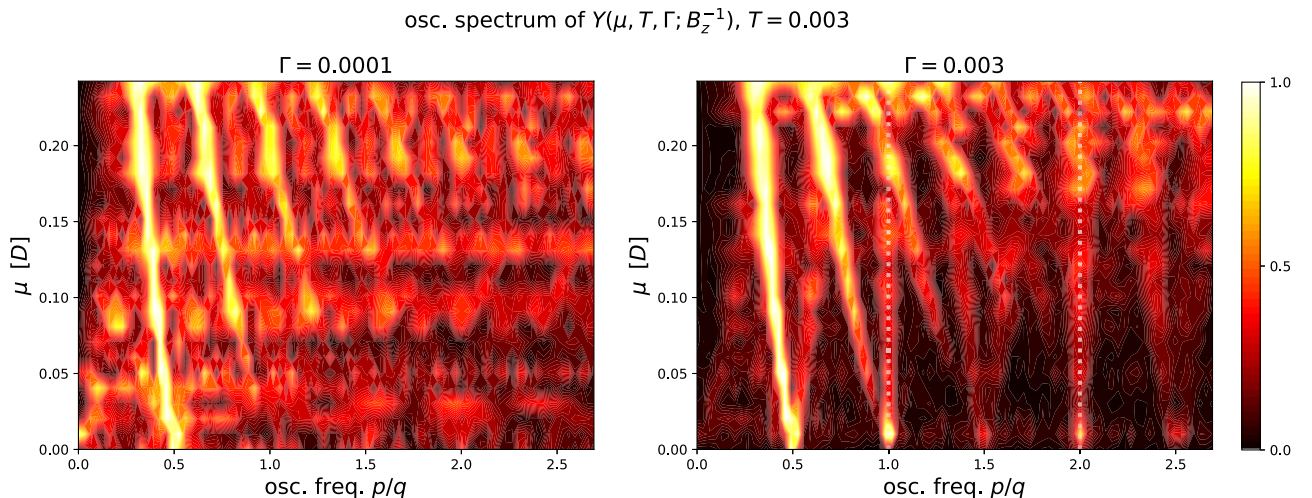


FIG. 16. Evolution of the oscillation spectrum of the current vertex (as quantified by Y) with chemical potential, for two values of Γ .

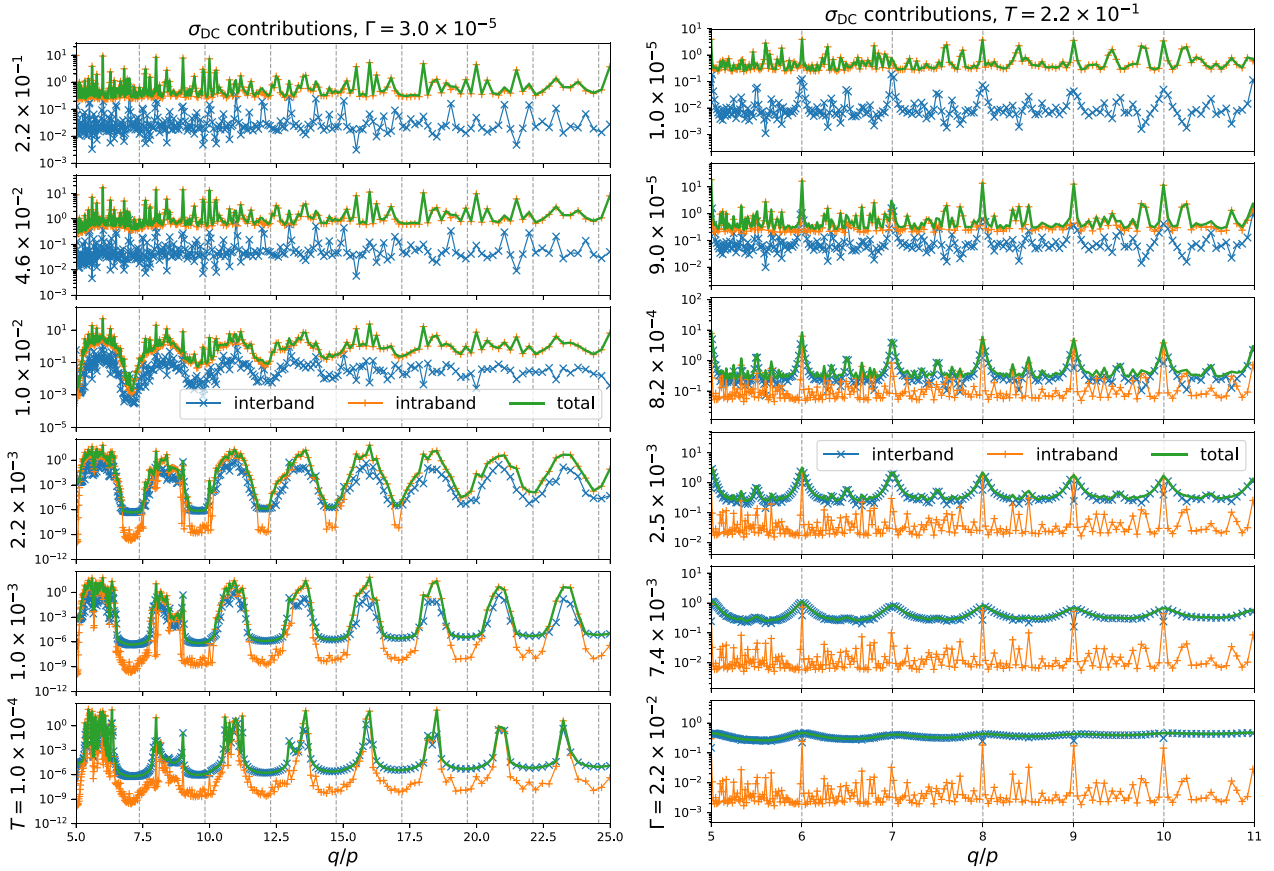


FIG. 17. Longitudinal dc conductivity within FLA: the total result and the contributions from interband and intraband processes. Left: different plots correspond to different temperatures at a fixed scattering rate. Right: different plots correspond to different Γ 's at a fixed temperature.

bubble (70). We are in particular interested in the trends with respect to temperature and scattering rate, and we wish to inspect the relative contributions of $\varepsilon \approx \varepsilon'$ and $\varepsilon \neq \varepsilon'$ terms in the double integral. We split the contributions by $d = |\varepsilon - \varepsilon'|$: the contributions with $d > 0.0003$ we consider “interband” contributions, where the particle and the hole of the particle-hole pair reside in different bands; the contributions with $d < 0.0003$ we consider “intraband” contributions, where the particle and the hole reside either in the same band, or two different bands which are very close in energy. The choice for the threshold value 0.0003 is made based on the finite-energy resolution that we can achieve and the systematic error made in energy levels due to finite lattice size.

The results are shown in Fig. 17 as a function of inverse magnetic field, i.e., q/p . On the plots on the left, we take a small value for the scattering rate $\Gamma \approx 3 \times 10^{-5}$, and show the two contributions to conductivity as well as the total result at several different temperatures. At low temperature, the dips in conductivity roughly coincide with $q/p = 0.407/i$, with i integer (denoted with vertical gray dashed lines). This clearly corresponds to SdH oscillations, and signals that the occupancy at $\mu = -0.1D$ is about $\langle n_\sigma \rangle = 0.407$. It is immediately clear that with increasing temperature, the SdH oscillations subside, and what is left is apparently a fractal-like behavior which cannot be fully resolved with our current resolution.

At low temperature, both intraband and interband processes contribute, while at high temperature, the intraband processes are dominant.

On the plots on the right in Fig. 17, we take a high temperature $T \approx 0.215$ and show results for different values of Γ . As Γ is increased, the interband processes contribute increasingly, and ultimately become fully dominant; the fractal behavior is replaced by regular oscillations, with maxima coinciding with $q/p = q/1$. These are the high-frequency (or B-Z) oscillations, which appear only when the scattering rate is sufficiently high.

We illustrate the trends with respect to temperature and the scattering rate on Fig. 18(a) where we plot the oscillation spectra obtained by the Fourier transform of the data in the range of the field $p/q \in [0.03, 0.15]$. The results show clearly that at low Γ , high-frequency oscillations are never observed, but that at sufficiently high Γ , they are observed above some threshold temperature, but up to indefinite temperature: note that the highest temperature that we show is 10 in units of half-bandwidth, with no sign of weakening of the high-frequency oscillations. In contrast, the SdH oscillations subside simply due to increasing temperature. All oscillations disappear at very high scattering rate, and there seems to be a well-defined upper cutoff Γ for the observation of any oscillations. These findings are summarized in the rough phase diagram of the FLA model in Fig. 18(b).

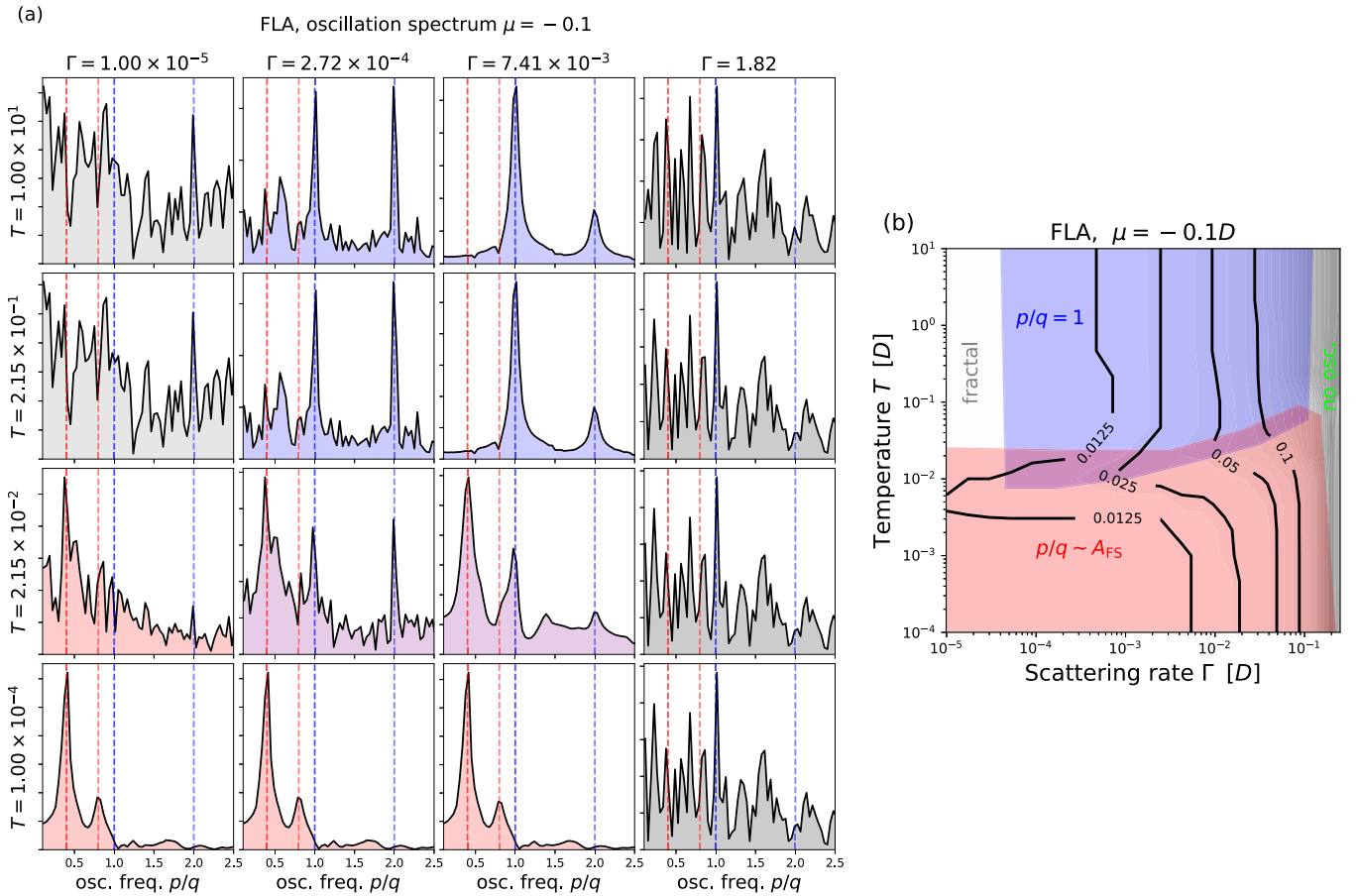


FIG. 18. (a) Oscillation spectra of longitudinal dc conductivity obtained within the FLA, at different Γ and T . Coloring is analogous to Fig. 15. (b) The phase diagram of the FLA toy model. Grayscale color coding in the background and the black contours correspond to the onset field for the nonmonotonic behavior $(p/q)^*$.

It is also interesting to compare the doping dependence of the quantum oscillation phenomenology in FLA and DMFT. On Fig. 19 we show the color plot of $\log_{10} \sigma^{xx}(\nu = 0)$ in the doping-field plane, at a high temperature where SdH oscillations are already thermally washed out. We see opposite trends in the two plots: in FLA, the oscillations are the strongest close to half-filling ($\mu = 0$), while in DMFT, the oscillatory features become stronger in the empty-band limit ($\langle n_\sigma \rangle \rightarrow 0$). The difference must be due to the fact that in the Hubbard model, the scattering rate is maximal at half-filling and vanishes as the number of electrons goes to zero. In FLA, the scattering rate is simply held fixed at all dopings. The FLA result on Fig. 19 is in solid agreement with the experimental results in Ref. [45]. This indicates that the scattering rate in experiment is not vanishing with doping, as one would have in the pure Hubbard model. The additional scattering in experiment probably comes from phonons, or even impurities.

IV. CONCLUSIONS AND PROSPECTS

In this paper we have identified several important features of the DMFT results for conductivity in the square-lattice Hubbard model in a perpendicular magnetic field. First, the T -linear resistivity at high temperature is not strongly affected by magnetic field. At high temperature, varying the interaction

also does not strongly affect the resistivity, but rather sets the temperature scale in a linear fashion. Next, we observe that the effect of the magnetic field comes mainly through the current-vertex factor (which only contains kinetic effects), and not the self-energy (which involves dynamic effects and defines the energy and momentum windows with significant contribution in the integration). We are able to reproduce the SdH effect and observe quantum oscillations in $1/\sigma^{xx}(B^{-1})$ with the expected frequency $B_z \sim p/q = \langle n_\sigma \rangle$. However, we also observe oscillations on a different, higher frequency $B_z \sim p/q = 1$, independently of doping. For this behavior, the prerequisites appear to be moderate scattering rate, moderate temperature and relatively high magnetic field flux per unit cell. Our observations are in line with the experimental results of recent experiments on moiré (graphene superlattice) systems [44–46].

For the future work it will be necessary to investigate how much of the observed phenomenology is representative of the exact solution, and how much is an artifact of the DMFT approximation. At the level of DMFT the two important simplifications are (1) the self-energy is fully local (which means that the Green's function is diagonal in the eigenbasis of the noninteracting Hamiltonian), and (2) the vertex corrections cancel. This question can in principle be addressed with cluster DMFT calculations [67], but these may

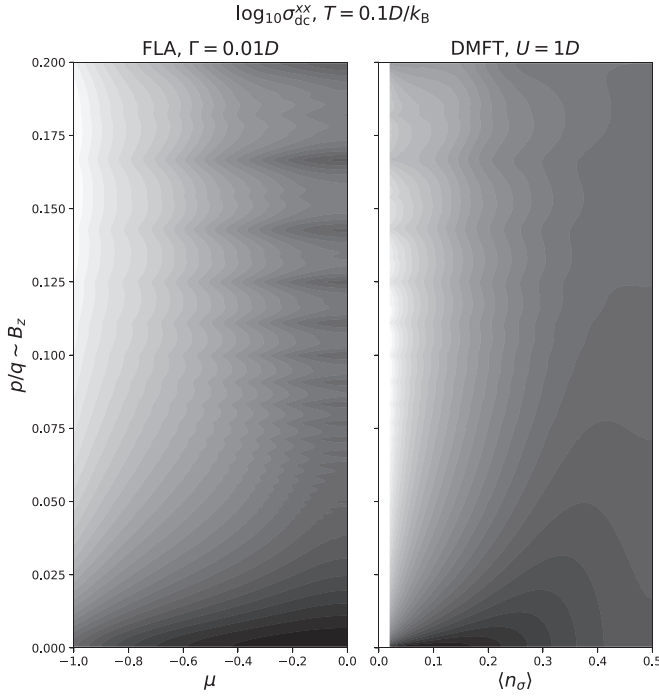


FIG. 19. The doping-field dependence of longitudinal dc conductivity within FLA and DMFT. Color code is logarithmic: white is -2.40 and -3.12 , respectively; black is 0.98 and 1.03 , respectively.

not be trivial to formulate or execute. Additionally, analytical continuation of self-energy data might be difficult [or an exact diagonalization (ED) solver might be used, which introduces additional systematic error]. Finally, calculation of vertex corrections in cluster DMFT schemes is notoriously difficult [68–72]. Another possibility is to use recently developed DiagMC technique which requires no analytical continuation [73–77], and can access the thermodynamic limit directly. As the observed phenomena are not restricted to very high values of the coupling and can already be observed at $U = 0.5 - 1D$, a DiagMC calculation with only several orders could be sufficient to work out the generic effect of self-energy nonlocality and vertex corrections.

ACKNOWLEDGMENTS

Computations were performed on the PARADOX supercomputing facility (Scientific Computing Laboratory, Center for the Study of Complex Systems, Institute of Physics Belgrade). J.V. acknowledges funding provided by the Institute of Physics Belgrade, through the grant by the Ministry of Education, Science, and Technological Development of the Republic of Serbia, as well as by the Science Fund of the Republic of Serbia, under the Key2SM project (PROMIS program, Grant No. 6066160). R.Ž. is supported by the Slovenian Research Agency (ARRS) under Program No. P1-0044 and Projects No. J1-1696 and No. J1-2458.

APPENDIX A: PEIERLS PHASE IN LANDAU GAUGE [PROOF OF EQ. (9)]

For the following derivation, we introduce $\mathbf{r}(\alpha) = a(x(\alpha), y(\alpha)) = a[\mathbf{r}_i + \alpha(\mathbf{r}_j - \mathbf{r}_i)]$ and $d\mathbf{r} = a d\alpha$, with $\mathbf{d} = \mathbf{r}_j - \mathbf{r}_i$, while keeping $\mathbf{r}_i = (x_i, y_i)$ dimensionless and x_i, y_i integers. The Peierls phase for the uniform magnetic field per-

pendicular to the lattice $\mathbf{B} = (0, 0, B_z)$, in the Landau gauge (7) can be expressed as

$$\begin{aligned}
 f_{ij} &= \frac{e}{\hbar} \int_{\mathbf{r}_i}^{\mathbf{r}_j} \mathbf{A}(\mathbf{r}) \cdot d\mathbf{r} \\
 &= \frac{ea}{\hbar} \int_0^1 d\alpha \mathbf{A}(\mathbf{r}(\alpha)) \cdot \mathbf{d} \\
 &= \frac{ea^2}{\hbar} B_z \int_0^1 d\alpha x(\alpha) \mathbf{e}_y \cdot \mathbf{d} \\
 &= \frac{ea^2}{\hbar} B_z (y_j - y_i) \int_0^1 d\alpha (x_i + \alpha d_x) \\
 &= \frac{ea^2}{\hbar} B_z (y_j - y_i) \left[x_i + d_x \int_0^1 d\alpha \alpha \right] \\
 &= \frac{ea^2}{\hbar} B_z (y_j - y_i) \left[x_i + d_x \frac{\alpha^2}{2} \Big|_0^1 \right].
 \end{aligned}$$

We finally have

$$\begin{aligned}
 f_{ij} &= \frac{ea^2}{\hbar} B_z (y_j - y_i) \left[x_i + \frac{x_j - x_i}{2} \right] \\
 &= \frac{ea^2}{\hbar} \frac{B_z}{2} (y_j - y_i) (x_i + x_j). \tag{A1}
 \end{aligned}$$

When doing real-space calculations on a finite cyclic lattice, it is necessary to always consider the shortest distance between the sites and take instead the following periodicized expression:

$$f_{ij}^{\text{fin. latt.}} = \frac{ea^2}{\hbar} B_z (y_j \ominus y_i) \left[x_i + \frac{x_j \ominus x_i}{2} \right], \tag{A2}$$

where \ominus denotes the shortest distance on a finite cyclic lattice.

APPENDIX B: PROOF OF UNIT-CELL SIZE

We prove now that in the Landau gauge, the size of the unit cell in the x direction is q . Consider that we shift both \mathbf{r}_i and \mathbf{r}_j by $q\mathbf{e}_x = (q, 0)$ [we remind the reader that we use dimensionless $\mathbf{r}_i = (x_i, y_i)$ as arguments of f]. We must show that the additional phase shift must be an integer number times 2π :

$$\begin{aligned}
 f_{\mathbf{r}_i+q\mathbf{e}_x, \mathbf{r}_j+q\mathbf{e}_x} &= \frac{ea^2}{\hbar} \frac{B_z}{2} (y_j - y_i) (x_i + q + x_j + q) \\
 &= f_{\mathbf{r}_i, \mathbf{r}_j} + \frac{ea^2}{\hbar} \frac{B_z}{2} (y_j - y_i) 2q. \tag{B1}
 \end{aligned}$$

We now apply $B_z = 2\pi \frac{p}{q} \left(\frac{ea^2}{\hbar}\right)^{-1}$:

$$\begin{aligned}
 f_{\mathbf{r}_i+q\mathbf{e}_x, \mathbf{r}_j+q\mathbf{e}_x} &= f_{\mathbf{r}_i, \mathbf{r}_j} + \frac{2\pi p}{2} (y_j - y_i) 2q \\
 &= f_{\mathbf{r}_i, \mathbf{r}_j} + 2\pi p (y_j - y_i). \tag{B2}
 \end{aligned}$$

As $p(y_j - y_i)$ is an integer, the condition (10) indeed satisfies periodicity along the x direction.

APPENDIX C: PROOF OF EQ. (14)

Here we rewrite in momentum space the kinetic term in the Hamiltonian (12) to reach Eq. (14):

$$\begin{aligned}
H_{\text{kin},\sigma} &= -t \frac{1}{N} \sum_{\mathbf{k}, \mathbf{k}'} \sum_{i, \mathbf{u} \in \{\mathbf{e}_x, \mathbf{e}_y\}} e^{i2\pi \frac{\mathbf{u} \cdot \mathbf{x}_i}{L}} e^{-i\mathbf{k} \cdot \mathbf{r}_i} c_{\mathbf{k},\sigma}^\dagger e^{i\mathbf{k}' \cdot (\mathbf{r}_i + \mathbf{u})} c_{\mathbf{k}',\sigma} + \text{H.c.} \\
&= -2t \sum_{\mathbf{k}, \sigma} \cos k_x n_{\mathbf{k},\sigma} - t \frac{1}{N} \sum_{\mathbf{k}, \mathbf{k}'} \sum_i e^{i2\pi \frac{\mathbf{x}_i}{L}} e^{-i\mathbf{k} \cdot \mathbf{r}_i} c_{\mathbf{k},\sigma}^\dagger e^{i\mathbf{k}' \cdot (\mathbf{r}_i + \mathbf{e}_y)} c_{\mathbf{k}',\sigma} + \text{H.c.} \\
&= -2t \sum_{\mathbf{k}, \sigma} \cos k_x n_{\mathbf{k},\sigma} - t \frac{1}{N} \sum_{\mathbf{k}, \mathbf{k}'} \sum_i e^{i2\pi \frac{\mathbf{r}_i \cdot \mathbf{e}_x}{L}} e^{-i\mathbf{k} \cdot \mathbf{r}_i} c_{\mathbf{k},\sigma}^\dagger e^{i\mathbf{k}' \cdot (\mathbf{r}_i + \mathbf{e}_y)} c_{\mathbf{k}',\sigma} + \text{H.c.} \\
&= -2t \sum_{\mathbf{k}, \sigma} \cos k_x n_{\mathbf{k},\sigma} - t \frac{1}{N} \sum_{\mathbf{k}, \mathbf{k}'} e^{i\mathbf{k}' \cdot \mathbf{e}_y} c_{\mathbf{k},\sigma}^\dagger c_{\mathbf{k}',\sigma} \sum_{i,\sigma} e^{i\mathbf{r}_i \cdot (\mathbf{k}' - \mathbf{k} + 2\pi \frac{\mathbf{e}_x}{L})} + \text{H.c.} \\
&= -2t \sum_{\mathbf{k}, \sigma} \cos k_x n_{\mathbf{k},\sigma} - t \sum_{\mathbf{k}, \mathbf{k}'} e^{i\mathbf{k}' \cdot \mathbf{e}_y} c_{\mathbf{k},\sigma}^\dagger c_{\mathbf{k}',\sigma} \delta_{\mathbf{k}', \mathbf{k} - 2\pi \frac{\mathbf{e}_x}{L}} + \text{H.c.} \\
&= -2t \sum_{\mathbf{k}, \sigma} \cos k_x n_{\mathbf{k},\sigma} - t \sum_{\mathbf{k}, \sigma} e^{i\mathbf{k}_y} c_{\mathbf{k},\sigma}^\dagger c_{\mathbf{k} - 2\pi \frac{\mathbf{e}_x}{L}, \sigma} + \text{H.c.} \tag{C1}
\end{aligned}$$

APPENDIX D: PERIODICITY WITH k_y

We prove here the periodicity of the noninteracting eigenproblem along the k_y axis, as stated in Eqs. (24) and (25). We start by reordering rows and columns of the Hamiltonian (15): one can achieve that by redefining $|\tilde{\mathbf{k}}, l, \sigma\rangle \equiv |\mathbf{k} + 2\pi l \frac{\mathbf{e}_y}{q}, \sigma\rangle$, or simply $|\tilde{\mathbf{k}}, lp \bmod q, \sigma\rangle \rightarrow |\tilde{\mathbf{k}}, l, \sigma\rangle$. In that case, the Hamiltonian reads as

$$\begin{aligned}
[\tilde{H}_{0,\tilde{\mathbf{k}},\sigma}]_{l,l'} &= \left(-\mu_\sigma - 2t \cos \left(\tilde{k}_x + 2\pi l \frac{p}{q} \right) \right) \delta_{l,l'} \\
&\quad - t (e^{ik_y} \delta_{l,l' \oplus 1} + e^{-ik_y} \delta_{l \oplus 1, l'}). \tag{D1}
\end{aligned}$$

This transformation does not affect the eigenvectors and eigenvalues.

Now, we apply a unitary transformation defined by $[U_{\tilde{\mathbf{k}}}]_{ll'} = \delta_{ll'} e^{-il\tilde{k}_y}$ and apply it to the Hamiltonian as

$$\check{H}_{0,\tilde{\mathbf{k}},\sigma} \equiv U_{\tilde{\mathbf{k}}} \tilde{H}_{0,\tilde{\mathbf{k}},\sigma} U_{\tilde{\mathbf{k}}}^\dagger. \tag{D2}$$

The transformed Hamiltonian $\check{H}_{0,\tilde{\mathbf{k}},\sigma}$ has the same eigenvalues as $\tilde{H}_{0,\tilde{\mathbf{k}},\sigma}$, and the original eigenvectors can be obtained from the eigenvectors of $\check{H}_{0,\tilde{\mathbf{k}},\sigma}$ as $|m, \tilde{\mathbf{k}}, \sigma\rangle = U_{\tilde{\mathbf{k}}}^\dagger |\check{m}, \tilde{\mathbf{k}}, \sigma\rangle$. As $U_{\tilde{\mathbf{k}}}$ is diagonal, the element-wise equation for $\check{H}_{\tilde{\mathbf{k}},\sigma}$ reads as

$$[\check{H}_{0,\tilde{\mathbf{k}},\sigma}]_{ll'} = [U_{\tilde{\mathbf{k}}}]_{ll} [\tilde{H}_{0,\tilde{\mathbf{k}},\sigma}]_{ll'} [U_{\tilde{\mathbf{k}}}]_{l'l'}^*. \tag{D3}$$

The diagonal elements remain unchanged, and we must consider two special cases for the off-diagonal elements: (a) $|l - l'| = q - 1$, and (b) $|l - l'| = 1$. The two cases correspond to whether the hopping between momenta winds around the BZ or not. In the latter case, we have for

$$\begin{aligned}
[\check{H}_{0,\tilde{\mathbf{k}},\sigma}]_{l>1, l'=l-1} &= e^{-il\tilde{k}_y} e^{ik_y} e^{i(l-1)\tilde{k}_y} \\
&= e^{i(1-l)\tilde{k}_y} e^{i(l-1)\tilde{k}_y} \\
&= 1 \\
&= [\check{H}_{0,\tilde{\mathbf{k}},\sigma}]_{l<q-1, l'=l+1}. \tag{D4}
\end{aligned}$$

But in the case when there is winding around the BZ, we get

$$\begin{aligned}
[\check{H}_{0,\tilde{\mathbf{k}},\sigma}]_{l=q-1, l'=0} &= e^{-i(q-1)\tilde{k}_y} e^{-ik_y} \\
&= e^{-iq\tilde{k}_y} \\
&= [\check{H}_{0,\tilde{\mathbf{k}},\sigma}]_{l=0, l'=q-1}^*. \tag{D5}
\end{aligned}$$

These are the only elements of the matrix that depend on \tilde{k}_y , which means that the blocks of the Hamiltonian are invariant under a transformation

$$\tilde{\mathbf{k}} \rightarrow (\tilde{k}_x, \tilde{k}_y + 2\pi C/q), \tag{D6}$$

where $C \in \mathbb{Z}$.

For the basis-change matrix elements, this periodicity means

$$\begin{aligned}
&\mathbf{H}_{0,\tilde{\mathbf{k}},\sigma}, [\alpha_{\mathbf{k},\sigma}]_{lp \bmod q,m} \\
&\xrightarrow{\text{permute}} \check{\mathbf{H}}_{0,\tilde{\mathbf{k}},\sigma}, [\alpha_{\mathbf{k},\sigma}]_{l,m} \\
&\xrightarrow{\text{unitary tr.}} \check{\mathbf{H}}_{0,\tilde{\mathbf{k}},\sigma}, e^{-ik_y l} [\alpha_{\mathbf{k},\sigma}]_{lm} \\
&\xrightarrow{\text{translate}} \check{\mathbf{H}}_{0,\tilde{\mathbf{k}}+(2\pi C/q)\mathbf{e}_y,\sigma}, e^{-ik_y l} [\alpha_{\mathbf{k},\sigma}]_{lm} \\
&\xrightarrow{\text{inv. unit. tr.}} \check{\mathbf{H}}_{0,\tilde{\mathbf{k}}+(2\pi C/q)\mathbf{e}_y,\sigma}, e^{-ik_y l} [\alpha_{\mathbf{k},\sigma}]_{lm} e^{i(k_y + 2\pi C/q)l} \\
&= e^{i(2\pi C/q)l} [\alpha_{\mathbf{k},\sigma}]_{lm} \\
&\xrightarrow{\text{permute back}} \mathbf{H}_{0,\mathbf{k}+(2\pi C/q)\mathbf{e}_y,\sigma}, e^{i(2\pi C/q)l} [\alpha_{\mathbf{k},\sigma}]_{lp \bmod q,m}. \tag{D7}
\end{aligned}$$

APPENDIX E: DECOMPOSITION INTO DIAMAGNETIC AND PARAMAGNETIC CURRENTS

The current operator can be divided into the paramagnetic and diamagnetic parts

$$\mathbf{j}_r = \mathbf{j}_{r,P} + \mathbf{j}_{r,D}, \tag{E1}$$

where we use Eq. (46) with

$$\boldsymbol{\gamma}_{\mathbf{r},\mathbf{P}} = (1, 1), \quad (\text{E2})$$

$$\boldsymbol{\gamma}_{\mathbf{r},\mathbf{D}} = \boldsymbol{\gamma}_{\mathbf{r}} - \boldsymbol{\gamma}_{\mathbf{r},\mathbf{P}}. \quad (\text{E3})$$

Because the inversion symmetry is preserved along the x axis, the diamagnetic part of j^x is going to be zero. This does not hold along the y axis, so there will be nonzero paramagnetic and diamagnetic parts in j^y , but $\langle \mathbf{j}_{\mathbf{r},\mathbf{P}} \rangle = -\langle \mathbf{j}_{\mathbf{r},\mathbf{D}} \rangle$ so that the total current is zero. This must hold as the total current is a physical observable, and thus a gauge-invariant quantity. Using the gauge-invariant Green's function, this can be easily proven: up to the constant prefactor, the thermal average of the paramagnetic part is simply

$$\begin{aligned} \langle \mathbf{j}_{\mathbf{r},\mathbf{P}} \rangle &= iG_{\mathbf{r}+\mathbf{e}_y,\mathbf{r}}(\tau=0^-) - iG_{\mathbf{r},\mathbf{r}+\mathbf{e}_y}(\tau=0^-) \\ &= i(e^{if_{\mathbf{r}+\mathbf{e}_y,\mathbf{r}}} - e^{-if_{\mathbf{r},\mathbf{r}+\mathbf{e}_y}})\bar{G}_{\mathbf{r},\mathbf{r}+\mathbf{e}_y}(\tau=0^-) \\ &= i(e^{-i\frac{ea^2}{\hbar}B_z x} - e^{i\frac{ea^2}{\hbar}B_z x})\bar{G}_{\mathbf{r},\mathbf{r}+\mathbf{e}_y}(\tau=0^-), \end{aligned} \quad (\text{E4})$$

and similarly

$$\langle \mathbf{j}_{\mathbf{r},\mathbf{D}} \rangle = i(e^{i\frac{ea^2}{\hbar}B_z x} - e^{-i\frac{ea^2}{\hbar}B_z x})\bar{G}_{\mathbf{r},\mathbf{r}+\mathbf{e}_y}(\tau=0^-) = -\langle \mathbf{j}_{\mathbf{r},\mathbf{P}} \rangle. \quad (\text{E5})$$

APPENDIX F: PROOF OF GAUGE INVARIANCE OF THE KUBO BUBBLE

We start with the expression for the site-space matrix (operator) for the current coupled to a vanishing external gauge field \mathbf{A}^{ext} , and in the presence of a rotary gauge field \mathbf{A} describing a perpendicular magnetic field. The total gauge field is $\mathbf{A}^{\text{tot}} = \mathbf{A}^{\text{ext}} + \mathbf{A}$. The corresponding contributions to the Peierls phase (which is additive as well) yield $\mathbf{f}^{\text{tot}} = \mathbf{f}^{\text{ext}} + \mathbf{f}$:

$$\begin{aligned} j_{\mathbf{r}}^{\eta} &= -\frac{\partial \mathbf{H}_{\text{kin}}}{\partial A_{\mathbf{r}}^{\text{ext},\eta}} \Big|_{\mathbf{A}^{\text{ext}} \rightarrow 0} \\ &= -\frac{\partial (e^{i\mathbf{f}^{\text{tot}}} \circ \mathbf{H}_{\text{kin}}[\mathbf{A}^{\text{tot}} = 0])}{\partial A_{\mathbf{r}}^{\text{ext},\eta}} \Big|_{\mathbf{A}^{\text{ext}} \rightarrow 0} \\ &= -\frac{\partial e^{i\mathbf{f}^{\text{tot}}}}{\partial A_{\mathbf{r}}^{\text{ext},\eta}} \Big|_{\mathbf{A}^{\text{ext}} \rightarrow 0} \circ \mathbf{H}_{\text{kin}}[\mathbf{A}^{\text{tot}} = 0] \\ &= -i \frac{\partial \mathbf{f}^{\text{ext}}}{\partial A_{\mathbf{r}}^{\text{ext},\eta}} \Big|_{\mathbf{A}^{\text{ext}} \rightarrow 0} \circ e^{i\mathbf{f}} \circ \mathbf{H}_{\text{kin}}[\mathbf{A}^{\text{tot}} = 0]. \end{aligned} \quad (\text{F1})$$

Expressed in terms of second-quantized operators, for the general TB Hamiltonian

$$\begin{aligned} j_{\mathbf{r}}^{\eta} &= -\sum_{\mathbf{u}} t_{\mathbf{r},\mathbf{r}+\mathbf{u}} \frac{\partial f_{\mathbf{r},\mathbf{r}+\mathbf{u}}^{\text{ext}}}{\partial A_{\mathbf{r}}^{\text{ext},\eta}} \Big|_{\mathbf{A}^{\text{ext}} \rightarrow 0} \\ &\quad \times (ie^{if_{\mathbf{r},\mathbf{r}+\mathbf{u}}} c_{\mathbf{r}}^{\dagger} c_{\mathbf{r}+\mathbf{u}} - ie^{-if_{\mathbf{r},\mathbf{r}+\mathbf{u}}} c_{\mathbf{r}+\mathbf{u}}^{\dagger} c_{\mathbf{r}}), \end{aligned} \quad (\text{F2})$$

where the sum over \mathbf{u} goes over all sites, and we have omitted the spin indices and the sum over spin for the sake of brevity.

The current-current correlation function is then

$$\begin{aligned} \Lambda_{\mathbf{r},\mathbf{r}'}^{\eta,\eta'}(\tau) &= \sum_{\mathbf{u},\mathbf{u}'} t_{\mathbf{r},\mathbf{r}+\mathbf{u}} t_{\mathbf{r}',\mathbf{r}'+\mathbf{u}'} \frac{\partial f_{\mathbf{r},\mathbf{r}+\mathbf{u}}^{\text{ext}}}{\partial A_{\mathbf{r}}^{\text{ext},\eta}} \Big|_{\mathbf{A}^{\text{ext}} \rightarrow 0} \frac{\partial f_{\mathbf{r}',\mathbf{r}'+\mathbf{u}'}^{\text{ext}}}{\partial A_{\mathbf{r}'}^{\text{ext},\eta'}} \Big|_{\mathbf{A}^{\text{ext}} \rightarrow 0} \\ &\quad \times \sum_{\sigma,\sigma'} (-1)^{b+b'+1} e^{i(-1)^b f_{\mathbf{r},\mathbf{r}+\mathbf{u}}} e^{i(-1)^{b'} f_{\mathbf{r}',\mathbf{r}'+\mathbf{u}'}} \sum_{\sigma,\sigma'} \langle c_{\mathbf{r}+\mathbf{b}\mathbf{u},\sigma}^{\dagger}(\tau) c_{\mathbf{r}+(1-b)\mathbf{u},\sigma}(\tau) c_{\mathbf{r}'+\mathbf{b}'\mathbf{u}',\sigma'}^{\dagger}(0) c_{\mathbf{r}'+(1-b')\mathbf{u}',\sigma'}(0) \rangle. \end{aligned} \quad (\text{F3})$$

The dynamic and disconnected part is

$$\begin{aligned} \Lambda_{\mathbf{r},\mathbf{r}'}^{\eta,\eta'}(\tau) &= \sum_{\mathbf{u},\mathbf{u}'} t_{\mathbf{r},\mathbf{r}+\mathbf{u}} t_{\mathbf{r}',\mathbf{r}'+\mathbf{u}'} \frac{\partial f_{\mathbf{r},\mathbf{r}+\mathbf{u}}^{\text{ext}}}{\partial A_{\mathbf{r}}^{\text{ext},\eta}} \Big|_{\mathbf{A}^{\text{ext}} \rightarrow 0} \frac{\partial f_{\mathbf{r}',\mathbf{r}'+\mathbf{u}'}^{\text{ext}}}{\partial A_{\mathbf{r}'}^{\text{ext},\eta'}} \Big|_{\mathbf{A}^{\text{ext}} \rightarrow 0} \\ &\quad \times \sum_{b,b' \in \{0,1\}} (-1)^{b+b'+1} e^{i(-1)^b f_{\mathbf{r},\mathbf{r}+\mathbf{u}}} e^{i(-1)^{b'} f_{\mathbf{r}',\mathbf{r}'+\mathbf{u}'}} \\ &\quad \times \sum_{\sigma} [-G_{\mathbf{r}+(1-b)\mathbf{u},\mathbf{r}'+\mathbf{b}'\mathbf{u}',\sigma}(\tau)] G_{\mathbf{r}'+(1-b')\mathbf{u}',\mathbf{r}+\mathbf{b}\mathbf{u},\sigma}(-\tau), \end{aligned} \quad (\text{F4})$$

where the Green's functions are obtained with $\mathbf{A}^{\text{ext}} = 0$. We now rewrite in terms of the gauge-invariant Green's function

$$\begin{aligned} \Lambda_{\mathbf{r},\mathbf{r}'}^{\eta,\eta'}(\tau) &= \sum_{\mathbf{u},\mathbf{u}'} t_{\mathbf{r},\mathbf{r}+\mathbf{u}} t_{\mathbf{r}',\mathbf{r}'+\mathbf{u}'} \frac{\partial f_{\mathbf{r},\mathbf{r}+\mathbf{u}}^{\text{ext}}}{\partial A_{\mathbf{r}}^{\text{ext},\eta}} \Big|_{\mathbf{A}^{\text{ext}} \rightarrow 0} \frac{\partial f_{\mathbf{r}',\mathbf{r}'+\mathbf{u}'}^{\text{ext}}}{\partial A_{\mathbf{r}'}^{\text{ext},\eta'}} \Big|_{\mathbf{A}^{\text{ext}} \rightarrow 0} \\ &\quad \times \sum_{b,b' \in \{0,1\}} (-1)^{b+b'} e^{i(-1)^b f_{\mathbf{r},\mathbf{r}+\mathbf{u}}} e^{i(-1)^{b'} f_{\mathbf{r}',\mathbf{r}'+\mathbf{u}'}} \\ &\quad \times e^{if_{\mathbf{r}+(1-b)\mathbf{u},\mathbf{r}'+\mathbf{b}'\mathbf{u}'}} e^{if_{\mathbf{r}'+\mathbf{b}\mathbf{u},\mathbf{r}+(1-b')\mathbf{u}'}} \\ &\quad \times \sum_{\sigma} \bar{G}_{\mathbf{r}+(1-b)\mathbf{u},\mathbf{r}'+\mathbf{b}'\mathbf{u}',\sigma}(\tau) \bar{G}_{\mathbf{r}'+(1-b')\mathbf{u}',\mathbf{r}+\mathbf{b}\mathbf{u},\sigma}(-\tau). \end{aligned} \quad (\text{F5})$$

The sum over b, b' yields four terms with exponential prefactors,

$$\begin{aligned} b=0, b'=0: & e^{if_{\mathbf{r},\mathbf{r}+\mathbf{u}}} e^{if_{\mathbf{r}',\mathbf{r}'+\mathbf{u}'}} e^{if_{\mathbf{r}+\mathbf{u},\mathbf{r}'}} e^{if_{\mathbf{r}',\mathbf{r}'+\mathbf{u}'}} \\ b=0, b'=1: & e^{if_{\mathbf{r},\mathbf{r}+\mathbf{u}}} e^{if_{\mathbf{r}',\mathbf{r}'+\mathbf{u}'}} e^{if_{\mathbf{r}+\mathbf{u},\mathbf{r}'+\mathbf{u}'}} e^{if_{\mathbf{r}',\mathbf{r}'}} \\ b=1, b'=0: & e^{if_{\mathbf{r}+\mathbf{u},\mathbf{r}}} e^{if_{\mathbf{r}',\mathbf{r}'+\mathbf{u}'}} e^{if_{\mathbf{r},\mathbf{r}'}} e^{if_{\mathbf{r}',\mathbf{r}'+\mathbf{u}'}} \\ b=1, b'=1: & e^{if_{\mathbf{r}+\mathbf{u},\mathbf{r}}} e^{if_{\mathbf{r}',\mathbf{r}'+\mathbf{u}'}} e^{if_{\mathbf{r},\mathbf{r}'+\mathbf{u}'}} e^{if_{\mathbf{r}',\mathbf{r}'+\mathbf{u}'}} \end{aligned} \quad (\text{F6})$$

and each factor above is gauge invariant. Therefore, what determines whether the Kubo bubble is gauge invariant are the factors of the type $\frac{\partial f_{\mathbf{r},\mathbf{r}+\mathbf{u}}^{\text{ext}}}{\partial A_{\mathbf{r}}^{\text{ext},\eta}} \Big|_{\mathbf{A}^{\text{ext}} \rightarrow 0}$ which clearly do not depend on the choice of the gauge for \mathbf{A} . A vanishing uniform electric field $\mathbf{E} = \partial_t \mathbf{A}^{\text{ext}}$, can be achieved by letting $\mathbf{A}^{\text{ext}}(\mathbf{r}, t) \rightarrow \mathbf{A}^{\text{ext}}$, i.e., by having a constant and uniform vector potential. The only gauge freedom for the external electric field then corresponds to choosing the inertial reference frame, which is a trivial transformation that our calculation is certainly invariant to; the slowly varying field approximation holds, and we have

$$\frac{\partial}{\partial A_{\mathbf{r}}^{\text{ext},\eta}} \int_{\mathbf{r}}^{\mathbf{r}+\mathbf{u}} \mathbf{A}^{\text{ext}}(\tilde{\mathbf{r}}) \cdot d\tilde{\mathbf{r}} = \frac{\partial}{\partial A_{\mathbf{r}}^{\text{ext},\eta}} (\mathbf{A}^{\text{ext}} \cdot \mathbf{u}) = u^{\eta} \quad (\text{F7})$$

which clearly does not depend on the precise choice of the uniform \mathbf{A}^{ext} . We therefore conclude that for the calculation of the linear response to a spatially uniform $\mathbf{q} = 0$ electric field, the Kubo bubble (47) is *gauge invariant*.

We also emphasize that the bubble for the charge-charge correlation function is trivially gauge invariant because $G_{ij}G_{ji} = \bar{G}_{ij}\bar{G}_{ji}$.

APPENDIX G: CURRENT OPERATOR IN MOMENTUM SPACE

Here we derive the current operator in momentum space. The general form is

$$j_{\mathbf{q}=0}^\eta = \frac{it}{N} \frac{e}{ac\hbar} \sum_{\sigma} \sum_{\tilde{\mathbf{k}}, m, m'} v_{\tilde{\mathbf{k}}, m, m', \sigma}^\eta c_{\tilde{\mathbf{k}}, m, \sigma}^\dagger c_{\tilde{\mathbf{k}}, m', \sigma}. \quad (\text{G1})$$

The goal of this section is to get expressions for the vertex factors $v_{\tilde{\mathbf{k}}, m, m', \sigma}^\eta$. We start with the current along the x direction. The local contribution is given in Eq. (46). After plugging this in Eq. (53) and applying the basis transformation from Eq. (37), we obtain

$$\begin{aligned} j_{\mathbf{q}=0}^x &= \frac{it}{N} \frac{e}{ac\hbar} \sum_{\sigma} \sum_{\tilde{\mathbf{k}}, m, \tilde{\mathbf{k}}', m'} c_{\tilde{\mathbf{k}}, m, \sigma}^\dagger c_{\tilde{\mathbf{k}}', m', \sigma} \sum_{l, l'} [\alpha_{\tilde{\mathbf{k}}, \sigma}]_{l, m} [\alpha_{\tilde{\mathbf{k}}', \sigma}]_{l', m'}^* \frac{1}{N} \sum_{\mathbf{r}} e^{-i(\tilde{\mathbf{k}}+l\frac{2\pi}{q}\mathbf{e}_x)\cdot\mathbf{r}} e^{i(\tilde{\mathbf{k}}'+l'\frac{2\pi}{q}\mathbf{e}_x)\cdot(\mathbf{r}+\mathbf{e}_x)} + \text{H.c.} \\ &= \frac{it}{N} \frac{e}{ac\hbar} \sum_{\sigma} \sum_{\tilde{\mathbf{k}}, m, \tilde{\mathbf{k}}', m'} c_{\tilde{\mathbf{k}}, m, \sigma}^\dagger c_{\tilde{\mathbf{k}}', m', \sigma} \sum_{l, l'} [\alpha_{\tilde{\mathbf{k}}, \sigma}]_{l, m} [\alpha_{\tilde{\mathbf{k}}', \sigma}]_{l', m'}^* e^{i(\tilde{\mathbf{k}}'+l'\frac{2\pi}{q}\mathbf{e}_x)\cdot\mathbf{e}_x} \delta_{\mathbf{k}, \mathbf{k}'} \delta_{l, l'} + \text{H.c.} \\ &= \frac{it}{N} \frac{e}{ac\hbar} \sum_{\sigma} \sum_{\tilde{\mathbf{k}}, m, m'} c_{\tilde{\mathbf{k}}, m, \sigma}^\dagger c_{\tilde{\mathbf{k}}, m', \sigma} \sum_l [\alpha_{\tilde{\mathbf{k}}, \sigma}]_{l, m} [\alpha_{\tilde{\mathbf{k}}, \sigma}]_{l, m'}^* e^{i(\tilde{\mathbf{k}}+l\frac{2\pi}{q}\mathbf{e}_x)\cdot\mathbf{e}_x} + \text{H.c.} \\ &= \frac{it}{N} \frac{e}{ac\hbar} \sum_{\sigma} \sum_{\tilde{\mathbf{k}}, m, m'} c_{\tilde{\mathbf{k}}, m, \sigma}^\dagger c_{\tilde{\mathbf{k}}, m', \sigma} e^{i\tilde{\mathbf{k}}_x} \sum_l [\alpha_{\tilde{\mathbf{k}}, \sigma}]_{l, m} [\alpha_{\tilde{\mathbf{k}}, \sigma}]_{l, m'}^* e^{il\frac{2\pi}{q}} + \text{H.c.} \\ &= \frac{it}{N} \frac{e}{ac\hbar} \sum_{\sigma} \sum_{\tilde{\mathbf{k}}, m, m'} \left[c_{\tilde{\mathbf{k}}, m, \sigma}^\dagger c_{\tilde{\mathbf{k}}, m', \sigma} e^{i\tilde{\mathbf{k}}_x} \sum_l [\alpha_{\tilde{\mathbf{k}}, \sigma}]_{l, m} [\alpha_{\tilde{\mathbf{k}}, \sigma}]_{l, m'}^* e^{il\frac{2\pi}{q}} - c_{\tilde{\mathbf{k}}, m', \sigma}^\dagger c_{\tilde{\mathbf{k}}, m, \sigma} e^{-i\tilde{\mathbf{k}}_x} \sum_l [\alpha_{\tilde{\mathbf{k}}, \sigma}]_{l, m} [\alpha_{\tilde{\mathbf{k}}, \sigma}]_{l, m'}^* e^{-il\frac{2\pi}{q}} \right]. \quad (\text{G2}) \end{aligned}$$

We are free to swap m and m' in the last term:

$$\begin{aligned} j_{\mathbf{q}=0}^x &= \frac{it}{N} \frac{e}{ac\hbar} \sum_{\sigma} \sum_{\tilde{\mathbf{k}}, m, m'} \left[c_{\tilde{\mathbf{k}}, m, \sigma}^\dagger c_{\tilde{\mathbf{k}}, m', \sigma} e^{i\tilde{\mathbf{k}}_x} \sum_l [\alpha_{\tilde{\mathbf{k}}, \sigma}]_{l, m} [\alpha_{\tilde{\mathbf{k}}, \sigma}]_{l, m'}^* e^{il\frac{2\pi}{q}} - c_{\tilde{\mathbf{k}}, m, \sigma}^\dagger c_{\tilde{\mathbf{k}}, m', \sigma} e^{-i\tilde{\mathbf{k}}_x} \sum_l [\alpha_{\tilde{\mathbf{k}}, \sigma}]_{l, m} [\alpha_{\tilde{\mathbf{k}}, \sigma}]_{l, m'}^* e^{-il\frac{2\pi}{q}} \right] \\ &= \frac{it}{N} \frac{e}{ac\hbar} \sum_{\sigma} \sum_{\tilde{\mathbf{k}}, m, m'} c_{\tilde{\mathbf{k}}, m, \sigma}^\dagger c_{\tilde{\mathbf{k}}, m', \sigma} \sum_l [\alpha_{\tilde{\mathbf{k}}, \sigma}]_{l, m} [\alpha_{\tilde{\mathbf{k}}, \sigma}]_{l, m'}^* \left[e^{i\tilde{\mathbf{k}}_x} e^{il\frac{2\pi}{q}} - e^{-i\tilde{\mathbf{k}}_x} e^{-il\frac{2\pi}{q}} \right], \quad (\text{G3}) \end{aligned}$$

and we can simply read off Eq. (55).

Along the y direction, similarly we have

$$\begin{aligned} N \frac{ac\hbar}{e} j_{\mathbf{q}=0}^y &= it \sum_{\sigma} \sum_{\tilde{\mathbf{k}}, m, \tilde{\mathbf{k}}', m'} c_{\tilde{\mathbf{k}}, m, \sigma}^\dagger c_{\tilde{\mathbf{k}}', m', \sigma} \sum_{l, l'} [\alpha_{\tilde{\mathbf{k}}, \sigma}]_{l, m} [\alpha_{\tilde{\mathbf{k}}', \sigma}]_{l', m'}^* \frac{1}{N} \sum_{\mathbf{r}} e^{2i\pi\frac{e}{q}\mathbf{r}\cdot\mathbf{e}_y} e^{-i(\tilde{\mathbf{k}}+l\frac{2\pi}{q}\mathbf{e}_x)\cdot\mathbf{r}} e^{i(\tilde{\mathbf{k}}'+l'\frac{2\pi}{q}\mathbf{e}_x)\cdot(\mathbf{r}+\mathbf{e}_y)} + \text{H.c.} \\ &= it \sum_{\sigma} \sum_{\tilde{\mathbf{k}}, m, \tilde{\mathbf{k}}', m'} c_{\tilde{\mathbf{k}}, m, \sigma}^\dagger c_{\tilde{\mathbf{k}}', m', \sigma} \sum_{l, l'} [\alpha_{\tilde{\mathbf{k}}, \sigma}]_{l, m} [\alpha_{\tilde{\mathbf{k}}', \sigma}]_{l', m'}^* \frac{1}{N} \sum_{\mathbf{r}} e^{i(\tilde{\mathbf{k}}'+l'\frac{2\pi}{q}\mathbf{e}_x - \tilde{\mathbf{k}} - l\frac{2\pi}{q}\mathbf{e}_x + p\frac{2\pi}{q}\mathbf{e}_x)\cdot\mathbf{r}} e^{i(\tilde{\mathbf{k}}'+l'\frac{2\pi}{q}\mathbf{e}_x)\cdot\mathbf{e}_y} + \text{H.c.} \\ &= it \sum_{\sigma} \sum_{\tilde{\mathbf{k}}, m, \tilde{\mathbf{k}}', m'} e^{i\tilde{\mathbf{k}}'_y} c_{\tilde{\mathbf{k}}, m, \sigma}^\dagger c_{\tilde{\mathbf{k}}', m', \sigma} \sum_{l, l'} [\alpha_{\tilde{\mathbf{k}}, \sigma}]_{l, m} [\alpha_{\tilde{\mathbf{k}}', \sigma}]_{l', m'}^* \delta_{\tilde{\mathbf{k}}, \tilde{\mathbf{k}}} \delta_{l', l \oplus p} + \text{H.c.} \\ &= it \sum_{\sigma} \sum_{\tilde{\mathbf{k}}, m, m'} e^{i\tilde{\mathbf{k}}_y} c_{\tilde{\mathbf{k}}, m, \sigma}^\dagger c_{\tilde{\mathbf{k}}, m', \sigma} \sum_l [\alpha_{\tilde{\mathbf{k}}, \sigma}]_{l, m} [\alpha_{\tilde{\mathbf{k}}, \sigma}]_{l \oplus p, m'}^* + \text{H.c.} \\ &= it \sum_{\sigma} \sum_{\tilde{\mathbf{k}}, m, m'} \left[e^{i\tilde{\mathbf{k}}_y} c_{\tilde{\mathbf{k}}, m, \sigma}^\dagger c_{\tilde{\mathbf{k}}, m', \sigma} \sum_l [\alpha_{\tilde{\mathbf{k}}, \sigma}]_{l, m} [\alpha_{\tilde{\mathbf{k}}, \sigma}]_{l \oplus p, m'}^* - e^{-i\tilde{\mathbf{k}}_y} c_{\tilde{\mathbf{k}}, m', \sigma}^\dagger c_{\tilde{\mathbf{k}}, m, \sigma} \sum_l [\alpha_{\tilde{\mathbf{k}}, \sigma}]_{l, m} [\alpha_{\tilde{\mathbf{k}}, \sigma}]_{l \oplus p, m'}^* \right] \\ &= it \sum_{\sigma} \sum_{\tilde{\mathbf{k}}, m, m'} c_{\tilde{\mathbf{k}}, m, \sigma}^\dagger c_{\tilde{\mathbf{k}}, m', \sigma} \left[e^{i\tilde{\mathbf{k}}_y} \sum_l [\alpha_{\tilde{\mathbf{k}}, \sigma}]_{l, m} [\alpha_{\tilde{\mathbf{k}}, \sigma}]_{l \oplus p, m'}^* - e^{-i\tilde{\mathbf{k}}_y} \sum_l [\alpha_{\tilde{\mathbf{k}}, \sigma}]_{l, m} [\alpha_{\tilde{\mathbf{k}}, \sigma}]_{l \oplus p, m'}^* \right] \quad (\text{G4}) \end{aligned}$$

and we can immediately recognize Eq. (56).

We can use the property of the basis change matrix elements (23) to work out a symmetry of v^x with respect to momentum inversion:

$$v_{-\tilde{\mathbf{k}}, m, m', \sigma}^x = \sum_l [\alpha_{-\tilde{\mathbf{k}}, \sigma}]_{l, m} [\alpha_{-\tilde{\mathbf{k}}, \sigma}]_{l, m'}^* \left[e^{-i\tilde{\mathbf{k}}_x} e^{il\frac{2\pi}{q}} - e^{i\tilde{\mathbf{k}}_x} e^{-il\frac{2\pi}{q}} \right] \quad (\text{G5})$$

$$= \sum_l [\alpha_{\tilde{\mathbf{k}}, \sigma}]_{q-l, m} [\alpha_{\tilde{\mathbf{k}}, \sigma}]_{q-l, m'}^* \left[e^{-i\tilde{\mathbf{k}}_x} e^{il\frac{2\pi}{q}} - e^{i\tilde{\mathbf{k}}_x} e^{-il\frac{2\pi}{q}} \right]. \quad (\text{G6})$$

We now make a change of variables, $l' = q - l$, $l = q - l'$:

$$v_{-\tilde{\mathbf{k}},m,m',\sigma}^x = \sum_{l'} [\alpha_{\tilde{\mathbf{k}},\sigma}]_{l',m} [\alpha_{\tilde{\mathbf{k}},\sigma}]_{l',m'}^* [e^{-i\tilde{k}_x} e^{i(q-l')\frac{2\pi}{q}} - e^{i\tilde{k}_x} e^{-i(q-l')\frac{2\pi}{q}}] = \sum_{l'} [\alpha_{\tilde{\mathbf{k}},\sigma}]_{l',m} [\alpha_{\tilde{\mathbf{k}},\sigma}]_{l',m'}^* [e^{-i\tilde{k}_x} e^{-il'\frac{2\pi}{q}} - e^{i\tilde{k}_x} e^{il'\frac{2\pi}{q}}]. \quad (\text{G7})$$

Therefore,

$$v_{-\tilde{\mathbf{k}},m,m',\sigma}^x = -v_{\tilde{\mathbf{k}},m,m',\sigma}^x. \quad (\text{G8})$$

Furthermore, by noting that v can be more simply written as

$$v_{\tilde{\mathbf{k}},m,m',\sigma}^x = -2i \sum_l [\alpha_{\tilde{\mathbf{k}},\sigma}]_{l',m} [\alpha_{\tilde{\mathbf{k}},\sigma}]_{l',m'}^* \sin\left(\tilde{k}_x + l\frac{2\pi}{q}\right), \quad (\text{G9})$$

we can easily prove

$$v_{\tilde{\mathbf{k}},m,m',\sigma}^x = -(v_{\tilde{\mathbf{k}},m',m,\sigma}^x)^*. \quad (\text{G10})$$

The matrix $[v_{\tilde{\mathbf{k}},\sigma}^x]_{mm'}$ is hence anti-Hermitian, which also implies $\text{Re} v_{\tilde{\mathbf{k}},m,m}^x = 0$. Also, by using Eq. (21), it is easily proven that

$$v_{(\tilde{k}_x, -\tilde{k}_y),m,m',\sigma}^x = v_{(\tilde{k}_x, \tilde{k}_y),m',m,\sigma}^x. \quad (\text{G11})$$

APPENDIX H: DERIVATION FOR $\Lambda_{\mathbf{q}=0}^{\eta,\eta',\text{disc}}(i\nu)$

The disconnected part of Eq. (57) reads as

$$\Lambda_{\mathbf{q}=0}^{\eta,\eta',\text{disc}}(i\nu) = \frac{1}{2\hbar} \int_{-\beta\hbar}^{\beta\hbar} d\tau e^{i\nu\tau} \frac{t^2 e^2}{c\hbar^2} \frac{1}{N} \sum_{\sigma} \sum_{\tilde{\mathbf{k}},m_1,m'_1,m_2,m'_2} v_{\tilde{\mathbf{k}},m_1,m'_1,\sigma}^{\eta} v_{\tilde{\mathbf{k}},m_2,m'_2,\sigma}^{\eta'} G_{\tilde{\mathbf{k}},m'_2,m_1\sigma}(-\tau) G_{\tilde{\mathbf{k}},m'_1,m_2,\sigma}(\tau). \quad (\text{H1})$$

We now apply inverse Fourier transform to the Green's functions

$$G(\tau) = \frac{1}{\beta} \sum_{i\omega} e^{-i\omega\tau} G(i\omega), \quad (\text{H2})$$

to obtain

$$\Lambda_{\mathbf{q}=0}^{\eta,\eta',\text{disc}}(i\nu) = \frac{t^2 e^2}{c\hbar^2} \frac{1}{N} \sum_{\sigma} \sum_{\tilde{\mathbf{k}},m_1,m'_1,m_2,m'_2} v_{\tilde{\mathbf{k}},m_1,m'_1,\sigma}^{\eta} v_{\tilde{\mathbf{k}},m_2,m'_2,\sigma}^{\eta'} \frac{1}{\beta^2} \sum_{i\omega,i\omega'} G_{\tilde{\mathbf{k}},m'_2,m_1\sigma}(i\omega) G_{\tilde{\mathbf{k}},m'_1,m_2,\sigma}(i\omega') \frac{1}{2\hbar} \int_{-\beta\hbar}^{\beta\hbar} d\tau e^{i(\nu+\omega-\omega')\tau}, \quad (\text{H3})$$

where $\int_{-\beta\hbar}^{\beta\hbar} d\tau e^{i(\nu+\omega-\omega')\tau} = 2\beta\hbar \delta_{\nu+\omega-\omega'}$, which immediately yields Eq. (58).

APPENDIX I: PROOF THAT DMFT SELF-ENERGY IS DIAGONAL IN THE NONINTERACTING EIGENBASIS

The following shows that a local self-energy is also diagonal in the basis of $|\tilde{\mathbf{k}}, m, \sigma\rangle$ states. We have

$$[\Sigma_{\tilde{\mathbf{k}},\sigma}(z)]_{ll'} = \langle \tilde{\mathbf{k}}, l, \sigma | \Sigma_{\sigma} | \tilde{\mathbf{k}}, l', \sigma \rangle = \sum_i [w_{\sigma}]_{(\tilde{\mathbf{k}},l),i}^* [w_{\sigma}]_{(\tilde{\mathbf{k}},l'),i} \Sigma_{ii,\sigma}(z) = \Sigma_{\sigma}(z) \sum_i [w_{\sigma}]_{(\tilde{\mathbf{k}},l),i}^* [w_{\sigma}]_{(\tilde{\mathbf{k}},l'),i} = \Sigma_{\sigma}(z) \delta_{ll'}, \quad (\text{I1})$$

where w_{σ} is the basis change matrix, for the transformation from site space to $\tilde{\mathbf{k}}, l$ space. We can, therefore, write

$$[\Sigma_{\tilde{\mathbf{k}},\sigma}(z)]_{mm'} = \langle \tilde{\mathbf{k}}, m, \sigma | \Sigma_{\sigma} | \tilde{\mathbf{k}}, m', \sigma \rangle = \sum_l [\alpha_{\tilde{\mathbf{k}},\sigma}^{-1}]_{m,l}^* [\alpha_{\tilde{\mathbf{k}},\sigma}^{-1}]_{m',l} \Sigma_{ll,\sigma}(z) = \Sigma_{\sigma}(z) \delta_{mm'}, \quad (\text{I2})$$

which immediately yields Eq. (63).

APPENDIX J: CALCULATION OF LOCAL GREEN'S FUNCTION IN DMFT USING THE NONINTERACTING DENSITY OF STATES

Here we prove Eq. (65):

$$\begin{aligned} G_{ii,\sigma}(z) &= \langle i, \sigma | \mathbf{G}_{\sigma}(z) | i, \sigma \rangle \\ &= \frac{1}{N} \sum_{\tilde{\mathbf{k}},m} \sum_{l,l'} e^{-i(\tilde{\mathbf{k}}+l\frac{2\pi}{q}\mathbf{e}_x)\cdot\mathbf{r}_i} e^{i(\tilde{\mathbf{k}}+l'\frac{2\pi}{q}\mathbf{e}_x)\cdot\mathbf{r}_i} [\alpha_{\tilde{\mathbf{k}},\sigma}]_{l,m} [\alpha_{\tilde{\mathbf{k}},\sigma}]_{l',m}^* \langle \tilde{\mathbf{k}}, m, \sigma | \mathbf{G}_{\sigma}(z) | \tilde{\mathbf{k}}, m, \sigma \rangle \\ &= \frac{1}{N} \sum_{\tilde{\mathbf{k}},m} \sum_{l,l'} e^{-i((l-l')\frac{2\pi}{q}\mathbf{e}_x)\cdot\mathbf{r}_i} [\alpha_{\tilde{\mathbf{k}},\sigma}]_{l,m} [\alpha_{\tilde{\mathbf{k}},\sigma}]_{l',m}^* \langle \tilde{\mathbf{k}}, m, \sigma | \mathbf{G}_{\sigma}(z) | \tilde{\mathbf{k}}, m, \sigma \rangle. \end{aligned} \quad (\text{J1})$$

Because we know that $G_{ii}(z)$ must be uniform, we can define

$$\begin{aligned}
G_{\text{loc},\sigma}(z) &= \frac{1}{N} \sum_i G_{ii,\sigma}(z) \\
&= \frac{1}{N^2} \sum_{\tilde{\mathbf{k}},m} \sum_{l,l'} [\alpha_{\tilde{\mathbf{k}},\sigma}]_{l,m} [\alpha_{\tilde{\mathbf{k}},\sigma}]_{l',m}^* \sum_i e^{-i((l-l')\frac{2\pi}{q}\mathbf{e}_x)\cdot\mathbf{r}_i} \langle \tilde{\mathbf{k}}, m, \sigma | \mathbf{G}_\sigma(z) | \tilde{\mathbf{k}}, m, \sigma \rangle \\
&= \frac{1}{N^2} \sum_{\tilde{\mathbf{k}},m} \sum_{l,l'} [\alpha_{\tilde{\mathbf{k}},\sigma}]_{l,m} [\alpha_{\tilde{\mathbf{k}},\sigma}]_{l',m}^* N \delta_{ll'} \langle \tilde{\mathbf{k}}, m, \sigma | \mathbf{G}_\sigma(z) | \tilde{\mathbf{k}}, m, \sigma \rangle \\
&= \frac{1}{N} \sum_{\tilde{\mathbf{k}},m} \langle \tilde{\mathbf{k}}, m, \sigma | \mathbf{G}_\sigma(z) | \tilde{\mathbf{k}}, m, \sigma \rangle \sum_l |[\alpha_{\tilde{\mathbf{k}},\sigma}]_{l,m}|^2 \\
&= \frac{1}{N} \sum_{\tilde{\mathbf{k}},m} \langle \tilde{\mathbf{k}}, m, \sigma | \mathbf{G}_\sigma(z) | \tilde{\mathbf{k}}, m, \sigma \rangle.
\end{aligned} \tag{J2}$$

Therefore, we can identify

$$G_{ii,\sigma}(z) = \frac{1}{N} \sum_{\tilde{\mathbf{k}},m} \frac{1}{\hbar z - \varepsilon_{\tilde{\mathbf{k}},m,\sigma} - \Sigma_\sigma(z)} = \int d\varepsilon \frac{\rho_0(\varepsilon)}{\hbar z - \varepsilon - \Sigma_\sigma(z)}. \tag{J3}$$

APPENDIX K: CONDUCTIVITY EXPRESSION IN DMFT: PROOF OF EQS. (70) AND (71)

Starting from Eq. (67), we first perform the Hilbert transform of the Green's function

$$G(i\omega) = -\frac{1}{\pi} \int d\varepsilon \frac{\text{Im}G(\varepsilon + i0^+)}{i\omega - \varepsilon}, \tag{K1}$$

where ε and $i\omega$ have the units of frequency. We obtain

$$\Lambda_{\mathbf{q}=\mathbf{0}}^{\eta\eta',\text{disc}}(i\nu) = \frac{t^2 e^2}{c\hbar^2 \pi^2} \sum_\sigma \frac{1}{\beta} \sum_{i\omega} \int d\varepsilon \int d\varepsilon' v_\sigma^{\eta\eta'}(\varepsilon, \varepsilon') \int d\omega \int d\omega' \frac{\text{Im}G(\varepsilon, \omega)}{i\omega + i\nu - \omega} \frac{\text{Im}G(\varepsilon', \omega')}{i\omega - \omega'}. \tag{K2}$$

Now we apply the partial fraction expansion $\frac{1}{z-a} \frac{1}{z-b} = \frac{1}{a-b} (\frac{1}{z-a} - \frac{1}{z-b})$:

$$\begin{aligned}
\Lambda_{\mathbf{q}=\mathbf{0}}^{\eta\eta',\text{disc}}(i\nu) &= \frac{t^2 e^2}{c\hbar^2 \pi^2} \sum_\sigma \frac{1}{\beta} \sum_{i\omega} \int d\varepsilon \int d\varepsilon' v_\sigma^{\eta\eta'}(\varepsilon, \varepsilon') \int d\omega \int d\omega' \text{Im}G(\varepsilon, \omega) \text{Im}G(\varepsilon', \omega') \\
&\quad \times \frac{1}{-i\nu + \omega - \omega'} \left[\frac{1}{i\omega + i\nu - \omega} - \frac{1}{i\omega - \omega'} \right].
\end{aligned} \tag{K3}$$

We apply $\frac{1}{\beta} \sum_{i\omega} \frac{1}{\hbar(i\omega - z)} = n_F(z)$:

$$\Lambda_{\mathbf{q}=\mathbf{0}}^{\eta\eta',\text{disc}}(i\nu) = \frac{t^2 e^2}{c\hbar \pi^2} \sum_\sigma \int d\varepsilon \int d\varepsilon' v_\sigma^{\eta\eta'}(\varepsilon, \varepsilon') \int d\omega \int d\omega' \text{Im}G(\varepsilon, \omega) \text{Im}G(\varepsilon', \omega') \frac{1}{-i\nu + \omega - \omega'} [n_F(-i\nu + \omega) - n_F(\omega')]. \tag{K4}$$

The bosonic frequency does nothing in the argument of n_F so we can rewrite

$$\Lambda_{\mathbf{q}=\mathbf{0}}^{\eta\eta',\text{disc}}(i\nu) = \frac{t^2 e^2}{c\hbar \pi^2} \sum_\sigma \int d\varepsilon \int d\varepsilon' v_\sigma^{\eta\eta'}(\varepsilon, \varepsilon') \int d\omega \int d\omega' \text{Im}G(\varepsilon, \omega) \text{Im}G(\varepsilon', \omega') \frac{1}{-i\nu + \omega - \omega'} [n_F(\omega) - n_F(\omega')]. \tag{K5}$$

Formal continuation to the real axis is performed by replacing $i\nu \rightarrow \nu$:

$$\Lambda_{\mathbf{q}=\mathbf{0}}^{\eta\eta',\text{disc}}(\nu) = \frac{t^2 e^2}{c\hbar \pi^2} \sum_\sigma \int d\varepsilon \int d\varepsilon' v_\sigma^{\eta\eta'}(\varepsilon, \varepsilon') \int d\omega \int d\omega' \text{Im}G(\varepsilon, \omega) \text{Im}G(\varepsilon', \omega') \frac{1}{-\nu + \omega - \omega'} [n_F(\omega) - n_F(\omega')]. \tag{K6}$$

As we are interested in the real part of the conductivity, and having in mind $\text{Im}\Lambda^{\eta,\eta'}(\nu=0) = 0$, we get

$$\begin{aligned} \text{Re}\sigma_{\mathbf{q}=\mathbf{0}}^{\eta,\eta',\text{disc}}(\nu) &= c \frac{\text{Im}\Lambda_{\mathbf{q}=\mathbf{0}}^{\eta,\eta',\text{disc}}(\nu)}{\nu} \\ &= \frac{t^2 e^2}{\hbar\pi^2} \sum_{\sigma} \text{Im} \int d\varepsilon \int d\varepsilon' v_{\sigma}^{\eta,\eta'}(\varepsilon, \varepsilon') \int d\omega \int d\omega' \text{Im}G(\varepsilon, \omega) \text{Im}G(\varepsilon', \omega') \frac{1}{-\nu + \omega - \omega'} \frac{[n_{\text{F}}(\omega) - n_{\text{F}}(\omega')]}{\nu}. \end{aligned} \quad (\text{K7})$$

For the longitudinal conductivity specifically, $v^{\eta,\eta'}$ is purely real, so the imaginary part comes from the delta-peak part of the ω, ω' integrals through $\int dx \frac{1}{x-y+i0} = \mathcal{P} \int dx \frac{1}{x-y} + i\pi\delta(x-y)$. In the limit $\nu \rightarrow 0$ we get Eq. (70).

For Hall conductivity the imaginary part comes from the principal part of the integral, and one can estimate it through [38] $\mathcal{P} \int d\omega \int d\omega' \frac{1}{\nu - \nu + \omega - \omega'} = \mathcal{P} \int d\omega \int d\omega' \frac{1}{\nu} \frac{-\nu + \omega - \omega'}{(-\nu + \omega - \omega')^2} = -\int d\omega \int d\omega' \frac{1}{(-\nu + \omega - \omega')^2} + \int d\omega \int d\omega' \frac{1}{\nu} \frac{\omega - \omega'}{(-\nu + \omega - \omega')^2}$. In the limit $\nu \rightarrow 0$ the second term cancels exactly due to the antisymmetry of the integrand with respect to the exchange $\omega \leftrightarrow \omega'$, and we get Eq. (71).

APPENDIX L: OSCILLATIONS IN THERMODYNAMIC PROPERTIES

With the NRG impurity solver, it is possible to directly calculate the thermodynamic properties of the lattice problem (i.e., without any integrations over parameters such as T or μ , which is error prone). This is based on Eq. (46) from Ref. [58], which relates the lattice grand potential (Landau free energy) $\Omega = F - \mu N_{\text{tot}} = E - TS - \mu N_{\text{tot}}$ (N_{tot} is total number of particles) and the impurity grand potential $\Phi_{\text{imp}} = F_{\text{imp}} - \mu n_{\text{imp}}$:

$$\begin{aligned} \frac{\Omega}{N} &= \Omega_{\text{imp}} - k_{\text{B}}T \sum_{i\omega, \sigma} \left(\int_{-\infty}^{+\infty} d\varepsilon \rho_0(\varepsilon) \right. \\ &\quad \left. \times \ln\{[i\omega\hbar + \mu - \Sigma_{\sigma}(i\omega) - \varepsilon]G_{\sigma}(i\omega)\} \right), \end{aligned} \quad (\text{L1})$$

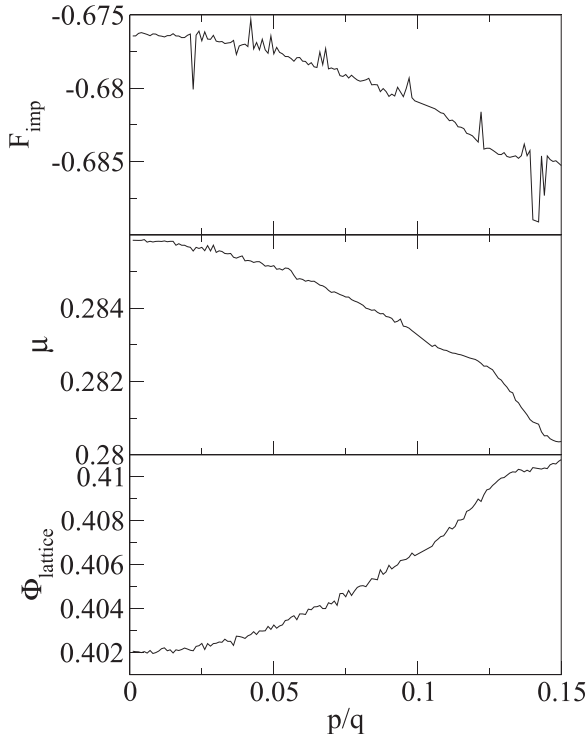


FIG. 20. Dependence of total free energy and its components on the magnetic field.

where G_{σ} is the local Green's function. This may be analytically continued to the real axis to give [78,79]

$$\begin{aligned} \frac{\Omega}{N} &= \Omega_{\text{imp}} + \frac{1}{\pi} \sum_{\sigma} \int_{-\infty}^{+\infty} d\varepsilon \rho_0(\varepsilon) \int_{-\infty}^{+\infty} d\omega \\ &\quad \times \text{Im} \ln \{[\hbar\omega + \mu - \Sigma_{\sigma}(\omega) - \varepsilon]G_{\sigma}(\omega)\} n_{\text{F}}(\omega), \end{aligned} \quad (\text{L2})$$

with the Fermi-Dirac distribution $n_{\text{F}}(\omega) = 1/(1 + \exp[\hbar\omega/Tk_{\text{B}}])$. The impurity free energy can be directly calculated in the NRG using the full-density-matrix approach.

We consider the case shown in Fig. 5 which exhibited significant transport oscillations at the high frequency, while the self-energy and the Green's function showed instead oscillations at the SdH frequency. In fact, at this temperature, the Fourier transform of the oscillatory part of the inverse conductivity shows no component at the SdH frequency, it is already thermally washed out. Indeed, we find no remnants of the SdH/dHvA oscillations in the thermodynamic properties either. In Fig. 20 we plot three elements that enter the full thermodynamic potential: impurity free energy F_{imp} , the chemical potential μ (which enters as $-\mu n_{\text{imp}}$ with constant $n_{\text{imp}} = n = 0.85$), and the lattice contribution from the double integration Φ_{lattice} . None of these show any clear oscillations;

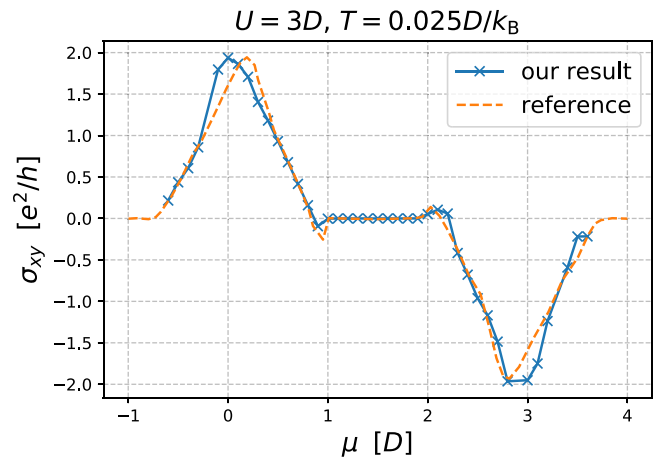


FIG. 21. Benchmark with the data from Markov *et al.* [38]. Our data: DMFT(NRG solver). Reference data: DMFT(exact diagonalization solver with five bath sites)+Padé analytical continuation used to obtain continuous spectra.

if they exist, they are below the numerical uncertainty. We only observe a weak quadratic dependence on the magnetic field in all three contributions. This confirms yet again that the high-frequency quantum oscillations show up exclusively in the transport properties through the vertex factors, thus they are, in this sense, a purely kinetic effect.

APPENDIX M: BENCHMARK

To benchmark our formalism and implementation, we cross-check our $\sigma^{xy}(v=0)$ results with the data from Ref. [38]. We perform a chemical potential scan at a fixed $U =$

$3D$ and $T = 0.025D/k_B$, which corresponds to the (doped) Mott insulator regime. The results are shown in Fig. 21. The agreement is solid. Neither of the curves fully satisfy $\sigma^{xy}(v=0; \mu) = -\sigma^{xy}(v=0; -\mu)$, which reveals the extent of the systematic error bars. The biggest difference is the position of the two peaks in the curves, which can be attributed to the difference in the impurity solvers used (we have used NRG [62–65], directly on the real axis; in Ref. [38] they used exact diagonalization with five bath sites, and Padé analytical continuation to obtain continuous spectra). We reproduce the change of sign of $\sigma^{xy}(v=0)$ as chemical potential crosses the edge of the Hubbard band into the Mott gap (at around $\mu = 1$ and 2), which appears to be a robust feature of the solution.

-
- [1] H. Takagi, B. Batlogg, H. L. Kao, J. Kwo, R. J. Cava, J. J. Krajewski, and W. F. Peck, *Phys. Rev. Lett.* **69**, 2975 (1992).
- [2] B. Keimer, S. A. Kivelson, M. R. Norman, S. Uchida, and J. Zaanen, *Nature (London)* **518**, 179 (2015).
- [3] A. Legros, S. Benhabib, W. Tabis, F. Laliberté, M. Dion, M. Lizaire, B. Vignolle, D. Vignolles, H. Raffy, Z. Z. Li, P. Auban-Senzier, N. Doiron-Leyraud, P. Fournier, D. Colson, L. Taillefer, and C. Proust, *Nat. Phys.* **15**, 142 (2018).
- [4] T. Pruschke, D. L. Cox, and M. Jarrell, *Phys. Rev. B* **47**, 3553 (1993).
- [5] M. Jarrell and T. Pruschke, *Phys. Rev. B* **49**, 1458 (1994).
- [6] D. Bergeron, V. Hankevych, B. Kyung, and A.-M. S. Tremblay, *Phys. Rev. B* **84**, 085128 (2011).
- [7] X. Deng, J. Mravlje, R. Žitko, M. Ferrero, G. Kotliar, and A. Georges, *Phys. Rev. Lett.* **110**, 086401 (2013).
- [8] J. Vučićević, D. Tanasković, M. J. Rozenberg, and V. Dobrosavljević, *Phys. Rev. Lett.* **114**, 246402 (2015).
- [9] E. Perepelitsky, A. Galatas, J. Mravlje, R. Žitko, E. Khatami, B. S. Shastry, and A. Georges, *Phys. Rev. B* **94**, 235115 (2016).
- [10] J. Kokalj, *Phys. Rev. B* **95**, 041110(R) (2017).
- [11] J. Vučićević, J. Kokalj, R. Žitko, N. Wentzell, D. Tanasković, and J. Mravlje, *Phys. Rev. Lett.* **123**, 036601 (2019).
- [12] E. W. Huang, R. Sheppard, B. Moritz, and T. P. Devereaux, *Science* **366**, 987 (2019).
- [13] A. Vranić, J. Vučićević, J. Kokalj, J. Skolimowski, R. Žitko, J. Mravlje, and D. Tanasković, *Phys. Rev. B* **102**, 115142 (2020).
- [14] P. T. Brown, D. Mitra, E. Guardado-Sanchez, R. Nourafkan, A. Reymbaut, C.-D. Hébert, S. Bergeron, A.-M. S. Tremblay, J. Kokalj, D. A. Huse, P. Schauß, and W. S. Bakr, *Science* **363**, 379 (2018).
- [15] H. Terletska, J. Vučićević, D. Tanasković, and V. Dobrosavljević, *Phys. Rev. Lett.* **107**, 026401 (2011).
- [16] J. Vučićević, H. Terletska, D. Tanasković, and V. Dobrosavljević, *Phys. Rev. B* **88**, 075143 (2013).
- [17] W. Witczak-Krempa, P. Ghaemi, T. Senthil, and Y. B. Kim, *Phys. Rev. B* **86**, 245102 (2012).
- [18] J. D. Rameau, T. J. Reber, H.-B. Yang, S. Akhanjee, G. D. Gu, P. D. Johnson, and S. Campbell, *Phys. Rev. B* **90**, 134509 (2014).
- [19] S. A. Hartnoll, *Nat. Phys.* **11**, 54 (2014).
- [20] W. Thomson, *Proc. R. Soc. London* **8**, 546 (1857).
- [21] K. v. Klitzing, G. Dorda, and M. Pepper, *Phys. Rev. Lett.* **45**, 494 (1980).
- [22] D. J. Thouless, M. Kohmoto, M. P. Nightingale, and M. den Nijs, *Phys. Rev. Lett.* **49**, 405 (1982).
- [23] Q. Niu, D. J. Thouless, and Y.-S. Wu, *Phys. Rev. B* **31**, 3372 (1985).
- [24] Z. F. Ezawa, *Quantum Hall Effects* (World Scientific, Singapore, 2008).
- [25] D. C. Tsui, H. L. Stormer, and A. C. Gossard, *Phys. Rev. Lett.* **48**, 1559 (1982).
- [26] R. B. Laughlin, *Phys. Rev. Lett.* **50**, 1395 (1983).
- [27] L. Schubnikow and W. J. De Haas, *Proc. R. Netherlands Acad. Arts Sci.* **33**, 130 (1930).
- [28] D. Schoenberg, *Magnetic Oscillations in Metals* (Cambridge University Press, Cambridge, UK, 1984).
- [29] D. LeBoeuf, N. Doiron-Leyraud, J. Levallois, R. Daou, J.-B. Bonnemaison, N. E. Hussey, L. Balicas, B. J. Ramshaw, R. Liang, D. A. Bonn, W. N. Hardy, S. Adachi, C. Proust, and L. Taillefer, *Nature (London)* **450**, 533 (2007).
- [30] P. Moetakef, D. G. Ouellette, J. R. Williams, S. J. Allen, L. Balents, D. Goldhaber-Gordon, and S. Stemmer, *Appl. Phys. Lett.* **101**, 151604 (2012).
- [31] S. E. Sebastian and C. Proust, *Annu. Rev. Condens. Matter Phys.* **6**, 411 (2015).
- [32] P. Voruganti, A. Golubentsev, and S. John, *Phys. Rev. B* **45**, 13945 (1992).
- [33] W. Ding, R. Žitko, and B. S. Shastry, *Phys. Rev. B* **96**, 115153 (2017).
- [34] W. O. Wang, J. K. Ding, B. Moritz, Y. Schattner, E. W. Huang, and T. P. Devereaux, *Phys. Rev. Research* **3**, 033033 (2021).
- [35] A. Auerbach, *Phys. Rev. B* **99**, 115115 (2019).
- [36] P. G. Wijesinghe and K. W. Gamalath, *Int. Lett. Chem., Phys. Astron.* **82**, 21 (2019).
- [37] F. F. Assaad and M. Imada, *Phys. Rev. Lett.* **74**, 3868 (1995).
- [38] A. A. Markov, G. Rohringer, and A. N. Rubtsov, *Phys. Rev. B* **100**, 115102 (2019).
- [39] W. O. Wang, J. K. Ding, B. Moritz, E. W. Huang, and T. P. Devereaux, *npj Quantum Mater.* **5**, 51 (2020).
- [40] A. Sherman, *Phys. Lett. A* **379**, 1912 (2015).
- [41] S. Acheche, L.-F. Arsenault, and A.-M. S. Tremblay, *Phys. Rev. B* **96**, 235135 (2017).
- [42] A. Khurana, *Phys. Rev. Lett.* **64**, 1990 (1990).

- [43] I. M. Lifshitz and A. M. Kosevich, *Zh. Éksp. Teor. Fiz.* **29**, 730 (1955) [*Sov. Phys.–JETP* **2**, 636 (1956)].
- [44] B. Hunt, J. D. Sanchez-Yamagishi, A. F. Young, M. Yankowitz, B. J. LeRoy, K. Watanabe, T. Taniguchi, P. Moon, M. Koshino, P. Jarillo-Herrero, and R. C. Ashoori, *Science* **340**, 1427 (2013).
- [45] R. K. Kumar, X. Chen, G. H. Auton, A. Mishchenko, D. A. Bandurin, S. V. Morozov, Y. Cao, E. Khestanova, M. B. Shalom, A. V. Kretinin, K. S. Novoselov, L. Eaves, I. V. Grigorieva, L. A. Ponomarenko, V. I. Fal'ko, and A. K. Geim, *Science* **357**, 181 (2017).
- [46] R. K. Kumar, A. Mishchenko, X. Chen, S. Pezzini, G. H. Auton, L. A. Ponomarenko, U. Zeitler, L. Eaves, V. I. Fal'ko, and A. K. Geim, *Proc. Natl. Acad. Sci. U.S.A.* **115**, 5135 (2018).
- [47] J. Barrier, P. Kumaravadivel, R. K. Kumar, L. A. Ponomarenko, N. Xin, M. Holwill, C. Mullan, M. Kim, R. V. Gorbachev, M. D. Thompson, J. R. Prance, T. Taniguchi, K. Watanabe, I. V. Grigorieva, K. S. Novoselov, A. Mishchenko, V. I. Fal'ko, A. K. Geim, and A. I. Berdyugin, *Nat. Commun.* **11**, 5756 (2020).
- [48] J. Vučičević and R. Žitko, *Phys. Rev. Lett.* **127**, 196601 (2021).
- [49] R. Peierls, *Z. Phys.* **80**, 763 (1933).
- [50] G. H. Wannier, *Rev. Mod. Phys.* **34**, 645 (1962).
- [51] E. Y. Andrei, D. K. Efetov, P. Jarillo-Herrero, A. H. MacDonald, K. F. Mak, T. Senthil, E. Tutuc, A. Yazdani, and A. F. Young, *Nat. Rev. Mater.* **6**, 201 (2021).
- [52] N. R. Cooper, J. Dalibard, and I. B. Spielman, *Rev. Mod. Phys.* **91**, 015005 (2019).
- [53] J. Dalibard, F. Gerbier, G. Juzeliūnas, and P. Öhberg, *Rev. Mod. Phys.* **83**, 1523 (2011).
- [54] P. G. Harper, *Proc. Phys. Soc. London A* **68**, 874 (1955).
- [55] D. R. Hofstadter, *Phys. Rev. B* **14**, 2239 (1976).
- [56] K.-T. Chen and P. A. Lee, *Phys. Rev. B* **84**, 205137 (2011).
- [57] M. Berciu and A. M. Cook, *Europhys. Lett.* **92**, 40003 (2010).
- [58] A. Georges, G. Kotliar, W. Krauth, and M. J. Rozenberg, *Rev. Mod. Phys.* **68**, 13 (1996).
- [59] M. Potthoff and W. Nolting, *Eur. Phys. J. B* **8**, 555 (1999).
- [60] M. Potthoff and W. Nolting, *Phys. Rev. B* **59**, 2549 (1999).
- [61] M. Potthoff and W. Nolting, *Phys. Rev. B* **60**, 7834 (1999).
- [62] K. G. Wilson, *Rev. Mod. Phys.* **47**, 773 (1975).
- [63] H. R. Krishna-murthy, J. W. Wilkins, and K. G. Wilson, *Phys. Rev. B* **21**, 1003 (1980).
- [64] R. Bulla, T. A. Costi, and T. Pruschke, *Rev. Mod. Phys.* **80**, 395 (2008).
- [65] R. Žitko and T. Pruschke, *Phys. Rev. B* **79**, 085106 (2009).
- [66] J. Vučičević, N. Wentzell, M. Ferrero, and O. Parcollet, *Phys. Rev. B* **97**, 125141 (2018).
- [67] T. Maier, M. Jarrell, T. Pruschke, and M. H. Hettler, *Rev. Mod. Phys.* **77**, 1027 (2005).
- [68] N. Lin, E. Gull, and A. J. Millis, *Phys. Rev. B* **80**, 161105(R) (2009).
- [69] N. Lin, E. Gull, and A. J. Millis, *Phys. Rev. B* **82**, 045104 (2010).
- [70] N. Lin, E. Gull, and A. J. Millis, *Phys. Rev. Lett.* **109**, 106401 (2012).
- [71] T. Sato, K. Hattori, and H. Tsunetsugu, *Phys. Rev. B* **86**, 235137 (2012).
- [72] H. Sato, M. Arita, Y. Utsumi, Y. Mukaegawa, M. Sasaki, A. Ohnishi, M. Kitaura, H. Namatame, and M. Taniguchi, *Phys. Rev. B* **89**, 155137 (2014).
- [73] A. Taheridehkordi, S. H. Curnoe, and J. P. F. LeBlanc, *Phys. Rev. B* **99**, 035120 (2019).
- [74] J. Vučičević and M. Ferrero, *Phys. Rev. B* **101**, 075113 (2020).
- [75] A. Taheridehkordi, S. H. Curnoe, and J. P. F. LeBlanc, *Phys. Rev. B* **101**, 125109 (2020).
- [76] A. Taheridehkordi, S. H. Curnoe, and J. P. F. LeBlanc, *Phys. Rev. B* **102**, 045115 (2020).
- [77] J. Vučičević, P. Stipsić, and M. Ferrero, *Phys. Rev. Research* **3**, 023082 (2021).
- [78] U. Brandt and C. Mielsch, *Z. Phys. B* **82**, 37 (1991).
- [79] A. M. Shvaika and J. K. Freericks, *Phys. Rev. B* **67**, 153103 (2003).

Analytical solution for time integrals in diagrammatic expansions: Application to real-frequency diagrammatic Monte Carlo

J. Vučičević,¹ P. Stipsić^{1,2} and M. Ferrero^{3,4}

¹*Scientific Computing Laboratory, Center for the Study of Complex Systems, Institute of Physics Belgrade, University of Belgrade, Pregrevica 118, 11080 Belgrade, Serbia*

²*Faculty of Physics, University of Belgrade, Studentski trg 12, 11001 Belgrade, Serbia*

³*CPHT, CNRS, Ecole Polytechnique, Institut Polytechnique de Paris, Route de Saclay, 91128 Palaiseau, France*

⁴*Collège de France, 11 place Marcelin Berthelot, 75005 Paris, France*



(Received 19 November 2020; accepted 25 March 2021; published 29 April 2021)

Recent years have seen a revived interest in the diagrammatic Monte Carlo (DiagMC) methods for interacting fermions on a lattice. A promising recent development allows one to now circumvent the analytical continuation of dynamic observables in DiagMC calculations within the Matsubara formalism. This is made possible by symbolic algebra algorithms, which can be used to analytically solve the internal Matsubara frequency summations of Feynman diagrams. In this paper, we take a different approach and show that it yields improved results. We present a closed-form analytical solution of imaginary-time integrals that appear in the time-domain formulation of Feynman diagrams. We implement and test a DiagMC algorithm based on this analytical solution and show that it has numerous significant advantages. Most importantly, the algorithm is general enough for any kind of single-time correlation function series, involving any single-particle vertex insertions. Therefore, it readily allows for the use of action-shifted schemes, aimed at improving the convergence properties of the series. By performing a frequency-resolved action-shift tuning, we are able to further improve the method and converge the self-energy in a nontrivial regime, with only 3–4 perturbation orders. Finally, we identify time integrals of the same general form in many commonly used Monte Carlo algorithms and therefore expect a broader usage of our analytical solution.

DOI: [10.1103/PhysRevResearch.3.023082](https://doi.org/10.1103/PhysRevResearch.3.023082)

I. INTRODUCTION

Finding controlled solutions of the Hubbard model is one of the central challenges in condensed matter physics [1–4]. Many common approaches to this problem rely on the stochastic (Monte Carlo) summation of various expansions and decompositions of relevant physical quantities. However, Monte Carlo (MC) algorithms are often plagued by two notorious problems: the fermionic sign problem and the analytical continuation of frequency-dependent quantities in calculations based on the Matsubara formalism [5–8] (alternatively, the dynamical sign problem in the Kadanoff-Baym and Keldysh formalism calculations [9–23]). In diagrammatic Monte Carlo (DiagMC) methods [24–38] (as opposed to determinantal methods such as continuous-time interaction-expansion quantum Monte Carlo (CTINT) or, auxiliary-field quantum Monte Carlo (CTAUX) [39–42]), an additional problem is often the slow (or absence of) convergence of the series with respect to the perturbation order. In recent years, several works have started to address the problems of obtaining

real-frequency quantities [43–51] and series convergence in DiagMC [52–57].

In Refs. [43,52], it has been shown that a convenient transformation of the interaction-expansion series can be used to significantly improve its convergence and sometimes allows one to converge the electronic self-energy with only a few perturbation orders where it would have otherwise been impossible. The method relies on a transformation of the action which affects the bare propagator at the cost of an additional expansion, i.e., more diagram topologies need to be taken into account. Alternatively, this transformation can be viewed as a Maclaurin expansion of the bare propagator with respect to a small chemical potential shift. The resulting convergence speedup comes from an increased convergence radius of the transformed series.

In a separate line of work, DiagMC methods have been proposed that are based on the Matsubara formalism that do not require an ill-defined analytical continuation [47]. Such methods have so far been implemented for the calculation of the self-energy [48,49] and the dynamical spin susceptibility [50]. The algorithms differ in some aspects, but all rely on the symbolic algebra solution of the internal Matsubara frequency summations appearing in Feynman diagrams. However, this approach has some downsides. First, numerical regulators are needed to properly evaluate Bose-Einstein distribution functions and diverging ratios that appear in the analytical expressions, and also poles on the real axis (effec-

Published by the American Physical Society under the terms of the [Creative Commons Attribution 4.0 International](https://creativecommons.org/licenses/by/4.0/) license. Further distribution of this work must maintain attribution to the author(s) and the published article's title, journal citation, and DOI.

tive broadening of the real-frequency results). In the case of finite cyclic lattice calculations, multiple precision algebra is needed in order to cancel divergences even with relatively large regulators [48]. Most importantly, in the Matsubara summation algorithm, applying the series transformation from Refs. [43,52] would require a separate analytical solution for each of the additional diagram topologies, which are very numerous, and the calculation would become rather impractical. More generally, treating any distinct diagram requires that the Matsubara frequency summations be performed algorithmically beforehand. This makes it difficult to devise MC sampling algorithms that go to indefinite perturbation orders, unless the Matsubara summation part is sufficiently optimized so that it no longer presents a prohibitive performance penalty if performed at the time of the Monte Carlo sampling.

In this paper, we show that it can be advantageous to start from the imaginary-time domain formulation of Feynman diagrams. A diagram contribution then features a multiple imaginary-time integral, rather than sums over Matsubara frequencies. The multiple integral can be solved analytically and we present a general solution. This analytical solution, although equivalent to the analytical Matsubara summation, has a simpler and more convenient form that does not feature Bose-Einstein distribution functions or diverging ratios. As a result, numerical regulators are not needed and the need for multiple precision arithmetic may arise only at very high perturbation orders. The numerical evaluation yields a sum of poles of various orders on a uniform grid on the real axis. The ability to separate contributions of poles of different orders allows one to formally extract the real-frequency result without any numerical broadening. Finally, the analytical solution is general and applies to all diagram topologies that would appear in the transformed series proposed in Refs. [43,52] or any other diagrammatic series for single-time correlation functions. This paves the way for real-frequency diagrammatic algorithms formulated in real space that are not *a priori* limited to small perturbation orders (similarly to CTINT or CTAUX [42]).

In this work, we apply the analytical time integral to the momentum-space DiagMC for the calculation of the self-energy, and implement and thoroughly test the method. We reproduce the self-energy results from Ref. [52] and supplement them with real-axis results, free of the uncontrolled systematic error that would otherwise come from the analytical continuation. Furthermore, we show that even if a full convergence is not possible with a single choice of the action-tuning parameter, one can choose the optimal tuning parameter for each frequency independently [46]. Such a frequency-resolved resummation can be used to improve the solution and in some cases systematically eliminate the non-physical features that appear in the result due to the truncation of the series at a finite order.

The paper is organized as follows. In Sec. II, we define the model and the basic assumptions of our calculations. In Sec. III, we introduce our method in detail. First, in Sec. III A, we present the analytical solution of the general multiple-time integral that appears in the time-domain formulation of Feynman diagrams and discuss the numerical evaluation of the final expression. Then, in Sec. III B, we show the analytical solution for the Fourier transform of the Maclaurin expansion

of the bare propagator, which is essential for our DiagMC algorithm. In Sec. III C, we discuss in detail how our analytical solutions can be applied in the context of DiagMC for the self-energy. In Sec. IV, we discuss our results and benchmarks and then give closing remarks in Sec. V. Additional details of the analytical derivations and further benchmarks and examples of the calculations can be found in the appendices.

II. MODEL

We solve the Hubbard model given by the Hamiltonian

$$H = - \sum_{\sigma, ij} t_{ij} c_{\sigma, i}^{\dagger} c_{\sigma, j} + U \sum_i n_{\uparrow, i} n_{\downarrow, i} - \mu \sum_{\sigma, i} n_{\sigma, i}, \quad (1)$$

where $\sigma \in \{\uparrow, \downarrow\}$, i, j enumerate lattice sites, t_{ij} is the hopping amplitude between the sites i and j , U is the on-site coupling constant, and μ is the chemical potential. We only consider the Hubbard model on the square lattice with the nearest-neighbor hopping t and next-nearest-neighbor hopping t' . The bare dispersion is given by

$$\varepsilon_{\mathbf{k}} = -2t(\cos k_x + \cos k_y) - 4t' \cos k_x \cos k_y. \quad (2)$$

We define $D = 4t$, which will be used as the unit of energy unless stated otherwise. We restrict to thermal equilibrium and paramagnetic phases with full lattice symmetry.

III. METHODS

The idea of DiagMC algorithms is to stochastically compute the coefficients of a perturbation series describing some physical quantity. We will focus on expansions in the coupling constant U and a shift in the chemical potential $\delta\mu$. The calculation of each coefficient involves the evaluation of many Feynman diagrams expressed in terms of the bare propagator, in our case taken as a function of momentum and two imaginary times. The evaluation of a diagram then boils down to a sum over multiple momentum variables and a multiple imaginary-time integral that is always of the same generic form. The goal of this section is to find a general analytical solution for these time integrals and reformulate the perturbation series as a function of a complex frequency z .

A. Analytical solution of time integrals

We are interested in analytically solving $(N - 1)$ -fold integrals over $\{\tau_{i=2\dots N}\}$ of the form

$$\mathcal{I}_{\mathbf{X}}(i\Omega_{\eta}) = \prod_{i=2}^N \int_0^{\tau_{i+1}} d\tau_i \tau_i^{l_i} e^{\tau_i(i\Omega_{\eta}\delta_{r,i} + \omega_i)}, \quad (3)$$

where the parameters of the integrand are given by

$$\mathbf{X} = (r, \{l_2 \dots l_N\}, \{\omega_2 \dots \omega_N\}). \quad (4)$$

The argument r is an integer and determines which of the times τ_i is multiplied by the external Matsubara frequency $i\Omega_{\eta}$ in the exponential. The frequency $i\Omega_{\eta}$ can be any Matsubara frequency, either fermionic or bosonic, depending on η ; $i\Omega_{\eta=-1} \equiv i\omega \equiv i(2m+1)\pi T$ and $i\Omega_{\eta=1} \equiv i\nu \equiv 2im\pi T$, with $m \in \mathbb{Z}$. The integer powers of τ_i outside of the exponent are given by $l_i \geq 0$, and the parameters ω_i may be complex.

The limit of the outermost integration is the inverse temperature $\tau_{N+1} \equiv \beta$. We denote by $\delta_{x,y}$ the Kronecker delta (it will be used throughout this paper, also in the shortened version $\delta_x \equiv \delta_{x,0}$). The reason for our choice to label times starting from 2 will become clear later.

The main insight is that upon applying the innermost integral, one gets a number of terms, but each new integrand has the same general form $\sim \tau^n e^{\tau z}$. The solution therefore boils down to a recursive application of

$$\int_0^{\tau_f} \tau^n e^{\tau z} d\tau = \sum_{k=0}^{n+1} (-)^k C_{nk} \frac{\tau_f^{n+1-k-B_{nk}} e^{B_{nk} z \tau_f}}{z^{k+B_{nk}}}, \quad (5)$$

with $B_{nk} = 1 - \delta_{k,n+1}$ and $C_{nk} = \frac{n!}{(n-k+\delta_{k,n+1})!}$ (for the proof, see Appendix D), and

$$\lim_{z \rightarrow 0} \int_0^{\tau_f} \tau^n e^{\tau z} d\tau = \frac{\tau_f^{n+1}}{n+1}. \quad (6)$$

The number of terms obtained after each integration is apparently $1 + (1 - \delta_z)(n + 1)$, and we can enumerate all terms obtained after the full integration by a set of integers, $\{k_{i=2 \dots N}\}$, where $k_i \geq 0$ denotes the choice of the term of the integral i (over $d\tau_i$).

For a given choice of $\{k_i\}$, the propagation of exponents $[n$ and z in Eqs. (5) and (6)] across successive integrals can be fully described by a simple set of auxiliary quantities. We denote the exponent of e in the integration i as \tilde{z}_i , and it is given by

$$\tilde{z}_i \equiv z_i + b_{i-1} \tilde{z}_{i-1}, \quad \tilde{z}_2 \equiv z_2, \quad (7)$$

$$z_i \equiv \delta_{i,r} i\Omega_\eta + \omega_i, \quad (8)$$

where we introduced $b_i \equiv B_{n_i, k_i}$. The meaning of b_i can be understood by looking at Eq. (5): The exponent of e that enters the integral on the left-hand side survives in all but the last term ($k = n + 1$) on the right-hand side. Therefore, $b_i = 1$ means that the exponent propagates from integration i to integration $i + 1$, while $b_i = 0$ means it does not, and the calculation of the recursive \tilde{z}_i is reset with each $b_i = 0$. The auxiliary quantity n_i are the exponents of τ_i and is specified below.

We will need to obtain a more convenient expression for the exponent \tilde{z}_i , where $i\Omega_\eta$ appears explicitly. Straightforwardly, we can write

$$\tilde{z}_i = i\Omega_\eta h_i + \tilde{\omega}_i, \quad (9)$$

with auxiliary quantities

$$\tilde{\omega}_i \equiv \omega_i + b_{i-1} \tilde{\omega}_{i-1}, \quad \tilde{\omega}_2 \equiv \omega_2, \quad (10)$$

and

$$h_i \equiv \begin{cases} 0, & i < r \\ 1, & i = r \\ b_{i-1} h_{i-1}, & i > r. \end{cases} \quad (11)$$

To be able to determine whether the exponent in the integrand, \tilde{z}_i , is zero and then employ Eq. (6) if needed, we can now use

$$\delta_{\tilde{z}_i} = \begin{cases} 1, & h_i = 0 \wedge \tilde{\omega}_i = 0 \\ 0 & \text{otherwise.} \end{cases} \quad (12)$$

It is important to note that at the time of integration, $i\Omega_\eta$ is unspecified and whether \tilde{z}_i is zero cannot be tested by numerical means, unless $i\Omega_\eta$ does not appear in \tilde{z}_i . With the convenient rewriting of Eq. (7) as Eq. (9), one can tell whether $i\Omega_\eta$ appears in \tilde{z}_i by looking at h_i . If $i\Omega_\eta$ does appear in \tilde{z}_i (i.e., $h_i = 1$), we cannot use Eq. (6) even if one can find such $i\Omega_\eta$ that cancels $\tilde{\omega}_i$. This is because we are working towards an analytical expression which ought to be general for all possible $i\Omega_\eta$.

The exponent of τ that will be carried over from integration i to integration $i + 1$ depends on the choice of the term from the integral i , and is given by $\text{Pos}(n_i - k_i)$, where Pos denotes the positive part of the number [$\text{Pos}(x) = (x + |x|)/2$]. n_i denotes the maximum exponent that can be carried over from integration i , and is obtained as

$$n_i = \begin{cases} \delta_{\tilde{z}_i} + l_i + \text{Pos}(n_{i-1} - k_{i-1}), & i > 2 \\ \delta_{\tilde{z}_i} + l_i, & i = 2. \end{cases} \quad (13)$$

In the case of Eq. (5), the maximal exponent that can be carried over to the next integration coincides with the exponent that entered the integral [the integral given by Eq. (5) does not raise the power of τ], so the definition of n_i coincides with the meaning of n in Eq. (5). In the case of the integral given by Eq. (6), n_i rather denotes the exponent after the integration, i.e., $n + 1$.

After the last integration, it can happen that $i\Omega_\eta$ appears in the exponent of e (this is signaled by $h_N b_N = 1$). We can then use the property $e^{i\Omega_\eta \beta} = (-1)^{\delta_{\eta-1}}$ to eliminate it from this exponent. Then, the solution for the integral can be continued to the whole of the complex plane $i\Omega_\eta \rightarrow z$, and can be written as (introducing the additional superscript η because the fermionic/bosonic nature of the expression can no longer be inferred from the external Matsubara frequency)

$$\begin{aligned} \mathcal{I}_X^\eta(z) &= \sum_{\{b_i \in \{\delta_{\tilde{z}_i}, 1\}\}_{i=2 \dots N}} e^{b_N \beta \tilde{\omega}_N} \sum_{\{k_i \in \{0, (1-\delta_{\tilde{z}_i}) n_i\}\}_{i: b_i=1}} \\ &\times \prod_{i: \delta_{\tilde{z}_i}=1} \frac{1}{n_i} \\ &\times (-1)^{b_N h_N \delta_{\eta-1} + \sum_{i=2}^N k_i} \times \beta^{n_N+1-b_N-k_N} \\ &\times \prod_{i: h_i=0 \wedge \tilde{\omega}_i \neq 0} \frac{C_{n_i, k_i}}{\tilde{\omega}_i^{k_i+b_i}} \prod_{i: h_i=1} \frac{C_{n_i, k_i}}{(z + \tilde{\omega}_i)^{k_i+b_i}}. \end{aligned} \quad (14)$$

Note that we have expressed the sum over $\{k_i\}$ as a sum over $\{b_i\}$ and a partial (inner) sum over $\{k_i\}$. This is not necessary, being that b_i is a function of k_i . Each b_i is fully determined by k_i , but not the other way around, so the inner sum over k_i in Eq. (14) goes over values that are allowed by the corresponding b_i . We present this form of Eq. (14) to emphasize that the factor $e^{b_N \beta \tilde{\omega}_N}$ depends only on $\{b_i\}$, and can thus be pulled out of the inner $\{k_i\}$ sum. The notation “ $i : b_i = 1$ ” means that we only consider indices i such that $b_i = 1$. We therefore only sum over those k_i for which the corresponding $b_i = 1$. The remaining k_i are fixed to $n_i + 1$, which is the only possibility if $b_i = 0$. The notation is applied analogously in other products over i .

TABLE I. Illustration of the calculation of a single term in Eq. (14). Rows correspond to successive integrations over $d\tau_i$. The second to fourth columns are parameters of the integrand. The choice of the term is colored red. The remaining columns are auxiliary quantities, the integrand before and after each integration. The prefactors that are “collected” after each integration are written in blue. The full contribution is written in the last column and then simplified to the form of a term in Eq. (16).

i	$\delta_{r,i}$	l_i	ω_i	k_i	b_i	n_i	$\tilde{\omega}_i$	h_i	δ_{z_i}	Integrand	Integral	Total
2	0	0	1	0	1	0	1	0	0	$e^{\tau_2 1}$	$\frac{1}{1} e^{\tau_3 1} - \frac{1}{1} 1$	
3	0	1	2	1	1	1	3	0	0	$\tau_3 e^{\tau_3(2+1)}$	$\frac{1}{3} \tau_4 e^{\tau_4 3} - \frac{1}{3^2} e^{\tau_4 3} + \frac{1}{3^2} 1$	
4	1	0	1	1	0	0	4	1	0	$e^{\tau_4(i\Omega_\eta+1+3)}$	$\frac{1}{i\Omega_\eta+4} e^{\tau_5(i\Omega_\eta+4)} - \frac{1}{i\Omega_\eta+4} 1$	$\frac{1}{1} (-\frac{1}{3^2}) (-\frac{1}{i\Omega_\eta+4}) \frac{1}{1} \frac{1}{4} \beta e^{\beta 4}$
5	0	0	0	0	1	1	0	0	1	$e^{\tau_5 0}$	$\frac{1}{1} \tau_6^1$	$\rightarrow \frac{\beta e^{A\beta}/36}{[z-(-4)]^1}$
6	0	0	4	0	1	1	4	0	0	$\tau_6 e^{\tau_6 4}$	$\frac{1}{4} \beta e^{\beta 4} - \frac{1}{4^2} e^{\beta 4} + \frac{1}{4^2} 1$	

The only remaining step is to expand the product of poles in Eq. (14) into a sum of poles (see Ref. [48] for more details),

$$\prod_\gamma \frac{1}{(z - z_\gamma)^{m_\gamma}} = \sum_\gamma \sum_{r=1}^{m_\gamma} \frac{1}{(z - z_\gamma)^r} \times (-1)^{m_\gamma - r} \sum_{\mathcal{C}\{p_{\gamma'} \in \mathbb{N}_0 : \sum_{\gamma' \neq \gamma} p_{\gamma'} = m_\gamma - r\}} \times \prod_{\gamma' \neq \gamma} \frac{(m_{\gamma'} + p_{\gamma'} - 1)!}{p_{\gamma'}! (m_{\gamma'} - 1)!} \frac{1}{(z_\gamma - z_{\gamma'})^{m_{\gamma'} + p_{\gamma'}}}, \tag{15}$$

and the final expression has the form

$$\mathcal{I}_X^\eta(z) = \sum_{j,p \in \mathbb{N}} \frac{A_{j,p}}{(z - Z_j)^p}. \tag{16}$$

In order to illustrate our solution, we present in tabular form (Table I) a summary of all intermediate steps, integrand parameters, and auxiliary quantities that are used in calculating the contribution for a single choice of $\{k_i\}$, in an example with $N = 6$ and $r = 4$.

Also note that if $r \notin [2, N]$ (no Matsubara frequency appearing in any exponent), the result of the integral is a number, rather than a frequency-dependent quantity. In that case, the integral can be straightforwardly generalized to the case of real time, where integrations go to some externally given time t (instead of β), and the resulting expression is a function of that time. The step given by Eq. (15) is then not needed. See Appendix A for details.

Numerical evaluation of the analytical expression and relation to other algorithms

The implementation of Eq. (14) is rather straightforward and much simpler than the algorithmic Matsubara summations in our previous work [48]. Indeed, most of the calculations just require the numerical evaluation of an analytical expression and it is not necessary to implement a dedicated symbolic algebra to manipulate the expressions. The only exception is the last step, Eq. (15). This transformation was the centerpiece of the algorithm in Ref. [48] and was applied recursively many times, leading to complex bookkeeping and data structures. Ultimately, the result was a symbolic expression that was stored, and a separate

implementation was needed for the comprehension and numerical evaluation of such a general symbolic expression. In the present context, however, Eq. (15) is applied only once to produce numbers, and is simple to implement.

The other important point is that we analytically treat cases with $\delta_{z_i} = 1$ by employing Eq. (6). With the frequency-summation algorithms [48,49], one cannot take into account possible cancellations of the ω_i terms in Eq. (10) without computing a large number of separate analytical solutions. When untreated, these cancellations yield diverging ratios in the final expressions, which need to be regularized. On the contrary, in Eq. (14), the ratio $1/\tilde{\omega}_i^{k_i+b_i}$ cannot have a vanishing denominator and its size will, in practice, be limited by the energy resolution. This will also allow us to have the final result in the form of a sum of poles on an equidistant grid on the real axis, and extract the real-axis results without any numerical pole broadening (see Sec. III C 2 and Appendix B).

It is interesting to compare the computational effort for the numerical evaluation of our analytical solution to the straightforward numerical integration. In the most straightforward integration algorithm, one would discretize the imaginary-time interval $[0, \beta]$ with N_τ times, and then perform the summation which has the complexity $O(N_\tau^{N-1})$ for each external τ , so that overall $O(N_\tau^N)$. With our algorithm, we do not have to go through all of the configurations of internal times, but we do need to go through all of the possible permutations of the internal times, and for each permutation there is at least 2^{N-1} terms to be summed over. So the number of terms one has to sum grows at least as $O[(N-1)!2^{N-1}]$. At sufficiently high N , this number is bound to outgrow the exponential N_τ^N , whatever the N_τ . This will happen, however, only at very large N . For example, if $N_\tau = 30$, the analytical solution becomes slower at around $N = 40$. Moreover, one actually needs a much larger N_τ , especially at low temperature. In any case, the additional computational effort can be understood as coming from the difference in the information content of the result, which is a lot more substantial in the case of the analytical solution.

At orders $N < 6$ (within context of DiagMC), we find that the implementation of our algorithm is significantly more efficient than our current implementation of the Matsubara summations from Ref. [48], and at $N = 6$, they are about equally efficient. However, we anticipate that further optimizations will be possible at the level of Eq. (14).

B. Expansion of the bare propagator

The central quantity is the Green's function defined in Matsubara formalism as

$$G_{\sigma\mathbf{k}}(\tau - \tau') = -\langle T_{\tau} c_{\sigma\mathbf{k}}(\tau) c_{\sigma\mathbf{k}}^{\dagger}(\tau') \rangle = \begin{cases} -\langle c_{\sigma\mathbf{k}}(\tau) c_{\sigma\mathbf{k}}^{\dagger}(\tau') \rangle, & \tau > \tau' \\ \langle c_{\sigma\mathbf{k}}^{\dagger}(\tau') c_{\sigma\mathbf{k}}(\tau) \rangle, & \tau' > \tau, \end{cases} \quad (17)$$

where $\tau, \tau' \in [0, \beta]$. The noninteracting Green's function (or the bare propagator) in the eigenbasis of the noninteracting Hamiltonian has a very simple general form,

$$G_0(\varepsilon, i\omega) \equiv \frac{1}{i\omega - \varepsilon}, \quad (18)$$

and for the plane wave \mathbf{k} , the propagator is $G_{0,\mathbf{k}}(i\omega) = G_0(\varepsilon_{\mathbf{k}} - \mu, i\omega)$.

As we will discuss below, the diagrammatic series for the self-energy will, in general, be constructed from different powers of the bare propagator,

$$G_0^l(\varepsilon, i\omega) \equiv \frac{1}{(i\omega - \varepsilon)^l}. \quad (19)$$

Indeed, these powers naturally arise after expanding the bare propagator in a Maclaurin series, $\frac{1}{z+x} = \sum_{n=0}^{\infty} \frac{(-x)^n}{z^{n+1}}$, around a small chemical potential shift,

$$G_0(\varepsilon, i\omega) = \sum_{l=1}^{\infty} (-\delta\mu)^{l-1} G_0^l(\varepsilon + \delta\mu, i\omega). \quad (20)$$

This series converges (for all $i\omega$) if $\delta\mu$ is smaller in amplitude than the first Matsubara frequency: $|\delta\mu| < \pi T$. Nevertheless, this expression will become a part of a larger series with additional expansion parameters, which may result in a modified convergence radius of the overall series with respect to $\delta\mu$.

We anticipate that the Feynman diagrams will be formulated in the imaginary-time domain, so it is essential to work out the Fourier transform of $G_0^l(\varepsilon, i\omega)$. We present the full derivation in Appendix E and here only write the final solution,

$$G_0^l(\varepsilon, \tau - \tau') = s_{\tau, \tau'} e^{-\varepsilon(\tau - \tau')} n_{\text{F}}(s_{\tau, \tau'} \varepsilon) \sum_{\zeta=0}^{l-1} \sum_{\varsigma=0}^{l-\zeta-1} c_{l, \zeta, \varsigma}^{s_{\tau, \tau'}}(\varepsilon) \tau^{\zeta} \tau'^{\varsigma}, \quad (21)$$

with $s_{\tau, \tau'} = \text{sgn}(\tau' - \tau)$. In our notation, l in G_0^l is a superscript index, rather than the power of G_0 [although these meanings coincide in the case of $G_0^l(\varepsilon, i\omega)$]. The Fermi function is defined as $n_{\text{F}}(\varepsilon) = 1/(e^{\beta\varepsilon} + 1)$ and the coefficients that go with the $\tau^{\zeta} \tau'^{\varsigma}$ terms are

$$c_{l, \zeta, \varsigma}^{-}(\varepsilon) = \sum_{n=0}^{l-\zeta-\varsigma-1} \frac{n! (-1)^{l+\varsigma-1} [-n_{\text{F}}(\varepsilon)]^n \beta^{l-\zeta-\varsigma-1}}{(l-\zeta-\varsigma-1)!(\zeta+\varsigma)!} \times \left\{ \begin{matrix} l-\zeta-\varsigma-1 \\ n \end{matrix} \right\} \binom{\zeta+\varsigma}{\zeta}, \quad (22)$$

and $c_{l, \zeta, \varsigma}^{+}(\varepsilon) = (-1)^{l-1} c_{l, \zeta, \varsigma}^{-}(-\varepsilon)$. Here we make use of binomial coefficients $\binom{n}{k} = \frac{n!}{k!(n-k)!}$ and the Stirling number of the second kind, $\left\{ \begin{matrix} n \\ k \end{matrix} \right\} = \sum_{i=0}^k \frac{(-1)^i}{k!} \binom{k}{i} (k-i)^n$.

C. Application to DiagMC

In the following, we apply the analytic time integral and the expansion of the bare propagator in the context of DiagMC. We discuss two kinds of self-energy series (Hartree shifted and bare) and the corresponding implementation details. Note that some symbols will be redefined with respect to previous sections.

1. Hartree-shifted series

In this section, we discuss the construction of the self-energy series, where all tadpolelike insertions are omitted in the topologies of the diagrams. Rather, the full Hartree shift is absorbed in the bare propagator. The diagrams are therefore expressed in terms of the Hartree-shifted bare propagator,

$$G_{0,\mathbf{k}}^{\text{HF}}(i\omega) = G_0(\tilde{\varepsilon}_{\mathbf{k}}, i\omega), \quad (23)$$

with the Hartree-shifted dispersion defined as

$$\tilde{\varepsilon}_{\mathbf{k}} = \varepsilon_{\mathbf{k}} - \mu + U \langle n_{\sigma} \rangle, \quad (24)$$

where $\langle n_{\sigma} \rangle$ is the average site occupation per spin.

After constructing the tadpoleless topologies, we are free to expand all propagators that appear in the diagrams according to Eq. (20):

$$G_{0,\mathbf{k}}^{\text{HF}}(i\omega) = \sum_{l=1}^{\infty} (-\delta\mu)^{l-1} G_0^l(\tilde{\varepsilon}_{\mathbf{k}} + \delta\mu, i\omega). \quad (25)$$

In the frequency domain, this step can be viewed as introducing new topologies: we now have diagrams with any number of single-particle-vertex ($\delta\mu$) insertions on any of the propagator lines. Each arrangement of these additional single-particle vertices on the diagram does require a separate solution by the symbolic algebra algorithm, as presented in Refs. [48,49]. Nevertheless, as a $\delta\mu$ vertex cannot carry any momentum or energy, the formal effect of it is that it just raises the power l of the propagator that passes through it. In the imaginary-time domain, it turns out that the contribution of the $\delta\mu$ -dressed diagrams is readily treatable by the analytical expression (14) and we no longer have to view the $\delta\mu$ insertions as changes to topology, but rather as additional internal degrees of freedom to be summed over. This is illustrated in Fig. 1.

Up to the Hartree shift, the self-energy expansion can now be made in powers of the interaction U and the small chemical-potential shift $\delta\mu$,

$$\Sigma_{\mathbf{k}}^{(\text{HF})}(\tau) = \sum_N (-U)^N \times \sum_{l_1, \dots, l_{2N-1}=1}^{\infty} (-\delta\mu)^{\sum_j (l_j-1)} \sum_{\Upsilon_N} D_{\Upsilon_N, \mathbf{k}, \{l_j\}, \delta\mu}(\tau), \quad (26)$$

where j enumerates the propagators, of which there are $N_{\text{prop}} = 2N - 1$, N is the perturbation order in U , each l_j goes from 1 to ∞ , Υ_N enumerates distinct topologies of the diagram at order N (without any $\delta\mu$ or Hartree insertions), and D is the contribution of the diagram. The general form of the

where $i(p_i)$ is the vertex index i of the permuted index p_i and we have introduced a new expansion variable $L = \sum_j (l_j - 1)$ and a convenient variable $\tilde{l}_j = l_j - 1$, so that

$$\Sigma_{\mathbf{k}}^{(\text{HF})}(z) = \sum_{K=2}^{\infty} \sum_{N=2}^K \sum_{L=0}^{K-N} (-U)^N (-\delta\mu)^L \sum_{\Upsilon_N} D_{\Upsilon_N, \mathbf{k}, L, \delta\mu}(z), \quad (32)$$

which is the series that we implement and use in practice. The meaning of K is the number of all independent (internal and external) times in the diagram. Note that in \mathcal{D} , we perform only $N - 1$ integrations over time. Those are the times associated with N interaction vertices, minus the one that is fixed to zero. The integrations of the times associated with $\delta\mu$ insertions have already been performed in Eq. (21), and there are L such integrals. Overall, the number of independent times is $K = N + L$. Ultimately, we group contributions by the expansion order K and look for convergence with respect to this parameter.

2. Numerical implementation of DiagMC and relation to other algorithms

The expression (31) is very convenient for numerical evaluation. First, we restrict the values of $\bar{\epsilon}_{\mathbf{k}}$ to a uniform grid on the real axis with the step $\Delta\omega$ ($\bar{\epsilon}_{\mathbf{k}} = j\Delta\omega$). These appear in $\omega_2, \dots, \omega_K$ as terms with integer coefficients, which means that $\{\omega_i\}$ entering $\mathcal{I}_{\mathbf{X}}$ will also be restricted to the same uniform grid. The final result therefore has the form

$$D_{\Upsilon_N, \mathbf{k}, L, \delta\mu}(z) = \sum_{j \in \mathbb{Z}, p \in \mathbb{N}} \frac{\mathcal{A}_{j,p}}{(z - j\Delta\omega)^p}. \quad (33)$$

This form allows us to reinterpret the finite-lattice results as that of the thermodynamic limit and extract $D_{\Upsilon_N, \mathbf{k}, L, \delta\mu}(\omega + i0^+)$ without any numerical broadening (see Appendix B for details).

In our present implementation, we perform a flat-weight (uniform) MC sampling over internal momenta $\{\mathbf{k}_i\}$, do a full summation of all the other sums, and accumulate the amplitudes $\mathcal{A}_{j,p}$. There are, however, other options. For example, one may sample $\{\mathbf{k}_i\}, \{p_i\}, \{b_i\}$ and use $P \equiv \prod_j n_{\mathbb{F}}(s_j \bar{\epsilon}_{\mathbf{k}_j}) e^{b_N \beta \tilde{\omega}_N}$ as the weighting function. We have thoroughly checked that the factor P closely correlates with the contribution to $\mathcal{A}_{j,p}$ coming from a given choice of the $\{\mathbf{k}_i\}, \{p_i\}, \{b_i\}$ variables (with other variables summed over), and thus P could be a good choice for a weighting function. However, this requires additional operations related to move proposals and trials, and we have not yet been able to make such an algorithm more efficient than the flat-weight MC. Nevertheless, it is apparent that our approach offers more flexibility than the algorithmic Matsubara summations (AMS). In AMS, no convenient weighting function can be defined for the Monte Carlo, so one either does the flat-weight summation [48] or uses the whole contribution to the result as the weight, which comes at the price of having to repeat the calculation for each frequency of interest [49] (on the contrary, in Ref. [48], as well as in this paper, the entire frequency dependence of the self-energy is obtained in a single MC run). At present, it is unclear which scheme is best—whether one should evaluate

$D(z)$ one z at a time or capture all z at once as we do here. This choice, as well as the choice of the weighting function, likely needs to be made on a case-by-case basis, as it is probable that in different regimes, different approaches will be optimal. In that sense, the added flexibility of our time-integration approach in terms of the choice of the weighting function may prove valuable in the future.

Concerning floating-point arithmetic, it is important that the factor $e^{b_N \beta \tilde{\omega}_N}$ stemming from $\mathcal{I}_{\mathbf{X}}$ can always be absorbed into the product of $n_{\mathbb{F}}$ functions in the second row of Eq. (31). This can be understood as follows. A given $\bar{\epsilon}_{\mathbf{k}_j}$ can, at most, appear twice as a term in $\tilde{\omega}_N$, once with sign $+1$ and once with sign -1 , corresponding to the incoming $\tilde{\tau}'_j$ and outgoing $\tilde{\tau}_j$ ends of the propagator j . In that case, the exponent cancels. The other possibility is that it appears only once, in which case it must correspond to the later time in the given permutation. If the later time is the outgoing end of the propagator, then the propagator is forward facing and the sign in front is $s = -1$; if it is the incoming end, then the propagator is backward facing and the sign in front is $s = 1$. In both cases, we can make use of

$$e^{s\beta\epsilon} n_{\mathbb{F}}(s\epsilon) = n_{\mathbb{F}}(-s\epsilon). \quad (34)$$

Therefore, no exponentials will appear in the final expression. A product of $n_{\mathbb{F}}$ functions is, at most, 1 and the coefficients c are not particularly big. Then, the size of the pole amplitudes that come out of Eq. (14) is determined by the energy resolution ($1/\Delta\omega$) and temperature ($\beta^{n_N+1-b_N-k_N}$). In our calculations so far, the amplitudes remain relatively small. Our approach ensures that we do not have very large canceling terms, such as we had in Ref. [48]. Indeed, we have successfully implemented Eq. (31) without the need for multiple-precision floating-point types.

Compared to the Matsubara-frequency summation algorithm [47–49], Eq. (31) presents an improved generality. Equation (31) is valid for any number and arrangement of instantaneous (i.e., frequency-independent) insertions, i.e., any choice of $\{\tilde{l}_j\}$. In contrast, the algorithmic Matsubara summation has to be performed for each choice of $\{\tilde{l}_j\}$ independently, and the resulting symbolic expressions need to be stored. For example, at $N = 4$, we have 12 Υ_N topologies. Therefore, at $L = 0$, the number of analytical solutions to prepare is 12. However, at $L = 2$, this number is 336, i.e., 28-fold bigger (we can place $L = 2$ insertions on $2N - 1 = 7$ fermionic lines in $7 \times 6/2 + 7 = 28$ ways, times 12 Υ_N topologies, i.e., 336).

3. Bare series

We are also interested in constructing a bare series where tadpole insertions are present in diagram topologies. Tadpole (or Hartree) insertions are instantaneous and an evaluation of their amplitudes can be done relatively simply by various means. At the level of the Hubbard model, the Hartree insertions factor out: For each Hartree diagram, the internal momentum summations and time integrations can be performed beforehand and only once, leading to a significant speedup.

In the expression (31), there is no difference between a Hartree insertion and a chemical-potential vertex insertion. Therefore, the inclusion of the Hartree insertions can be en-

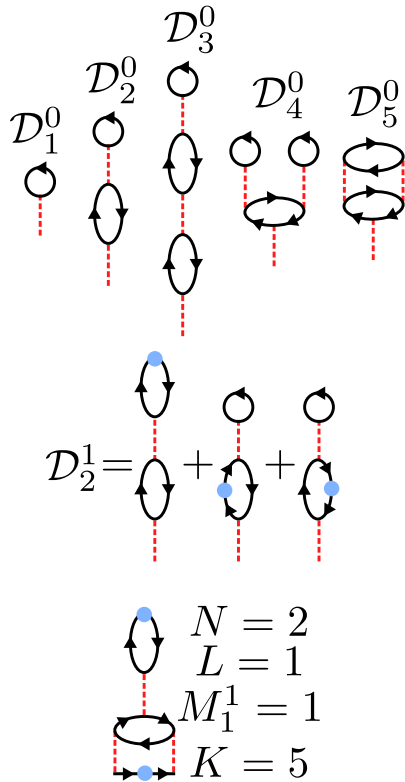


FIG. 2. Top: Illustration of possible Hartree diagrams, without any $\delta\mu$ insertions. Middle: Amplitude of a Hartree diagram with a single $\delta\mu$ insertion. Bottom: An example of a diagram dressed with both Hartree and $\delta\mu$ insertions, and the values of the parameters $N, L, \{M_i^L\}, K$ that it falls under (with $M_{i \neq 1}^{L \neq 1} = 0$).

tirely accounted for in the resummation of the $D_{\Upsilon_N, \mathbf{k}, L, \delta\mu}(z)$ contributions from the previous section, with the replacement

$$\bar{\varepsilon}_{\mathbf{k}} \equiv \varepsilon_{\mathbf{k}} - \mu + \delta\mu \quad (35)$$

(i.e., full Hartree shift excluded).

Note that the expansion of the propagators in $\delta\mu$ is performed in Hartree insertions as well, so we need to account for possible additional $\delta\mu$ insertions inside the Hartree diagrams. As before, our expansion order will be K , which is the total number of independent times, with each time associated to a single interaction or a $\delta\mu$ vertex, including those within Hartree insertions.

We will for now focus on the series up to $K = 5$. As the number of interactions in Υ_N is at least two, we can have, at most, three interaction vertices in a Hartree insertion. There are only five such Hartree diagrams (Fig. 2). We can evaluate these five amplitudes with very little effort by making use of spatial and temporal Fourier transforms.

Before we proceed with the calculation of the amplitudes \mathcal{D} of possible Hartree insertions relevant for the series up to $K = 5$, we define some auxiliary quantities. We first define the bare density,

$$n_0^{\bar{l}} = \sum_{\mathbf{k}} G_0^{l=1+\bar{l}}(\bar{\varepsilon}_{\mathbf{k}}, \tau = 0^-), \quad (36)$$

and the real-space propagator,

$$G_{0, \mathbf{r}}^{l=1+\bar{l}} = \sum_{\mathbf{k}} e^{i\mathbf{k} \cdot \mathbf{r}} G_0^{l=1+\bar{l}}(\bar{\varepsilon}_{\mathbf{k}}, \tau = 0^-). \quad (37)$$

We will also need the polarization bubble diagram,

$$\chi_{0, \mathbf{r}}^{\bar{l}_1, \bar{l}_2}(\tau) = G_{0, \mathbf{r}}^{l=1+\bar{l}_1}(\tau) G_{0, -\mathbf{r}}^{l=1+\bar{l}_2}(-\tau), \quad (38)$$

$$\chi_{0, \mathbf{q}=0}^{\bar{l}_1, \bar{l}_2}(i\nu = 0) = \sum_{\mathbf{r}} \int d\tau \chi_{0, \mathbf{r}}^{\bar{l}_1, \bar{l}_2}(\tau), \quad (39)$$

and the second-order self-energy diagram (up to the constant prefactor),

$$\Sigma_{2, \mathbf{r}}^{\bar{l}_1, \bar{l}_2, \bar{l}_3}(\tau) = G_{0, \mathbf{r}}^{l=1+\bar{l}_1}(\tau) \chi_{0, \mathbf{r}}^{\bar{l}_2, \bar{l}_3}(\tau), \quad (40)$$

which can be Fourier transformed to yield $\Sigma_{2, \mathbf{k}}^{\bar{l}_1, \bar{l}_2, \bar{l}_3}(i\omega)$.

We can now calculate the amplitudes of the possible Hartree insertions with a number L of $\delta\mu$ insertions on them, in any arrangement

$$\mathcal{D}_1^L = (-) n_0^L, \quad (41)$$

$$\mathcal{D}_2^L = (-)^2 \sum_{\substack{\bar{l}_1, \bar{l}_2, \bar{l}_3 \\ \bar{l}_1 + \bar{l}_2 + \bar{l}_3 = L}} n_0^{\bar{l}_1} \chi_{0, \mathbf{q}=0}^{\bar{l}_2, \bar{l}_3}(i\nu = 0), \quad (42)$$

$$\mathcal{D}_3^L = (-)^3 \sum_{\substack{\bar{l}_1, \dots, \bar{l}_5 \\ \sum_i \bar{l}_i = L}} n_0^{\bar{l}_1} \chi_{0, \mathbf{q}=0}^{\bar{l}_2, \bar{l}_3}(i\nu = 0) \chi_{0, \mathbf{q}=0}^{\bar{l}_4, \bar{l}_5}(i\nu = 0), \quad (43)$$

$$\mathcal{D}_4^L = (-)^3 \sum_{\substack{\bar{l}_1, \dots, \bar{l}_3 \\ \sum_i \bar{l}_i = L}} \binom{2 + \bar{l}_3}{2} n_0^{\bar{l}_1} n_0^{\bar{l}_2} n_0^{2+\bar{l}_3}, \quad (44)$$

$$\mathcal{D}_5^L = (-)^2 \sum_{\substack{\bar{l}_1, \dots, \bar{l}_5 \\ \sum_i \bar{l}_i = L}} T \sum_{i\omega} e^{-i\omega 0^-} \sum_{\mathbf{k}} G_{0, \mathbf{k}}^{l=1+\bar{l}_1}(i\omega) \Sigma_{2, \mathbf{k}}^{\bar{l}_2, \bar{l}_3, \bar{l}_4}(i\omega) G_{0, \mathbf{k}}^{l=1+\bar{l}_5}(i\omega). \quad (45)$$

As we are restricting to $K \leq 5$ calculations, the $\mathcal{D}_{3 \dots 5}^L$ insertions can only be added once, and only with $L = 0$. We now define M_i^L as the number of insertions of \mathcal{D}_i^L tadpoles, and we define N_i as the number of interaction vertices contained in the tadpole \mathcal{D}_i (regardless of L , we have $N_1 = 1, N_2 = 2, N_3 = N_4 = N_5 = 3$).

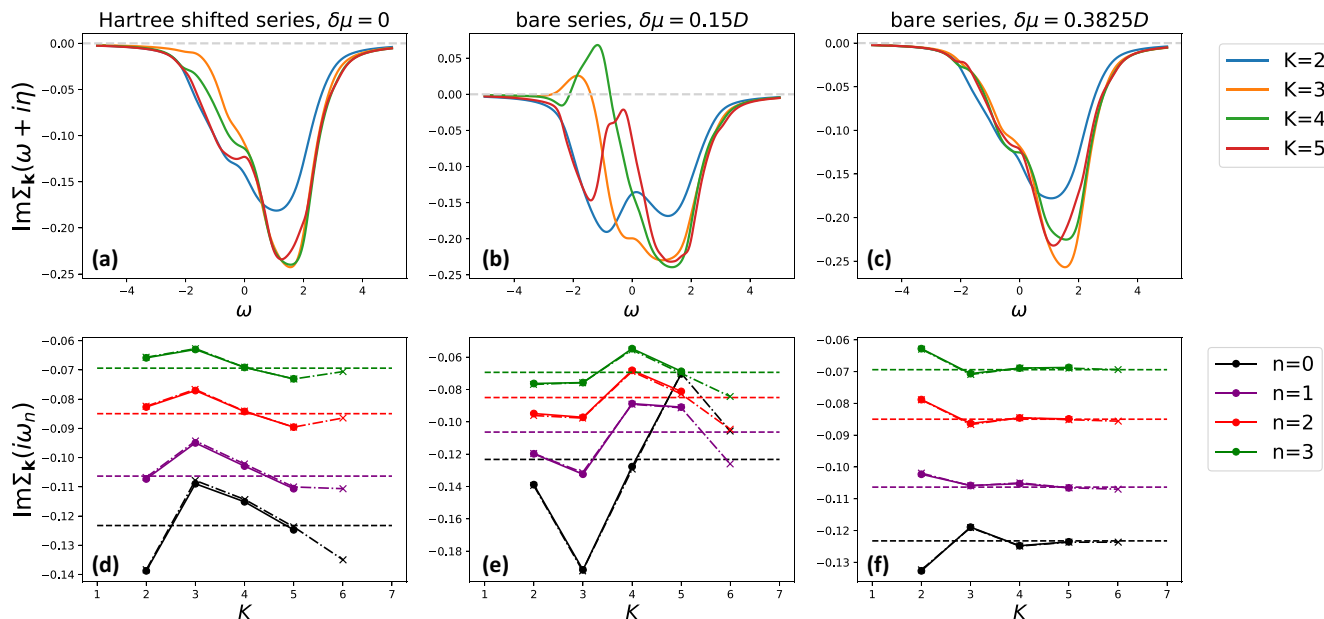


FIG. 3. DiagMC solution for the Hubbard model on a square lattice. Parameters of the model are $t' = -0.3t$, $\mu = 0$, $U = 1D$, and $T = 0.125D$, which corresponds to $\langle n_\sigma \rangle \approx 0.3625$. Top row: Imaginary part of self-energy at $\mathbf{k} = (\pi/4, \pi)$ on the real axis (with broadening $\eta = 0.3D$) obtained with three different series, up to perturbation order K . Bottom row: Illustration of convergence with respect to perturbation order K , using values of the imaginary part of the self-energy at the lowest four Matsubara frequencies, $i\omega_{n=0\dots3}$. Full lines are our result, dash-dotted lines with crosses are the analogous result with a numerical τ -integration algorithm from Ref. [52], and horizontal dashed lines are the determinantal QMC result on a 16×16 lattice from Ref. [52].

The series can now be resummed as

$$\Sigma_{\mathbf{k}}^{(\text{HF})}(z) = \sum_{K=2}^{\infty} \sum_{N=2}^K \sum_{L=0}^{K-N} \sum_{\substack{\{M_i^{L'}\}=0 \\ N+L+\sum_{i,L'} M_i^{L'}(N_i+L')=K}}^{K-N-L} (-U)^{N+\sum_{i,L'} M_i^{L'} N_i} (-\delta\mu)^{L+\sum_{i,L'} M_i^{L'} L'} \prod_{i,L'} (\mathcal{D}_i^{L'})^{M_i^{L'}} \Omega(L, \{M_i^{L'}\}) \times \sum_{\Upsilon_N} D_{\Upsilon_N, \mathbf{k}, L+\sum_{i,L'} M_i^{L'}}(z), \quad (46)$$

where $\Omega(L, \{M_i^{L'}\})$ is the combinatorial prefactor which counts all the possible ways the selected single-particle vertices $\delta\mu, \{\mathcal{D}_i\}$ can be arranged. This corresponds to the number of permutations of the multisets,

$$\Omega(L, \{M_i^{L'}\}) = \frac{(L + \sum_{i,L'} M_i^{L'})!}{L! \prod_{i,L'} M_i^{L'}!}. \quad (47)$$

We emphasize that Eq. (46) is fully general, but at orders $K \geq 5$, additional Hartree insertions \mathcal{D} [compared to Eqs. (41)–(45)] need to be considered.

Finally, we stress that our analytical time-integral solution and action-shift tuning scheme in DiagMC are not restricted to the treatment of the Hubbard Hamiltonian. See Appendix F for a discussion of DiagMC in the case of a general Hamiltonian with two-body interactions.

IV. RESULTS

A. Convergence speedup with $\delta\mu$ expansion in the bare series

Here we focus on supplementing the results from Ref. [52] with real-frequency self-energies calculated without any numerically ill-defined analytical continuation.

The model parameters are $t' = -0.3t$, $\mu = 0$, $U = 1.0D$, $T = 0.125D$, and $\langle n_\sigma \rangle = 0.3625$. In Ref. [52], the calculation was performed with the Hartree-shifted series with $\delta\mu = 0$, as well as with the bare series, with two values of $\delta\mu$, namely, $0.15D$ and $0.3825D$. We repeat these calculations with our method. We use lattice size 32×32 , and project the dispersion onto a uniform energy grid, as described in Ref. [48] and discussed in Sec. III C 2. In Fig. 3, we show our results and compare them with the results of Ref. [52].

In the upper row of Fig. 3 are the real-frequency self-energies calculated up to order $K \leq 5$. We are keeping a finite broadening $\eta = 0.3D$ to smoothen the curves. As discussed in Appendix B, in our method, numerical pole broadening is not a formal necessity. However, there is still a significant amount of statistical noise in our real-frequency result (although the imaginary-frequency result is already very well converged). It is important to note that some of the noisy features in our real-frequency result may be artifacts of the finite-lattice size that would not vanish with increasing number of MC steps. However, by comparing the result with a 256×256 lattice calculation (Appendix C), we check that already at $\eta = 0.2D$, no such artifact should be visible. It appears that for the given

external \mathbf{k} and broadening $\eta = 0.2D$, increasing the lattice size further from 32×32 brings no new information, but it also does not present an additional cost: at $\eta = 0.2D$, our 256×256 lattice calculation appears equally well converged as the 32×32 lattice calculation, with the equal number of MC steps and a similar runtime, and yields a result that is on top of the 32×32 calculation.

In the bottom row of Fig. 3, we show the change in the imaginary part of the self-energy at the first four Matsubara frequencies, as a function of the maximal order K . Full-line and dots are the result of our calculations. The dash-dotted lines with crosses are data points taken from Ref. [52]. The horizontal dashed lines are the 16×16 -lattice determinantal QMC result, also from Ref. [52].

The excellent agreement with the results from Ref. [52] serves as a stringent test of our implementation. In the $\delta\mu = 0.3825D$ calculation, even on the real axis, the self-energy does appear well converged by order $K = 5$, although there is some discrepancy between $K = 4$ and $K = 5$ at around $\omega = 1.5D$.

B. ω -resolved resummation

We can now go one step further by resumming the series presented in Figs. 3(a) and 3(c) for each ω individually, using an ω -dependent optimal shift $\delta\mu^*(\omega)$. The results are shown in Figs. 4 and 5.

We determine the optimal $\delta\mu^*(\omega)$ by minimizing the spread of the $\text{Im}\Sigma(\omega + i\eta)$ results between orders $K = 3$ and $K = 5$. This spread as a function of ω and $\delta\mu$ is color plotted in Figs. 4 and 5. We have results for a discrete set of $\delta\mu \in \{\delta\mu_i\}$, so the optimal $\delta\mu^*(\omega)$ is *a priori* a discontinuous curve. As this is clearly unsatisfactory, we smoothen the curve (shown with the blue line on the top panels in Figs. 4 and 5). However, we do not have results for each precise value of this optimal $\delta\mu^*(\omega)$. One could take, for each ω , the available $\delta\mu_i$ that is closest to $\delta\mu^*(\omega)$, but this would, again, result in a discontinuous curve. To avoid this, we average the available results as

$$\Sigma(\omega) = \frac{\sum_i \Delta\delta\mu_i \Sigma(\omega; \delta\mu_i) w(\delta\mu^*(\omega), \delta\mu_i)}{\sum_i \Delta\delta\mu_i w(\delta\mu^*(\omega), \delta\mu_i)}, \quad (48)$$

where $\Delta\delta\mu_i$ is the size of the $\delta\mu$ step in the available results at the i th value (allows for nonuniform grids). We use a narrow Gaussian weighting kernel,

$$w(\delta\mu^*(\omega), \delta\mu_i) = e^{-(\delta\mu_i - \delta\mu^*(\omega))^2 / W^2}. \quad (49)$$

The width of the kernel W is chosen such that it is as narrow as possible, while still encompassing at least 3–4 $\delta\mu_i$ points, so that the final result is reasonably smooth as a function of ω ; W is therefore determined according to the resolution in $\delta\mu$. We use $W = 0.05$ and $\Delta\delta\mu_i \approx 0.02$ and have checked that the results are insensitive to the precise choice of this numerical parameter.

The results of the averaging around the optimal $\delta\mu^*(\omega)$ are shown in the middle and bottom panels of Figs. 4 and 5. In both cases, the ω -resolved resummation helps to converge the result. In the case of the bare series, the convergence is now almost perfect, and already order $K = 3$ is on top of the exact result. In the case of the Hartree-shifted series, the results are

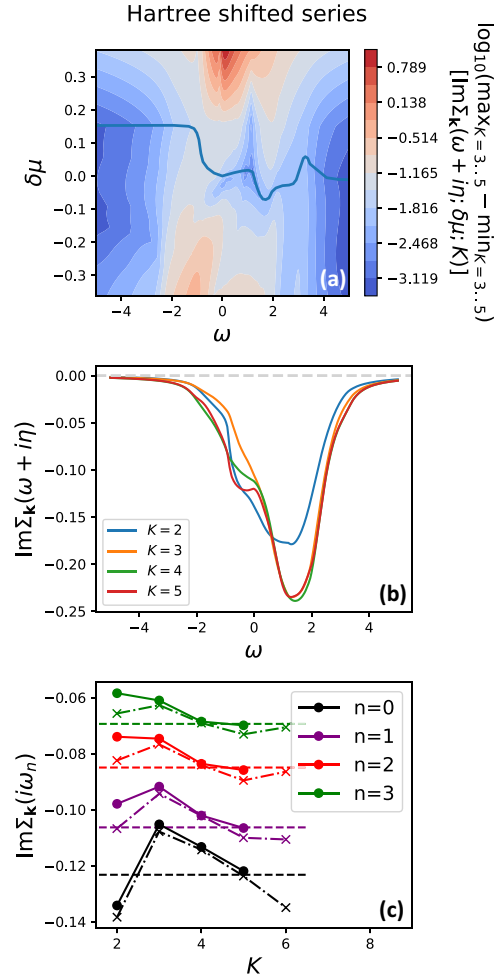


FIG. 4. Results of the Hartree-shifted series with ω -resolved resummation, to be compared to Figs. 3(a) and 3(d) (all parameters are the same). Top panel: Color plot of the spread of the imaginary part of the self-energy at a given $\omega + i\eta$ between orders $K = 3$ and 5 , in a calculation with a given $\delta\mu$. The blue line smoothly connects the minima of the spread (at each ω), and defines the ω -dependent optimal shift $\delta\mu^*(\omega)$ used in the resummation. Middle and bottom panels are analogous to Figs. 3(a) and 3(d). In the bottom panel, the dash-dotted and dashed lines are the same as in Fig. 3(d).

not perfectly converged at $\omega < 0$, yet the $K = 5$ calculation is practically on top of the exact result on the imaginary axis, and presents an improvement to the $\delta\mu = 0$ series in Fig. 3(a). Note that the improvement in convergence is seen on the imaginary axis, as well.

C. Removing nonphysical features

In this section, we focus on the parameters case discussed in Ref. [48]. We calculate the Hartree-shifted series with parameters of the model $t' = 0$, $\mu - U\langle n_\sigma \rangle = -0.1D$, $T = 0.1D$, and employ various $\delta\mu$ shifts. The lattice size is again 32×32 and we focus on the self-energy at $\mathbf{k} = (0, \pi)$. Note that in Hartree-shifted series, the quantity that enters the calculation is $\mu - U\langle n_\sigma \rangle$, rather than μ . If $\langle n \rangle$ is calculated, μ can be estimated *a posteriori*. In our calculation, we fix

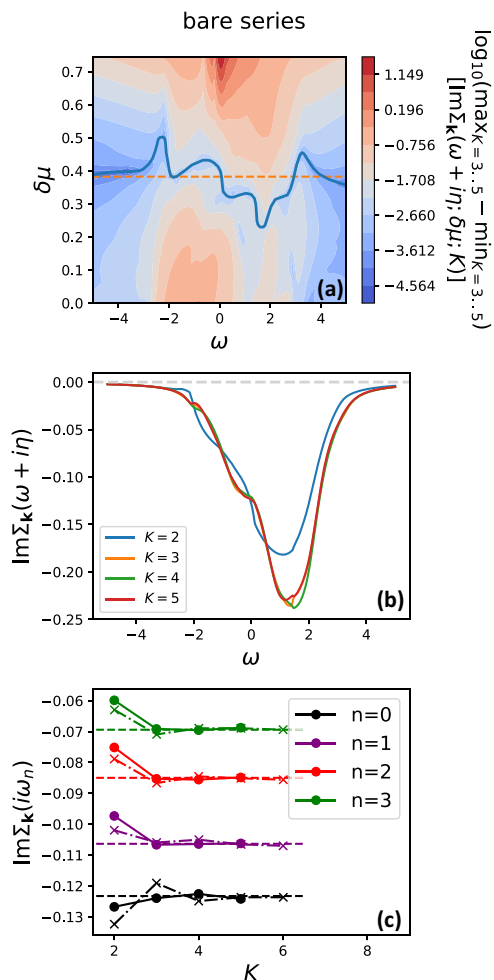


FIG. 5. Results of the bare series with ω -resolved resummation, to be compared to Figs. 3(c) and 3(f) (all parameters are the same). The top panel is analogous to Fig. 4(a). The horizontal orange dashed line denotes the value of $\delta\mu$ used in Figs. 3(c) and 3(f) to best converge the imaginary-axis result. The middle and bottom panels are analogous to Figs. 3(c) and 3(f). In the bottom panel, the dash-dotted and dashed lines are the same as in Fig. 3(f).

$\mu - U \langle n_\sigma \rangle$, and $\langle n_\sigma \rangle$ is then U dependent. Roughly, as given in Ref. [48], at $U = 1$, we have $\langle n_\sigma \rangle \approx 0.455$.

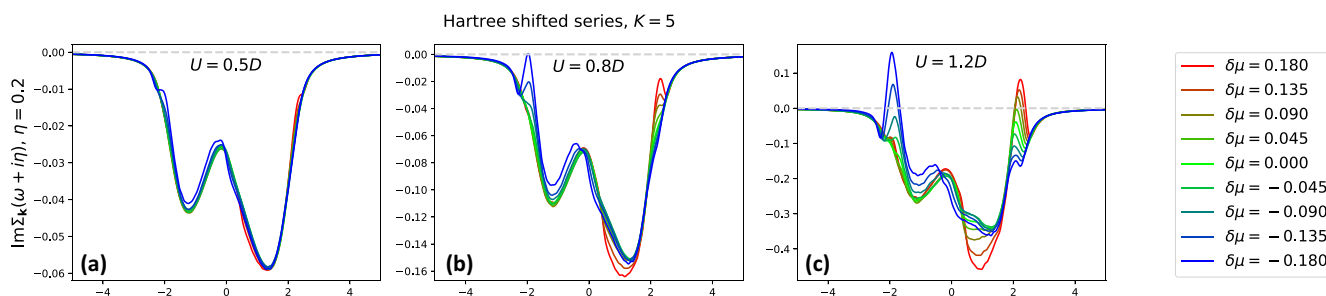


FIG. 6. Imaginary part of the self-energy on the real axis (with broadening η), at different values of coupling constant U , obtained with our method at $K = 5$ using different chemical-potential shifts $\delta\mu$. The parameters of the calculation are the same as in Ref. [48], i.e., $t' = 0$, $\mu - U \langle n_\sigma \rangle = -0.1D$, $T = 0.1D$. The self-energy is calculated at $\mathbf{k} = (0, \pi)$. Passing of the curves above the gray dashed line indicates breaking of causality.

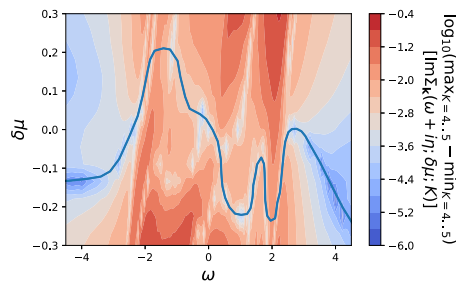


FIG. 7. Analogous to Fig. 4(a), for the parameters of the model corresponding to Fig. 6. The blue line is the optimal $\delta\mu^*$, to be used in Fig. 8.

The results are presented in Fig. 6 for three values of U . At low U , the series is well converged by $K = 5$, and the result is entirely insensitive to the choice of $\delta\mu$, as expected. At intermediate and high U , the result can be strongly $\delta\mu$ sensitive. The $\delta\mu$ dependence of the result, however, strongly varies with ω . It appears that for a given ω , there are ranges of the $\delta\mu$ value where the result (at fixed order K) is insensitive to the precise choice of $\delta\mu$. This presents an alternative way of choosing an optimal $\delta\mu$ (a similar idea was employed in a different context in Ref. [58]).

The striking feature at large U is the causality violations at $|\omega| \approx 2$ that were previously discussed in Ref. [48] (note that the broadening somewhat masks the extent of the problem). The dips in the self-energy spectrum appear to happen only at certain values of $\delta\mu$: at $\omega = -2$, the problem is present at $\delta\mu$ large and negative, and at $\omega = 2$, at $\delta\mu$ large and positive. In particular, at $\omega = 2$, the result appears to vary uniformly with $\delta\mu$, and one cannot select an optimal $\delta\mu$ based on the sensitivity of the result to the $\delta\mu$ value. We therefore repeat the procedure from the previous section and select the optimal $\delta\mu^*(\omega)$ based on the level of convergence between orders $K = 4$ and $K = 5$. The spread of the results and a smooth choice of $\delta\mu^*(\omega)$ are presented in Fig. 7.

In Fig. 8, the results of the averaging are shown and compared to the $\delta\mu = 0$ results at the highest available orders $K = 4$ and $K = 5$, at three values of U . The convergence is visibly better around our $\delta\mu^*$ than with $\delta\mu = 0$ at problematic frequencies $|\omega| \approx 2$. More importantly, the non-physical features are clearly absent. At $U = 1$, in the $\delta\mu = 0$

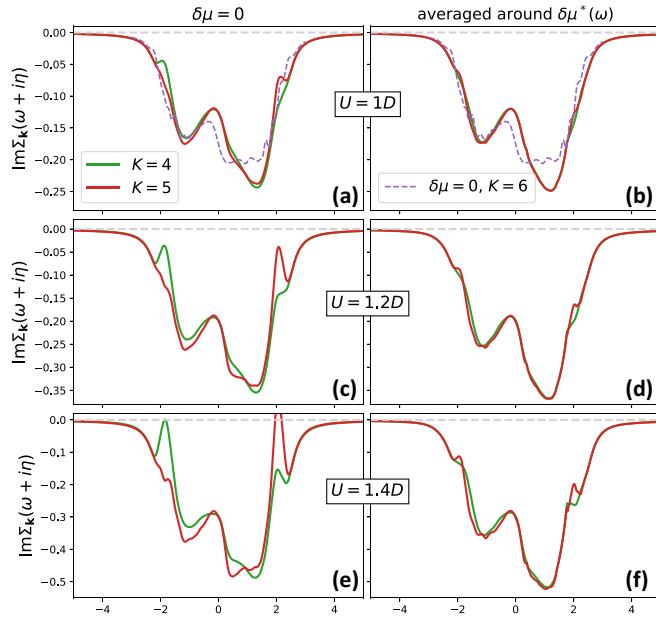


FIG. 8. Imaginary part of self-energy, real-frequency results (with broadening η). Right column: obtained with the ω -resolved resummation for the model parameters from Fig. 6, using the optimal $\delta\mu^*(\omega)$ from Fig. 7; to be compared to the standard $\delta\mu = 0$ calculation in the left column. Purple dashed lines in the top row are the $K = 6$ calculation with $\delta\mu = 0$.

calculation, the causality is not yet violated, but the dip at $\omega = 2$ is already starting to appear, which is clearly an artifact of the series truncation which should be removed systematically. It is important that the intermediate frequency behavior that we obtained by averaging results around the optimal $\delta\mu$ is indeed the correct one, and it will not change much further with increasing orders. We show in the top panels the $K = 6$, the $\delta\mu = 0$ result of which has been benchmarked against a fully converged imaginary-axis result in Fig. 9 (the converged result was obtained with the Σ Det method [59,60] at order

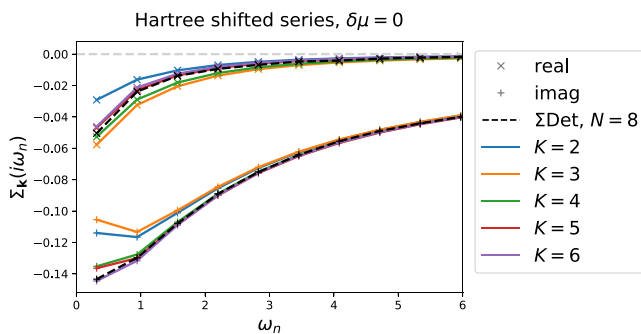


FIG. 9. Matsubara-frequency self-energy result, with model parameters as in Fig. 6. Crosses are the real part, pluses are the imaginary part, and lines are eye guides. Solid lines are the Hartree-shifted series with $\delta\mu = 0$ at different maximal K . The same result was obtained with both the algorithm presented in this work and the algorithmic Matsubara summation method from Ref. [48] (the two methods were compared diagram by diagram). Black dashed lines are the Σ Det result at maximal order $N = 8$.

8). Clearly, the improved convergence between orders 4 and 5 that we have achieved by choosing $\delta\mu$ appropriately does indeed mean an improved final result. However, our procedure does not improve the result at around $\omega = 0$, where the optimal $\delta\mu$ does appear to be close to 0. The $K = 6$, $\delta\mu = 0$ result shown in the upper panels of Fig. 8 is still a bit different from the $K = 5$, $\delta\mu \approx \delta\mu^*(\omega)$ results around $\omega = 0$.

In the case of $U = 1D$, it is interesting that a large negative $\delta\mu$ does bring the $\omega \approx 0$ result at order $K = 5$ much closer to the exact value. This can be anticipated from Fig. 6, where we show the corresponding results for $U = 0.8D$ and $U = 1.2D$. Also, by looking at the color plot in Fig. 7, we see that at $\omega = 0$, there is indeed a local minimum in the spread at around $\delta\mu = -0.2$, which could be used as the optimal $\delta\mu^*$. This minimum, however, cannot be continuously connected with the other minima that we observe at $\omega < 0$, so we chose a different trajectory in the $(\omega, \delta\mu)$ space. It would be interesting for future work to inspect the behavior at even more negative $\delta\mu$, where another continuous trajectory $\delta\mu^*(\omega)$ might be found.

V. DISCUSSION, CONCLUSIONS, AND PROSPECTS

In this paper, we have derived an analytical solution for the multiple-time integral that appears in the imaginary-time Feynman diagrams of an interaction series expansion. The solution is general for any diagram with a single external time or no external times. We find this generality to be a great advantage compared to the recently proposed algorithmic solutions of the corresponding Matsubara-frequency summations. Our analytical solution allowed us to develop a very flexible DiagMC algorithm that can make use of the possibility to optimize the series with shifted actions. As a result, we were able to almost perfectly converge a real-frequency self-energy in just 3–4 orders of perturbation, in a nontrivial regime and practically in the thermodynamic limit.

More importantly, the fact that one does not have to prepare a solution for each diagram topology individually opens the possibility to develop algorithms more akin to CTINT and allow the MC sampling to go to indefinite perturbation orders. In fact, upon a simple inspection of CTINT and continuous-time hybridization-expansion quantum Monte Carlo in the segment picture (segment-CTHYB) equations [42], it becomes clear that our solution can, in principle, be applied there, so as to reformulate these methods in real frequency. This would, however, come at the price of having to break into individual terms the determinant that captures all the contributions to the partition function at a given perturbation order. In turn, this may lead to a more significant sign problem, and an effective cap on the perturbation orders that can be handled in practice. On the other hand, it is not entirely clear how much of the sign problem comes from summing the individual terms and how much from the integration of the internal times, and we leave such considerations for future work. In any case, DiagMC algorithms based on hybridization expansion have been proposed before (see Refs. [23,28,61]), where our analytical solution may be applied.

Our solution also trivially generalizes to real-time integrals and may have use in Keldysh and Kadanoff-Baym [9]

calculations, where the infamous dynamical sign problem arises precisely due to oscillating time integrands. There have been recent works [62,63] with imaginary-time propagation of randomized walkers where our solution may also find application.

Finally, we emphasize that avoiding analytical continuation could be beneficial at high temperature where the Matsubara frequencies become distant from the real axis, and thus noisy imaginary-axis correlators contain little information [64,65]. The high-temperature regime is particularly relevant for optical lattice simulations of the Hubbard model [66]. In that context, we anticipate our method will find application in the calculation of conductivity and other response functions.

ACKNOWLEDGMENTS

We thank Fedor Šimkovic for useful discussions and for sharing his diagram topology data. Computations were performed on the PARADOX supercomputing facility (Scientific Computing Laboratory, Center for the Study of Complex Systems, Institute of Physics Belgrade) and the ALPHA cluster (Collège de France). This work was also granted access to the HPC resources of TGCC and IDRIS under the Allocations No. A0090510609 and No. A0070510609 attributed by GENCI (Grand Equipement National de Calcul Intensif). J.V. acknowledges funding provided by the Institute of Physics Belgrade, through the grant by the Ministry of Education, Science, and Technological Development of the Republic of Serbia, as well as by the Science Fund of the Republic of Serbia, under the Key2SM project (PROMIS program, Grant No. 6066160). M.F. acknowledges support by the Simons Foundation. We also acknowledge support by the European Research Council for the European Union Seventh Framework Program (FP7/2007-2013) with ERC Grant No. 319286 (QMAC).

APPENDIX A: REAL-TIME INTEGRATION

Let us consider the following special case of the integral given by Eq. (3), which is relevant for real-time integrations featuring integrands of the form e^{itE} :

$$\tilde{\mathcal{I}}_{\{l_2 \dots l_N\}, \{E_2 \dots E_N\}}(t) = \prod_{i=2}^N \int_0^{t_{i+1}} dt_i t_i^{l_i} e^{it_i E_i}, \quad (\text{A1})$$

with $t_{N+1} \equiv t$. This corresponds to the case $r \notin [2, N]$ in Eq. (3), and $\omega_i = iE_i$, and we will define \tilde{E}_i analogously to $\tilde{\omega}_i$. The result is then obtained straightforwardly from Eq. (14),

$$\begin{aligned} \tilde{\mathcal{I}}_{\{l_2 \dots l_N\}, \{E_2 \dots E_N\}}(t) &= \sum_{\{b_i \in [\delta_{z_i}, 1]\}_{i=2 \dots N}} e^{it \tilde{E}_N b_N} \sum_{\{k_i \in [0, (1-\delta_{z_i})n_i]\}_{i:b_i=1}} \\ &\times (-1)^{\sum_{i=2}^N k_i} \prod_{i:\delta_{z_i}=1} \frac{1}{n_i} \\ &\times t^{n_{N+1}-b_N-k_N} \prod_{i:\tilde{E}_i \neq 0} \frac{C_{n_i, k_i}}{(i\tilde{E}_i)^{k_i+b_i}}, \quad (\text{A2}) \end{aligned}$$

which has the following general form:

$$\tilde{\mathcal{I}}(t) = \sum_{j:p \in \mathbb{N}_0} \mathcal{Z}_{p,j} t^p e^{it \mathcal{E}_j}. \quad (\text{A3})$$

APPENDIX B: EXTRACTING REAL-AXIS RESULTS WITHOUT POLE BROADENING

In this section, we show how the results on the real axis can be extracted without any numerical broadening of the poles. Rather, we make use of the pole amplitudes by interpreting the result as being representative of the thermodynamic limit, where poles on the real axis merge into a branch cut, and thus we consider that the pole amplitude is a continuous function of the real frequency. We extract the imaginary part of the contribution $[\text{Im}D(\omega)]$, and then the Hilbert transform can be used to reconstruct the real part.

The procedure relies on the following construction: A function $f(z)$ which is analytic everywhere in the upper half of the complex plane ($z^+ = x + iy$ with $y > 0$) and decays to zero with $|z^+|$ satisfies the relation

$$f(z^+) = -\frac{1}{\pi} \int dx' \frac{\text{Im}f(x' + i0^+)}{z^+ - x'}. \quad (\text{B1})$$

After applying the p th derivative with respect to x (i.e., the real part of z^+) on both sides of the equation, one obtains

$$\begin{aligned} \partial_x^p f(z^+) &= -\frac{1}{\pi} \int dx' \partial_x^p \frac{\text{Im}f(x' + i0^+)}{z^+ - x'} \\ &= -\frac{1}{\pi} \int dx' (-1)^p (p+1)! \frac{\text{Im}f(x' + i0^+)}{(z^+ - x')^{p+1}}. \quad (\text{B2}) \end{aligned}$$

We can now move the constant prefactors to the left-hand side and rename $p+1 \rightarrow p$. Just above the real axis, we have

$$\frac{(-1)^p \pi}{p!} \partial_x^{p-1} f(x + i0^+) = \int dx' \frac{\text{Im}f(x' + i0^+)}{(x - x' + i0^+)^p}. \quad (\text{B3})$$

We can now discretize the expression on a uniform x grid with the step Δx , say, $x_j = j\Delta x$, and we see that the right-hand side has the form of a sum of poles of order p , equidistant along the real axis, and with amplitudes $\mathcal{A}_j = \text{Im}f(x_j + i0^+)$,

$$\frac{(-1)^p \pi}{p!} \tilde{\partial}_j^{p-1} \mathcal{A}_j \approx \text{Im} \sum_j \Delta x \frac{\mathcal{A}_j}{(x_j - x_j' + i0^+)^p}, \quad (\text{B4})$$

where $\tilde{\partial}$ is the finite-difference approximation for the derivative along the x axis. Clearly, the imaginary part of the entire sum of p -order poles at a certain point x_j can be estimated by looking only at the $(p-1)$ th derivative of the amplitudes of these poles at x_j , as given in the above expression.

The expression (B4) can be readily applied in our case [Eq. (33)] where the real axis is the frequency axis ω , with step $\Delta\omega$ and $\omega_j = j\Delta\omega$, and the sum of the poles determines our diagram contribution D . In general we have poles of various orders, but we can group the poles by order and treat their contributions separately. We therefore have

$$\text{Im}D(\omega_j + i0^+) \approx \frac{\pi}{\Delta\omega} \sum_p \frac{(-1)^p}{p!} \tilde{\partial}_j^{p-1} \mathcal{A}_{j,p}. \quad (\text{B5})$$

In the case of simple poles only, the contribution at any ω_j is simply proportional to the amplitude of the pole $\mathcal{A}_{j,1}$. Other-

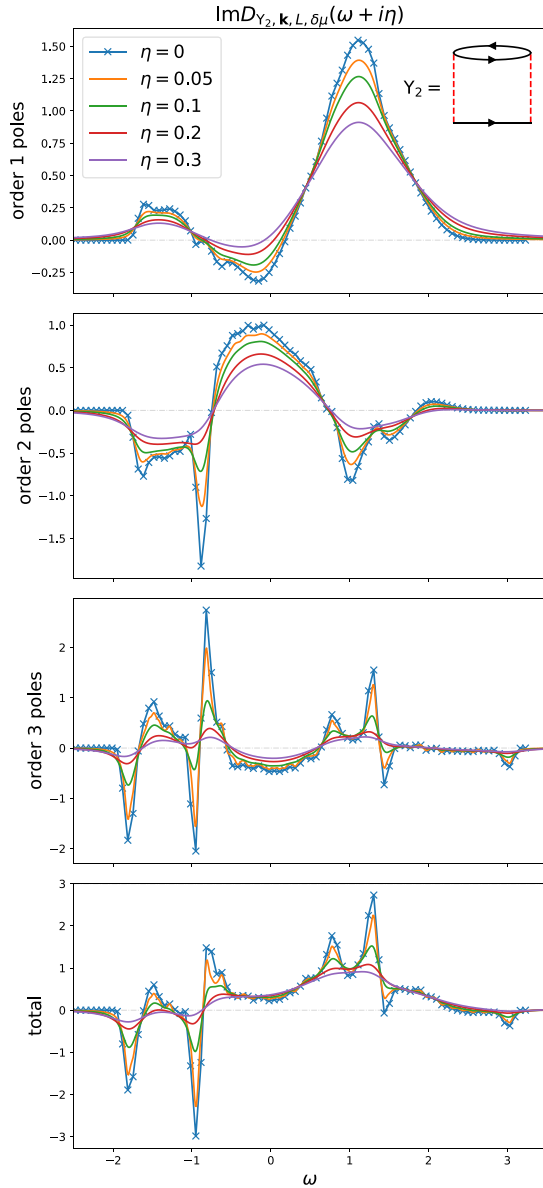


FIG. 10. Illustration of a $\eta = 0^+$ result obtained from Eq. (31) without any numerical broadening, based only on pole amplitudes. The diagram used is the second-order diagram (illustrated in the top panel), with $L = 2$. In the propagators, we take $\delta\mu = 0$. The rest of the parameters are $\mu - U\langle n_\sigma \rangle = -0.1D$, $T = 0.1D$, and the external momentum is $\mathbf{k} = (0, \pi)$. The top three panels are contributions from first-, second-, and third-order poles, respectively. The bottom panel is the total result. Lines with $\eta > 0$ are obtained with numerical broadening. The crosses on the $\eta = 0$ result denote the available frequencies (in between, we assume linear interpolation).

wise, the procedure requires that the pole amplitudes form a reasonably smooth function of the real frequency. Additionally, the energy resolution is a measure of the systematic error made in this procedure.

To avoid statistical noise and noisy features coming from the finite size of the lattice (see next section), we test our method on the example of a $N = 2$, $L = 2$ diagram, which we can solve with the full summation of Eq. (31), on a lattice

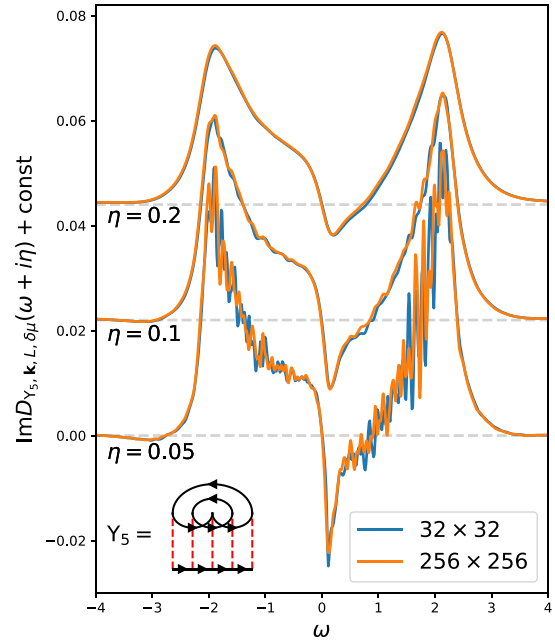


FIG. 11. Comparison of the real-frequency imaginary self-energy result for a single fifth-order diagram (illustrated in the bottom-left corner), for the lattice sizes 32×32 and 256×256 , at three different levels of broadening. The calculation is in both cases performed with the same number of MC steps and took similar time. The parameters are $L = 0$, $\delta\mu = 0$, $\mu - U\langle n_\sigma \rangle = -0.1D$, $T = 0.1D$, and the external momentum is $\mathbf{k} = (0, \pi)$.

of the size 96×96 . This diagram produces poles up to order 3. The result is shown in Fig. 10. In the first three panels, we show the contribution from the poles of each order, and in the bottom panel, we show the total result.

APPENDIX C: CONVERGENCE WITH LATTICE SIZE

In this section we discuss the convergence of the result with respect to the lattice size. In Fig. 11, we compare the results for a single $N = 5$, $L = 0$ diagram on the lattices of size 32×32 and 256×256 . We observe that the result is almost exactly the same at broadening level $\eta = 0.2$, which brings further confidence in the results in the main part of the paper.

In Fig. 12, we illustrate how the size of the lattice determines the highest energy resolution that one can have, under requirement that the results form a continuous curve on the real axis and are, therefore, representative of the thermodynamic limit. We perform the full summation for the second-order diagram with $L = 0$, with various sizes of the lattice and various resolutions. Clearly, the bigger the lattice, the higher the energy resolution one can set without affecting the smoothness of the results.

The numerical parameters of the calculation are therefore the size of the lattice, the energy resolution, and the broadening (the resolution and the broadening can be tuned *a posteriori*), and one can tune them to get the optimal ratio between performance and the error bar. If the pole amplitudes \mathcal{A}_{jP} are a relatively smooth function of j , no broadening is then needed at all.

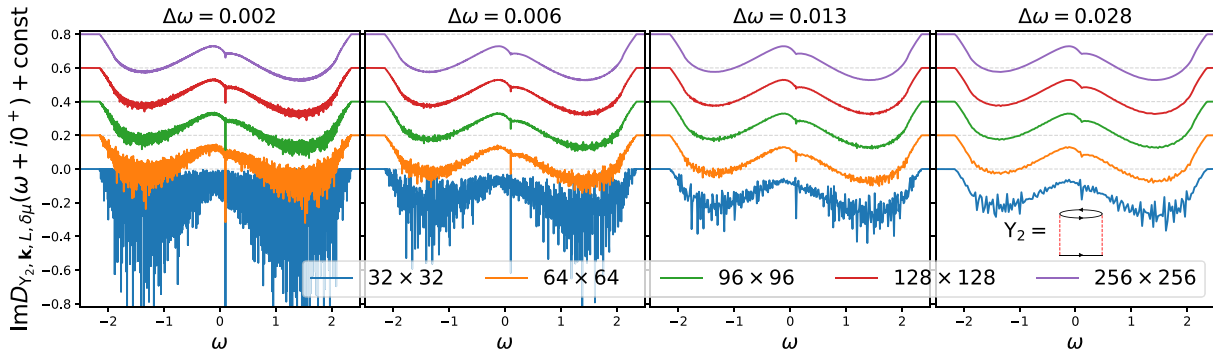


FIG. 12. Real-frequency result ($\eta = 0^+$) for the contribution of the lowest-order diagram (illustrated in the rightmost panel) at various lattice sizes and frequency resolutions, obtained with full summation (gray code). The step of the uniform energy grid is denoted $\Delta\omega$. The parameters are $L = 0$, $\delta\mu = 0$, $\mu - U\langle n_\sigma \rangle = -0.1D$, $T = 0.1D$, and the external momentum is $\mathbf{k} = (0, \pi)$.

APPENDIX D: DERIVATION OF EQ. (5)

After applying n times the partial integration over the integral from the left-hand side of Eq. (5), we get

$$\begin{aligned} \int_0^{\tau_f} \tau^n e^{\tau z} d\tau &= \frac{1}{z^{n+1}} \int_0^{\tau_f} \tau^n e^{\tau z} d\tau \\ &= \frac{1}{z^{n+1}} \left[e^{z\tau_f} (z\tau_f)^n - n e^{z\tau_f} (z\tau_f)^{n-1} + \dots + (-1)^n n! \int_0^{\tau_f} \tau^0 e^{\tau z} d\tau \right] \\ &= \frac{1}{z^{n+1}} \left[\frac{n!}{(n-0)!} (-1)^0 e^{z\tau_f} (z\tau_f)^{n-0} + (-1)^1 \frac{n!}{(n-1)!} e^{z\tau_f} (z\tau_f)^{n-1} + \dots + (-1)^n \frac{n!}{(n-n)!} \int_0^{\tau_f} \tau^0 e^{\tau z} d\tau \right] \\ &= \frac{1}{z^{n+1}} \left[\frac{n!}{(n-0)!} (-1)^0 e^{z\tau_f} (z\tau_f)^{n-0} + (-1)^1 \frac{n!}{(n-1)!} e^{z\tau_f} (z\tau_f)^{n-1} + \dots + (-1)^n \frac{n!}{(n-n)!} (z\tau_f)^0 (e^{z\tau_f} - 1) \right] \\ &= \frac{1}{z^{n+1}} e^{z\tau_f} \sum_{k=0}^n (-1)^k (z\tau_f)^{n-k} \frac{n!}{(n-k)!} - (-1)^n \frac{n!}{z^{n+1}}, \end{aligned} \tag{D1}$$

which can be readily identified with the right-hand side of Eq. (5).

APPENDIX E: DERIVATION OF EQ. (21)

We are looking for a solution of the Fourier transform

$$G_0^l(\varepsilon, \tau) = \frac{1}{\beta} \sum_{i\Omega_\eta} \frac{e^{-i\Omega_\eta \tau}}{(i\Omega_\eta - \varepsilon)^l}. \tag{E1}$$

For any τ , we can express the sum above as a contour integral, and we find

$$\begin{aligned} G_0^l(\varepsilon, \tau) &= -\text{Res}_{z=\varepsilon} \frac{e^{-z\tau}}{(z-\varepsilon)^l} \frac{\eta^{\lfloor \frac{x}{\beta} \rfloor} e^{\lfloor \frac{x}{\beta} \rfloor \beta z}}{1 - \eta e^{-\beta z}} dz \\ &= -\frac{\eta^{\lfloor \frac{x}{\beta} \rfloor}}{(l-1)!} \frac{d^{l-1}}{dz^{l-1}} \frac{e^{-\beta z \lfloor \frac{x}{\beta} \rfloor}}{1 - \eta e^{-\beta z}} \Big|_{z=\varepsilon}, \end{aligned} \tag{E2}$$

where $\lfloor \dots \rfloor$ denotes the integer part (floor function), and $\{x\} \equiv x - \lfloor x \rfloor$ denotes the fractional part.

We see that it will be useful to have an expression for derivatives of $(1 - \eta e^z)^{-1}$. They have the general form

$$\frac{d^k}{dz^k} \frac{1}{1 - \eta e^z} = \sum_{n=0}^k C_n^k \frac{(e^z)^n}{(1 - \eta e^z)^{n+1}}. \tag{E3}$$

By deriving this expression on both sides, one obtains a recursion for the coefficients C_n^k ,

$$C_n^{k+1} = n C_n^k + \eta n C_{n-1}^k, \tag{E4}$$

with holds for $k > -1$ and $n > 0$ with $C_0^0 = 1$. That can be rewritten

$$\frac{\eta^n}{n!} C_n^{k+1} = n \frac{\eta^n}{n!} C_n^k + \frac{\eta^{n-1}}{(n-1)!} C_{n-1}^k. \tag{E5}$$

If we define $S_n^k = \frac{\eta^n}{n!} C_n^k$, we have the recursion $S_n^{k+1} = n S_n^k + S_{n-1}^k$, which is the recursion for the Stirling numbers of the second kind. This allows one to have the following important result:

$$\begin{aligned} \frac{d^k}{dz^k} \frac{1}{1 - \eta e^z} &= \sum_{n=0}^k \eta^n n! \begin{Bmatrix} k \\ n \end{Bmatrix} \frac{(e^z)^n}{(1 - \eta e^z)^{n+1}} \\ &= \sum_{n=0}^k \eta^n n! \begin{Bmatrix} k \\ n \end{Bmatrix} \frac{e^{-z}}{(e^{-z} - \eta)^{n+1}}. \end{aligned} \tag{E6}$$

With this, one obtains the following expression:

$$G_0^l(\varepsilon, \tau) = -e^{\varepsilon\beta(1-\frac{\tau}{\beta})} \eta^{\lfloor \frac{\tau}{\beta} \rfloor + 1} (-\beta)^{l-1} \times \sum_{m=0}^{l-1} \sum_{n=0}^{l-m-1} \frac{n!}{(l-m-1)!m!} \begin{Bmatrix} l-m-1 \\ n \end{Bmatrix} \times \left(\frac{1}{\eta e^{\varepsilon\beta} - 1} \right)^{n+1} \left\{ \frac{\tau}{\beta} \right\}^m, \quad (E7)$$

which already satisfies the (anti)periodicity properties of the Green's function.

To make use of the result given by Eq. (E7), we need to express $G_0^l(\varepsilon, \tau)$ as a function of two times $G_0^l(\varepsilon, \tau, \tau') \equiv G_0^l(\varepsilon, \tau - \tau')$, with $\tau, \tau' \in [0, \beta]$. We first consider $\tau \geq \tau'$. By substituting $(\tau - \tau')^m = \sum_{\zeta=0}^m (-1)^{m-\zeta} \binom{m}{\zeta} \tau^\zeta \tau'^{m-\zeta}$ into Eq. (E7) and substituting $m - \zeta$ with ζ , we get

$$G_0^l(\varepsilon, \tau - \tau') = \eta e^{\varepsilon(\tau' - \tau)} n_\eta(-\varepsilon) \sum_{\zeta=0}^{l-1} \sum_{\zeta=0}^{l-\zeta-1} c_{l,\zeta,\zeta}^-(\varepsilon) \tau^\zeta \tau'^{\zeta}, \quad (E8)$$

with $c_{l,\zeta,\zeta}^-(\varepsilon)$ as defined in Eq. (22). The result for $\tau < \tau'$ can then be easily obtained by proving the property $G_0^l(\varepsilon, \tau) = (-1)^l G_0^l(-\varepsilon, -\tau)$,

$$\begin{aligned} G_0^l(\varepsilon, -\tau) &= \frac{1}{\beta} \sum_{n=-\infty}^{\infty} \frac{e^{i\Omega_\eta \tau}}{(i\Omega_\eta - \varepsilon)^l} \\ &= \frac{1}{\beta} \sum_{n=-\infty}^{\infty} \frac{e^{-i\Omega_\eta \tau}}{(-i\Omega_\eta - \varepsilon)^l} \\ &= (-1)^l \frac{1}{\beta} \sum_{n=-\infty}^{\infty} \frac{e^{-i\Omega_\eta \tau}}{(i\Omega_\eta + \varepsilon)^l} \\ &= (-1)^l G_0^l(-\varepsilon, \tau), \end{aligned}$$

which implies that in the definition (21), we must have

$$c_{l,\zeta,\zeta}^+(\varepsilon) = (-1)^{l-1} c_{l,\zeta,\zeta}^-(\varepsilon). \quad (E9)$$

APPENDIX F: GENERAL HAMILTONIAN CASE

It is important to show that our method is not restricted to a specific choice of Hamiltonian. The local density-density interaction and the single band of the Hubbard Hamiltonian bring many simplifications, but none of them are necessary for our imaginary-time integral solution or the chemical-potential tuning scheme.

Consider the general Hamiltonian

$$H = \sum_{\alpha} (\varepsilon_{\alpha} - \mu) + \sum_{\alpha_1 \alpha_2 \alpha_3 \alpha_4} U_{\alpha_1 \alpha_2 \alpha_3 \alpha_4} c_{\alpha_1}^{\dagger} c_{\alpha_2} c_{\alpha_3}^{\dagger} c_{\alpha_4}. \quad (F1)$$

The α are the eigenstates of the noninteracting Hamiltonian, e.g., a combined momentum, band, and spin index. The self-energy can be now expressed as a

series,

$$\begin{aligned} \Sigma_{\alpha, \alpha'}^{(\text{HF})}(\tau) &= \sum_N \sum_{\Upsilon_N} \prod_{j=1}^{2N-1} \sum_{l_j=1}^{\infty} \sum_{\alpha_{j,1} \dots \alpha_{j,l_j}} \prod_{n=1}^{l_j-1} \sum_{\mathbf{V}_{j,n}} \\ &\times [\mathbf{V}_{j,n}]_{\alpha_{j,n} \alpha_{j,n+1}} \prod_{i=1}^N U_{\alpha_{j_1}(i) \alpha_{j_2}(i) \alpha_{j_3}(i) \alpha_{j_4}(i)} \\ &\times \prod_{m=1}^{N-1+\sum_j(l_j-1)} \int_0^{\beta} d\tau_m G_0(\bar{\varepsilon}_{\alpha_{j,n}}, \tilde{\tau}_{j,n} - \tilde{\tau}'_{j,n}). \end{aligned} \quad (F2)$$

Similarly as before, Υ_N enumerates topologies without any instantaneous insertions (Hartree or chemical potential) at perturbation order N (the number of interaction vertices). The fermionic lines in the Υ_N topology are enumerated with j . On each fermionic line, we make any number $l_j - 1$ of instantaneous insertions with amplitudes $\mathbf{V}_{j,n}$ (interaction amplitudes in Hartree insertions are included in \mathbf{V} ; n enumerates the insertions at the fermionic line j). In general, Hartree insertions may contain off-diagonal terms in the α basis and are therefore a matrix in the α space. However, it is necessary that chemical-potential shifts are diagonal in this basis, as we want to have the bare propagator diagonal in this basis as well. Otherwise, the form of G_0 from Eq. (18) would no longer hold. Nevertheless, one may still have a separate chemical-potential shift for each state, $\delta\mu_{\alpha}$. After making insertions, the number of fermionic lines increases to $\sum_j l_j$. The fermionic lines are now enumerated with j, n , and the corresponding states are $\alpha_{j,n}$. The index i enumerates the interaction vertices outside of any Hartree insertions. We denote $\alpha_{j,1\dots 4}(i)$ as the single-particle states at four terminals of each interaction vertex. The interaction vertices at incoming ($i = 1$) and outgoing ($i = N$) terminals of the self-energy diagram are $\alpha_{j_1}(i = N) = \alpha$, $\alpha_{j_2}(i = 1) = \alpha'$. With m , we enumerate all times to be integrated over. With each interaction vertex $i > 1$, we associate one time, and there is a time associated to each instantaneous insertion of which there are $\sum_j (l_j - 1)$. We assume that the incoming time corresponding to the vertex $i = 1$ is 0. The times on the terminals of each bare propagator j, n are $\tilde{\tau}_{j,n}$ and $\tilde{\tau}'_{j,n}$ and they take on values from the set $\{\tau_m\}_{m=0 \dots N-1+\sum_j(l_j-1)}$, with the external incoming time fixed, $\tau_0 \equiv 0$. $\tilde{\tau}_{j,n}$, $\tilde{\tau}'_{j,n}$, and $\alpha_{j,1\dots 4}(i)$ are implicit functions of topology Υ_N . Finally, $\bar{\varepsilon}_{\alpha_{j,n}} \equiv \varepsilon_{\alpha_{j,n}} - \mu + \delta\mu_{\alpha_{j,n}}$. We can now focus only on the time-integral part and proceed completely analogously to Eqs. (27)–(31).

It is worth noting that with general interactions, pulling the coupling constant in front of the diagram contribution is impossible, as the frequency dependence of the contribution of each diagram will depend on the precise form of $U_{\alpha_1 \alpha_2 \alpha_3 \alpha_4}$. In the most general case, one must set specific values for $U_{\alpha_1 \alpha_2 \alpha_3 \alpha_4}$ and $\delta\mu_{\alpha}$ before performing the Monte Carlo summation. One can then choose the variables that will be sampled stochastically and the ones that will be fully summed over. In the end, the contributions can be easily grouped by total number of independent times (K), including those in Hartree insertions. The integration of times in Hartree insertions can always be performed beforehand. Therefore, in the fully

general case, the number of integrations to be performed at the time of Monte Carlo sampling is $N - 1 + \sum_j (l_j - 1)$. In the case of purely density-density interactions (as is the case in the Hubbard model) or spin-spin interactions in the absence of external magnetic fields, this simplifies further because instantaneous insertions lead to expressions of the type $\frac{1}{(i\omega - \varepsilon)^l}$ for which we can work out the temporal Fourier transform analytically [Eq. (21)] and the remaining number of integrations to perform is $N - 1$ [as we do in Eq. (31)]. In the general case, when Hartree insertions are not diagonal in the α basis, one has expressions of the type $\frac{1}{i\omega - \varepsilon_1} \frac{1}{i\omega - \varepsilon_2} \cdots \frac{1}{i\omega - \varepsilon_l}$. In

principle, one could prepare the analytical Fourier transforms for a general function of this form, but it might be increasingly involved at large l , so we assume one would do these integrations at the level of the Monte Carlo, when $\varepsilon_{1,\dots,l}$ are already specified.

We finally emphasize that even more general constructions are possible, even in bases other than the noninteracting eigenbasis. In such cases, the G_0 's are nondiagonal and may have a continuous real-frequency dependence, instead of being a single pole. We leave such considerations for future work.

-
- [1] The Hubbard model at half a century, *Nat. Phys.* **9**, 523 (2013).
- [2] J. P. F. LeBlanc, A. E. Antipov, F. Becca, I. W. Bulik, Garnet Kin-Lic Chan, Chia-Min Chung, Y. Deng, M. Ferrero, T. M. Henderson, C. A. Jiménez-Hoyos, E. Kozik, Xuan-Wen Liu, A. J. Millis, N. V. Prokof'ev, M. Qin, G. E. Scuseria, Hao Shi, B. V. Svistunov, L. F. Tocchio, I. S. Tupitsyn, S. R. White, S. Zhang, Bo-Xiao Zheng, Z. Zhu, and E. Gull (Simons Collaboration on the Many-Electron Problem), Solutions of the Two-Dimensional Hubbard Model: Benchmarks and Results from a Wide Range of Numerical Algorithms, *Phys. Rev. X* **5**, 041041 (2015).
- [3] G. Rohringer, H. Hafermann, A. Toschi, A. A. Katanin, A. E. Antipov, M. I. Katsnelson, A. I. Lichtenstein, A. N. Rubtsov, and K. Held, Diagrammatic routes to nonlocal correlations beyond dynamical mean field theory, *Rev. Mod. Phys.* **90**, 025003 (2018).
- [4] T. Schäfer, N. Wentzell, F. Šimkovic, Y.-Y. He, C. Hille, M. Klett, C. J. Eckhardt, B. Arzhang, V. Harkov, F.-M. Le Régent, A. Kirsch, Y. Wang, A. J. Kim, E. Kozik, E. A. Stepanov, A. Kauch, S. Andergassen, P. Hansmann, D. Rohe, Y. M. Vil'k, J. P. F. LeBlanc, S. Zhang, A.-M. S. Tremblay, M. Ferrero, O. Parcollet, and A. Georges, Tracking the Footprints of Spin Fluctuations: A MultiMethod, MultiMessenger Study of the Two-Dimensional Hubbard Model, *Phys. Rev. X* **11**, 011058 (2021).
- [5] A. W. Sandvik, Stochastic method for analytic continuation of quantum Monte Carlo data, *Phys. Rev. B* **57**, 10287 (1998).
- [6] O. F. Syljuåsen, Using the average spectrum method to extract dynamics from quantum Monte Carlo simulations, *Phys. Rev. B* **78**, 174429 (2008).
- [7] S. Fuchs, T. Pruschke, and M. Jarrell, Analytic continuation of quantum Monte Carlo data by stochastic analytical inference, *Phys. Rev. E* **81**, 056701 (2010).
- [8] K. Ghanem and E. Koch, Extending the average spectrum method: Grid point sampling and density averaging, *Phys. Rev. B* **102**, 035114 (2020).
- [9] H. Aoki, N. Tsuji, M. Eckstein, M. Kollar, T. Oka, and P. Werner, Nonequilibrium dynamical mean-field theory and its applications, *Rev. Mod. Phys.* **86**, 779 (2014).
- [10] J. K. Freericks, Quenching Bloch oscillations in a strongly correlated material: Nonequilibrium dynamical mean-field theory, *Phys. Rev. B* **77**, 075109 (2008).
- [11] M. Eckstein and M. Kollar, Nonthermal Steady States after an Interaction Quench in the Falicov-Kimball Model, *Phys. Rev. Lett.* **100**, 120404 (2008).
- [12] M. Schiró and M. Fabrizio, Real-time diagrammatic Monte Carlo for nonequilibrium quantum transport, *Phys. Rev. B* **79**, 153302 (2009).
- [13] P. Werner, T. Oka, and A. J. Millis, Diagrammatic Monte Carlo simulation of nonequilibrium systems, *Phys. Rev. B* **79**, 035320 (2009).
- [14] M. Eckstein, M. Kollar, and P. Werner, Thermalization after an Interaction Quench in the Hubbard Model, *Phys. Rev. Lett.* **103**, 056403 (2009).
- [15] M. Schiró and M. Fabrizio, Time-Dependent Mean Field Theory for Quench Dynamics in Correlated Electron Systems, *Phys. Rev. Lett.* **105**, 076401 (2010).
- [16] P. Werner, T. Oka, M. Eckstein, and A. J. Millis, Weak-coupling quantum Monte Carlo calculations on the Keldysh contour: Theory and application to the current-voltage characteristics of the Anderson model, *Phys. Rev. B* **81**, 035108 (2010).
- [17] M. Eckstein and P. Werner, Nonequilibrium dynamical mean-field calculations based on the noncrossing approximation and its generalizations, *Phys. Rev. B* **82**, 115115 (2010).
- [18] M. Schiró and M. Fabrizio, Quantum quenches in the Hubbard model: Time-dependent mean-field theory and the role of quantum fluctuations, *Phys. Rev. B* **83**, 165105 (2011).
- [19] P. Werner and M. Eckstein, Phonon-enhanced relaxation and excitation in the Holstein-Hubbard model, *Phys. Rev. B* **88**, 165108 (2013).
- [20] M. Eckstein and P. Werner, Nonequilibrium dynamical mean-field simulation of inhomogeneous systems, *Phys. Rev. B* **88**, 075135 (2013).
- [21] G. Cohen, D. R. Reichman, A. J. Millis, and E. Gull, Green's functions from real-time bold-line Monte Carlo, *Phys. Rev. B* **89**, 115139 (2014).
- [22] G. Cohen, E. Gull, D. R. Reichman, and A. J. Millis, Green's Functions from Real-Time Bold-Line Monte Carlo Calculations: Spectral Properties of the Nonequilibrium Anderson Impurity Model, *Phys. Rev. Lett.* **112**, 146802 (2014).
- [23] G. Cohen, E. Gull, D. R. Reichman, and A. J. Millis, Taming the Dynamical Sign Problem in Real-Time Evolution of Quantum Many-Body Problems, *Phys. Rev. Lett.* **115**, 266802 (2015).
- [24] N. V. Prokof'ev and B. V. Svistunov, Polaron Problem by Diagrammatic Quantum Monte Carlo, *Phys. Rev. Lett.* **81**, 2514 (1998).
- [25] A. S. Mishchenko, N. V. Prokof'ev, A. Sakamoto, and B. V. Svistunov, Diagrammatic quantum Monte Carlo study of the Fröhlich polaron, *Phys. Rev. B* **62**, 6317 (2000).

- [26] N. Prokof'ev and B. Svistunov, Bold Diagrammatic Monte Carlo Technique: When the Sign Problem Is Welcome, *Phys. Rev. Lett.* **99**, 250201 (2007).
- [27] N. V. Prokof'ev and B. V. Svistunov, Bold diagrammatic Monte Carlo: A generic sign-problem tolerant technique for polaron models and possibly interacting many-body problems, *Phys. Rev. B* **77**, 125101 (2008).
- [28] E. Gull, D. R. Reichman, and A. J. Millis, Bold-line diagrammatic Monte Carlo method: General formulation and application to expansion around the noncrossing approximation, *Phys. Rev. B* **82**, 075109 (2010).
- [29] E. Kozik, K. Van Houcke, E. Gull, L. Pollet, N. Prokof'ev, B. Svistunov, and M. Troyer, Diagrammatic Monte Carlo for correlated fermions, *Europhys. Lett.* **90**, 10004 (2010).
- [30] K. V. Houcke, E. Kozik, N. Prokof'ev, and B. Svistunov, Diagrammatic Monte Carlo, *Phys. Proc.* **6**, 95 (2010).
- [31] L. Pollet, Recent developments in quantum Monte Carlo simulations with applications for cold gases, *Rep. Prog. Phys.* **75**, 094501 (2012).
- [32] K. Van Houcke, F. Werner, E. Kozik, N. Prokof'ev, B. Svistunov, M. J. H. Ku, A. T. Sommer, L. W. Cheuk, A. Schirotzek, and M. W. Zwierlein, Feynman diagrams versus Fermi-gas Feynman emulator, *Nat. Phys.* **8**, 366 (2012).
- [33] S. A. Kulagin, N. Prokof'ev, O. A. Starykh, B. Svistunov, and C. N. Varney, Bold Diagrammatic Monte Carlo Method Applied to Fermionized Frustrated Spins, *Phys. Rev. Lett.* **110**, 070601 (2013).
- [34] S. A. Kulagin, N. Prokof'ev, O. A. Starykh, B. Svistunov, and C. N. Varney, Bold diagrammatic Monte Carlo technique for frustrated spin systems, *Phys. Rev. B* **87**, 024407 (2013).
- [35] R. Rossi, T. Ohgoe, E. Kozik, N. Prokof'ev, B. Svistunov, K. Van Houcke, and F. Werner, Contact and Momentum Distribution of the Unitary Fermi Gas, *Phys. Rev. Lett.* **121**, 130406 (2018).
- [36] R. Rossi, Determinant Diagrammatic Monte Carlo Algorithm in the Thermodynamic Limit, *Phys. Rev. Lett.* **119**, 045701 (2017).
- [37] K. Van Houcke, F. Werner, T. Ohgoe, N. V. Prokof'ev, and B. V. Svistunov, Diagrammatic Monte Carlo algorithm for the resonant Fermi gas, *Phys. Rev. B* **99**, 035140 (2019).
- [38] K. Chen and K. Haule, A combined variational and diagrammatic quantum Monte Carlo approach to the many-electron problem, *Nat. Commun.* **10**, 3725 (2019).
- [39] A. N. Rubtsov and A. I. Lichtenstein, Continuous-time quantum Monte Carlo method for fermions: Beyond auxiliary field framework, *J. Expt. Theor. Phys. Lett.* **80**, 61 (2004).
- [40] A. N. Rubtsov, V. V. Savkin, and A. I. Lichtenstein, Continuous-time quantum Monte Carlo method for fermions, *Phys. Rev. B* **72**, 035122 (2005).
- [41] E. Gull, P. Werner, O. Parcollet, and M. Troyer, Continuous-time auxiliary-field Monte Carlo for quantum impurity models, *Europhys. Lett.* **82**, 57003 (2008).
- [42] E. Gull, A. J. Millis, A. I. Lichtenstein, A. N. Rubtsov, M. Troyer, and P. Werner, Continuous-time Monte Carlo methods for quantum impurity models, *Rev. Mod. Phys.* **83**, 349 (2011).
- [43] R. E. V. Profumo, C. Groth, L. Messio, O. Parcollet, and X. Waintal, Quantum Monte Carlo for correlated out-of-equilibrium nanoelectronic devices, *Phys. Rev. B* **91**, 245154 (2015).
- [44] A. Moutenet, P. Seth, M. Ferrero, and O. Parcollet, Cancellation of vacuum diagrams and the long-time limit in out-of-equilibrium diagrammatic quantum Monte Carlo, *Phys. Rev. B* **100**, 085125 (2019).
- [45] C. Bertrand, O. Parcollet, A. Maillard, and X. Waintal, Quantum Monte Carlo algorithm for out-of-equilibrium Green's functions at long times, *Phys. Rev. B* **100**, 125129 (2019).
- [46] C. Bertrand, S. Florens, O. Parcollet, and X. Waintal, Reconstructing Nonequilibrium Regimes of Quantum Many-Body Systems from the Analytical Structure of Perturbative Expansions, *Phys. Rev. X* **9**, 041008 (2019).
- [47] A. Taheridehkordi, S. H. Curnoe, and J. P. F. LeBlanc, Algorithmic Matsubara integration for Hubbard-like models, *Phys. Rev. B* **99**, 035120 (2019).
- [48] J. Vučićević and M. Ferrero, Real-frequency diagrammatic Monte Carlo at finite temperature, *Phys. Rev. B* **101**, 075113 (2020).
- [49] A. Taheridehkordi, S. H. Curnoe, and J. P. F. LeBlanc, Optimal grouping of arbitrary diagrammatic expansions via analytic pole structure, *Phys. Rev. B* **101**, 125109 (2020).
- [50] A. Taheridehkordi, S. H. Curnoe, and J. P. F. LeBlanc, Algorithmic approach to diagrammatic expansions for real-frequency evaluation of susceptibility functions, *Phys. Rev. B* **102**, 045115 (2020).
- [51] M. Maček, P. T. Dumitrescu, C. Bertrand, B. Triggs, O. Parcollet, and X. Waintal, Quantum Quasi-Monte Carlo Technique for Many-Body Perturbative Expansions, *Phys. Rev. Lett.* **125**, 047702 (2020).
- [52] W. Wu, M. Ferrero, A. Georges, and E. Kozik, Controlling Feynman diagrammatic expansions: Physical nature of the pseudogap in the two-dimensional Hubbard model, *Phys. Rev. B* **96**, 041105(R) (2017).
- [53] R. Rossi, F. Šimkovic IV, and M. Ferrero, Renormalized perturbation theory at large expansion orders, *Europhys. Lett.* **132**, 11001 (2020).
- [54] F. Šimkovic IV, R. Rossi, and M. Ferrero, Efficient one-loop-renormalized vertex expansions with connected determinant diagrammatic Monte Carlo, *Phys. Rev. B* **102**, 195122 (2020).
- [55] F. Šimkovic IV, J. P. F. LeBlanc, A. J. Kim, Y. Deng, N. V. Prokof'ev, B. V. Svistunov, and E. Kozik, Extended Crossover from a Fermi Liquid to a Quasiantiferromagnet in the Half-Filled 2D Hubbard Model, *Phys. Rev. Lett.* **124**, 017003 (2020).
- [56] A. J. Kim, F. Šimkovic IV, and E. Kozik, Spin and Charge Correlations across the Metal-to-Insulator Crossover in the Half-Filled 2D Hubbard Model, *Phys. Rev. Lett.* **124**, 117602 (2020).
- [57] C. Lenihan, A. J. Kim, F. Šimkovic IV, and E. Kozik, Entropy in the Non-Fermi-Liquid Regime of the Doped 2D Hubbard Model, *Phys. Rev. Lett.* **126**, 105701 (2021).
- [58] T. Ayral, J. Vučićević, and O. Parcollet, Fierz Convergence Criterion: A Controlled Approach to Strongly Interacting Systems with Small Embedded Clusters, *Phys. Rev. Lett.* **119**, 166401 (2017).
- [59] A. Moutenet, W. Wu, and M. Ferrero, Determinant Monte Carlo algorithms for dynamical quantities in fermionic systems, *Phys. Rev. B* **97**, 085117 (2018).
- [60] F. Šimkovic IV and E. Kozik, Determinant Monte Carlo for irreducible Feynman diagrams in the strongly correlated regime, *Phys. Rev. B* **100**, 121102(R) (2019).

- [61] E. Eidelstein, E. Gull, and G. Cohen, Multiorbital Quantum Impurity Solver for General Interactions and Hybridizations, *Phys. Rev. Lett.* **124**, 206405 (2020).
- [62] A. A. Kunitsa and So Hirata, Grid-based diffusion Monte Carlo for fermions without the fixed-node approximation, *Phys. Rev. E* **101**, 013311 (2020).
- [63] M. Hutcheon, Stochastic nodal surfaces in quantum Monte Carlo calculations, *Phys. Rev. E* **102**, 042105 (2020).
- [64] J. Vučićević, J. Kokalj, R. Žitko, N. Wentzell, D. Tanasković, and J. Mravlje, Conductivity in the Square Lattice Hubbard Model at High Temperatures: Importance of Vertex Corrections, *Phys. Rev. Lett.* **123**, 036601 (2019).
- [65] E. W. Huang, R. Sheppard, B. Moritz, and T. P. Devereaux, Strange metallicity in the doped Hubbard model, *Science* **366**, 987 (2019).
- [66] P. T. Brown, D. Mitra, E. Guardado-Sanchez, R. Nourafkan, A. Reymbaut, Charles-David Hébert, S. Bergeron, A.-M. S. Tremblay, J. Kokalj, D. A. Huse, P. Schauß, and W. S. Bakr, Bad metallic transport in a cold atom Fermi-Hubbard system, *Science* **363**, 379 (2018).

Real-frequency diagrammatic Monte Carlo at finite temperature

J. Vučković¹ and M. Ferrero^{2,3}

¹*Scientific Computing Laboratory, Center for the Study of Complex Systems, Institute of Physics Belgrade, University of Belgrade, Pregrevica 118, 11080 Belgrade, Serbia*

²*CPHT, CNRS, Ecole Polytechnique, Institut Polytechnique de Paris, Route de Saclay, 91128 Palaiseau, France*

³*Collège de France, 11 place Marcelin Berthelot, 75005 Paris, France*



(Received 3 September 2019; revised manuscript received 15 January 2020; accepted 21 January 2020; published 12 February 2020)

Diagrammatic expansions are a central tool for treating correlated electron systems. At thermal equilibrium, they are most naturally defined within the Matsubara formalism. However, extracting any dynamic response function from a Matsubara calculation ultimately requires the ill-defined analytical continuation from the imaginary- to the real-frequency domain. It was recently proposed [A. Taheridehkordi *et al.*, *Phys. Rev. B* **99**, 035120 (2019)] that the internal Matsubara summations of any interaction-expansion diagram can be performed analytically by using symbolic algebra algorithms. The result of the summations is then an analytical function of the complex frequency rather than Matsubara frequency. Here we apply this principle and develop a diagrammatic Monte Carlo technique which yields results directly on the real-frequency axis. We present results for the self-energy $\Sigma(\omega)$ of the doped 32×32 cyclic square-lattice Hubbard model in a nontrivial parameter regime, where signatures of the pseudogap appear close to the antinode. We discuss the behavior of the perturbation series on the real-frequency axis and in particular show that one must be very careful when using the maximum entropy method on truncated perturbation series. Our approach holds great promise for future application in cases when analytical continuation is difficult and moderate-order perturbation theory may be sufficient to converge the result.

DOI: [10.1103/PhysRevB.101.075113](https://doi.org/10.1103/PhysRevB.101.075113)

I. INTRODUCTION

Interacting lattice fermions are one of the central subjects in condensed matter theory. Especially in two dimensions, a full many-body solution for even the simplest models (e.g., the Hubbard model) is a formidable task. In recent decades, great progress has been achieved using Monte Carlo algorithms for the summation of various diagrammatic expansions. The main advantage of this approach is that the approximations can be controlled; i.e., convergence of the results with respect to the control parameters can be systematically verified. The control parameters of the calculations are most commonly the lattice size and the maximal perturbation order. Some algorithms [1–16] are very efficient for small systems but have not yet reached very large lattice sizes, while others [17–24] can address the thermodynamic limit directly but are limited in the number of perturbation orders that can be computed.

In thermal equilibrium, expansions are naturally formulated within the Matsubara formalism, with all the propagators defined in imaginary time/frequency. Therefore, to obtain dynamic response functions, one needs to perform the analytical continuation from the imaginary- to the real-frequency domain. This procedure is notoriously ill defined and becomes especially difficult when the Matsubara axis data contain statistical noise, as is the case with all Monte Carlo results. The problem is further exacerbated with increasing temperature. As the discrete imaginary Matsubara frequencies spread out and move away from the real axis, the statistical noise chips away more and more information from the Matsubara data. The most common way of analytically continuing a noisy

result is the maximum entropy method (MEM) [25,26], but it requires “the default model,” an *a priori* qualitative knowledge of the real-frequency spectrum that may not always be available; it is difficult to control and estimate the error bars of any such procedure.

Analytical continuation is a common hurdle in finite-temperature calculations, and it came up recently in the study of transport in the optical lattice realizations of the Hubbard model [16,27]. It turns out that the direct-current resistivity is particularly difficult to extract from the imaginary-axis current-current correlation function. But even the self-energy is often interpreted only on the imaginary axis [24], as analytical continuation is considered ultimately unreliable. This particularly hinders the progress in the study of the pseudogap phase and superconductivity in the cuprates, where one would like to compare the momentum-resolved spectral function to experiments [28,29]. The ability to reliably calculate the spectral function becomes even more important in view of the recent photoemission measurements (ARPES) in the cold-atom realizations of the Hubbard model [30].

There are alternative routes that avoid analytical continuation altogether (Keldysh formalism [7–14,31], exact diagonalization techniques [16,32–34]), but those have so far been limited to impurity models or small lattice sizes. It is therefore of primary importance to try to develop methods that avoid the analytical continuation, but are not limited by lattice size.

As was recently proposed [35], an opportunity lies in symbolic algebra algorithms. One can implement a recursive transformation to perform analytically all the internal Matsubara frequency summations for any interaction-expansion

diagram, for any quantity. The result of the Matsubara frequency summations is an analytical expression for the contribution of a given diagram to the given dynamic quantity, in the whole of the complex-frequency plane, rather than just in the discrete set of points along the imaginary axis. The general idea is, however, not entirely new; at perturbation order 2, the Matsubara summations for the self-energy diagrams can be carried out by hand, which leads to the well-known real-axis iterative perturbation theory (RAIPT) [36–38]. Similarly, the bubble diagrams can be easily rewritten in terms of real frequencies, which has applications in the *GW* method [39–41] and the calculation of optical conductivity within the Kubo formalism [42–44]. In the context of diagrammatic Monte Carlo, however, obtaining the analytical expression for each diagram of interest is only a part of the problem. In fact, there are several immediate obstacles in applying the algorithmic Matsubara summations in a calculation of quantities at perturbation order ≥ 3 .

Here we address these problems and successfully develop and test a diagrammatic Monte Carlo technique that yields results directly on the real-frequency axis, yet can treat very large systems. We present solutions for the momentum-resolved self-energy for a doped 32×32 Hubbard lattice, in a nontrivial parameter regime where results are almost converged at order 5. Our results show that in this regime precursor signatures of the pseudogap are visible in the real-frequency antinodal self-energy. We also show that the truncation of the perturbation series leads to noncausal features that challenge the use of MEM to obtain real-frequency data from Matsubara axis results.

II. MODEL

We solve the Hubbard model on the square lattice

$$H = -t \sum_{\sigma, (i,j)} c_{\sigma i}^\dagger c_{\sigma j} + U \sum_i n_{\uparrow i} n_{\downarrow i} - \mu \sum_{\sigma, i} n_{\sigma i}, \quad (1)$$

where $c_{\sigma i}^\dagger/c_{\sigma i}$ create/annihilate an electron of spin σ at the lattice site i . The hopping amplitude between the nearest neighbors is denoted t , and we set $D = 4t$ as the unit of energy. The density operator is $n_{\sigma i} = c_{\sigma i}^\dagger c_{\sigma i}$, the chemical potential μ , and the on-site Hubbard interaction U . We restrict ourselves to paramagnetic solutions with full lattice symmetry.

III. METHOD

A. Symbolic algorithm

Following similar steps to those in Ref. [35], we first define the Hartree-shifted bare Green's function of the model $G_{0,\mathbf{k}}^{\text{HF}}(i\omega) = [i\omega - \varepsilon(\mathbf{k})]^{-1}$, where we absorbed the chemical potential and the Hartree shift in the dispersion $\varepsilon(\mathbf{k})$, i.e.,

$$\varepsilon(\mathbf{k}) = -\mu + U n_\sigma - 2t(\cos k_x + \cos k_y), \quad (2)$$

where $\mathbf{k} = (k_x, k_y)$ is the momentum. For the sake of clarity we omit the integer index n in the fermionic Matsubara frequency, $i\omega \equiv i\omega_n = i(2n + 1)\pi T$, where T is temperature. We reserve the subscript in $i\omega$ for denoting different Matsubara variables. We denote n_σ the density per spin evaluated in the interacting problem.

The self-energy Σ can be written as a series in the interaction amplitude U ,

$$\Sigma_{\mathbf{k}}(i\omega) = \sum_{N=1}^{\infty} (-U)^N \sum_{\alpha=1}^{\mathcal{N}_N} \mathcal{D}_{\mathbf{k}}^{N,\alpha}(i\omega), \quad (3)$$

where N is the perturbation order, \mathcal{N}_N is the number of distinct diagrams in the given expansion, α enumerates the diagrams, and $\mathcal{D}_{\mathbf{k}}^{N,\alpha}$ is the contribution of α th diagram in the N th order. If the diagrams are written in terms of the Hartree-shifted bare propagator there is no need for tadpole insertions in the topology of the diagrams (see Appendix A 8).

The contribution of a general diagram to the bare series for self-energy written in terms of $G_{0,\mathbf{k}}^{\text{HF}}(i\omega_n)$ is given by

$$\mathcal{D}_{\mathbf{k}}^{N,\alpha}(i\omega) = (-1)^{N_b} \sum_{\substack{\mathbf{k}_1 \dots \mathbf{k}_M \\ i\Omega_1 \dots i\Omega_M}} \prod_{\gamma} \frac{1}{\sum_{(s,j) \in \mathcal{K}_\gamma} s i\Omega_j - \varepsilon\left(\sum_{(s,j) \in \mathcal{K}_\gamma} s \mathbf{k}_j\right)}. \quad (4)$$

$N_b \equiv N_b^{N,\alpha}$ is the number of fermionic loops (bubbles) in the given diagram: each bubble carries one independent fermionic frequency and momentum. Each interaction carries a bosonic frequency $iv \equiv iv_n = 2n\pi T$ and momentum, but some are not independent due to conservation laws. We denote M the total number of independent degrees of freedom, each consisting of a frequency and momentum $(i\Omega_j, \mathbf{k}_j)$, where $i\Omega$ can be either fermionic or bosonic. There are $2N - 1$ Green's functions in each diagram, indexed by γ . Each Green's function depends on a certain subset of the internal degrees of freedom and possibly the external variables, indexed $j \in [0, M]$ (we take $\mathbf{k}_0 \equiv \mathbf{k}$, $i\Omega_0 \equiv i\omega$), and each entering with a sign $s = \pm 1$ in the corresponding sums. The Green's function γ is fully defined by a set of sign/index pairs $\mathcal{K}_\gamma \equiv \mathcal{K}_\gamma^{N,\alpha}$. The Green's functions may not be unique; i.e., it is possible that $\mathcal{K}_\gamma = \mathcal{K}_{\gamma'}$. For the discussion of the Feynman rules leading to the general expression Eq. (4), we refer the reader to the classic textbook Ref. [45]. For a worked-out example of Eq. (4) in the 4th order of perturbation, see Appendix A 3.

As a function of any given internal Matsubara frequency $i\Omega_c$, and for a fixed choice of the remaining internal and external degrees of freedom, the contribution to self-energy from any given diagram (N, α) has the form of a product of poles,

$$\mathcal{D}_{\mathbf{k}}(i\omega) = (-1)^{N_b} \sum_{\substack{\mathbf{k}_1 \dots \mathbf{k}_M \\ \{i\Omega_j\}_{j \neq c}}} P \sum_{i\Omega_c} \prod_{\gamma} \frac{1}{(i\Omega_c - z_\gamma)^{m_\gamma}}, \quad (5)$$

where P and z_γ implicitly depend on the rest of the internal and external variables, and here we assume that γ goes only over the unique Green's functions that depend on the given $i\Omega_c$, and $m_\gamma \in \mathbb{N}$ is the number of appearances of the γ th Green's function in the diagram. Using the partial fraction expansion, and an analytic expression for the derivative of a product of an arbitrary number of poles (see Appendix A 1),

we can perform the transformation

$$\begin{aligned} \prod_{\gamma} \frac{1}{(z - z_{\gamma})^{m_{\gamma}}} &= \sum_{\gamma} \sum_{r=1}^{m_{\gamma}} \frac{1}{(z - z_{\gamma})^r} \\ &\times (-1)^{m_{\gamma}-r} \sum_{\mathcal{C}\{p_{\gamma' \neq \gamma} \in \mathbb{N}_0\}; \sum_{\gamma' \neq \gamma} p_{\gamma'} = m_{\gamma} - r} \\ &\prod_{\gamma' \neq \gamma} \frac{(m_{\gamma'} + p_{\gamma'} - 1)!}{p_{\gamma'}! (m_{\gamma'} - 1)!} \frac{1}{(z_{\gamma'} - z_{\gamma})^{m_{\gamma'} + p_{\gamma'}}}. \end{aligned} \quad (6)$$

Here $\mathcal{C} \dots$ denotes all combinations of a non-negative-integer p per pole $\gamma' \neq \gamma$, such that the total sum of p 's is equal to $m_{\gamma} - r$. Therefore, after selecting one internal Matsubara variable, the full expression can be rewritten as a sum of poles in that Matsubara variable. Then, one may proceed to perform the Matsubara summation of each term using

$$\sum_{i\Omega} \frac{1}{(i\Omega - z)^r} = -\frac{\eta}{(r-1)!} \partial^{r-1} n_{\eta}(z) \quad (7)$$

with $\eta = \pm 1$ for bosonic/fermionic Matsubara frequency. n_{η} is the Bose/Fermi distribution function. Here we can immediately get rid of the complex part of z because

$$\partial_{\omega}^r n_{\eta}(\omega + i\Omega_{\eta'}) = \eta' \partial_{\omega}^r n_{\eta' \cdot \eta}(\omega), \quad (8)$$

where $\eta' = -1$ or $+1$ denotes whether $i\Omega_{\eta'}$ is fermionic or bosonic Matsubara frequency, respectively. Note that the derivatives $\partial^r n$ can be expressed analytically for the purpose of precise numerical evaluation (details in Appendix A 4).

Now the remaining Matsubara variables appear only in the denominators of fractions which can again be interpreted as poles with respect to these variables, and the procedure can be applied recursively until we have gotten rid of all the Matsubara variables. For a detailed example of the symbolic algorithm and an illustration of Eq. (5), see Appendix A 3.

The final result has the form of a sum of poles on the real axis

$$\mathcal{D}_{\mathbf{k}}(z) = (-1)^{N_{\mathbf{k}}} \sum_{\mathbf{k}_1 \dots \mathbf{k}_M} \sum_{\kappa} \frac{A_{\kappa}}{(z - \omega_{\kappa})^{m_{\kappa}}} \quad (9)$$

with $\omega_{\kappa} = \sum_{\gamma} s_{\gamma}^{\kappa} \varepsilon(\sum_{(s,j) \in \mathcal{K}_{\gamma}^{\kappa}} s \mathbf{k}_j)$, which is a series of terms equal up to the sign $s_{\gamma}^{\kappa} = \pm 1$ to the dispersion ε , evaluated at various possible linear combinations of the internal/external momenta, as they appear in the Green's functions (indexed γ). The series can be of any length $\leq 2N - 1$ and include an arbitrary subset of γ 's. The amplitude for each (unique) pole $(\omega_{\kappa}, m_{\kappa})$ is given by a large sum of terms of the general form

$$A_{\kappa} = \sum_{\zeta} \frac{a_{\zeta}}{b_{\zeta}} \prod_{\zeta} \frac{1}{\omega_{\zeta \zeta}^{m_{\zeta \zeta}}} \prod_{\varrho} \partial^{r_{\varrho \zeta}} n_{\eta_{\varrho}}(\omega_{\varrho \zeta}). \quad (10)$$

a, b are integers, m positive integers. $\omega_{\zeta \zeta}$ and $\omega_{\varrho \zeta}$ have the same general form as ω_{κ} , but do not necessarily coincide with any of the ω_{κ} 's, and may differ from one another. The products over ζ and ϱ may be of various lengths including 0. ω 's (and thus A_{κ} 's) are implicitly dependent on the internal and external momenta.

The symbolic forms for A_{κ} and ω_{κ} need be obtained only once for any given diagram, independently of the choice of the lattice geometry, parameters of the Hamiltonian, or

temperature. See Appendix A 2 for numbers of poles ω_{κ} and terms in A_{κ} at various perturbation orders.

B. Application in diagrammatic Monte Carlo

Evaluating the prefactor A_{κ} numerically is not straightforward for several reasons.

First, the terms in A_{κ} containing at least one ratio $1/\omega^m$ or a bosonic $\partial^r n_{\eta}(\omega)$ will diverge if the corresponding ω goes to zero. For any finite lattice this will occur regularly during the Monte Carlo sampling, but even in the thermodynamic limit, ω can approach arbitrarily close to zero. Our solution for this problem is to add small shifts to a certain choice of ε 's appearing in ω . This is done at the symbolic level, in a way that $|\omega|$ can never be smaller than a given value that we set to be $\sim 10^{-10}$ to 10^{-6} depending on the perturbation order. Note that even this will cause the terms in A_{κ} to be very large by absolute value (order as large as 10^{30}), yet they will cancel to produce contributions to A_{κ} of order $\lesssim 1$. This greatly exceeds the capability of standard precision arithmetic which handles only around ~ 16 digits. We have found the solution in using multiple precision floating point types which can store more digits and allow for subtraction of large numbers, as required in our algorithm. The additional approximation made by numerical shifts can be controlled, and we have checked on several examples that the result is insensitive to the precise choice of the numerical parameters (size of the shifts and the choice of the floating point precision). Surely, the shifts can be always made smaller if the precision is made greater, but this has an adverse effect on performance. For more details see Appendix A 6.

Next, one needs to perform the remaining sums over momenta, numerically. For smaller lattices it is possible to do the full summation, but otherwise we employ a flat-weight Monte Carlo (see Appendix B; for an alternative algorithm useful in the case of local self-energy, see Appendix A 7). In each step, we select randomly the internal momenta $\mathbf{k}_1 \dots \mathbf{k}_M$, evaluate all A_{κ} , and permanently store the triplets $(\omega_{\kappa}, m_{\kappa}, A_{\kappa})$. We perform ‘‘on the fly’’ integration for any reappearing values of ω_{κ} . Even for modest lattice sizes, the number of possible values of ω_{κ} will be very large. To avoid immense outputs, we project $\varepsilon(\mathbf{k})$ on a uniform energy grid, so that linear combinations of ε 's and thus ω_{κ} 's always fall on the same uniform grid. The small shifts discussed in the previous paragraph also fall on a uniform grid of a much smaller step, so there will generally be several values of ω_{κ} concentrated around each point in the ‘‘big’’ ε grid. This way, the number of different values of ω_{κ} one can obtain is determined by the resolution of the energy grid, i.e., the step $\Delta \varepsilon$. Again, this is a well-controlled approximation, and one can easily push the resolution so that the approximation is negligible compared to statistical noise. See Appendix A 5 for details.

Note also that it is essential for performance to store the different values of $\omega_{\kappa}, \omega_{\zeta \zeta}, \omega_{\varrho \zeta}$ and the corresponding $\partial^r n_{\eta}(\omega)$, and reuse them whenever possible during the Monte Carlo sampling.

The Monte Carlo run is then performed for a given choice of the external momentum, temperature, lattice geometry, and the Hartree-shifted chemical potential $\mu - U n_{\sigma}$ (the doping can be determined *a posteriori*). Once enough measurements

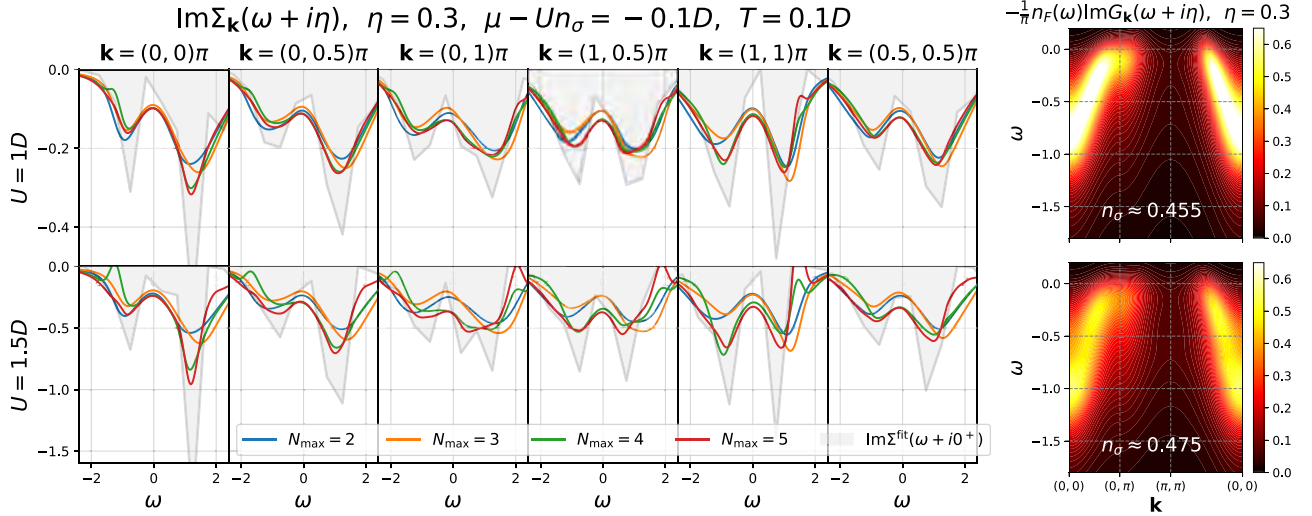


FIG. 1. Calculation for the 32×32 Hubbard lattice at two values of U , $T = 0.1D$, and $\mu - Un_\sigma = 0.1D$. These parameters correspond to densities per spin indicated in the rightmost panels, i.e., dopings $\delta(U = 1) \approx 9\%$ and $\delta(U = 1.5) \approx 5\%$. Left: Imaginary part of the self-energy $\text{Im} \Sigma(\omega + i\eta)$, at a distance $\eta = 0.3D$ from the real axis, for various \mathbf{k} vectors. Different lines correspond to different maximal perturbation orders in the calculation, N_{\max} . Gray-shaded curve is the piecewise-trapezoid fit at $\eta = i0^+$, obtained with resolution $\Delta\omega = 1.6\eta$. Right: The corresponding filled part of the spectral function, broadened with η , and interpolated in \mathbf{k} space. The result is obtained with 5.12×10^7 Monte Carlo steps per diagram.

of $(\omega_\kappa, m_\kappa, A_\kappa)$ have been collected, the result for $\Sigma_{\mathbf{k}}(z)$ for any z and any U can be obtained using Eq. (9) and then Eq. (3) (with $i\omega \rightarrow z$). However, the result is a discrete set of poles on the real axis, and requires regularization, similarly to exact diagonalization techniques. If it were just the simple poles on a dense uniform energy grid with a step $\Delta\varepsilon$, one could easily interpret $\text{Im} \Sigma_{\mathbf{k}}(\omega + i0^+)$ as continuous, but known with a finite resolution, simply through $\text{Im} \Sigma_{\mathbf{k}}(\omega_\kappa + i0^+) = -\pi A_\kappa / \Delta\varepsilon$. An analogous scheme could be performed even for higher-order poles on a uniform grid, order by order [46].

The problem is that the poles are not only on a uniform grid, but rather cluster around the grid points, due to the small numerical shifts discussed previously. It is also impossible to separate poles according to their order because multiple poles can combine to effectively form a single higher-order pole. This makes it very difficult to construct a binning scheme that would reinterpret the result directly on the real axis. A better strategy is to use broadening, i.e., evaluate the self-energy slightly away from the real axis, $\Sigma(\omega + i\eta)$. In our calculation, statistical noise dominates close to the real axis; thus we take η just large enough so that $\Sigma(\omega + i\eta)$ is a smooth function of ω .

To recover the desired $\omega + i0^+$ result, one can perform a fit based on the obtained $\Sigma(\omega + i\eta)$ and the Hilbert transform

$$\Sigma(\omega + i\eta) = -\frac{1}{\pi} \int d\varepsilon \frac{\text{Im} \Sigma^{\text{fit}}(\varepsilon)}{(\omega + i\eta) - \varepsilon}. \quad (11)$$

This procedure becomes trivial with $\eta \rightarrow 0$; it treats all frequencies on equal footing and is much better defined than $\Sigma(i\omega_n) \rightarrow \Sigma(\omega + i0^+)$ whenever η is small. Let us emphasize that the only limitation in taking a small η is the numerical noise: when the statistical error bars are small, the procedure is very reliable, numerically stable, and does not require

additional input (such as the default model for MEM). This is illustrated in the Appendix B, where the algorithm is benchmarked against the numerical renormalization group (NRG) [47] for the solution of an Anderson impurity model [48].

IV. RESULTS

We have benchmarked our method carefully on several simple examples (see Appendix B). We now consider a 32×32 cyclic Hubbard lattice at temperature $T = 0.1D$ and $\mu - Un_\sigma = -0.1D$ (hole doping). In this case we benchmark our method against 8th-order Σ Det [22,23] in imaginary frequency and find excellent agreement (see Appendix B 5).

In Fig. 1 we show the results for $\text{Im} \Sigma(\omega + i\eta)$ close to the real axis (finite $\eta < \pi T$, lower than the first fermionic Matsubara frequency). Closer than this, stronger noisy features start to appear. Let us emphasize that the statistical noise is far more pronounced on the real axis; i.e., convergence on the imaginary axis does not necessarily imply convergence on the real axis. Different lines represent calculations with different maximal perturbation orders N_{\max} , at 6 characteristic \mathbf{k} points and 2 values of U . The shaded region is a piecewise trapezoid $\text{Im} \Sigma^{\text{fit}}(\omega + i0^+)$ obtained with resolution $\Delta\omega = 1.6\eta$.

At $U = 1D$ fifth-order diagrams contribute very little and the result is practically converged with respect to N_{\max} . At $U = 1.5D$, the result is not fully converged by order 5, but is apparently close to convergence. We observe several non-causal features $\text{Im} \Sigma_{\mathbf{k}}(\omega) > 0$. At large negative ω , this happens at $\mathbf{k} = (0, 0)$ at order 4, but is then fixed by order 5. At large positive ω , the problem appears at order 5, and is likely to be fixed by higher orders in perturbation. These non-causal features do not appear to be artifacts of the statistical noise but rather a result of the truncation of the perturbation series.

This calls for great caution in the use of MEM. Indeed, MEM performed with built-in causality is bound to miss any such features and may compensate for them in an uncontrolled way.

It is interesting that in most cases $\text{Im } \Sigma(\omega)$ features two broad peaks with a dip around $\omega = 0$. However, at $U = 1.5D$ around $\mathbf{k} = (0, \pi)$, a third peak appears close to $\omega = 0$. We interpret this peak as a precursor for the pseudogap behavior: as temperature further decreases at this doping (around 5%), the peak may approach $\omega = 0$ and induce a larger, insulating-like self-energy as observed in imaginary-time calculations, e.g., Ref. [24].

Finally, the panels on the right present the filled part of the corresponding \mathbf{k} -resolved spectral functions. These plots are relevant for recent spectral function measurements in optical lattice realizations of the Hubbard model [30]. One can observe that the spectral function preserves the general form of the noninteracting limit, but spans a bigger energy range and becomes more incoherent (wider lines of lesser intensity) as interaction is increased.

V. CONCLUSIONS AND PROSPECTS

We have resolved the main conceptual issues regarding the application of algorithmic Matsubara summations in the context of diagrammatic Monte Carlo. This includes the precision and efficiency concerns in the evaluation of the pole amplitudes, as well as the extraction of the real-axis results. There is a possibility for further optimization which will likely allow us to push the method to higher perturbation orders in the future.

We demonstrate that our method is readily useful in the study of the single-particle spectra in the intermediate-coupling regime of the Hubbard model, which has been the subject of recent publications [30,49,50]. Finally, our method holds great promise for future work in the cases where analytical continuation is particularly difficult. These include, for example, high temperature and calculations of the current-current correlation function $\Lambda(\omega)$ [16]. Our approach even allows for a straightforward restriction to a selected window of energies; if one is interested in dc resistivity, one may calculate $\Lambda(\omega)$ only at very low frequency and that way gain an important speedup.

ACKNOWLEDGMENTS

We are grateful to Rok Žitko for providing NRG data. The exact-diagonalization results were obtained using the PyED code, written by Hugo Strand [51]. The continuous-time interaction expansion algorithm [1,2] was developed using the TRIQS [52] library. Computations were performed on the PARADOX supercomputing facility (Scientific Computing Laboratory of the Institute of Physics Belgrade) and ALPHA cluster (Collège de France) as well as using HPC resources from GENCI (Grant No. A0050510609). We thank Mihailo Čubrović for his help with the preparation of the manuscript. J.V. acknowledges funding provided by the Institute of Physics Belgrade, through the grant by the Ministry of Education, Science, and Technological Development of the Republic of Serbia.

APPENDIX A: FORMALISM DETAILS

1. Derivation of Eq. (6)

The partial fraction expansion employs the residue theorem, and the textbook expression reads

$$\begin{aligned} & \prod_{\gamma} \frac{1}{(z - z_{\gamma})^{m_{\gamma}}} \\ &= \sum_{\gamma} \sum_{r=1}^{m_{\gamma}} \frac{1}{(z - z_{\gamma})^r} \frac{1}{(m_{\gamma} - r)!} \lim_{z \rightarrow z_{\gamma}} \partial_z^{m_{\gamma} - r} \prod_{\gamma' \neq \gamma} \frac{1}{(z - z_{\gamma'})^{m_{\gamma'}}}. \end{aligned} \quad (\text{A1})$$

The derivative of a product of poles can be expressed in the following way:

$$\begin{aligned} \partial_z^n \prod_{\gamma} \frac{1}{(z - z_{\gamma})^{m_{\gamma}}} &= (-1)^n n! \sum_{\mathcal{C} \{p_{\gamma} \in \mathbb{N}_0 : \sum_{\gamma} p_{\gamma} = n\}} \\ & \prod_{\gamma} \frac{(m_{\gamma} + p_{\gamma} - 1)!}{p_{\gamma}! (m_{\gamma} - 1)!} \frac{1}{(z - z_{\gamma})^{m_{\gamma} + p_{\gamma}}}. \end{aligned} \quad (\text{A2})$$

Here the sum goes over all combinations \mathcal{C} of a choice of a non-negative-integer p per pole γ , such that their sum is n .

Putting together the equations Eq. (A1) and Eq. (A2), one obtains Eq. (6).

The derivation of Eq. (A2) relies on performing $\partial_z [f(z)g(z)] = [\partial_z f(z)]g(z) + f(z)[\partial_z g(z)]$ and $\partial_z \frac{1}{(z - z_{\gamma})^{m_{\gamma}}} = -m_{\gamma} \frac{1}{(z - z_{\gamma})^{m_{\gamma} + 1}}$, recursively. Having these in mind, it is clear that the final result will consist of a number of terms, each term being a product of the original poles, some with increased orders. In each term, we will have acted with the derivative upon each pole γ a certain number of times $p_{\gamma} \geq 0$, so as to use up all the derivatives, i.e., $\sum_{\gamma} p_{\gamma} = n$. For each pole that is acted upon at least once, this leads to $\partial_z^{p_{\gamma}} \frac{1}{(z - z_{\gamma})^{m_{\gamma}}} = (-1)^{p_{\gamma}} m_{\gamma} (m_{\gamma} + 1) \dots (m_{\gamma} + p_{\gamma} - 1) \frac{1}{(z - z_{\gamma})^{m_{\gamma} + p_{\gamma}}}$. Hence the overall sign $\prod_{\gamma} (-1)^{p_{\gamma}} = (-1)^n$. However, we can apply derivatives in any order, so there is also a combinatorial factor corresponding to permutation of multisets $n! / (\prod_{\gamma} p_{\gamma}!)$ (number of distinct anagrams of an n -long word consisting of unique letters indexed by γ , each appearing p_{γ} times in the word).

Let us check and illustrate Eq. (A2) on a simple example, where one can carry out the derivatives by hand. Say

$$\begin{aligned} & \partial_z^3 \frac{1}{z - z_1} \frac{1}{(z - z_2)^2} \\ &= -6 \left(4 \frac{1}{z - z_1} \frac{1}{(z - z_2)^5} + 3 \frac{1}{(z - z_1)^2} \frac{1}{(z - z_2)^4} \right. \\ & \quad \left. + 2 \frac{1}{(z - z_1)^3} \frac{1}{(z - z_2)^3} + \frac{1}{(z - z_1)^4} \frac{1}{(z - z_2)^2} \right). \end{aligned} \quad (\text{A3})$$

We can immediately identify the prefactor $(-1)^n n! = (-1)^3 3! = -6$. Also, we see there are 4 terms corresponding to 4 possible choices of (p_1, p_2) such that $p_1 + p_2 = n = 3$, respectively,

$$\mathcal{C} = \{(0, 3), (1, 2), (2, 1), (3, 0)\}. \quad (\text{A4})$$

TABLE I. Numbers of poles and terms in the symbolic expression obtained by analytical Matsubara summations.

N	N_{poles}	$N_{\text{poles}}^{\text{typ}}$	N_{terms}	$N_{\text{terms}}^{\text{typ}}$
2	1	1	4	4
3	2	2	12–14	13
4	3–4	3.5	16–70	29.7
5	4–8	5.6	32–482	97.9
6	5–14	8.9	32–5092	296.2

Now the prefactors $\prod_{\gamma} (m_{\gamma} + p_{\gamma} - 1)! / [p_{\gamma}! (m_{\gamma} - 1)!]$ can be evaluated for each combination

$$\begin{aligned}
 (0, 3) &: \frac{(1+0-1)! (2+3-1)!}{0!0! 3!1!} = \frac{1 \cdot 4!}{1 \cdot 3!} = 4, \\
 (1, 2) &: \frac{(1+1-1)! (2+2-1)!}{1!0! 2!1!} = \frac{1 \cdot 3!}{1 \cdot 2!} = 3, \\
 (2, 1) &: \frac{(1+2-1)! (2+1-1)!}{2!0! 1!1!} = \frac{2! \cdot 2!}{2! \cdot 1!} = 2, \\
 (3, 0) &: \frac{(1+3-1)! (2+0-1)!}{3!0! 0!1!} = \frac{3! \cdot 1}{3! \cdot 1} = 1,
 \end{aligned} \tag{A5}$$

all of which we can readily identify on the right-hand side of Eq. (A3).

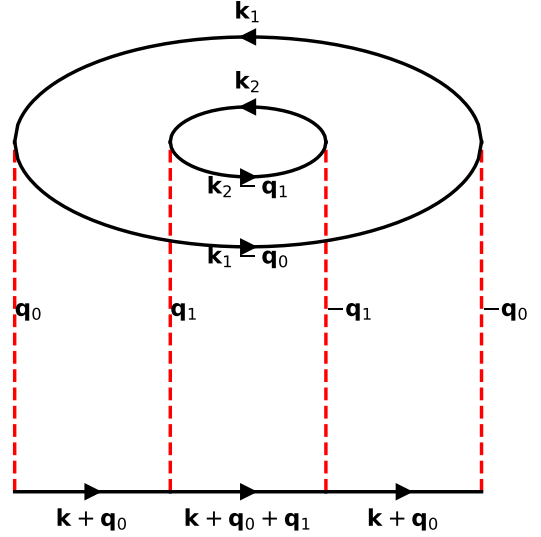


FIG. 2. An example of a momentum-labeled 4th-order diagram on the lattice.

2. Numbers of poles and terms per diagram

Equation (9) in the main text is the final result of Matsubara summations for a given diagram. It is a sum of a certain number N_{poles} of distinct poles $(\omega_{\kappa}, m_{\kappa})$, each with N_{terms} distinct terms in the amplitude A_{κ} . We tabulate in Table I the range and the geometrical average (typical value) of these numbers for each perturbation order N .

3. Results of symbolic algebra

We present here an example of the analytic expression for the contribution of a self-energy diagram. We choose the 4th-order diagram presented in Fig. 2. We start from the expression of the form Eq. (4):

$$\begin{aligned}
 \mathcal{D}_{\mathbf{k}}(i\omega) &= (-1)^2 \sum_{\mathbf{k}_1, \mathbf{k}_2} \sum_{\mathbf{q}_0, \mathbf{q}_1} \sum_{i\omega_1, i\omega_2} \sum_{i\nu_0, i\nu_1} \\
 &\times G_{\mathbf{k}+\mathbf{q}_0}^{\text{HF}}(i\omega + i\nu_0) G_{\mathbf{k}+\mathbf{q}_0+\mathbf{q}_1}^{\text{HF}}(i\omega + i\nu_0 + i\nu_1) G_{\mathbf{k}+\mathbf{q}_0}^{\text{HF}}(i\omega + i\nu_0) G_{\mathbf{k}_1}^{\text{HF}}(i\omega_1) G_{\mathbf{k}_1-\mathbf{q}_0}^{\text{HF}}(i\omega_1 - i\nu_0) \\
 &G_{\mathbf{k}_2}^{\text{HF}}(i\omega_2) G_{\mathbf{k}_2-\mathbf{q}_1}^{\text{HF}}(i\omega_2 - i\nu_1) \\
 &= (-1)^2 \sum_{\mathbf{k}_1, \mathbf{k}_2} \sum_{\mathbf{q}_0, \mathbf{q}_1} \sum_{i\omega_1, i\omega_2} \sum_{i\nu_0, i\nu_1} \\
 &\times \left(\frac{1}{i\omega + i\nu_0 - \varepsilon_{\mathbf{k}+\mathbf{q}_0}} \right)^2 \frac{1}{i\omega + i\nu_0 + i\nu_1 - \varepsilon_{\mathbf{k}+\mathbf{q}_0+\mathbf{q}_1}} \frac{1}{i\omega_1 - \varepsilon_{\mathbf{k}_1}} \frac{1}{i\omega_1 - i\nu_0 - \varepsilon_{\mathbf{k}_1-\mathbf{q}_0}} \frac{1}{i\omega_2 - \varepsilon_{\mathbf{k}_2}} \frac{1}{i\omega_2 - i\nu_1 - \varepsilon_{\mathbf{k}_2-\mathbf{q}_1}}. \tag{A6}
 \end{aligned}$$

Here we have already imposed momentum conservation, which leaves only two internal bosonic frequencies/momenta to be summed over (independent momenta carried by fermions and vertices are denoted in Fig. 2). For the sake of notational brevity, here, as well as in the rest of this Appendix, we take $\varepsilon_{\mathbf{k}} \equiv \varepsilon(\mathbf{k})$.

The first step in performing the analytical Matsubara frequency summations is to choose one internal Matsubara frequency, and then isolate the factors (poles) which depend on it. Say we choose $i\nu_0$. We can regroup the factors conveniently:

$$\begin{aligned}
 \mathcal{D}_{\mathbf{k}}(i\omega) &= (-1)^2 \sum_{\mathbf{k}_1, \mathbf{k}_2} \sum_{\mathbf{q}_0, \mathbf{q}_1} \sum_{i\omega_1, i\omega_2} \sum_{i\nu_1} \\
 &\times \frac{1}{i\omega_1 - \varepsilon_{\mathbf{k}_1}} \frac{1}{i\omega_2 - \varepsilon_{\mathbf{k}_2}} \frac{1}{i\omega_2 - i\nu_1 - \varepsilon_{\mathbf{k}_2-\mathbf{q}_1}} \sum_{i\nu_0} \frac{1}{[i\nu_0 - (-i\omega + \varepsilon_{\mathbf{k}+\mathbf{q}_0})]^2} \frac{1}{i\nu_0 - (-i\omega - i\nu_1 + \varepsilon_{\mathbf{k}+\mathbf{q}_0+\mathbf{q}_1})} \frac{-1}{i\nu_0 - (i\omega_1 - \varepsilon_{\mathbf{k}_1-\mathbf{q}_0})}. \tag{A7}
 \end{aligned}$$

Now the expression has the form of a product of poles with respect to iv_0 [Eq. (5)], where the rest can be considered a prefactor (denoted P). The product of poles can be then transformed using the main transformation Eq. (6):

$$\begin{aligned}
 \mathcal{D}_{\mathbf{k}}(i\omega) &= (-1)^2 \sum_{\mathbf{k}_1, \mathbf{k}_2} \sum_{\mathbf{q}_0, \mathbf{q}_1} \sum_{i\omega_1, i\omega_2} \sum_{iv_1} \frac{1}{i\omega_1 - \varepsilon_{\mathbf{k}_1}} \frac{1}{i\omega_2 - \varepsilon_{\mathbf{k}_2}} \frac{1}{i\omega_2 - iv_1 - \varepsilon_{\mathbf{k}_2 - \mathbf{q}_1}} \\
 &\times \left\{ \frac{1}{[i\omega_1 - \varepsilon_{\mathbf{k}_1 - \mathbf{q}_0} - (-i\omega + \varepsilon_{\mathbf{k} + \mathbf{q}_0})]^2} \frac{1}{i\omega_1 - \varepsilon_{\mathbf{k}_1 - \mathbf{q}_0} - (-i\omega - iv_1 + \varepsilon_{\mathbf{k} + \mathbf{q}_0 + \mathbf{q}_1})} \sum_{iv_0} \frac{-1}{iv_0 - (i\omega_1 - \varepsilon_{\mathbf{k}_1 - \mathbf{q}_0})} \right. \\
 &+ \frac{1}{[-i\omega - iv_1 + \varepsilon_{\mathbf{k} + \mathbf{q}_0 + \mathbf{q}_1} - (-i\omega + \varepsilon_{\mathbf{k} + \mathbf{q}_0})]^2} \frac{-1}{-i\omega - iv_1 + \varepsilon_{\mathbf{k} + \mathbf{q}_0 + \mathbf{q}_1} - (i\omega_1 - \varepsilon_{\mathbf{k}_1 - \mathbf{q}_0})} \sum_{iv_0} \frac{1}{iv_0 - (-i\omega - iv_1 + \varepsilon_{\mathbf{k} + \mathbf{q}_0 + \mathbf{q}_1})} \\
 &- \left[\left(\frac{1}{-i\omega + \varepsilon_{\mathbf{k} + \mathbf{q}_0} - (-i\omega - iv_1 + \varepsilon_{\mathbf{k} + \mathbf{q}_0 + \mathbf{q}_1})} \right)^2 \frac{-1}{-i\omega + \varepsilon_{\mathbf{k} + \mathbf{q}_0} - (i\omega_1 - \varepsilon_{\mathbf{k}_1 - \mathbf{q}_0})} \right. \\
 &+ \left. \frac{1}{-i\omega + \varepsilon_{\mathbf{k} + \mathbf{q}_0} - (-i\omega - iv_1 + \varepsilon_{\mathbf{k} + \mathbf{q}_0 + \mathbf{q}_1})} \left(\frac{-1}{-i\omega + \varepsilon_{\mathbf{k} + \mathbf{q}_0} - (i\omega_1 - \varepsilon_{\mathbf{k}_1 - \mathbf{q}_0})} \right)^2 \right] \sum_{iv_0} \frac{1}{iv_0 - (-i\omega + \varepsilon_{\mathbf{k} + \mathbf{q}_0})} \\
 &\left. + \frac{1}{-i\omega + \varepsilon_{\mathbf{k} + \mathbf{q}_0} - (-i\omega - iv_1 + \varepsilon_{\mathbf{k} + \mathbf{q}_0 + \mathbf{q}_1})} \frac{-1}{-i\omega + \varepsilon_{\mathbf{k} + \mathbf{q}_0} - (i\omega_1 - \varepsilon_{\mathbf{k}_1 - \mathbf{q}_0})} \sum_{iv_0} \frac{1}{[iv_0 - (-i\omega + \varepsilon_{\mathbf{k} + \mathbf{q}_0})]^2} \right\}. \quad (\text{A8})
 \end{aligned}$$

We can now evaluate the Matsubara frequency summations per iv_0 , using Eq. (7) and then Eq. (8). Then, the denominators can be simplified at the symbolic level:

$$\begin{aligned}
 \mathcal{D}_{\mathbf{k}}(i\omega) &= (-1)^2 \sum_{\mathbf{k}_1, \mathbf{k}_2} \sum_{\mathbf{q}_0, \mathbf{q}_1} \sum_{i\omega_1, i\omega_2} \sum_{iv_1} \frac{1}{i\omega_1 - \varepsilon_{\mathbf{k}_1}} \frac{1}{i\omega_2 - \varepsilon_{\mathbf{k}_2}} \frac{1}{i\omega_2 - iv_1 - \varepsilon_{\mathbf{k}_2 - \mathbf{q}_1}} \\
 &\times \left\{ \frac{1}{(i\omega + i\omega_1 - \varepsilon_{\mathbf{k}_1 - \mathbf{q}_0} - \varepsilon_{\mathbf{k} + \mathbf{q}_0})^2} \frac{1}{i\omega + iv_1 + i\omega_1 - \varepsilon_{\mathbf{k}_1 - \mathbf{q}_0} - \varepsilon_{\mathbf{k} + \mathbf{q}_0 + \mathbf{q}_1}} (-)^3 n_F(-\varepsilon_{\mathbf{k}_1 - \mathbf{q}_0}) \right. \\
 &+ \frac{1}{(-iv_1 + \varepsilon_{\mathbf{k} + \mathbf{q}_0 + \mathbf{q}_1} - \varepsilon_{\mathbf{k} + \mathbf{q}_0})^2} \frac{-1}{-i\omega - i\omega_1 - iv_1 + \varepsilon_{\mathbf{k} + \mathbf{q}_0 + \mathbf{q}_1} + \varepsilon_{\mathbf{k}_1 - \mathbf{q}_0}} (-)^2 n_F(\varepsilon_{\mathbf{k} + \mathbf{q}_0 + \mathbf{q}_1}) \\
 &- \left[\left(\frac{1}{iv_1 + \varepsilon_{\mathbf{k} + \mathbf{q}_0} - \varepsilon_{\mathbf{k} + \mathbf{q}_0 + \mathbf{q}_1} \right)^2 \frac{-1}{-i\omega - i\omega_1 + \varepsilon_{\mathbf{k} + \mathbf{q}_0} + \varepsilon_{\mathbf{k}_1 - \mathbf{q}_0}} \right. \\
 &+ \left. \frac{1}{iv_1 + \varepsilon_{\mathbf{k} + \mathbf{q}_0} - \varepsilon_{\mathbf{k} + \mathbf{q}_0 + \mathbf{q}_1} \left(\frac{-1}{-i\omega - i\omega_1 + \varepsilon_{\mathbf{k} + \mathbf{q}_0} + \varepsilon_{\mathbf{k}_1 - \mathbf{q}_0} \right)^2} \right] (-)^2 n_F(\varepsilon_{\mathbf{k} + \mathbf{q}_0}) \\
 &\left. + \frac{1}{iv_1 + \varepsilon_{\mathbf{k} + \mathbf{q}_0} - \varepsilon_{\mathbf{k} + \mathbf{q}_0 + \mathbf{q}_1} \frac{-1}{-i\omega - i\omega_1 + \varepsilon_{\mathbf{k} + \mathbf{q}_0} + \varepsilon_{\mathbf{k}_1 - \mathbf{q}_0}} (-)^2 \partial n_F(\varepsilon_{\mathbf{k} + \mathbf{q}_0}) \right\}. \quad (\text{A9})
 \end{aligned}$$

The procedure can now be repeated for the next choice of the Matsubara variable.

We now present the final result of the symbolic algorithm for the diagram presented in Fig. 2. The diagram contributes one second-order pole and two simple poles. The number of terms in the amplitudes for each pole is 16, 24, and 16, respectively. To display the expression easily, we only show several representative terms in the amplitude of each pole:

$$\begin{aligned}
 \mathcal{D}_{\mathbf{k}}(z) &= (-1)^2 \sum_{\mathbf{k}_1, \mathbf{k}_2} \sum_{\mathbf{q}_0, \mathbf{q}_1} \left\{ \frac{1}{(z + \varepsilon_{\mathbf{k}_1} - \varepsilon_{\mathbf{k}_1 - \mathbf{q}_0} - \varepsilon_{\mathbf{k} + \mathbf{q}_0})^2} \right. \\
 &\times \left[n_F(\varepsilon_{\mathbf{k}_2 - \mathbf{q}_1}) n_F(\varepsilon_{\mathbf{k}_1 - \mathbf{q}_0}) n_F(\varepsilon_{\mathbf{k} + \mathbf{q}_0 + \mathbf{q}_1}) \frac{1}{\varepsilon_{\mathbf{k}_2} - \varepsilon_{\mathbf{k} + \mathbf{q}_0 + \mathbf{q}_1} - \varepsilon_{\mathbf{k}_2 - \mathbf{q}_1} + \varepsilon_{\mathbf{k} + \mathbf{q}_0}} n_F(\varepsilon_{\mathbf{k} + \mathbf{q}_0}) \right. \\
 &+ n_F(\varepsilon_{\mathbf{k}_2 - \mathbf{q}_1}) n_F(\varepsilon_{\mathbf{k}_1 - \mathbf{q}_0}) n_B(\varepsilon_{\mathbf{k}_2} - \varepsilon_{\mathbf{k}_2 - \mathbf{q}_1}) \frac{1}{\varepsilon_{\mathbf{k}_2} - \varepsilon_{\mathbf{k} + \mathbf{q}_0 + \mathbf{q}_1} - \varepsilon_{\mathbf{k}_2 - \mathbf{q}_1} + \varepsilon_{\mathbf{k} + \mathbf{q}_0}} n_F(\varepsilon_{\mathbf{k} + \mathbf{q}_0}) \\
 &- n_F(\varepsilon_{\mathbf{k}_2 - \mathbf{q}_1}) n_F(\varepsilon_{\mathbf{k}_1}) n_F(\varepsilon_{\mathbf{k} + \mathbf{q}_0 + \mathbf{q}_1}) \frac{1}{\varepsilon_{\mathbf{k}_2} - \varepsilon_{\mathbf{k} + \mathbf{q}_0 + \mathbf{q}_1} - \varepsilon_{\mathbf{k}_2 - \mathbf{q}_1} + \varepsilon_{\mathbf{k} + \mathbf{q}_0}} n_F(\varepsilon_{\mathbf{k} + \mathbf{q}_0}) \\
 &\left. \left. - n_F(\varepsilon_{\mathbf{k}_2}) n_F(\varepsilon_{\mathbf{k}_1 - \mathbf{q}_0}) n_B(\varepsilon_{\mathbf{k}_2} - \varepsilon_{\mathbf{k}_2 - \mathbf{q}_1}) \frac{1}{\varepsilon_{\mathbf{k}_2} - \varepsilon_{\mathbf{k} + \mathbf{q}_0 + \mathbf{q}_1} - \varepsilon_{\mathbf{k}_2 - \mathbf{q}_1} + \varepsilon_{\mathbf{k} + \mathbf{q}_0}} n_F(\varepsilon_{\mathbf{k} + \mathbf{q}_0}) + \dots \right] \right\}
 \end{aligned}$$

$$\begin{aligned}
 & + \frac{1}{z + \varepsilon_{\mathbf{k}_1} - \varepsilon_{\mathbf{k}_1 - \mathbf{q}_0} - \varepsilon_{\mathbf{k} + \mathbf{q}_0}} \\
 & \times \left[n_F(\varepsilon_{\mathbf{k}_2 - \mathbf{q}_1}) n_F(\varepsilon_{\mathbf{k}_1 - \mathbf{q}_0}) n_F(\varepsilon_{\mathbf{k} + \mathbf{q}_0 + \mathbf{q}_1}) \frac{1}{\varepsilon_{\mathbf{k}_2} - \varepsilon_{\mathbf{k} + \mathbf{q}_0 + \mathbf{q}_1} - \varepsilon_{\mathbf{k}_2 - \mathbf{q}_1} + \varepsilon_{\mathbf{k} + \mathbf{q}_0}} \partial n_F(\varepsilon_{\mathbf{k} + \mathbf{q}_0}) \right. \\
 & + n_F(\varepsilon_{\mathbf{k}_2 - \mathbf{q}_1}) n_F(\varepsilon_{\mathbf{k}_1}) n_F(\varepsilon_{\mathbf{k} + \mathbf{q}_0 + \mathbf{q}_1}) n_B(\varepsilon_{\mathbf{k}_1} - \varepsilon_{\mathbf{k}_1 - \mathbf{q}_0}) \frac{1}{(\varepsilon_{\mathbf{k}_2} + \varepsilon_{\mathbf{k} + \mathbf{q}_0} - \varepsilon_{\mathbf{k} + \mathbf{q}_0 + \mathbf{q}_1} - \varepsilon_{\mathbf{k}_2 - \mathbf{q}_1})^2} \\
 & - n_F(\varepsilon_{\mathbf{k}_2}) n_F(\varepsilon_{\mathbf{k}_1 - \mathbf{q}_0}) n_F(\varepsilon_{\mathbf{k} + \mathbf{q}_0 + \mathbf{q}_1}) \frac{1}{\varepsilon_{\mathbf{k}_2} - \varepsilon_{\mathbf{k} + \mathbf{q}_0 + \mathbf{q}_1} - \varepsilon_{\mathbf{k}_2 - \mathbf{q}_1} + \varepsilon_{\mathbf{k} + \mathbf{q}_0}} \partial n_F(\varepsilon_{\mathbf{k} + \mathbf{q}_0}) \\
 & \left. - n_F(\varepsilon_{\mathbf{k}_2}) n_F(\varepsilon_{\mathbf{k}_1}) n_B(\varepsilon_{\mathbf{k}_2} - \varepsilon_{\mathbf{k}_2 - \mathbf{q}_1}) \frac{1}{(\varepsilon_{\mathbf{k}_2} - \varepsilon_{\mathbf{k} + \mathbf{q}_0 + \mathbf{q}_1} - \varepsilon_{\mathbf{k}_2 - \mathbf{q}_1} + \varepsilon_{\mathbf{k} + \mathbf{q}_0})^2} n_F(\varepsilon_{\mathbf{k} + \mathbf{q}_0}) + \dots \right] \\
 & + \frac{1}{z + \varepsilon_{\mathbf{k}_2} + \varepsilon_{\mathbf{k}_1} - \varepsilon_{\mathbf{k} + \mathbf{q}_0 + \mathbf{q}_1} - \varepsilon_{\mathbf{k}_2 - \mathbf{q}_1} - \varepsilon_{\mathbf{k}_1 - \mathbf{q}_0}} \\
 & \times \left[n_F(\varepsilon_{\mathbf{k}_2 - \mathbf{q}_1}) n_F(\varepsilon_{\mathbf{k}_1 - \mathbf{q}_0}) n_F(\varepsilon_{\mathbf{k} + \mathbf{q}_0 + \mathbf{q}_1}) \frac{1}{(-\varepsilon_{\mathbf{k}_2} + \varepsilon_{\mathbf{k} + \mathbf{q}_0 + \mathbf{q}_1} + \varepsilon_{\mathbf{k}_2 - \mathbf{q}_1} - \varepsilon_{\mathbf{k} + \mathbf{q}_0})^2} \right. \\
 & \times n_F(-\varepsilon_{\mathbf{k}_2} + \varepsilon_{\mathbf{k} + \mathbf{q}_0 + \mathbf{q}_1} + \varepsilon_{\mathbf{k}_2 - \mathbf{q}_1}) \\
 & + n_F(\varepsilon_{\mathbf{k}_2 - \mathbf{q}_1}) n_F(\varepsilon_{\mathbf{k}_1 - \mathbf{q}_0}) n_F(\varepsilon_{\mathbf{k} + \mathbf{q}_0 + \mathbf{q}_1}) n_B(\varepsilon_{\mathbf{k}_1} - \varepsilon_{\mathbf{k}_1 - \mathbf{q}_0}) \frac{1}{(-\varepsilon_{\mathbf{k}_2} - \varepsilon_{\mathbf{k} + \mathbf{q}_0} + \varepsilon_{\mathbf{k} + \mathbf{q}_0 + \mathbf{q}_1} + \varepsilon_{\mathbf{k}_2 - \mathbf{q}_1})^2} \\
 & - n_F(\varepsilon_{\mathbf{k}_2}) n_F(\varepsilon_{\mathbf{k}_1 - \mathbf{q}_0}) n_F(\varepsilon_{\mathbf{k} + \mathbf{q}_0 + \mathbf{q}_1}) \frac{1}{(-\varepsilon_{\mathbf{k}_2} + \varepsilon_{\mathbf{k} + \mathbf{q}_0 + \mathbf{q}_1} + \varepsilon_{\mathbf{k}_2 - \mathbf{q}_1} - \varepsilon_{\mathbf{k} + \mathbf{q}_0})^2} \\
 & \left. \times n_F(-\varepsilon_{\mathbf{k}_2} + \varepsilon_{\mathbf{k} + \mathbf{q}_0 + \mathbf{q}_1} + \varepsilon_{\mathbf{k}_2 - \mathbf{q}_1}) + \dots \right] \}. \tag{A10}
 \end{aligned}$$

4. Calculation of Fermi/Bose function derivatives

In the numerical evaluation of the amplitudes of the poles $[A_k; \text{Eq. (9) and Eq. (10)}]$, we use the general expression for the derivatives of the Fermi/Bose distribution function,

$$\partial_\omega^r n_\eta(\omega) = -\beta^r \sum_{k=0}^r \frac{(-)^{k+1} f_{r,k} e^{k\beta\omega}}{(e^{\beta\omega} - \eta)^{k+1}} \tag{A11}$$

with $f_{r,k} \in \mathbb{N}_0$ tabulated here:

$r \setminus k$	0	1	2	3	4	5	6
0	1						
1	0	1					
2	0	1	2				
3	0	1	6	6			
4	0	1	14	36	24		
5	0	1	30	150	240	120	
6	0	1	62	540	1560	1800	720

5. Dispersion on an equidistant grid

We present here in detail the numerical trick that we use to avoid unmanageable outputs from the Monte Carlo summation. For a given lattice size (in our case 32×32), we approximate $\varepsilon_{\mathbf{k}}$ so that it takes on values only from a given

set Ξ of equidistant numbers spanning the bandwidth (in our case the number of points is $N_\Xi = 151$). The new approximate dispersion therefore has the property

$$\tilde{\varepsilon}_{\mathbf{k}} \in \Xi, \forall \mathbf{k} \tag{A12}$$

with

$$\Xi = \{\min_{\mathbf{k}} \varepsilon_{\mathbf{k}} + j \Delta \varepsilon\}_{j=0}^{N_\Xi - 1} \tag{A13}$$

and

$$\Delta \varepsilon = \frac{\max_{\mathbf{k}} \varepsilon_{\mathbf{k}} - \min_{\mathbf{k}} \varepsilon_{\mathbf{k}}}{N_\Xi - 1}, \tag{A14}$$

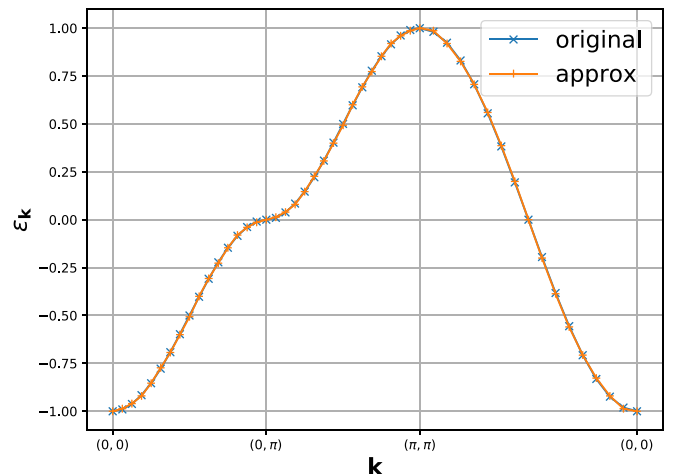


FIG. 3. Approximation of the dispersion used to avoid unmanageable outputs.

and is determined simply by choosing the closest value to the original dispersion:

$$\tilde{\varepsilon}_{\mathbf{k}} \equiv \text{closest}(\Xi, \varepsilon_{\mathbf{k}}). \quad (\text{A15})$$

With a sufficiently dense grid Ξ , the approximation becomes negligible. We present the approximate $\tilde{\varepsilon}_{\mathbf{k}}$ we used in our calculations in comparison to the exact dispersion in Fig. 3.

6. Multiple precision algebra and regulators

To illustrate the need for multiple precision algebra, we focus here on the simplest example, which is the second-order diagram. The Matsubara summations here can be easily carried out by hand:

$$\begin{aligned} \mathcal{D}_{\mathbf{k}}(i\omega) &= (-1) \sum_{i\omega', iv} \sum_{\mathbf{k}', \mathbf{q}} G_{0, \mathbf{k}'}^{\text{HF}}(i\omega') G_{0, \mathbf{k}'+\mathbf{q}}^{\text{HF}}(i\omega' + iv) G_{0, \mathbf{k}-\mathbf{q}}^{\text{HF}}(i\omega - iv) \\ &= (-1) \sum_{i\omega', iv} \sum_{\mathbf{k}', \mathbf{q}} \frac{1}{i\omega' - \varepsilon_{\mathbf{k}'}} \frac{1}{i\omega' + iv - \varepsilon_{\mathbf{k}'+\mathbf{q}}} \frac{1}{i\omega - iv - \varepsilon_{\mathbf{k}-\mathbf{q}}} \\ &= \sum_{\mathbf{k}', \mathbf{q}} \frac{n_F(\varepsilon_{\mathbf{k}'}) n_B(\varepsilon_{\mathbf{k}'+\mathbf{q}} - \varepsilon_{\mathbf{k}'}) + n_F(\varepsilon_{\mathbf{k}'}) n_F(-\varepsilon_{\mathbf{k}-\mathbf{q}}) - n_F(\varepsilon_{\mathbf{k}'+\mathbf{q}}) n_B(\varepsilon_{\mathbf{k}'+\mathbf{q}} - \varepsilon_{\mathbf{k}'}) - n_F(\varepsilon_{\mathbf{k}'+\mathbf{q}}) n_F(-\varepsilon_{\mathbf{k}-\mathbf{q}})}{i\omega - \varepsilon_{\mathbf{k}'+\mathbf{q}} - \varepsilon_{\mathbf{k}-\mathbf{q}} + \varepsilon_{\mathbf{k}'}}. \end{aligned} \quad (\text{A16})$$

We see that the final result has four terms in total, and that the two terms featuring n_B diverge as $\mathbf{q} \rightarrow 0$, or equivalently as $t \rightarrow 0$, i.e., $\varepsilon_{\mathbf{k}} \rightarrow 0, \forall \mathbf{k}$. Nevertheless, the contribution of the diagram is *finite* as the following limit is well defined:

$$\lim_{\varepsilon \rightarrow 0} [n_F(0) n_B(\varepsilon) - n_F(\varepsilon) n_B(\varepsilon)] = \frac{1}{4}. \quad (\text{A17})$$

However, in numerical implementation one cannot simply let $\varepsilon \rightarrow 0$ in the above expression as n_B becomes ill defined. We find the solution in adding small shifts in the symbolic expression. At second order, it suffices to associate a small shift ϵ to $\varepsilon_{\mathbf{k}'}$:

$$\begin{aligned} \mathcal{D}_{\mathbf{k}}(i\omega) &\approx \sum_{\mathbf{k}', \mathbf{q}} \frac{1}{i\omega - \varepsilon_{\mathbf{k}'+\mathbf{q}} - \varepsilon_{\mathbf{k}-\mathbf{q}} + \varepsilon_{\mathbf{k}'} + \epsilon} \\ &\times [n_F(\varepsilon_{\mathbf{k}'} + \epsilon) n_B(\varepsilon_{\mathbf{k}'+\mathbf{q}} - \varepsilon_{\mathbf{k}'} - \epsilon) + n_F(\varepsilon_{\mathbf{k}'} + \epsilon) n_F(-\varepsilon_{\mathbf{k}-\mathbf{q}}) - n_F(\varepsilon_{\mathbf{k}'+\mathbf{q}}) n_B(\varepsilon_{\mathbf{k}'+\mathbf{q}} - \varepsilon_{\mathbf{k}'} - \epsilon) - n_F(\varepsilon_{\mathbf{k}'+\mathbf{q}}) n_F(-\varepsilon_{\mathbf{k}-\mathbf{q}})]. \end{aligned} \quad (\text{A18})$$

That solves the problem as n_B will no longer be ill defined even when $\mathbf{q} = 0$. However, depending on the size of ϵ and β , the two problematic terms may become large. Consider $\epsilon = 10^{-20}$ and $\beta = 1$. In that case the terms featuring n_B can become as big as 10^{20} . The subtraction of two numbers of size 10^{20} that are different only by $\frac{1}{4}$ will fail if performed in standard (double) precision, as it handles only up to ~ 16 digits. While in the case of the second-order diagram one can clearly use a larger ϵ and avoid any problems, at higher perturbation orders there will be products of several diverging n_B , multiplied also with expressions of the type $1/0$, and ever larger shifts would be needed; increasing the numerical shifts would eventually start introducing noticeable systematic error. The solution is then to use larger floating point data types that can store more digits. In our implementation we use the GNU Multiple Precision Arithmetic (GMP) C++ library and its Python wrapper GMPY2 and use floating point type of 350 bits, and we keep the shifts perturbation-order dependent, $\sim 10^{-12+N}$.

7. Monte Carlo application to local self-energy

We also devise an algorithm to treat directly the local self-energy. This algorithm relies on rewriting the diagrams in real space. In notation analogous to Eq. (4), the contribution of a general real-space diagram has the following form:

$$\begin{aligned} \mathcal{D}_{\mathbf{i}_0 \mathbf{i}_N}(i\omega) &= (-1)^{N_b} \sum_{\mathbf{i}_1, \dots, \mathbf{i}_{N-1}} \sum_{i\Omega_1, \dots, i\Omega_M} \\ &\int d\varepsilon_1 \dots d\varepsilon_{2N-1} \prod_{\gamma} \frac{\rho_{\mathbf{r}(\gamma; \mathbf{i}_0, \dots, \mathbf{i}_N)}(\varepsilon_{\gamma})}{\sum_{(s,j) \in \mathcal{K}_{\gamma}} s i \Omega_j - \varepsilon_{\gamma}}, \end{aligned} \quad (\text{A19})$$

where \mathbf{i}_i denote the lattice sites where the interaction vertices are positioned (the first and last are the external site indices). The energy integrals come from the Hilbert transform

$$G_{\mathbf{r}}(i\omega) = -\frac{1}{\pi} \int d\epsilon \frac{\text{Im} G_{\mathbf{r}}(\epsilon + i0^+)}{i\omega - \epsilon} \quad (\text{A20})$$

and

$$\begin{aligned} \rho_{\mathbf{r}}(\varepsilon) &= -\frac{1}{\pi} \text{Im} G_{\mathbf{r}}(\varepsilon + i0^+) \\ &= -\frac{1}{\pi} \text{Im} \sum_{\mathbf{k}} e^{i\mathbf{k} \cdot \mathbf{r}} G_{\mathbf{k}}(\varepsilon + i0^+) \\ &= \sum_{\mathbf{k}} e^{i\mathbf{k} \cdot \mathbf{r}} \delta_{\varepsilon, \varepsilon_{\mathbf{k}}} \\ &= 2 \sum_{0 < k_x, k_y < \pi} [\cos(\mathbf{k} \cdot \mathbf{r}) + \cos(\mathbf{k} \sigma^z \mathbf{r})] \delta_{\varepsilon, \varepsilon_{\mathbf{k}}}, \end{aligned} \quad (\text{A21})$$

where $\mathbf{k} \sigma^z \mathbf{r} = k_x r_x - k_y r_y$. The above can be evaluated numerically to high precision. It is important to note that

$$\int d\varepsilon \rho_{\mathbf{r}=(0,0)}(\varepsilon) = 1, \quad (\text{A22})$$

$$\int d\varepsilon \rho_{\mathbf{r} \neq (0,0)}(\varepsilon) = 0. \quad (\text{A23})$$

Now note that only ρ actually depends on the choice of lattice sites. We rewrite the expression in a way that is more revealing:

$$\begin{aligned} \mathcal{D}_{\mathbf{i}_0\mathbf{i}_N}(i\omega) &= (-1)^{N_b} \sum_{i\Omega_1 \dots i\Omega_M} \int d\varepsilon_1 \dots d\varepsilon_{2N-1} \prod_{\gamma} \\ &\times \frac{1}{\sum_{(s,j) \in \mathcal{K}_\gamma} s i\Omega_j - \varepsilon_\gamma} \sum_{\mathbf{i}_1 \dots \mathbf{i}_{N-1}} \rho_{\mathbf{r}(\gamma; \mathbf{i}_0 \dots \mathbf{i}_N)}(\varepsilon_\gamma). \end{aligned} \quad (\text{A24})$$

For a given choice of ε 's and \mathbf{i} 's, this is formally the same as what we had in Eq. (4) in the main text. A completely analogous symbolic algebra algorithm can be used to resolve the Matsubara summations, but the results will be different. The difference from the \mathbf{k} -space case is that all the ε 's are now independent, which will lead to different analytical expressions for each diagram. The final expressions will, however, have the same general form [Eq. (9) and Eq. (10) in the main text], yet slightly simplified: now one obtains only simple poles because no two Green's functions are identical, i.e., $m_\gamma = 1, \forall \gamma$. In fact, even in the \mathbf{k} -space case, higher-order poles appear only in dressed diagrams; a skeleton series would not have this feature. After the analytical summation of the Matsubara frequencies, the remaining expression to be evaluated has the form

$$\begin{aligned} \mathcal{D}_{\mathbf{i}_0\mathbf{i}_N}(z) &= (-1)^{N_b} \int d\varepsilon_1 \dots d\varepsilon_{2N-1} \sum_{\kappa} \frac{A_\kappa}{z - \omega_\kappa} \\ &\times \prod_{\gamma} \sum_{\mathbf{i}_1 \dots \mathbf{i}_{N-1}} \rho_{\mathbf{r}(\gamma; \mathbf{i}_0 \dots \mathbf{i}_N)}(\varepsilon_\gamma), \end{aligned} \quad (\text{A25})$$

where A and ω implicitly depend on $\varepsilon_1 \dots \varepsilon_{2N-1}$. The remaining variables to be summed over now include both the energies ε and the lattice sites \mathbf{i} . Note, however, that A and ω do *not* depend on the \mathbf{i} 's, so recalculating them for each configuration of \mathbf{i} 's would be inefficient. We are immediately inclined to use $\prod_{\gamma} \sum_{\mathbf{i}_1 \dots \mathbf{i}_{N-1}} \rho_{\mathbf{r}(\gamma; \mathbf{i}_0 \dots \mathbf{i}_N)}(\varepsilon_\gamma)$ as the weight for Monte Carlo over the space of ε 's. We recall the general expression

$$\frac{\int f(x)w(x)dx}{\int w(x)dx} = \frac{\sum_{x \in \text{MC}(|w|)} f(x) \text{sgn}[w(x)]}{\sum_{x \in \text{MC}(|w|)} \text{sgn}[w(x)]}, \quad (\text{A26})$$

where $\text{MC}(|w|)$ is the Markov chain constructed with respect to $|w|$ as the weight. Therefore it is necessary that the overall integral of our weight function is known and nonzero. However, this will only be the case if $\mathbf{i}_0 = \mathbf{i}_N$. First, the integrals over our proposed weight decouple:

$$\begin{aligned} &\int d\varepsilon_1 \dots d\varepsilon_{2N-1} \prod_{\gamma} \sum_{\mathbf{i}_1 \dots \mathbf{i}_{N-1}} \rho_{\mathbf{r}(\gamma; \mathbf{i}_0 \dots \mathbf{i}_N)}(\varepsilon_\gamma) \\ &= \sum_{\mathbf{i}_1 \dots \mathbf{i}_{N-1}} \prod_{\gamma} \int d\varepsilon_\gamma \rho_{\mathbf{r}(\gamma; \mathbf{i}_0 \dots \mathbf{i}_N)}(\varepsilon_\gamma). \end{aligned} \quad (\text{A27})$$

We see that the only contribution comes from the choice $\mathbf{i}_0 = \mathbf{i}_1 = \dots = \mathbf{i}_N$ in which case $\mathbf{r}(\gamma; \mathbf{i}_0 \dots \mathbf{i}_N) = (0, 0), \forall \gamma$, and so each integral over energy equals 1, and the total integral of the weight is also equal 1. Otherwise, if $\mathbf{i}_0 \neq \mathbf{i}_N$, there will always be at least one nonlocal $\rho_{\mathbf{r}}(\varepsilon)$ involved, the integral of which is 0. Therefore, the proposed weight has total integral zero for any nonlocal self-energy component and cannot be used in this purpose. Nevertheless, one can use it

for calculating the local self-energy. Furthermore, in a local problem, e.g., Anderson impurity [48], this scheme can be used straightforwardly without the summations over lattice sites. We use it in our Anderson impurity benchmark below.

8. Diagram topologies

In Fig. 4 we present all the topologies of the interaction-expansion diagrams up to order 5. Full lines are the Hartree-shifted bare propagators, and the dashed lines are interactions. All the drawn diagrams went into calculation of the self-energy in Fig. 1.

APPENDIX B: BENCHMARK

Here we benchmark our method in the following cases:

- (i) atomic limit against analytic result;
- (ii) 4-site Hubbard chain against exact diagonalization (ED) [51];
- (iii) 4×4 lattice against numerically exact Rubtsov algorithm, continuous-time interaction-expansion quantum Monte Carlo (CTINT) [1,2,52];
- (iv) single Anderson impurity problem against the approximate NRG [47];
- (v) 32×32 lattice against imaginary-time diagrammatic Monte Carlo, Σ Det, up to 8th order in perturbation theory [22,23].

1. Atomic limit

We start by benchmarking our method in the case of the half-filled Hubbard atom. It corresponds to setting $t = 0, \mu = U/2$ (and $n_\sigma = 0.5$ in the definition of the Hartree-shifted bare propagator). As there is no longer \mathbf{k} dependence in the dispersion, the \mathbf{k} sums now reduce to a single term, and each diagram needs to be evaluated only once, for $\varepsilon_{\mathbf{k}} = 0$. As explained in Appendix A 6, this cannot be done straightforwardly because it would lead to divergent terms in the analytical expression, namely of the form $n_B(0)$ and $1/0$ [see Eq. (10) and the example Eq. (A10)]. The numerical treatment boils down to adding small shifts to a certain number of ε 's at the symbolic level so that zeros are avoided in the arguments of n_B and denominators of fractions, and only then letting the original ε 's go to zero (say, $\varepsilon_{\mathbf{k}_2 - \mathbf{q}_1} \rightarrow \varepsilon_{\mathbf{k}_2 - \mathbf{q}_1} + \zeta, \varepsilon_{\mathbf{k}_1} \rightarrow \varepsilon_{\mathbf{k}_1} + 2\zeta$, and so on, simultaneously across all terms in a given diagram; the shifts are integer multiples of ζ which we set depending on perturbation order $\zeta = 10^{-12+N}$; the choice of ε 's to be shifted is nonunique). This will *a priori* lead to systematic numerical error and here we check whether the numerical treatment is satisfactory (the atomic limit is the worst case scenario in this respect).

First, we recall the analytical expression for the self-energy beyond the Hartree shift:

$$\Sigma^{(\text{HF})}(i\omega_n) = \frac{U^2}{4} \frac{1}{i\omega_n}. \quad (\text{B1})$$

It can be shown that this expression corresponds to the second-order diagram in the U series written down in terms of the Hartree-shifted bare propagator. The contribution of higher orders is zero ‘‘order by order,’’ but individual higher-order diagrams are not necessarily zero. Therefore, it is a stringent

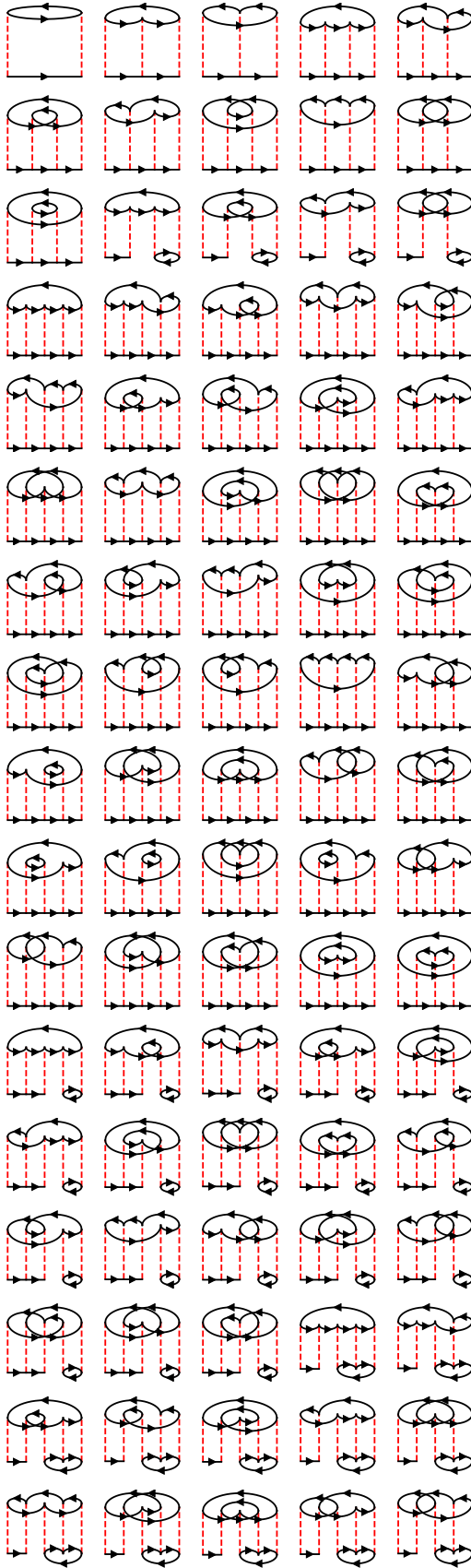


FIG. 4. Hartree-shifted self-energy series up to 5th order. The numbers of diagrams per order are 1, 2, 12, 70, 515, ... starting from the second order, respectively.

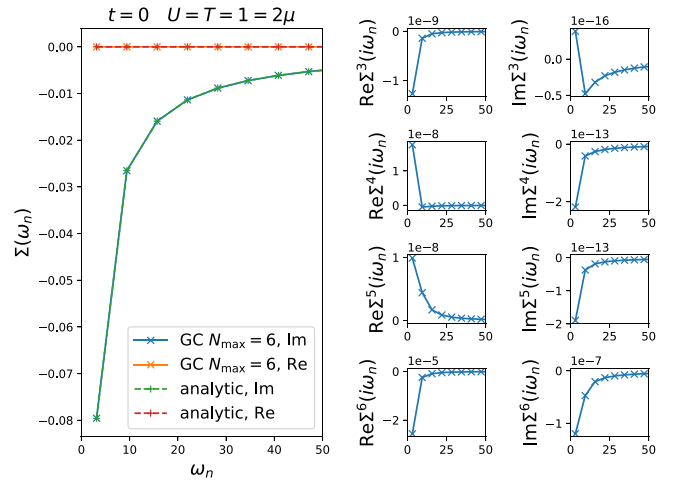


FIG. 5. Benchmark in the case of an isolated Hubbard atom at half filling. Big panel: Our method (GC) is compared to the analytical expression. Smaller panels on the right: Self-energy contributions order by order; the only contribution comes from the second-order diagram.

check of our method to show that the higher orders truly cancel.

We present the results in Fig. 5. We evaluate all the diagrams up to and including the 6th order, at a fixed $U = T = 1$. The total series is in excellent agreement with the analytical result (big panel). On the smaller panels on the right, we examine the contributions order by order (Σ^N denotes contribution at order N). Indeed, the only contribution comes from the second-order diagram, while the contributions of higher orders are negligible. However, the numerical error grows with approaching the real axis, and with growing order. The real part of self-energy coming from the 6th-order diagrams already reaches 10^{-5} . This is expected, as we use bigger numerical shifts in higher-order diagrams. Alternatively, one would need to drastically increase the floating-point precision in the evaluation of higher-order diagrams, which is not suitable for lattice computations, so we do not consider this approach; rather, we keep the floating-point precision fixed across orders.

In the atomic limit, the real-frequency self-energy cannot be reliably extracted from our method. This is, however, a somewhat pathological case where the self-energy is a single simple pole at $\omega = 0$. Due to numerical shifts and cutting the series at finite order, our numerical self-energy here is composed of multiple poles of various orders at various small frequencies $\sim \zeta$. Very close to the real axis, these numerical artifacts become apparent, and the method is of little use.

2. 4-site Hubbard chain

Next, we benchmark our method in the case of the half-filled 4-site cyclic Hubbard chain at temperature $T = 0.2D = 0.8t$ (note that the actual half-bandwidth in this case is $2t$). This small system can be solved using exact diagonalization (ED). In our method, the \mathbf{k} summations go over only 4 points and can be performed fully, so we denote our method GC

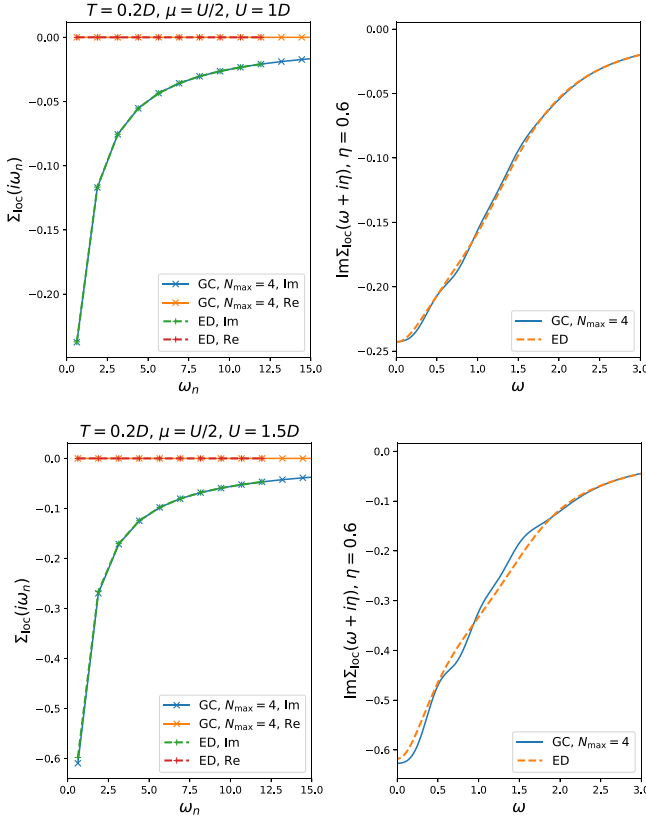


FIG. 6. Benchmark in the case of the 4-site cyclic Hubbard chain at half filling.

(gray code). In this case we go up to order 4 [due to particle-hole (PH) symmetry, the order 5 does not contribute, but order 6 we cannot fully sum].

We present our result in Fig. 6. The agreement is excellent at $U = 1D$, yet at $U = 1.5D$ higher orders become important.

Similarly to the atomic limit, the self-energy in the 4-site chain is composed of a relatively small number of poles on the real axis, and does not form a smooth frequency spectrum. On the other hand, having that $\varepsilon_{\mathbf{k}}$ takes on only three distinct values ($-0.5, 0, 0.5$), our method can yield poles only at frequencies which are integer multiples of $1/2$ (plus/minus small numerical shifts). The immediate question is then, How does one recover the correct self-energy even with an infinite self-energy series? One would expect the poles in self-energy to appear at various different frequencies and even move continuously with increasing U , yet our analytical expression seemingly does not support that. The answer is that all the higher-order poles ultimately merge into (shifted) simple poles through

$$\sum_{k=1}^{\infty} \frac{a^{k-1}}{z^k} = \frac{1}{z-a} \quad (\text{B2})$$

and that way recover the correct physical result. Note, however, that the principle part of the Laurent series Eq. (B2) cut at a finite order no longer resembles a simple pole at $\eta \lesssim a$, irrespective of the maximum order in the series. Therefore, it makes no sense to look at $\Sigma(\omega + i\eta)$ results at small η . One reasoning is that we should take η proportional to the

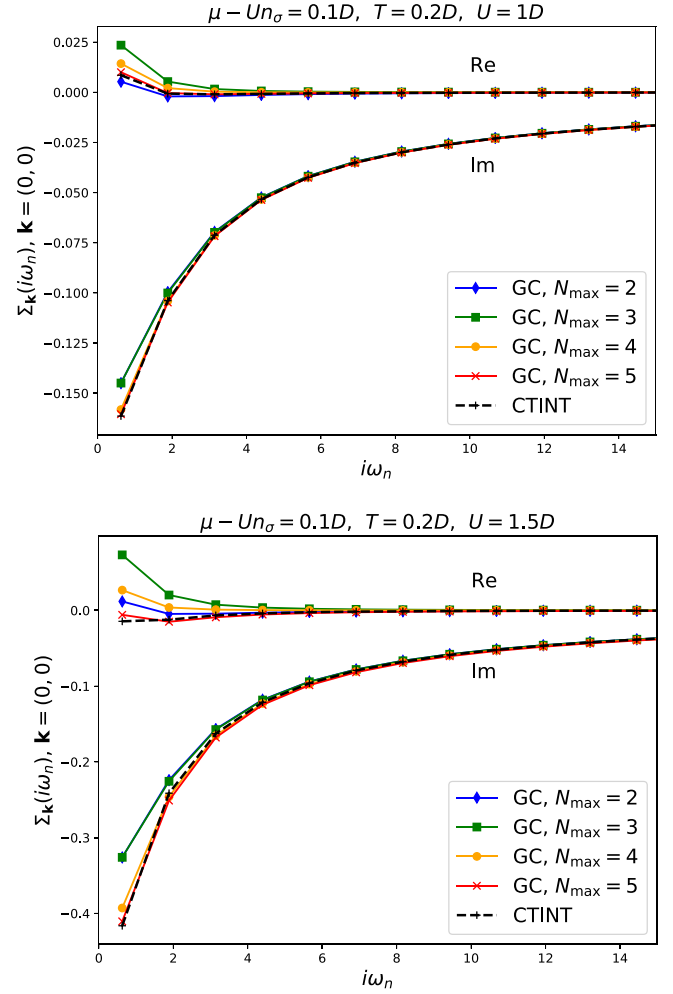


FIG. 7. Benchmark of the method in the case of 4×4 cyclic Hubbard cluster.

distance between the poles we get, which is in this case 0.5. We therefore compare our result to ED at $\eta = 0.6$ which is just below the first Matsubara frequency πT and find similarly good agreement to that on the imaginary axis.

Again, our method cannot be used to reliably extract discrete spectra on the real axis. Fitting the result at $\eta = 0.6$ to a causal and piecewise constant spectrum on the real axis does reproduce the correspondingly binned ED result, but the detailed pole structure cannot be inferred.

3. 4×4 lattice

We now turn to the 4×4 cyclic Hubbard cluster. This system cannot easily be solved with ED, so we use the Rubtsov algorithm continuous-time interaction expansion Monte Carlo (CTINT) which is numerically exact. However the comparison can now only be made on the imaginary axis. In our method, full \mathbf{k} summations can be performed up to order 5.

In Fig. 7 we show the results at $\mu - Un_{\sigma} = 0.1D$, $T = 0.2D$, $\mathbf{k} = (0, 0)$. Additionally, we show the GC results for different perturbation-order cutoffs $N_{\max} = 2 \dots 5$. At $U = 1D$ the agreement is excellent and the perturbation series

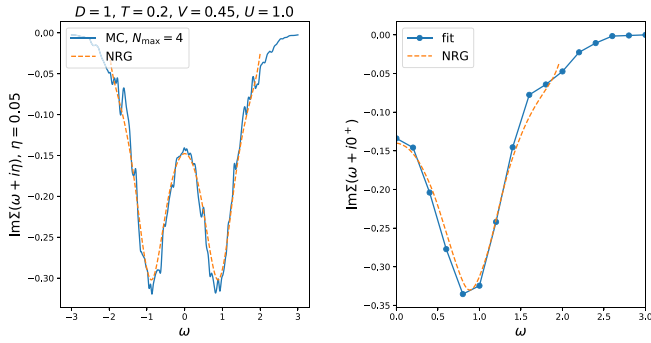


FIG. 8. Benchmark of our method in the case of the single-impurity Anderson model with a semicircular bath.

seems converged at order 5. At $U = 1.5D$ the agreement is solid, but 5th order still makes a sizable contribution.

As for the real-frequency spectrum, there is a similar problem as in the 4-site chain case: dispersion now assumes only the values $(\pm 1, \pm 0.5, 0)$, and again one obtains poles only at integer multiples of 0.5 plus an integer multiple of $\mu - Un_\sigma$. Although discrete, the exact self-energy spectrum is expected to be much denser, and any kind of fit to the $\eta \sim 0.5$ result is likely to miss details of it. Our method is suitable only for continuous spectra, as we will show in the following sections.

4. Anderson impurity

To test our method in the continuous spectrum case, we start with the simplest possible model: the Anderson impurity model with a semicircular bath. We consider only the PH-symmetric case. The Hartree-shifted bare propagator is given by

$$G_0^{\text{HF}}(z) = \frac{1}{z - \Delta(z)} \quad (\text{B3})$$

and the hybridization function

$$\Delta(z) = V^2 \int d\varepsilon \frac{\rho(\varepsilon)}{z - \varepsilon}, \quad (\text{B4})$$

$$\rho(\varepsilon) = \theta(D - |\varepsilon|) 2\sqrt{D^2 - \varepsilon^2} / (\pi D^2), \quad (\text{B5})$$

where V^2 sets the norm, and D sets the width of $\text{Im}\Delta(\omega)$.

This model can be solved approximately using numerical renormalization group (NRG). NRG yields the self-energy directly on the real axis.

In our method, we utilize the real-space algorithm introduced in Appendix A 7, with the important simplification that there are no sums over lattice sites. We discretize the energy (200 points between -1 and 1), and perform Monte Carlo integration for the ε integrals using the product $\prod_\gamma \rho(\varepsilon_\gamma)$ as the weight.

A priori, now we should be able to approach the real axis to around $\eta \sim 1/100$. However, the statistical error now also plays the role, and we find that $\text{Im} \Sigma(\omega + i\eta)$ becomes noisy below $\eta \sim 0.05D$. Nevertheless, this should be sufficient to resolve all the details of the spectrum. We compare our results to NRG at $\eta = 0.05$ and find excellent agreement (Fig. 8). Note that we do not impose PH symmetry, but the result is PH-symmetric apparently within the level of noise in the curve. Next, we fit our result at $\eta = 0.05D$ to a PH-symmetric piecewise-trapezoid spectrum on the real axis with resolution ~ 0.1 and compare to the NRG result on the real axis. The agreement is excellent, and the resolution is sufficient to capture all the features in $\text{Im} \Sigma(\omega + i0^+)$.

5. 32×32 lattice

Finally, we benchmark our method in the 32×32 Hubbard lattice case. The best available result is that of the

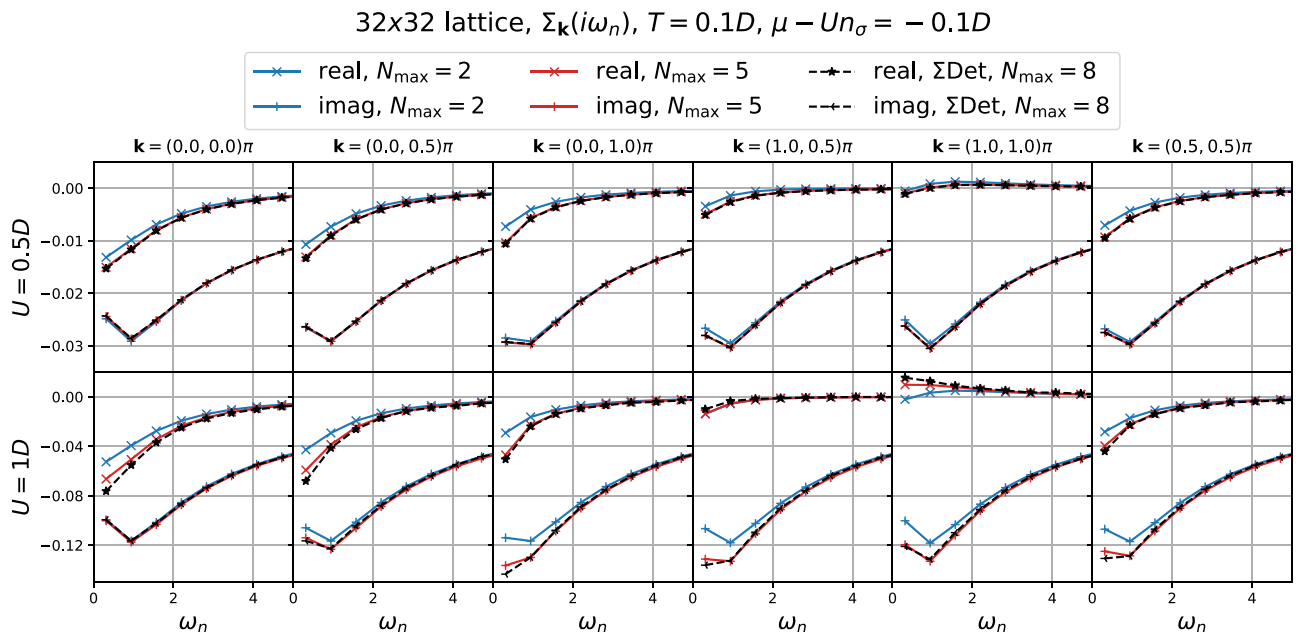


FIG. 9. Matsubara self-energy on the 32×32 Hubbard lattice: benchmark against the Σ Det method at 8th order.

imaginary-time Σ Det diagrammatic Monte Carlo calculation, performed up to 8th order. We compare the two methods on the Matsubara axis in Fig. 9.

At $U = 0.5D$ the agreement is excellent, and the calculation is clearly converged by order 5, but clearly not by order 2.

At $U = 1D$ higher orders still contribute, and there is a bit of discrepancy at low frequency. From the real-

frequency results (Fig. 1 in the main text), however, it is clear that the self-energy is qualitatively converged, although some corrections are expected with inclusion of higher orders.

We do not benchmark using $U = 1.5$ data, as in that case the higher orders are expected to contribute more, and results are not expected to coincide.

-
- [1] A. N. Rubtsov and A. I. Lichtenstein, *J. Exp. Theor. Phys. Lett.* **80**, 61 (2004).
- [2] A. N. Rubtsov, V. V. Savkin, and A. I. Lichtenstein, *Phys. Rev. B* **72**, 035122 (2005).
- [3] P. Werner, A. Comanac, L. de' Medici, M. Troyer, and A. J. Millis, *Phys. Rev. Lett.* **97**, 076405 (2006).
- [4] P. Werner and A. J. Millis, *Phys. Rev. B* **74**, 155107 (2006).
- [5] E. Gull, P. Werner, O. Parcollet, and M. Troyer, *Europhys. Lett.* **82**, 57003 (2008).
- [6] E. Gull, A. J. Millis, A. I. Lichtenstein, A. N. Rubtsov, M. Troyer, and P. Werner, *Rev. Mod. Phys.* **83**, 349 (2011).
- [7] R. E. V. Profumo, C. Groth, L. Messio, O. Parcollet, and X. Waintal, *Phys. Rev. B* **91**, 245154 (2015).
- [8] A. Moutenet, P. Seth, M. Ferrero, and O. Parcollet, *Phys. Rev. B* **100**, 085125 (2019).
- [9] C. Bertrand, O. Parcollet, A. Maillard, and X. Waintal, *Phys. Rev. B* **100**, 125129 (2019).
- [10] C. Bertrand, S. Florens, O. Parcollet, and X. Waintal, *Phys. Rev. X* **9**, 041008 (2019).
- [11] G. Cohen, D. R. Reichman, A. J. Millis, and E. Gull, *Phys. Rev. B* **89**, 115139 (2014).
- [12] G. Cohen, E. Gull, D. R. Reichman, and A. J. Millis, *Phys. Rev. Lett.* **112**, 146802 (2014).
- [13] G. Cohen, E. Gull, D. R. Reichman, and A. J. Millis, *Phys. Rev. Lett.* **115**, 266802 (2015).
- [14] A. Boag, E. Gull, and G. Cohen, *Phys. Rev. B* **98**, 115152 (2018).
- [15] E. Eidelstein, E. Gull, and G. Cohen, [arXiv:1907.08570](https://arxiv.org/abs/1907.08570).
- [16] J. Vučićević, J. Kokalj, R. Žitko, N. Wentzell, D. Tanasković, and J. Mravlje, *Phys. Rev. Lett.* **123**, 036601 (2019).
- [17] N. V. Prokof'ev and B. V. Svistunov, *Phys. Rev. Lett.* **81**, 2514 (1998).
- [18] N. Prokof'ev and B. Svistunov, *Phys. Rev. Lett.* **99**, 250201 (2007).
- [19] K. V. Houcke, E. Kozik, N. Prokof'ev, and B. Svistunov, *Phys. Procedia* **6**, 95 (2010).
- [20] E. Bourovski, N. Prokof'ev, and B. Svistunov, *Phys. Rev. B* **70**, 193101 (2004).
- [21] R. Rossi, *Phys. Rev. Lett.* **119**, 045701 (2017).
- [22] A. Moutenet, W. Wu, and M. Ferrero, *Phys. Rev. B* **97**, 085117 (2018).
- [23] F. Šimkovic and E. Kozik, *Phys. Rev. B* **100**, 121102(R) (2019).
- [24] W. Wu, M. Ferrero, A. Georges, and E. Kozik, *Phys. Rev. B* **96**, 041105(R) (2017).
- [25] A. Macridin, S. P. Doluweera, M. Jarrell, and Th. Maier, [arXiv:cond-mat/0410098](https://arxiv.org/abs/cond-mat/0410098).
- [26] R. Levy, J. LeBlanc, and E. Gull, *Comput. Phys. Commun.* **215**, 149 (2017).
- [27] E. W. Huang, R. Sheppard, B. Moritz, and T. P. Devereaux, *Science* **366**, 987 (2019).
- [28] P. Staar, T. Maier, and T. C. Schulthess, *Phys. Rev. B* **89**, 195133 (2014).
- [29] E. Gull and A. J. Millis, *Phys. Rev. B* **91**, 085116 (2015).
- [30] P. T. Brown, E. Guardado-Sanchez, B. M. Spar, E. W. Huang, T. P. Devereaux, and W. S. Bakr, *Nat. Phys.* **16**, 26 (2020).
- [31] H. Aoki, N. Tsuji, M. Eckstein, M. Kollar, T. Oka, and P. Werner, *Rev. Mod. Phys.* **86**, 779 (2014).
- [32] M. Rigol, T. Bryant, and R. R. P. Singh, *Phys. Rev. Lett.* **97**, 187202 (2006).
- [33] J. Kokalj, *Phys. Rev. B* **95**, 041110(R) (2017).
- [34] P. T. Brown, D. Mitra, E. Guardado-Sanchez, R. Nourafkan, A. Reymbaut, C.-D. Hébert, S. Bergeron, A.-M. S. Tremblay, J. Kokalj, D. A. Huse, P. Schauf, and W. S. Bakr, *Science* **363**, 379 (2018).
- [35] A. Taheridehkordi, S. H. Curnoe, and J. P. F. LeBlanc, *Phys. Rev. B* **99**, 035120 (2019).
- [36] H. Kajueter and G. Kotliar, *Phys. Rev. Lett.* **77**, 131 (1996).
- [37] M. Potthoff, T. Wegner, and W. Nolting, *Phys. Rev. B* **55**, 16132 (1997).
- [38] N. Dasari, W. R. Mondal, P. Zhang, J. Moreno, M. Jarrell, and N. S. Vidhyadhiraja, *Eur. Phys. J. B* **89**, 202 (2016).
- [39] F. Onufrieva and P. Pfeuty, *Phys. Rev. B* **65**, 054515 (2002).
- [40] F. Onufrieva and P. Pfeuty, *Phys. Rev. Lett.* **102**, 207003 (2009).
- [41] F. Onufrieva and P. Pfeuty, *Phys. Rev. Lett.* **109**, 257001 (2012).
- [42] H. Terletska, J. Vučićević, D. Tanasković, and V. Dobrosavljević, *Phys. Rev. Lett.* **107**, 026401 (2011).
- [43] J. Vučićević, H. Terletska, D. Tanasković, and V. Dobrosavljević, *Phys. Rev. B* **88**, 075143 (2013).
- [44] J. Vučićević, D. Tanasković, M. J. Rozenberg, and V. Dobrosavljević, *Phys. Rev. Lett.* **114**, 246402 (2015).
- [45] R. D. Mattuck, *A Guide to Feynman Diagrams in the Many-Body Problem*, 2nd ed. (Dover Publications, Inc., New York, 1992).
- [46] $(m+1)$ th-order poles contribute to the m th ω derivative of $\Sigma(\omega+i0^+)$ through $\partial_\omega^m A(\omega+i0^+) = -\frac{(-1)^m m!}{\pi} \int_{-\infty}^{\infty} d\varepsilon \frac{\text{Im}A(\varepsilon+i0^+)}{(\omega+i0^+-\varepsilon)^{m+1}}$.
- [47] R. Žitko and T. Pruschke, *Phys. Rev. B* **79**, 085106 (2009).
- [48] A. C. Hewson, *The Kondo Problem to Heavy Fermions*, Cambridge Studies in Magnetism (Cambridge University Press, Cambridge, UK, 1993).
- [49] F. Šimkovic, IV, J. P. F. LeBlanc, A. J. Kim, Y. Deng, N. V. Prokof'ev, B. V. Svistunov, and E. Kozik, *Phys. Rev. Lett.* **124**, 017003 (2020).
- [50] A. J. Kim, F. Šimkovic, IV, and E. Kozik, [arXiv:1905.13337](https://arxiv.org/abs/1905.13337).
- [51] H. U. Strand, PYED: Exact Diagonalization for Finite Quantum Systems, <https://github.com/HugoStrand/pyed>.
- [52] O. Parcollet, M. Ferrero, T. Ayrál, H. Hafermann, I. Krivenko, L. Messio, and P. Seth, *Comput. Phys. Commun.* **196**, 398 (2015).

Charge transport in the Hubbard model at high temperatures: Triangular versus square latticeA. Vranić¹, J. Vučičević¹, J. Kokalj^{2,3}, J. Skolimowski^{3,4}, R. Žitko^{3,5}, J. Mravlje³, and D. Tanasković¹¹*Institute of Physics Belgrade, University of Belgrade, Pregrevica 118, 11080 Belgrade, Serbia*²*University of Ljubljana, Faculty of Civil and Geodetic Engineering, Jamova 2, Ljubljana, Slovenia*³*Jožef Stefan Institute, Jamova 39, SI-1000 Ljubljana, Slovenia*⁴*International School for Advanced Studies (SISSA), Via Bonomea 265, I-34136 Trieste, Italy*⁵*University of Ljubljana, Faculty of Mathematics and Physics, Jadranska 19, Ljubljana, Slovenia*

(Received 3 June 2020; revised 7 August 2020; accepted 2 September 2020; published 21 September 2020)

High-temperature bad-metal transport has been recently studied both theoretically and in experiments as one of the key signatures of strong electronic correlations. Here we use the dynamical mean field theory and its cluster extensions, as well as the finite-temperature Lanczos method to explore the influence of lattice frustration on the thermodynamic and transport properties of the Hubbard model at high temperatures. We consider the triangular and the square lattices at half-filling and at 15% hole doping. We find that for $T \gtrsim 1.5t$ the self-energy becomes practically local, while the finite-size effects become small at lattice size 4×4 for both lattice types and doping levels. The vertex corrections to optical conductivity, which are significant on the square lattice even at high temperatures, contribute less on the triangular lattice. We find approximately linear temperature dependence of dc resistivity in doped Mott insulator for both types of lattices.

DOI: [10.1103/PhysRevB.102.115142](https://doi.org/10.1103/PhysRevB.102.115142)**I. INTRODUCTION**

Strong correlation effects in the proximity of the Mott metal-insulator transition are among the most studied problems in modern condensed matter physics. At low temperatures, material-specific details play a role, and competing mechanisms can lead to various types of magnetic and charge density wave order, or superconductivity [1–5]. At higher temperatures, physical properties become more universal, often featuring peculiarly high and linear-in-temperature resistivity (the bad-metal regime) [6–12] and gradual metal-insulator crossover obeying typical quantum critical scaling laws [13–17].

There are a number of theoretical studies of transport in the high- T regime based on numerical solutions of the Hubbard model [10,12,13,18,19], high- T expansion [20], and field theory [21–23]. Finding numerically precise results is particularly timely having in mind a very recent laboratory realization of the Hubbard model using ultracold atoms on the optical lattice [24]. This system enables fine tuning of physical parameters in a system without disorder and other complications of bulk crystals, which enables a direct comparison between theory and experiment. In our previous work (Ref. [25]) we have performed a detailed analysis of single- and two-particle correlation functions and finite-size effects on the square lattice using several complementary state-of-the-art numerical methods, and established that a finite-temperature Lanczos method (FTLM) solution on the 4×4 lattice is nearly exact at high temperatures. The FTLM, which calculates the correlation functions directly on the real-frequency axis, is recognized [25] as the most reliable method for calculating the transport properties of the Hubbard model at high temperatures. The dependence of charge transport and

thermodynamics on the lattice geometry has not been examined in Ref. [25] and it is the subject of this work.

Numerical methods that we use are (cluster) dynamical mean field theory (DMFT) and FTLM. The DMFT treats an embedded cluster in a self-consistently determined environment [26]. Such a method captures long-distance quantum fluctuations, but only local (in single-site DMFT), or short-range correlations (in cluster DMFT) [27]. The results are expected to converge faster with the size of the cluster than in the FTLM, which treats a finite cluster with periodic boundary conditions [28]. FTLM suffers from the finite-size effects in propagators as well as in correlations. The conductivity calculation in DMFT is, however, restricted just to the bubble diagram, while neglecting the vertex corrections. Approximate calculation of vertex corrections is presented in few recent works [29–34]. This shortcoming of DMFT is overcome in FTLM where one calculates directly the current-current correlation function which includes all contributions to the conductivity. Also, the FTLM calculates conductivity directly on the real-frequency axis, thus eliminating the need for analytical continuation from the Matsubara axis which can, otherwise, lead to unreliable results (see Supplemental Material of Ref. [25]). Both DMFT and FTLM methods are expected to work better at high temperatures [35] when single- and two-particle correlations become more local, and finite-size effects less pronounced. Earlier work has shown that the single-particle nonlocal correlations become small for $T \gtrsim t$ for both the triangular and the square lattices [25,36,37].

In this paper we calculate the kinetic and potential energy, specific heat, charge susceptibility, optical and dc conductivity in the Hubbard model on a triangular lattice and make a comparison with the square-lattice results. We consider strongly correlated regime at half-filling and at 15% hole doping. In

agreement with the expectations, we find that at high temperatures, $T \gtrsim 1.5t$, the nonlocal correlations become negligible and the results for thermodynamic quantities obtained with different methods coincide, regardless of the lattice type and doping. At intermediate temperatures, $0.5t \lesssim T \lesssim 1.5t$, the difference between DMFT and FTLM remains rather small. Interestingly, we do not find that the thermodynamic quantities are more affected by nonlocal correlations on the square lattice in this temperature range, although the self-energy becomes more local on the triangular lattice due to the magnetic frustration. On the other hand, the vertex corrections to optical conductivity remain important even at high temperatures for both lattice types, but we find that they are substantially smaller in the case of a triangular lattice. For the doped triangular and square lattice the temperature dependence of resistivity is approximately linear for temperatures where the finite-size effects become negligible and where the FTLM solution is close to exact.

The paper is organized as follows. In Sec. II we briefly describe different methods for solving the Hubbard model. Thermodynamic and charge transport results are shown in Sec. III, and conclusions in Sec. IV. The Appendix contains a detailed comparison of the DMFT optical conductivity obtained with different impurity solvers, a brief discussion of the finite-size effects at low temperatures, and an illustration of the density of states in different transport regimes.

II. MODEL AND METHODS

We consider the Hubbard model given by the Hamiltonian

$$H = -t \sum_{\langle i,j \rangle, \sigma} c_{i\sigma}^\dagger c_{j\sigma} + U \sum_i n_{i\uparrow} n_{i\downarrow} - \mu \sum_{i\sigma} n_{i\sigma}, \quad (1)$$

where t is the hopping between the nearest neighbors on either triangular or square lattice. $c_{i\sigma}^\dagger$ and $c_{i\sigma}$ are the creation and annihilation operators, U is the onsite repulsion, $n_{i\sigma}$ is the occupation number operator, and μ is the chemical potential. We set $U = 10t$, $t = 1$, lattice constant $a = 1$, $e = \hbar = k_B = 1$ and consider the paramagnetic solution for $p = 1 - n = 1 - \sum_{\sigma} n_{\sigma} = 0.15$ hole doping and at half-filling.

We use the FTLM and DMFT with its cluster extensions to solve the Hamiltonian. FTLM is a method based on the exact diagonalization of small clusters (4×4 in this work). It employs the Lanczos procedure to obtain approximate eigenstates and uses sampling over random starting vectors to calculate the finite-temperature properties from the standard expectation values [28]. To reduce the finite-size effects, we further employ averaging over twisted boundary conditions.

The (cluster) DMFT equations reduce to solving a (cluster) impurity problem in a self-consistently determined effective medium. We consider the single-site DMFT, as well as two implementations of cluster DMFT: cellular DMFT (CDMFT) [38,39] and dynamical cluster approximation (DCA) [27]. In DMFT the density of states is the only lattice-specific quantity that enters into the equations. In CDMFT we construct the supercells in the real space and the self-energy obtains short-ranged nonlocal components within the supercell. In DCA we divide the Brillouin zone into several patches and the number of independent components of the self-energy equals the number of inequivalent patches. The DCA results on 4×4 and

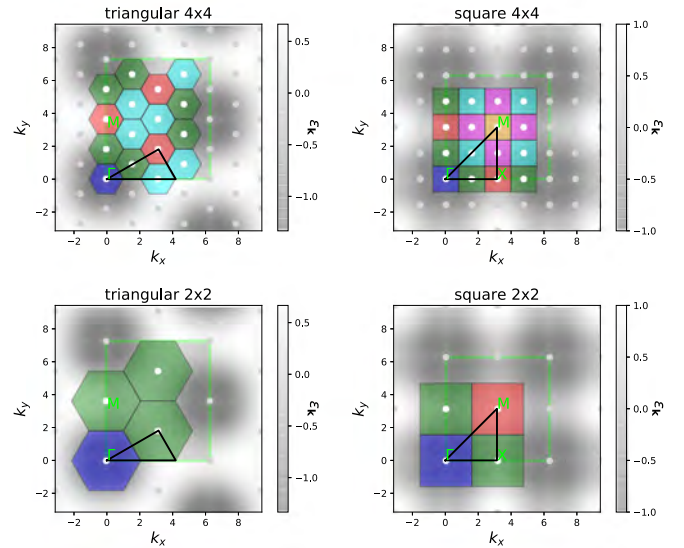


FIG. 1. DCA patches in the Brillouin zone. The irreducible Brillouin zone is marked by the black triangle. The dispersion relation is shown in gray shading. Note the position of the Γ point in the center of the first Brillouin zone which is not marked in this figure.

2×2 clusters are obtained by patching the Brillouin zone in a way that obeys the symmetry of the lattice, as shown in Fig. 1. As the impurity solver we use the continuous-time interaction expansion (CTINT) quantum Monte Carlo (QMC) algorithm [40,41]. In the single-site DMFT we also use the numerical renormalization group (NRG) impurity solver [42–45].

The (cluster) DMFT with QMC impurity solver (DMFT-QMC) gives the correlation functions on the imaginary (Matsubara) frequency axis, from which static quantities can be easily evaluated. The kinetic energy per lattice site is equal to

$$E_{\text{kin}} = \frac{1}{N} \sum_{\mathbf{k}} \varepsilon_{\mathbf{k}} n_{\mathbf{k}\sigma} = \frac{2}{N} \sum_{\mathbf{k}} \varepsilon_{\mathbf{k}} G_{\mathbf{k}}(\tau = 0^-), \quad (2)$$

where for the triangular lattice $\varepsilon_{\mathbf{k}} = -2t[\cos k_x + 2 \cos(\frac{1}{2}k_x) \cos(\frac{\sqrt{3}}{2}k_y)]$ and for the square lattice $\varepsilon_{\mathbf{k}} = -2t(\cos k_x + \cos k_y)$ (gray shading in Fig. 1). The noninteracting band for the triangular lattice goes from $-6t$ to $3t$ with the van Hove singularity at $\varepsilon = t$. The potential energy is equal to

$$E_{\text{pot}} = Ud = \frac{1}{N} T \sum_{\mathbf{k}, i\omega_n} e^{i\omega_n 0^+} G_{\mathbf{k}}(i\omega_n) \Sigma_{\mathbf{k}}(i\omega_n), \quad (3)$$

where $d = \langle n_{i\uparrow} n_{i\downarrow} \rangle$ is the average double occupation. In DCA the cluster double occupation is the same as on the lattice, and we used the direct calculation of d in the cluster solver to cross check the consistency and precision of the numerical data. In CDMFT we calculated E_{pot} from periodized quantities G and Σ , where the periodization is performed on the self-energy and then the lattice Green's function is calculated from it. The total energy is $E_{\text{tot}} = E_{\text{kin}} + E_{\text{pot}}$. The specific heat $C = dE_{\text{tot}}/dT|_n$ is obtained by interpolating $E_{\text{tot}}(T)$ and then taking a derivative with respect to temperature. C is shown only in the DMFT solution where we had enough points

at low temperatures. The charge susceptibility $\chi_c = \partial n / \partial \mu$ is obtained from a finite difference using two independent calculations with μ that differs by a small shift $\delta\mu = 0.1t$. In the FTLM, C and χ_c are calculated without taking the explicit numerical derivative since the derivation can be done analytically from a definition of the expectation values,

$$\begin{aligned} C &= C_\mu - \frac{T\zeta^2}{\chi_c} \\ &= \frac{1}{N} \frac{1}{T^2} \left[\langle H^2 \rangle - \langle H \rangle^2 - \frac{(\langle HN_e \rangle - \langle H \rangle \langle N_e \rangle)^2}{\langle N_e^2 \rangle - \langle N_e \rangle^2} \right], \end{aligned} \quad (4)$$

which is directly calculated in FTLM. Here, $C_\mu = \frac{1}{N} \frac{1}{T^2} [\langle (H - \mu N_e)^2 \rangle - \langle H - \mu N_e \rangle^2]$, $\zeta = \frac{1}{N^2} \frac{1}{T^2} [\langle (H - \mu N_e) N_e \rangle - \langle H - \mu N_e \rangle \langle N_e \rangle]$, $\chi_c = \frac{1}{N} \frac{1}{T} (\langle N_e^2 \rangle - \langle N_e \rangle^2)$, and $N_e = \sum_{i\sigma} n_{i\sigma}$ is the operator for the total number of electrons on the lattice.

We calculate the conductivity using DMFT and FTLM. Within the DMFT the optical conductivity is calculated from the bubble diagram as

$$\begin{aligned} \sigma(\omega) &= \sigma_0 \iint d\varepsilon d\nu X(\varepsilon) A(\varepsilon, \nu) A(\varepsilon, \nu + \omega) \\ &\quad \times \frac{f(\nu) - f(\nu + \omega)}{\omega}, \end{aligned} \quad (5)$$

where $X(\varepsilon) = \frac{1}{N} \sum_{\mathbf{k}} \left(\frac{\partial \varepsilon_{\mathbf{k}}}{\partial k_x} \right)^2 \delta(\varepsilon - \varepsilon_{\mathbf{k}})$ is the transport function, $A(\varepsilon, \nu) = -\frac{1}{\pi} \text{Im}[\nu + \mu - \varepsilon - \Sigma(\nu)]^{-1}$, and f is the Fermi function. For the square lattice $\sigma_0 = 2\pi$ and for triangular $\sigma_0 = 4\pi/\sqrt{3}$. For the calculation of conductivity in DMFT-QMC we need the real-frequency self-energy $\Sigma(\omega)$, which we obtain by Padé analytical continuation of the DMFT-QMC $\Sigma(i\omega_n)$. In the DMFT with NRG impurity solver (DMFT-NRG) we obtain the correlation functions directly on the real-frequency axis, but this method involves certain numerical approximations (see Appendix A).

In order to put into perspective the interaction strength $U = 10t$ and the temperature range that we consider, in Fig. 2 we sketch the paramagnetic (cluster) DMFT phase diagram for the triangular and square lattices at half-filling adapted from Refs. [46,47] (see also Refs. [36,37,48–54]). In the DMFT solution (blue lines) the critical interaction for the Mott metal-insulator transition (MIT) is $U_c \sim 2.5D$, where the half-bandwidth D is $4.5t$ and $4t$ for the triangular and the square lattice, respectively. The phase diagram features the region of coexistence of metallic and insulating solution below the critical end point at $T_c \approx 0.1t$. In this work we consider the temperatures above T_c . We set $U = 10t$, which is near U_c for the MIT in DMFT, but well within the Mott insulating part of the cluster DMFT and FTLM phase diagram.

III. RESULTS

We will first present the results for the thermodynamic properties in order to precisely identify the temperature range where the nonlocal correlations and finite-size effects are small or even negligible. In addition, from the thermodynamic quantities, e.g., from the specific heat, we can clearly identify the coherence temperature above which we observe the bad-metal transport regime. We then proceed with the key result

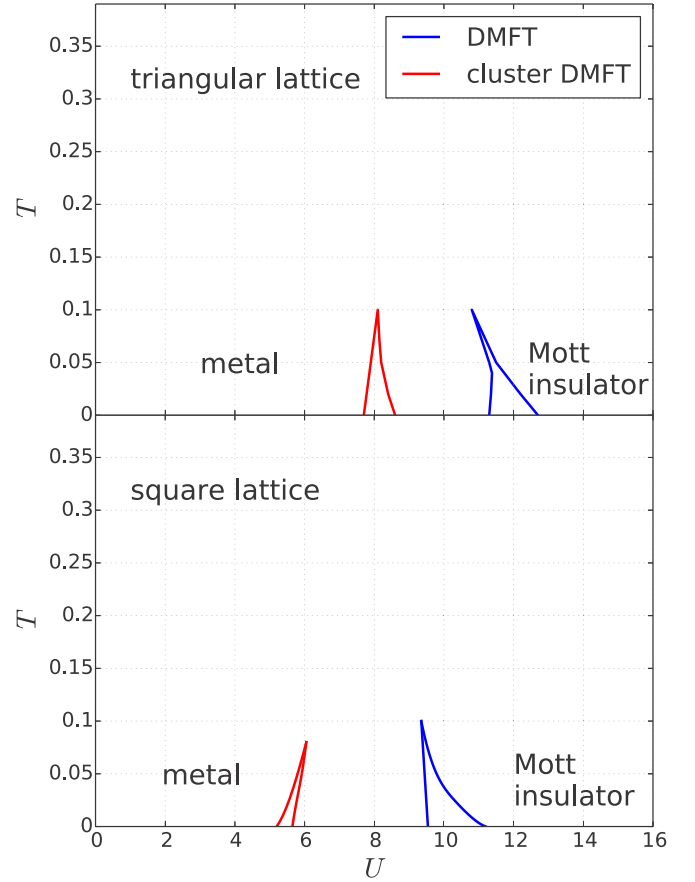


FIG. 2. Sketch of the paramagnetic phase diagram at half-filling, adapted from Refs. [46,47]. There is a region of the coexistence of metallic and insulating solution below the critical end point at T_c . The critical interaction is smaller in the cluster DMFT solution. Above T_c there is a gradual crossover from a metal to the Mott insulator. In this work we consider $T > T_c$ and $U = 10t$.

of this work by showing the contribution of vertex corrections to the resistivity and optical conductivity.

Before going into this detailed analysis, and in order to obtain a quick insight into the strength of nonlocal correlations, we compare in Fig. 3 the self-energy components in the cluster DMFT solution at two representative temperatures. We show the imaginary part of the DCA 4×4 self-energy at different patches of the Brillouin zone according to the color scheme of Fig. 1. The statistical error bar of the $\text{Im} \Sigma$ results presented in Fig. 3 we estimate by looking at the difference in $\text{Im} \Sigma$ between the last two iterations of the cluster DMFT loop. We monitor all \mathbf{K} points and the lowest three Matsubara frequencies. At lower temperature (bottom row), this difference is smaller than 0.05 (0.01) for the square (triangular) lattice, respectively. At higher temperature (upper row), these values are both 10 times lower and the error bar is much smaller than the size of the symbol. At $T = 0.4t$ the differences in the self-energy components are more pronounced on the square than on the triangular lattice, which goes along the general expectations that the larger connectivity ($z = 6$) and the frustrated magnetic fluctuations lead to the more local self-energy. At $T \sim 1.5t$ all the components of the self-energy almost coincide for both lattices. We note that for the triangular

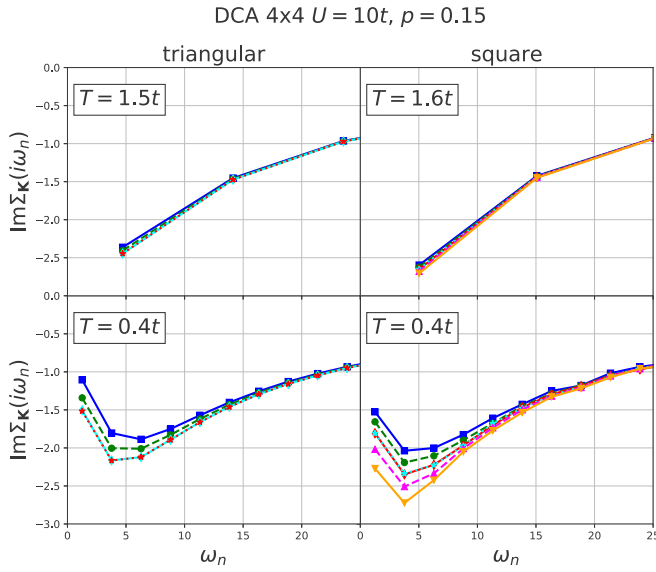


FIG. 3. Imaginary part of the self-energy at the Matsubara frequencies at different patches of the Brillouin zone for several temperatures for $p = 0.15$ hole doping. The position of the patches is indicated by the same colors as in Fig. 1. The solid lines are guide to the eye.

lattice the components of the self-energy marked by red and cyan colors are similar, but they do not coincide completely. There are four independent patches in this case. For the square lattice the red and cyan components of the self-energy are very similar, while we have six independent patches.

A. Thermodynamics

1. $p = 0.15$

We first show the results for hole doping $p = 0.15$. The results for the triangular lattice are shown in the left column of Fig. 4, and the results for the square lattice in the right column. Different rows correspond to the kinetic energy per lattice site E_{kin} , potential energy E_{pot} , total energy E_{tot} , specific heat $C = dE_{\text{tot}}/dT|_n$, and charge susceptibility χ_c . The DMFT results are shown with blue solid lines and FTLM with red dashed lines. The red circles correspond to DCA 4×4 , light green to DCA 2×2 , green to CDMFT 2×2 , and magenta to the CDMFT 2×1 result.

The FTLM results are shown down to $T = 0.2t$. The FTLM finite-size effects in thermodynamic quantities are small for $T \gtrsim 0.2t$ (see Appendix B). The DMFT results are shown for $T \gtrsim 0.05t$ and cluster DMFT for $T \gtrsim 0.2t$. Overall, the (cluster) DMFT and FTLM results for 15% doping look rather similar. The kinetic and potential energy do not differ much on the scale of the plots, and the specific heat looks similar.

The Fermi-liquid region, with $C \propto T$, is restricted to very low temperatures. For the triangular lattice we find a distinct maximum in $C(T)$ at $T \approx 0.4t$ in FTLM, and at $T \approx 0.3t$ in DMFT. This maximum is a signature of the coherence-incoherence crossover, when the quasiparticle peak in the density of states gradually diminishes and the bad-metal regime starts. The increase in the specific heat for $T \gtrsim 2t$ is

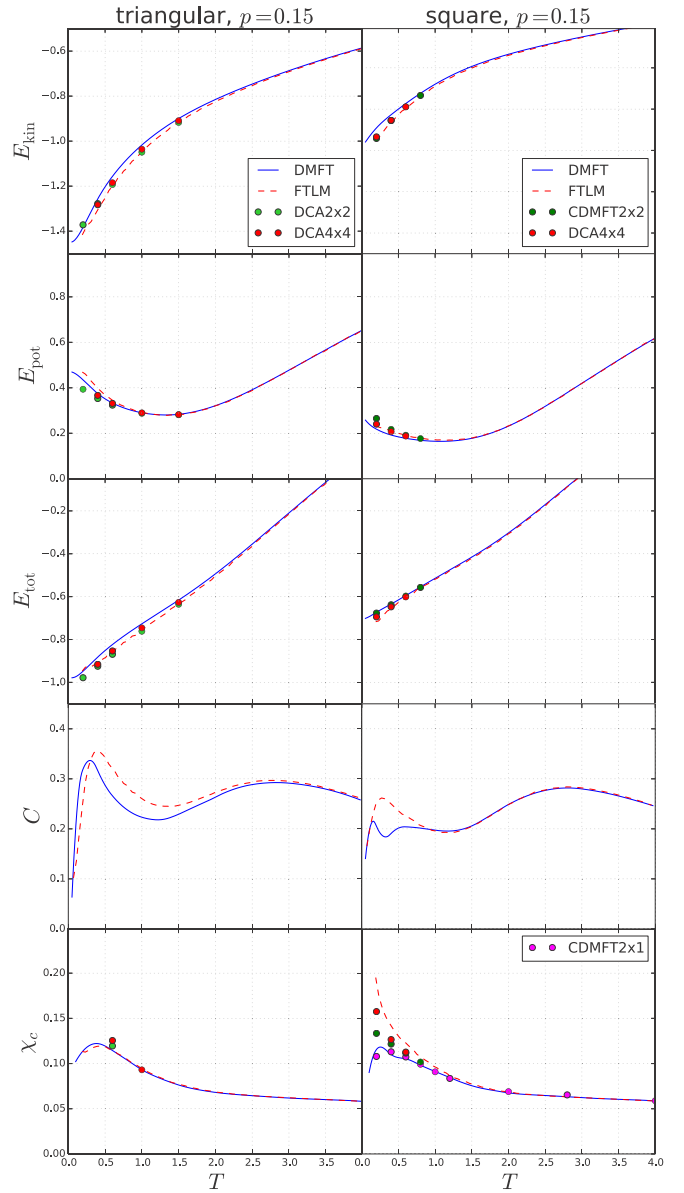


FIG. 4. Kinetic, potential, total energy, specific heat, and charge susceptibility as a function of temperature for the triangular and the square lattice at 15% doping.

caused by the charge excitations to the Hubbard band. The specific heat of the square lattice looks qualitatively the same. [A very small dip in the DMFT specific heat near $T = 0.4t$ for the square lattice may be an artifact of the numerics, where C is calculated by taking a derivative with respect to temperature of the interpolated $E_{\text{tot}}(T)$.] We note that the specific heat, shown here for the fixed particle density, is slightly different than the one for the fixed chemical potential $C_\mu = dE_{\text{tot}}/dT|_\mu$, as in Refs. [28,51,55].

For the square lattice all thermodynamic quantities obtained with different methods practically coincide for $T \gtrsim t$. This means that both the nonlocal correlations and the finite-size effects have negligible effect on thermodynamic quantities. For $T \lesssim t$ the DMFT and FTLM results start to differ. Interestingly, for the triangular lattice there is a small

difference in the DMFT and FTLM kinetic energy up to higher temperatures $T \sim 1.5t$. The FTLM and DCA 4×4 results coincide for $T \gtrsim t$, implying the absence of finite-size effects in the kinetic energy for both lattice types. We also note that the agreement of the CDMFT and DMFT solutions for the total energy on the square lattice at low temperatures is coincidental, as a result of a cancellation of differences in E_{kin} and E_{pot} .

The intersite correlations in the square lattice lead to an increase in the charge susceptibility at low temperatures (bottom panel in Fig. 4). Here, the FTLM and DCA 4×4 results are in rather good agreement. For the triangular lattice we found a sudden increase of χ_c at low temperatures in the DCA results (see Appendix B) but not in FTLM. These DCA points are not shown in Fig. 4 since we believe that they are an artifact of the particular choice of patching of the Brillouin zone. In order to keep the lattice symmetry, we had only four (in DCA 4×4) and two (in DCA 2×2) independent patches in the Brillouin zone for triangular lattice (Fig. 1). The average over twisted boundary conditions in FTLM reduces the finite-size error (see Appendix B), and hence we believe that the FTLM result for χ_c is correct down to $T = 0.2t$. We note that an increase of χ_c cannot be inferred from the ladder dual-fermion extension of DMFT [37] either. Still, further work would be needed to precisely resolve the low- T behavior of charge susceptibility for the triangular lattice.

2. $p = 0$

We now focus on thermodynamic quantities at half-filling (Fig. 5). In this case, the results can strongly depend on the method, especially since we have set the interaction to $U = 10t$, which is near the critical value for the Mott MIT in DMFT, while well within the insulating phase in the cluster DMFT and FTLM. The results with different methods almost coincide for $T \gtrsim 2t$ and are very similar down to $T \sim t$. The difference between the cluster DMFT and FTLM at half-filling is small, which means that the finite-size effects are small down to the lowest shown temperature $T = 0.2t$. Therefore, the substantial difference between the FTLM and single-site DMFT solutions at half-filling is mostly due to the absence of nonlocal correlations in DMFT.

The specific heat at half-filling is strongly affected by nonlocal correlations and lattice frustration. For triangular lattice the low-temperature maximum in $C(T)$ has different origin in the DMFT and FTLM solutions. The maximum in the FTLM is due to the low-energy spin excitations in frustrated triangular lattice, while in DMFT it is associated with the narrow quasiparticle peak since the DMFT solution becomes metallic as $T \rightarrow 0$. Our DMFT result agrees very well with the early work from Ref. [36] for $T \gtrsim t$. At lower temperatures there is some numerical discrepancy which we ascribe to the error due to the imaginary-time discretization in the Hirsch-Fye method used in that reference. For the square lattice the DMFT and FTLM solutions are both insulating. The maximum in the FTLM $C(T)$ is due to the spin excitations at energies $\sim 4t^2/U = 0.4t$, and it is absent in the paramagnetic DMFT solution which does not include dynamic nonlocal correlations. The increase in $C(T)$ at higher temperatures is due to the charge excitations to the upper Hubbard band.

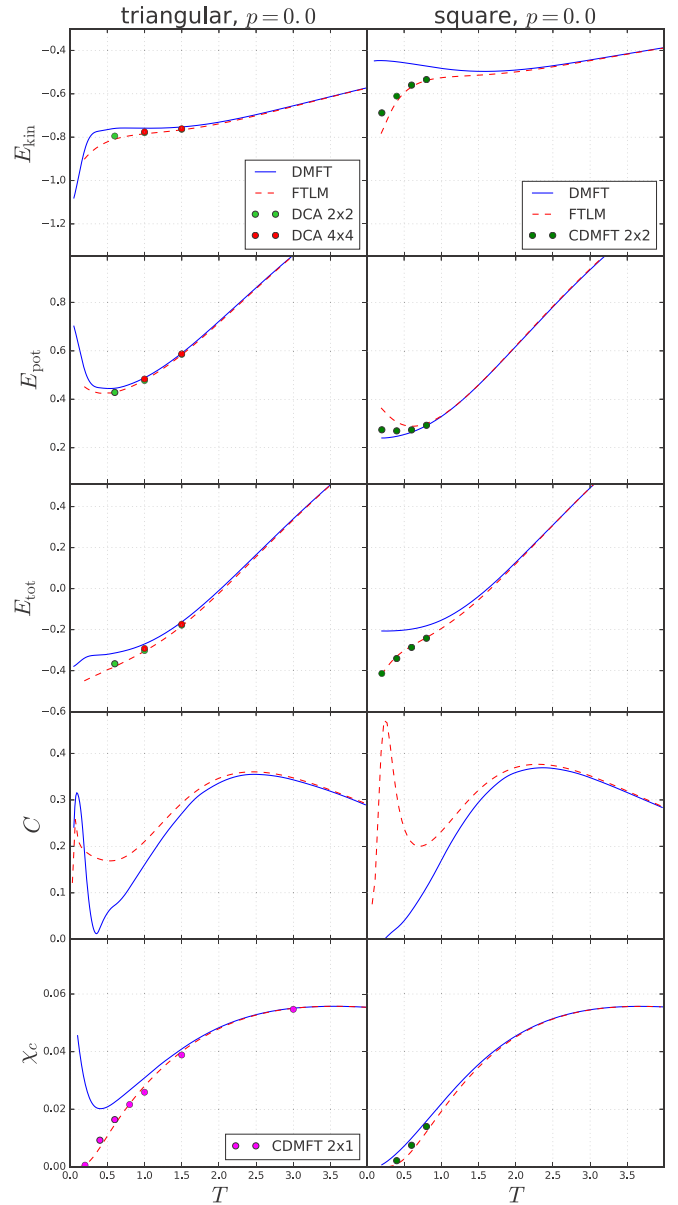


FIG. 5. Kinetic, potential, total energy, specific heat, and charge compressibility as a function of temperature for the triangular and the square lattice at half-filling.

B. Charge transport

The analysis of thermodynamic quantities has shown that the FTLM results for static quantities are close to exact down to $T \sim 0.5t$ or even $0.2t$. For charge transport we show the results for higher temperatures $T \gtrsim t$ since the finite-size effects are more pronounced in the current-current correlation function at lower temperatures.

An indication of the finite-size effects in optical conductivity can be obtained from the optical sum rule

$$\int_0^\infty d\omega \sigma(\omega) = \frac{\pi}{4V_{uc}} (-E_{\text{kin}}), \quad (6)$$

where V_{uc} is equal to 1 and $\frac{\sqrt{3}}{2}$ for the square and triangular lattice, respectively. The deviation from the sum rule in FTLM

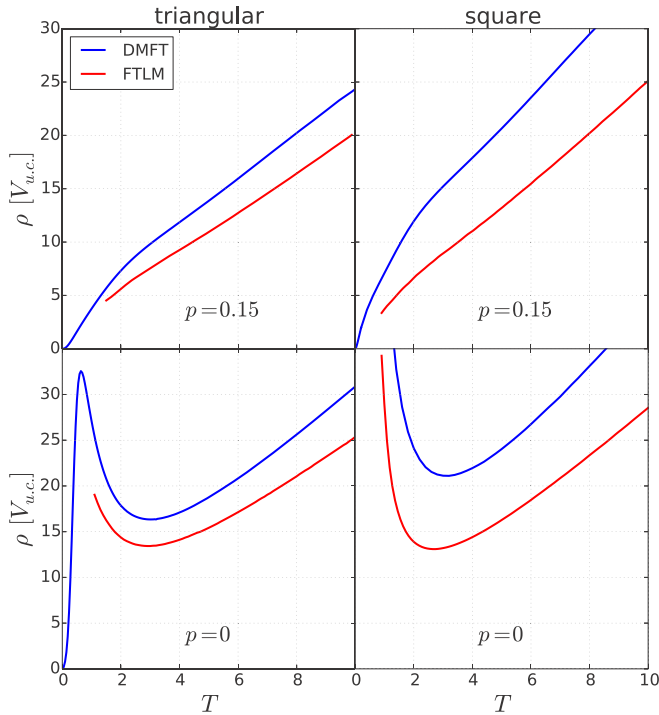
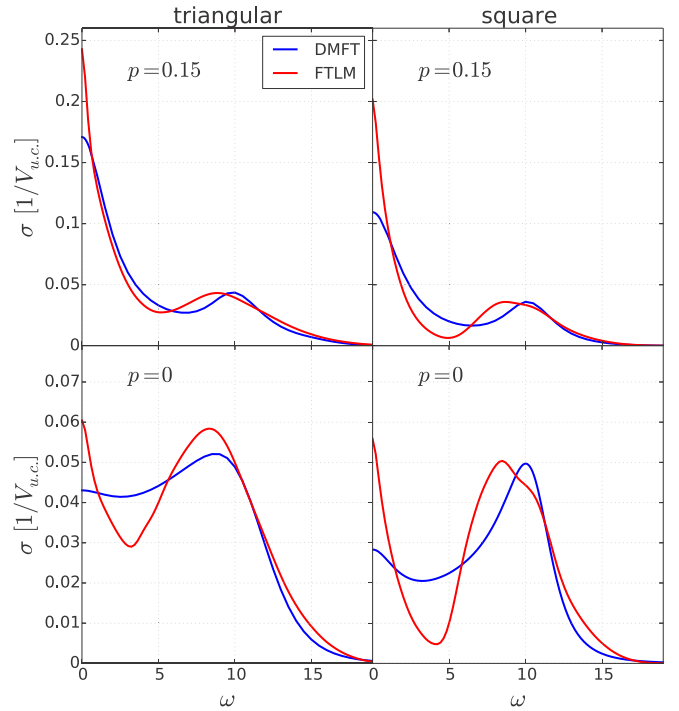


FIG. 6. Resistivity as a function of temperature.

can be ascribed to the finite charge stiffness and δ function at zero frequency in optical conductivity [28]. The FTLM result for dc resistivity, shown by the red lines in Fig. 6, corresponds the temperature range where the weight of the δ -function peak at zero frequency (charge stiffness) [28] is smaller than 0.5% of the total spectral weight. The other finite-size effects are small and the FTLM resistivity is expected to be close to the exact solution of the Hubbard model. The remaining uncertainty, due to the frequency broadening, is estimated to be below 10% (see Supplemental Material in Ref. [25]). Smallness of the finite-size effects for the square lattice at $T \gtrsim t$ was also confirmed from the current-current correlation function calculated on the 4×4 and 8×8 lattices using CTINT QMC (see Ref. [25]). For doped triangular lattice we show the conductivity data for $T \gtrsim 1.5t$ since below this temperature the weight of the charge stiffness δ function is larger than 0.5% of the total weight, which indicates larger finite-size effects.

The DMFT resistivity is shown in Fig. 6 by the blue lines. It is obtained using the NRG impurity solver. Numerical error of the DMFT-NRG method is small, as we confirmed by a comparison with the DMFT-QMC calculation followed by the Padé analytical continuation (see Appendix A). We note that we do not show the conductivity data in the DCA since in this approximation we cannot reliably calculate the conductivity beyond the bubble term. At high temperatures the bubble-term contribution in cluster DMFT does not differ from the one in single-site DMFT since the self-energy becomes local [25].

Since the FTLM resistivity in Fig. 6 is shown only for temperatures when both the nonlocal correlations and the finite-size effects are small, the difference between the DMFT and FTLM resistivity is due to the vertex corrections. Their contribution corresponds to the connected part of the current-current correlation function whereas the DMFT conductivity

FIG. 7. Optical conductivity at $T = 1.4$.

is given by the bubble diagram. A detailed analysis of vertex corrections for the square lattice is given in our previous work (Ref. [25]). Here, our main focus is on the comparison of the importance of vertex corrections for different lattices: the numerical results show that the vertex corrections to conductivity are less important in the case of the triangular lattice.

In the doped case, the FTLM solution gives the resistivity which is approximately linear in the entire temperature range shown in Fig. 6. This bad-metal linear- T temperature dependence is one of the key signatures of strong electronic correlations. The resistivity is here above the Mott-Ioffe-Regel limit which corresponds to the scattering length one lattice spacing within the Boltzmann theory. The Mott-Ioffe-Regel limit can be estimated as [6] $\rho_{\text{MIR}} \sim \sqrt{2\pi} \approx 2.5$.

At half-filling and low temperatures the result qualitatively depends on the applied method. For the half-filled triangular lattice at $U = 10t$ the DMFT solution gives a metal, whereas the nonlocal correlations lead to the Mott insulating state. Still, similar as for thermodynamic quantities, the numerically cheap DMFT gives an insulatinglike behavior and a rather good approximation down to $T \sim 0.5t$.

The optical conductivity, shown in Fig. 7 for $T = 1.4t$, provides further insight into the dependence of the vertex correction on the lattice geometry. The DMFT-QMC conductivity is calculated using Eq. (5) with $\Sigma(\omega)$ obtained by the Padé analytical continuation of $\Sigma(i\omega_n)$ (see Appendix A for a comparison with DMFT-NRG). In the DMFT solution, the Hubbard peak is determined by the single-particle processes and it is centered precisely at $\omega = U$. The vertex corrections in FTLM shift the position of the Hubbard peak to lower frequencies. The total spectral weight is the same in FTLM and DMFT solution since it obeys the sum rule of Eq. (6), while the kinetic energies coincide. The Ward identity for

vertex corrections [25,31]

$$\Lambda^{\text{conn}}(i\nu = 0) = -2T \frac{1}{N} \sum_{\mathbf{k}} v_{\mathbf{k}} \sum_{i\omega_n} G_{\mathbf{k}}^2(i\omega_n) \partial_{k_x} \Sigma_{\mathbf{k}}(i\omega_n) \quad (7)$$

also implies that the vertex corrections do not affect the sum rule if the self-energy is local. Here, $\Lambda(i\nu)$ is the current-current correlation function and $\Lambda(i\nu = 0) = \frac{1}{\pi} \int d\omega \sigma(\omega)$.

The results clearly show the much stronger effect of vertex corrections on the square lattice on all energy scales. In addition to a very different $\omega \rightarrow 0$ (dc) limit, we observe the more significant reduction of the Drude-like peak width and a larger shift of the Hubbard peak on the square lattice, with a more pronounced suppression of the optical weight at intermediate frequencies. We note that a broad low-frequency peak in conductivity is due to incoherent short-lived excitations characteristic of the bad-metal regime. The structure of the density of states in different transport regimes is discussed in Appendix C.

IV. CONCLUSION

In summary, we have performed a detailed comparison of the thermodynamic and charge transport properties of the Hubbard model on a triangular and square lattice. We identified the temperatures when the finite-size effects become negligible and the FTLM results on the 4×4 cluster are close to exact. In the doped case, for both lattice types, the resistivity is approximately linear in temperature for $T \gtrsim 1.5t$. In particular, we found that the contribution of vertex corrections to the optical and dc conductivity is smaller in the case of a triangular lattice, where it leads to $\sim 20\%$ decrease in dc resistivity as compared to the bubble term. The vertex corrections also leave a fingerprint on the position of the Hubbard peak in the optical conductivity, which is shifted from $\omega = U$ to slightly lower frequencies.

On general grounds, higher connectivity and/or magnetic frustration should lead to more local self-energy and smaller vertex corrections in the case of triangular lattice, as it is observed. However, the precise role of these physical mechanisms and possible other factors remains to be established. Another important open question is to find an efficient approximate scheme to evaluate the vertex corrections, which would be sufficiently numerically cheap to enable calculations of transport at lower temperatures and in real materials. These issues are to be addressed in the future, but we are now better positioned as we have established reliable results that can serve as a reference point.

With this work we also made a benchmark of several state-of-the-art numerical methods for solving the Hubbard model and calculating the conductivity at high temperatures. This may be a useful reference for calculations of conductivity using a recent approach that calculates perturbatively the correlation functions directly on the real-frequency axis [56–59], thus eliminating a need for analytical continuation, while going beyond the calculation on the 4×4 cluster.

ACKNOWLEDGMENTS

J.M. acknowledges useful discussions with F. Krien. A.V., J.V., and D.T. acknowledge funding provided by the Institute of Physics Belgrade, through the grant by

the Ministry of Education, Science, and Technological Development of the Republic of Serbia. J.K., R.Ž., and J.M. are supported by the Slovenian Research Agency (ARRS) under Programs No. P1-0044, No. J1-1696, and No. J1-2458. Numerical simulations were performed on the PARADOX supercomputing facility at the Scientific Computing Laboratory of the Institute of Physics Belgrade. The CTINT algorithm has been implemented using the TRIQS toolbox [60].

APPENDIX A: COMPARISON OF THE DMFT-NRG AND DMFT-QMC CONDUCTIVITY

Here, we compare the DMFT results for the dc resistivity and optical conductivity obtained with two different impurity solvers. The optical conductivity $\sigma(\omega)$ is calculated according to Eq. (5). The dc resistivity is equal to $\rho = \sigma^{-1}(\omega \rightarrow 0)$.

Within DMFT-NRG solver the self-energy is obtained directly on the real-frequency axis. There are three sources of errors in this approach: discretization errors, truncation errors, and (over)broadening errors. The method is based on the discretization of the continuum of states in the bath; the ensuing discretization errors can be reduced by performing the calculation for several different discretization meshes with interleaved points and averaging these results. It has been shown [45] that in the absence of interactions, the discretization error can be fully eliminated in a systematic manner. For an interacting problem, the cancellation of artifacts is only approximate, but typically very good, so that this is a minor source of errors. The truncation errors arise because in the iterative diagonalization one discards high-energy states after each set of diagonalizations. For static quantities this error is negligible, but it affects the dynamical (frequency-resolved) quantities because they are calculated from contributions linking kept and discarded states [61–63]. Finally, the raw spectral function in the form of δ peaks needs to be broadened in order to obtain the smooth spectrum. If the results are overbroadened, this can result in a severe overestimation of resistivity, and this is typically the main source of error in the NRG for this quantity. Fortunately, the resistivity is calculated as an integrated quantity, thus, the broadening kernel width can be systematically reduced [20,64]. The lower limit is set by the possible convergence issues in the DMFT self-consistency cycle due to jagged aspect of all quantities, where the actual limit value is problem dependent. In the NRG results reported in this work, it was possible to use very narrow broadening kernel. By studying the dependence of the $\rho(T)$ curves on the kernel width, we estimate that the presented results have at most a few percent error even at the highest temperatures considered.

The DMFT-QMC gives the self-energy $\Sigma(i\omega_n)$ at the Matsubara frequencies and the analytical continuation is necessary to obtain $\Sigma(\omega)$. The statistical error in QMC makes the analytical continuation particularly challenging. However, at high temperatures the CTINT QMC algorithm is very efficient. Running a single DMFT iteration for 10 minutes on 128 cores and using 20 or more iterations, we obtained the self-energies with the statistical error $|\delta \Sigma(i\omega_0)| \approx 5 \times 10^{-4}$ and $|\delta G(i\omega_0)| \approx 2 \times 10^{-5}$ at the first Matsubara frequency at $T = t$. Such a small statistical error makes the Padé analytical continuation possible for temperatures $T \lesssim 2t$.

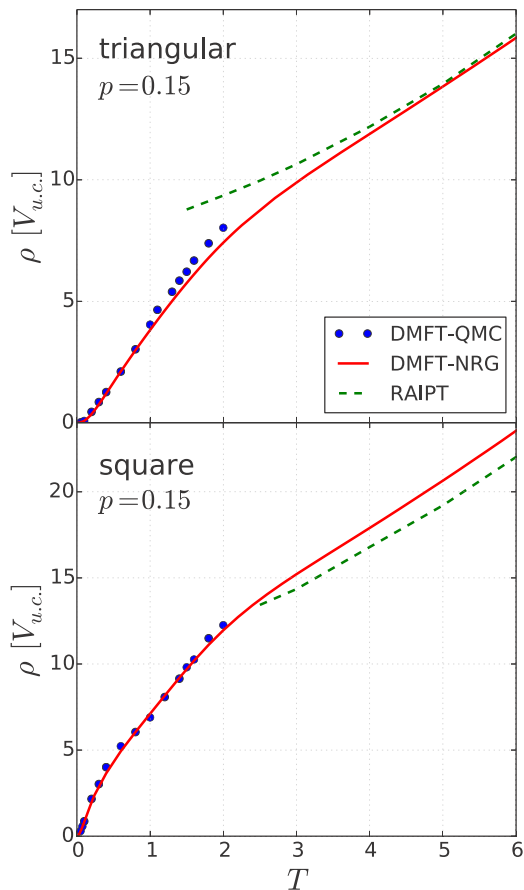


FIG. 8. DMFT-QMC (blue dots) and DMFT-NRG (red lines) resistivity as a function of temperature. The analytical continuation of the self-energy is performed with the Padé method. At high temperatures the DMFT-NRG result agrees rather well with the RAIPT (green dashed lines).

We have checked that Padé continuation gives similar results for $\Sigma(\omega)$ when performed on $\Sigma(i\omega_n)$ taken from last few DMFT iterations. We then used $\Sigma(i\omega_n)$ averaged over the last five iterations to further reduce the noise in $\Sigma(i\omega_n)$, before performing the Padé analytical continuation subsequently used in the calculation of the conductivity. We also obtained $G(\omega)$ directly by the Padé analytical continuation of $G(i\omega_n)$, and checked that the result is consistent with the one calculated as $G(\omega) = \int d\varepsilon \rho_0(\varepsilon)[\omega + \mu - \varepsilon - \Sigma(\omega)]^{-1}$. These cross checks have confirmed that Padé analytical continuation is rather reliable.

Figure 8 shows the temperature dependence of resistivity calculated with the DMFT-NRG (red lines) and DMFT-QMC (blue dots). For the square lattice we find excellent agreement between the two methods. For the triangular lattice we find some discrepancy for $T \sim 1.5t$, which is likely due to the approximations in DMFT-NRG. We also find that the real-axis iterative perturbation theory [65–67] (RAIPT) agrees rather well with the DMFT-NRG solution for $T \gtrsim 2t$.

It is also interesting to note how the lattice geometry can influence the range of the Fermi liquid $\rho \propto T^2$ behavior in the DMFT solution. In the DMFT equations the lattice structure enters only through the noninteracting density of states. We

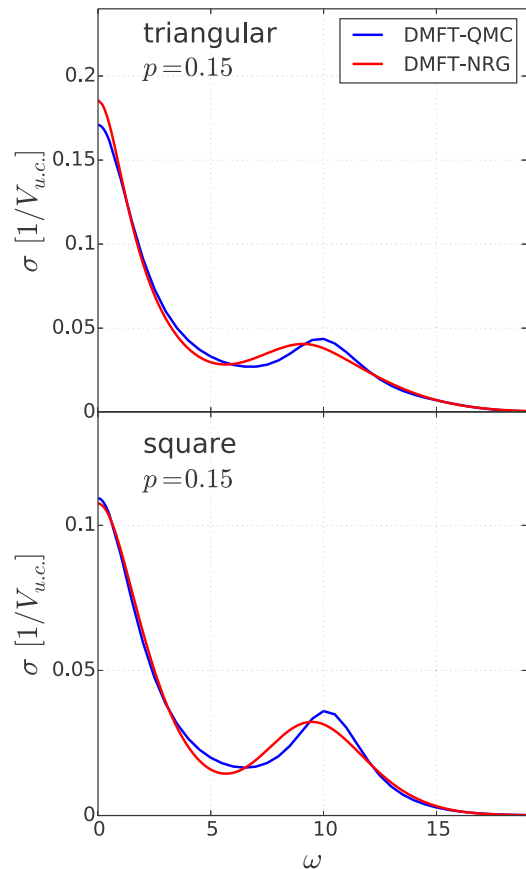


FIG. 9. DMFT-QMC and DMFT-NRG optical conductivity at $T = 1.4t$.

observe $\rho \propto T^2$ behavior up to much lower temperatures on the square lattice. In this case, $\rho \propto T^2$ region is hardly visible on the scale of the plot, while $\rho \propto T^2$ up to $T \sim 0.3t$ on the triangular lattice. This observation is in agreement with the extension of the $C \propto T$ region in $C(T)$, which is restricted to lower temperatures in the case of a square lattice (Fig. 4).

A comparison of the DMFT-NRG (red lines) and DMFT-QMC (blue lines) optical conductivity at $T = 1.4t$ is shown in Fig. 9. The overall agreement is very good. We, however, find a small discrepancy at $\omega \sim 10t$. The DMFT-QMC result has the Hubbard peak in $\sigma(\omega)$ centered exactly at $\omega = U$, whereas it is shifted to slightly lower frequency in the DMFT-NRG solution. This shift is an artifact of numerical approximations in DMFT-NRG. A position of the Hubbard peak at $U = 10t$ is another manifestation of the precision of analytical continuation of the QMC data.

APPENDIX B: FINITE-SIZE EFFECTS IN CHARGE SUSCEPTIBILITY

In Fig. 10 we show the charge susceptibility obtained with different methods. The single-site DMFT result agrees very well with the 4×4 FTLM after averaging over the twisted boundary conditions. We show χ_c averaged over $N_{\text{tbc}} = 1, 4, 16, 64,$ and 128 clusters with different boundary conditions. χ_c obtained with a single setup of boundary conditions deviates at low temperatures from the averaged values. The DCA results for $T \lesssim 0.5t$ are also inconsistent.

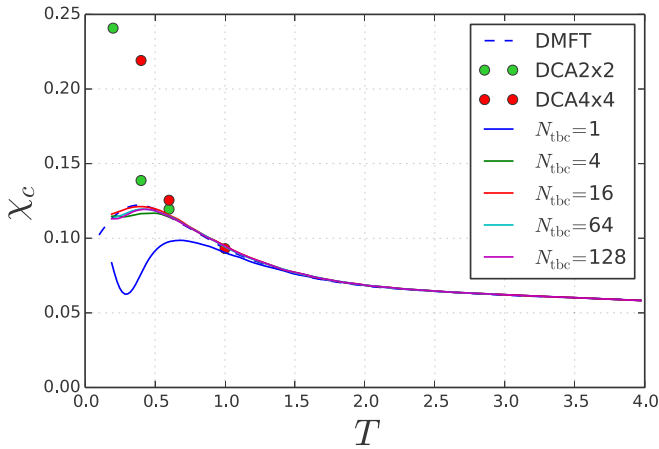


FIG. 10. Charge susceptibility as a function of temperature for the triangular lattice at $p = 0.15$ hole doping.

We believe that this is an artifact of the particular choice of the Brillouin zone patches. In DCA 4×4 and 2×2 we have just four and two independent patches in the Brillouin zone for triangular lattice, respectively.

APPENDIX C: DMFT DENSITY OF STATES

Here, we illustrate the density of states in different transport regimes in the DMFT solution. The results in Fig. 11 are obtained with the QMC solver followed by the Padé analytical continuation. We have checked that the density of states agrees with the DMFT-NRG result.

In the Fermi-liquid regime at low temperatures there is a peak in the density of states around the Fermi level. In the doped case the coherence-decoherence crossover is at temperature $T \sim 0.3$, as we established from the specific-heat data (see Fig. 4) and from the condition that the resistivity reaches the Mott-Ioffe-Regel limit (see Sec. III B). In agreement with earlier work [10,12], we see that at $T \sim 0.3$ there is a peak in the density of states even though long-lived quasiparticles are absent. At even higher temperatures (here shown $T = 1.4$), deeply in the bad-metal regime, the peak at the density of states at the Fermi level is completely washed out.

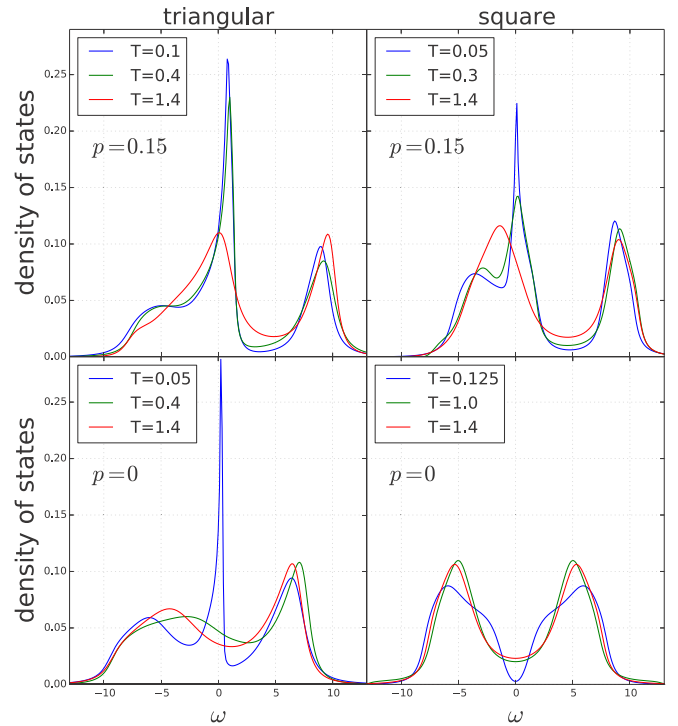


FIG. 11. Density of states in the Fermi liquid at low temperatures and in the bad-metal regime at high temperatures.

At half-filling the result is very sensitive to the exact position of parameters on the U - T phase diagram (see Fig. 2). For the triangular lattice at $U = 10$ the solution is metallic even at low temperature which leads to the formation of narrow quasiparticle peak at the Fermi level. This peak is quickly suppressed by thermal fluctuations which is accompanied by a sudden increase in the resistivity. For the square lattice at $U = 10$ the system is insulating above for $T \gtrsim 0.03$, while the Mott gap gradually gets filled as the temperature increases. We note that the low-temperature peak in optical conductivity in Fig. 7 is not connected to the existence of quasiparticles. It is just a consequence of a finite spectral density at the Fermi level (the absence of an energy gap), as expected in the bad-metal regime.

-
- [1] S. A. Kivelson, I. P. Bindloss, E. Fradkin, V. Oganesyan, J. M. Tranquada, A. Kapitulnik, and C. Howald, *Rev. Mod. Phys.* **75**, 1201 (2003).
 - [2] B. J. Powell and R. H. McKenzie, *Rep. Prog. Phys.* **74**, 056501 (2011).
 - [3] K. Miyagawa, A. Kawamoto, Y. Nakazawa, and K. Kanoda, *Phys. Rev. Lett.* **75**, 1174 (1995).
 - [4] Y. Shimizu, K. Miyagawa, K. Kanoda, M. Maesato, and G. Saito, *Phys. Rev. Lett.* **91**, 107001 (2003).
 - [5] V. Dobrosavljević, N. Trivedi, and J. M. Valles, Jr., *Conductor-Insulator Quantum Phase Transitions* (Oxford University Press, Oxford, 2012).
 - [6] O. Gunnarsson, M. Calandra, and J. E. Han, *Rev. Mod. Phys.* **75**, 1085 (2003).
 - [7] N. E. Hussey, K. Takenaka, and H. Takagi, *Philos. Mag.* **84**, 2847 (2004).
 - [8] M. M. Qazilbash, K. S. Burch, D. Whisler, D. Shrekenhamer, B. G. Chae, H. T. Kim, and D. N. Basov, *Phys. Rev. B* **74**, 205118 (2006).
 - [9] M. M. Qazilbash, J. J. Hamlin, R. E. Baumbach, L. Zhang, D. J. Singh, M. B. Maple, and D. N. Basov, *Nat. Phys.* **5**, 647 (2009).
 - [10] X. Deng, J. Mravlje, R. Žitko, M. Ferrero, G. Kotliar, and A. Georges, *Phys. Rev. Lett.* **110**, 086401 (2013).
 - [11] W. Xu, K. Haule, and G. Kotliar, *Phys. Rev. Lett.* **111**, 036401 (2013).
 - [12] J. Vučković, D. Tanasković, M. J. Rozenberg, and V. Dobrosavljević, *Phys. Rev. Lett.* **114**, 246402 (2015).

- [13] H. Terletska, J. Vučićević, D. Tanasković, and V. Dobrosavljević, *Phys. Rev. Lett.* **107**, 026401 (2011).
- [14] J. Vučićević, H. Terletska, D. Tanasković, and V. Dobrosavljević, *Phys. Rev. B* **88**, 075143 (2013).
- [15] T. Furukawa, K. Miyagawa, H. Taniguchi, R. Kato, and K. Kanoda, *Nat. Phys.* **11**, 221 (2015).
- [16] H. Eisenlohr, S.-S. B. Lee, and M. Vojta, *Phys. Rev. B* **100**, 155152 (2019).
- [17] B. H. Moon, G. H. Han, M. M. Radonjić, H. Ji, and V. Dobrosavljević, [arXiv:1911.02772](https://arxiv.org/abs/1911.02772).
- [18] J. Kokalj, *Phys. Rev. B* **95**, 041110(R) (2017).
- [19] E. W. Huang, R. Sheppard, B. Moritz, and T. P. Devereaux, *Science* **366**, 987 (2019).
- [20] E. Perepelitsky, A. Galatas, J. Mravlje, R. Žitko, E. Khatami, B. S. Shastry, and A. Georges, *Phys. Rev. B* **94**, 235115 (2016).
- [21] S. Hartnoll, *Nat. Phys.* **11**, 54 (2015).
- [22] S. A. Hartnoll, A. Lucas, and S. Sachdev, *Holographic Quantum Matter* (MIT Press, Cambridge, MA, 2018).
- [23] P. Cha, A. A. Patel, E. Gull, and E.-A. Kim, [arXiv:1910.07530](https://arxiv.org/abs/1910.07530).
- [24] P. T. Brown, D. Mitra, E. Guardado-Sanchez, R. Nourafkan, A. Reymbaut, C.-D. Hébert, S. Bergeron, A.-M. S. Tremblay, J. Kokalj, D. A. Huse, P. Schauß, and W. S. Bakr, *Science* **363**, 379 (2019).
- [25] J. Vučićević, J. Kokalj, R. Žitko, N. Wentzell, D. Tanasković, and J. Mravlje, *Phys. Rev. Lett.* **123**, 036601 (2019).
- [26] A. Georges, G. Kotliar, W. Krauth, and M. J. Rozenberg, *Rev. Mod. Phys.* **68**, 13 (1996).
- [27] T. A. Maier, M. Jarrell, T. Pruschke, and M. H. Hettler, *Rev. Mod. Phys.* **77**, 1027 (2005).
- [28] J. Jaklič and P. Prelovšek, *Adv. Phys.* **49**, 1 (2000).
- [29] N. Lin, E. Gull, and A. J. Millis, *Phys. Rev. B* **80**, 161105(R) (2009).
- [30] N. Lin, E. Gull, and A. J. Millis, *Phys. Rev. B* **82**, 045104 (2010).
- [31] D. Bergeron, V. Hankevych, B. Kyung, and A.-M. S. Tremblay, *Phys. Rev. B* **84**, 085128 (2011).
- [32] T. Sato, K. Hattori, and H. Tsunetsugu, *Phys. Rev. B* **86**, 235137 (2012).
- [33] T. Sato and H. Tsunetsugu, *Phys. Rev. B* **94**, 085110 (2016).
- [34] A. Kauch, P. Pudleiner, K. Astleithner, P. Thunström, T. Ribic, and K. Held, *Phys. Rev. Lett.* **124**, 047401 (2020).
- [35] A. Georges, *Ann. Phys. (Berlin)* **523**, 672 (2011).
- [36] K. Aryanpour, W. E. Pickett, and R. T. Scalettar, *Phys. Rev. B* **74**, 085117 (2006).
- [37] G. Li, A. E. Antipov, A. N. Rubtsov, S. Kirchner, and W. Hanke, *Phys. Rev. B* **89**, 161118(R) (2014).
- [38] G. Kotliar, S. Y. Savrasov, G. Pálsson, and G. Biroli, *Phys. Rev. Lett.* **87**, 186401 (2001).
- [39] G. Biroli and G. Kotliar, *Phys. Rev. B* **65**, 155112 (2002).
- [40] A. N. Rubtsov and A. I. Lichtenstein, *J. Exp. Theor. Phys. Lett.* **80**, 61 (2004).
- [41] E. Gull, A. J. Millis, A. I. Lichtenstein, A. N. Rubtsov, M. Troyer, and P. Werner, *Rev. Mod. Phys.* **83**, 349 (2011).
- [42] K. G. Wilson, *Rev. Mod. Phys.* **47**, 773 (1975).
- [43] H. R. Krishna-murthy, J. W. Wilkins, and K. G. Wilson, *Phys. Rev. B* **21**, 1003 (1980).
- [44] R. Bulla, T. A. Costi, and T. Pruschke, *Rev. Mod. Phys.* **80**, 395 (2008).
- [45] R. Žitko and T. Pruschke, *Phys. Rev. B* **79**, 085106 (2009).
- [46] H. T. Dang, X. Y. Xu, K.-S. Chen, Z. Y. Meng, and S. Wessel, *Phys. Rev. B* **91**, 155101 (2015).
- [47] H. Park, K. Haule, and G. Kotliar, *Phys. Rev. Lett.* **101**, 186403 (2008).
- [48] H. Lee, G. Li, and H. Monien, *Phys. Rev. B* **78**, 205117 (2008).
- [49] T. Shirakawa, T. Tohyama, J. Kokalj, S. Sota, and S. Yunoki, *Phys. Rev. B* **96**, 205130 (2017).
- [50] J. Merino, B. J. Powell, and R. H. McKenzie, *Phys. Rev. B* **73**, 235107 (2006).
- [51] J. Kokalj and R. H. McKenzie, *Phys. Rev. Lett.* **110**, 206402 (2013).
- [52] T. Schäfer, F. Geles, D. Rost, G. Rohringer, E. Arrigoni, K. Held, N. Blümer, M. Aichhorn, and A. Toschi, *Phys. Rev. B* **91**, 125109 (2015).
- [53] E. G. C. P. van Loon, M. I. Katsnelson, and H. Hafermann, *Phys. Rev. B* **98**, 155117 (2018).
- [54] C. Walsh, P. Sémon, D. Poulin, G. Sordi, and A.-M. S. Tremblay, *Phys. Rev. B* **99**, 075122 (2019).
- [55] J. Bonča and P. Prelovšek, *Phys. Rev. B* **67**, 085103 (2003).
- [56] J. Vučićević and M. Ferrero, *Phys. Rev. B* **101**, 075113 (2020).
- [57] A. Taheridehkordi, S. H. Curnoe, and J. P. F. LeBlanc, *Phys. Rev. B* **99**, 035120 (2019).
- [58] A. Taheridehkordi, S. H. Curnoe, and J. P. F. LeBlanc, *Phys. Rev. B* **101**, 125109 (2020).
- [59] A. Taheridehkordi, S. H. Curnoe, and J. P. F. LeBlanc, *Phys. Rev. B* **102**, 045115 (2020).
- [60] O. Parcollet, M. Ferrero, T. Ayrál, H. Hafermann, P. Seth, and I. S. Krivenko, *Comput. Phys. Commun.* **196**, 398 (2015).
- [61] R. Peters, T. Pruschke, and F. B. Anders, *Phys. Rev. B* **74**, 245114 (2006).
- [62] A. Weichselbaum and J. von Delft, *Phys. Rev. Lett.* **99**, 076402 (2007).
- [63] R. Žitko, *Phys. Rev. B* **84**, 085142 (2011).
- [64] R. Žitko, D. Hansen, E. Perepelitsky, J. Mravlje, A. Georges, and B. S. Shastry, *Phys. Rev. B* **88**, 235132 (2013).
- [65] H. Kajueter and G. Kotliar, *Phys. Rev. Lett.* **77**, 131 (1996).
- [66] M. Potthoff, T. Wegner, and W. Nolting, *Phys. Rev. B* **55**, 16132 (1997).
- [67] L.-F. Arsenault, P. Sémon, and A.-M. S. Tremblay, *Phys. Rev. B* **86**, 085133 (2012).

Modern Physics Letters B
 2030004 (23 pages)
 © World Scientific Publishing Company
 DOI: 10.1142/S0217984920300045



Pfaffian paired states for half-integer fractional quantum Hall effect

M. V. Milovanović^{*,‡}, S. Djurdjević^{†,§} and J. Vučičević^{*,¶}

**Scientific Computing Laboratory,
 Center for the Study of Complex Systems,
 Institute of Physics Belgrade, University of Belgrade,
 Pregrevica 118, Belgrade 11080, Serbia*

*†Faculty of Natural Sciences and Mathematics,
 University of Montenegro, Džordža Vašingtona bb,
 Podgorica 81000, Montenegro*

‡milica.milovanovic@ipb.ac.rs

§stevandj@ucg.ac.me

¶jaksa.vucicevic@ipb.ac.rs

L. Antonić

*Department of Physics, Technion, Haifa 32000, Israel
 luka.antoniac@campus.technion.ac.il*

Received 1 June 2020

Accepted 8 June 2020

Published 3 July 2020

In this review, the physics of Pfaffian paired states, in the context of fractional quantum Hall effect, is discussed using field-theoretical approaches. The Pfaffian states are prime examples of topological (p -wave) Cooper pairing and are characterized by non-Abelian statistics of their quasiparticles. Here we focus on conditions for their realization and competition among them at half-integer filling factors. Using the Dirac composite fermion description, in the presence of a mass term, we study the influence of Landau level mixing in selecting a particular Pfaffian state. While Pfaffian and anti-Pfaffian are selected when Landau level mixing is not strong, and can be taken into account perturbatively, the particle-hole (PH) Pfaffian state requires non-perturbative inclusion of at least two Landau levels. Our findings, for small Landau level mixing, are in accordance with numerical investigations in the literature, and call for a non-perturbative approach in the search for PH Pfaffian correlations. We demonstrated that a method based on the Chern–Simons field-theoretical approach can be used to generate characteristic interaction pseudo-potentials for Pfaffian paired states.

Keywords: Fractional quantum Hall effect; half-integer filling factor; Pfaffian paired states.

[‡]Corresponding author.

1. Introduction

The fractional quantum Hall effect (FQHE)¹ is a strongly correlated phenomenon of electrons that is observed when they are confined to two dimensions and subjected to a strong magnetic field perpendicular to the two-dimensional plane, in which electrons live and interact. At special filling factors, i.e. ratios between the number of electrons and the number of flux quanta piercing the two-dimensional plane, experiments reveal highly entangled topological states of electrons with fractionally quantized Hall conductance, for intervals of magnetic field (or density). Almost exclusively the denominator of these fractions is an odd number, which can be traced and connected to the fermionic statistics of electrons. A surprise came when an even-denominator FQHE, at filling factor $5/2$, was discovered.² This introduced a new paradigm in our understanding of (even-denominator) FQHE states: they may be Bardeen–Cooper–Schrieffer (BCS) paired states of underlying quasiparticles. If we neglect the role of spin in high magnetic fields, the most natural choice for a pairing in a fixed Landau level (LL) is the unconventional, p -wave pairing of spinless quasiparticles proposed in Ref. 3. The resulting state, Moore–Read state is also called Pfaffian due to the necessary antisymmetrization of a collection of pairs of quasiparticles — identical fermions, which do not possess any additional characteristic like spin.

The underlying quasiparticles at even-denominator fractions beside the possibility of having the BCS pairing correlations in a paired state, may in principle exist in its parent, Fermi-liquid-like (FLL) state.⁴ Indeed such a state was probed and detected at filling factor $1/2$,⁵ and firstly theoretically described in Ref. 6. The theoretical assessment of even-denominator FLL state(s) may lead also to further understanding of the physics of the BCS pairing of underlying quasiparticles. An important direction in this effort is the understanding of the FLL state that occurs at a half-integer (denominator 2) filling of the system, and, at the same time, in an artificial circumstance of a precisely half-filled LL. Namely, a LL is singled out and half-filled. This mathematical limit of the physical system is highly relevant for the understanding of the real system. Our understanding of FQHE phenomena and real circumstances of FQHE experiments call for the concept of the projection to a single LL. Very often the physics of FQHE is confined to a single LL, and we can neglect the LL mixing — the influence of other LLs. Thus if the system is at half(-integer) filling, it nearly possesses the particle–hole (PH) symmetry — the symmetry under exchange of electrons and holes that a half-filled LL has. The Halperin–Lee–Read (HLR) theory⁶ of the FLL state at half-filling does not possess this symmetry (because it is a theory that does not include a projection to a fixed LL), but a phenomenological, effective theory with Dirac quasiparticles, proposed in Ref. 7 is manifestly invariant under exchange of electrons and holes, and describes the artificial system of electrons that is confined to a single LL.

On the other hand, the Pfaffian paired state is not invariant under exchange of electrons and holes. When the PH symmetry operation is applied to the

Pfaffian, a new topological state is generated, Pfaffian's conjugated partner, known as anti-Pfaffian.^{8,9} Here we may ask whether a state exists, that is a collection of p -wave Cooper pairs and respects the PH symmetry. Indeed one may argue that the Dirac theory of the half-filled LL offers a distinct possibility⁷ known as PH Pfaffian (PH symmetric Pfaffian). Before the proposal of the Dirac theory, studies that were examining possibilities of additional, negative-flux pairing, in which angular momentum of p -wave has opposite sign with respect to the one in Pfaffian, also proposed the PH Pfaffian.^{10,11}

While the relevance of Pfaffian and especially anti-Pfaffian for the explanation of the FQHE at $5/2$ is firmly established in numerical experiments confined to a fixed LL with LL mixing (perturbatively) included via additional, three-body interactions,¹² we do not have a support for PH Pfaffian when numerical experiments are confined to a fixed LL.¹³ But a recent experiment¹⁴ on thermal Hall conductance is consistent with a PH Pfaffian scenario at $5/2$. That the PH Pfaffian correlations and topological order may be relevant even in the absence of the PH symmetry (as is the case in experiments) may be shown by careful examination of various experimental probes as discussed in Ref. 15.

Thus the question is whether for sufficiently strong LL mixing, that cannot be treated perturbatively (as it is done in all numerical experiments confined to a single LL), we can reach a regime in a uniform system when PH Pfaffian correlations prevail. Or, is disorder needed to install the effective PH Pfaffian correlations?^{16,17} In any case LL mixing may play decisive role in selecting a specific kind of Pfaffian state in experiments. In the following sections, Secs. 3 and 4, we will review our work^{18,19} that used Dirac and Chern–Simons (CS) field-theoretical description to examine the role of LL mixing and explore pairing at half-integer fillings, in general.

In Sec. 2, we will review the Dirac theory of the FLL state of underlying quasi-particles — composite fermions at a half-filled LL, and select and describe a version of the theory that is best fitted for a description of Pfaffian paired states. The mass term in this theory mimics LL mixing (for small LL mixing has the role of those additional (three-body) interactions in the electron representation), and the limiting behavior of large mass may be identified with the usual HLR picture of the FLL state of FQHE at half-filling.

In Sec. 3, within this version of the Dirac theory, we will probe the question of topological pairing instabilities in a mean-field approximation (as usual in topological explorations when we assume that topological characterization is immune to the neglect of fluctuations). Instabilities will originate from the minimal coupling term, i.e. the coupling with the CS gauge field, and we will be disregarding the remaining influence of the Coulomb interaction, which has a pair-breaking effect. Our interest will be to find which kind of Pfaffian will prevail at certain LL mixing, if we assume a pairing instability.

In Sec. 4, we will discuss which model Hamiltonians for electrons, i.e. effective interaction pseudo-potentials (PPs) in fixed LLs lead to Pfaffian states. Using CS field-theoretical description we recover dominant, already known PPs for

Pfaffian and anti-Pfaffian in a fixed LL, and discuss the necessity to include non-perturbatively at least one more LL to establish PH Pfaffian correlations, and list pertinent PPs.¹⁹ Section 5 is reserved for a discussion and conclusions.

2. Theoretical Approaches to the Physics at a Half-Integer Filling

2.1. Wave-function approach

The basic explanation of the FQHE rests on the Laughlin wave function — the ground state wave function for the most prominent effect at filling $1/3$.²⁰ The wave function captures the basic correlations of electrons in a constrained space of an isolated LL. To introduce the Laughlin wave function, we start with the single-particle Hamiltonian,

$$H = \frac{(\mathbf{p} - \mathbf{A})^2}{2m_e}, \quad (1)$$

of a particle in a constant magnetic field, $\mathbf{B} = B\mathbf{z}$, with $A_x = -(B/2)y$ and $A_y = (B/2)x$, in a rotationally symmetric gauge. We fixed $c = 1$, $e = 1$, and $\hbar = 1$. The physics of FQHE is largely confined to a fixed LL and in the case of filling factor $1/3$, to the lowest LL (LLL). In the rotationally symmetric gauge and in the LLL, the appropriate basis is given by the following single particle wave functions,

$$\Psi_n(\mathbf{r}) = \frac{1}{\sqrt{2\pi l_B^{2+2n} 2^n n!}} z^n \exp \left\{ - \left(\frac{1}{4l_B^2} \right) |z|^2 \right\}, \quad (2)$$

where $l_B = \sqrt{\frac{\hbar c}{eB}}$, and $n = 0, 1, 2, \dots$ is the guiding center angular momentum number. Apart from the exponential factor, these wave functions depend only on the coordinate $z = x + iy$, i.e. they make a holomorphic description, when we neglect the factor which is the same for each $\Psi_n(\mathbf{r})$. Thus many-body wave functions of frozen spin electrons become polynomials in the z coordinate(s) in the LLL, as in the following expression,

$$\Psi(\mathbf{r}_1, \mathbf{r}_2, \dots, \mathbf{r}_{N_e}) = P(z_1, z_2, \dots, z_{N_e}) \exp \left\{ - \left(\frac{1}{4l_B^2} \right) \sum_{i=1}^{N_e} |z_i|^2 \right\}. \quad (3)$$

The Laughlin wave function at filling factor $1/3$ is specified by the Laughlin–Jastrow choice for P ,

$$P_{L-J}(z_1, z_2, \dots, z_{N_e}) = \prod_{i < j} (z_i - z_j)^m, \quad (4)$$

with $m = 3$. In this polynomial, the highest power of any z_i ; $i = 1, 2, \dots, N_e$ is $N_m = m(N_e - 1)$ and this number also specifies the number of (single-particle) states available to the system, i.e. the number of flux-quanta piercing the system, $N_\phi = N_m + 1$. Thus the ratio N_e/N_ϕ becomes $1/3$ in the thermodynamic limit when $m = 3$.

For monotonically decreasing with distance repulsive interactions like Coulomb, we may expect an extreme capacity of the wave-function to minimize the interaction energy. Namely, as a function of a fixed electron coordinate, the wave function has all (N_m) zeros on the other electrons, $m = 3$ per electron, though only one zero is required by Fermi statistics. Equivalently, we may say that the zero on any other electron is of the m^{th} order as we study the limiting behavior when a fixed electron approaches any other in (4).

Following the same logic, we may attempt the same construction at filling factor $1/2$, but, because $m = 2$ in (4), in this case, we need additional factors that will ensure that the wave function is antisymmetric. These additional factors should not contribute or change the value of N_m in the thermodynamic limit (mN) , and thus, as additional factors in the total wave function, may be considered as its “neutral part” — the part that does not see the macroscopic flux. (The Laughlin–Jastrow part (4) would represent the charged part.) The neutral part may describe a collection of fermionic quasiparticles (that do not see any macroscopic flux, i.e. external magnetic field), and they may be in the first approximation non-interacting (make a FLL state), or they may come in BCS pairs (make a bosonic condensate and possibly a gapped state). Indeed experiment and theory are equivocal that the state at filling factor $1/2$ (in GaAs structures) is a FLL state of underlying quasiparticles, and the state at filling factor $5/2$ (in GaAs²) is effectively a gapped state of half-filled second LL of frozen-spin (spinless) electrons, in which quasiparticles may pair. The exact topological nature of the paired state at filling factor $5/2$ is still under debate.

But we may say that the most theoretically appealing (the most simple and natural BCS pairing) guess for the gapped state at the half-integer filling factors (in various experimental set-ups) is proposed in Ref. 3, and goes under name Moore–Read state or Pfaffian (state). The Pfaffian wave function in the LLL is

$$\Psi_{\text{Pf}} = \sum_{\sigma} \text{sgn } \sigma \left\{ \frac{1}{(z_{\sigma(1)} - z_{\sigma(2)})} \cdots \frac{1}{(z_{\sigma(N_e-1)} - z_{\sigma(N_e)})} \right\} \prod_{k < l} (z_k - z_l)^2, \quad (5)$$

where the sum is over all permutations of N_e objects where N_e is an even number. We omitted the exponential factors and the expression is unnormalized. In mathematics, if $A = \{a_{ij}\}$ is $N \times N$ antisymmetric matrix, and N is even, its Pfaffian is

$$\text{pf}(a_{ij}) = \text{pf}(A) = \frac{1}{2^{N/2}(N/2)!} \sum_{\sigma \in S_N} \text{sgn } \sigma \prod_{i=1}^{N/2} a_{\sigma(2i-1)\sigma(2i)}, \quad (6)$$

and $\text{pf}(A)^2 = \det(A)$. In more physical terms, we see that the sum in the Moore–Read wave function describes the antisymmetrization of a collection of Cooper pairs, where each pair wave function, $g(\mathbf{r})$, where \mathbf{r} is the relative coordinate of a pair, can be described as

$$g(\mathbf{r}) \sim \frac{1}{z}. \quad (7)$$

This special algebraic decay is the hallmark of the Pfaffian (Moore–Read) wave function, and expresses a special kind of topological, long-range entanglement in this function that represents a p -wave pairing. The construction is given in the LLL, but can be easily generalized and considered in the second LL, i.e. in any isolated LL.

The highest power of any z_i in the Pfaffian wave function is $N_m = 2N_e - 3$, i.e. $N_m = 2N_e - \mathcal{S}$, where $\mathcal{S} = 3$ is so-called shift — a topological number that characterizes a state of a FQHE system on a curved background, such as a sphere. If a state is PH symmetric, the shift should be invariant under the PH exchange. We require $N_e + N_h = N_m + 1$, i.e. the number of electrons, N_e , plus the number of holes, N_h , should be equal to the number of available single-particle states. Thus the state that we get by applying the PH transformation on Pfaffian, is a distinct state, anti-Pfaffian, with shift equal to -1 . This anti-Pfaffian state, that has distinct topological features with respect to Pfaffian, was firstly described in Refs. 8 and 9.

We may wonder whether we may still have a p -wave pairing (the smallest angular momentum pairing of spinless electrons) in a many-body wave function that is invariant under PH exchange. It is not hard to see that in this case we must have $N_m = 2N_e - 1$, and this implies some kind of a microscopic negative flux or simply reversed p -wave pairing as in

$$g_{\text{ph}}(\mathbf{r}) \sim \frac{1}{z^*}. \quad (8)$$

The naive guess would be that by doing the projection to the LLL, in the first approximation, we have

$$g_{\text{ph}}(\mathbf{r}) \sim z. \quad (9)$$

But, because for any set of complex numbers z_i , $i = 1, 2, \dots, N$; N even, and $N > 2$,

$$\text{pf}(z_i - z_j) = 0, \quad (10)$$

this does not lead to a non-trivial state in the LLL. Thus the question is whether a half-filled isolated LL with special interactions can support a gapped state with PH symmetry, i.e. PH (symmetric) Pfaffian. In the case of Pfaffian and anti-Pfaffian, special interactions exist in an isolated LL²¹ (and they do not respect the PH symmetry). Furthermore, the negative flux pairing expression in (8) calls for inclusion of other LLs, and maybe only with significant LL mixing, when the PH symmetry is broken, we can stabilize the pairing correlations in (8). Even in this case, we will call this exotic state PH Pfaffian.

2.2. Field-theoretical approach

2.2.1. Quasiparticles in the FQHE and the HLR theory at half-filling

We may separate the phase part from the rest of the Laughlin wave function at filling factor $1/m$, where $m = 3$, or from the Laughlin–Jastrow part of a ground

state wave function at half-filling, when $m = 2$, and, then, define a decomposition into two parts of any many-electron wave-function, Ψ_e , as

$$\Psi_e(\mathbf{r}_1, \mathbf{r}_2, \dots, \mathbf{r}_{N_e}) = \prod_{i < j} \frac{(z_i - z_j)^m}{|z_i - z_j|^m} \Psi_{\text{qp}}(\mathbf{r}_1, \mathbf{r}_2, \dots, \mathbf{r}_{N_e}). \quad (11)$$

The wave function $\Psi_{\text{qp}}(\mathbf{r}_1, \mathbf{r}_2, \dots, \mathbf{r}_{N_e})$ represents a wave function of quasiparticles after the unitary transformation defined by the phase factor: in the Laughlin ($m = 3$) case quasiparticles are bosons, and at half-filling ($m = 2$) they are fermions. This defines a CS transformation, or what we will refer to as a Zhang's construction of quasiparticles.²² In the field-theoretical terms, quasiparticles induce field \mathbf{a} — they are the sources of an artificial (internal) magnetic field b that also acts as an additional field on quasiparticles,

$$\rho_{\text{qp}} = -\frac{1}{m} \frac{\nabla \times \mathbf{a}}{2\pi} = -\frac{1}{m} b. \quad (12)$$

In (12) ρ_{qp} is the quasiparticle density. We will discuss the CS field-theoretical approach to the system at half-filling, i.e. the HLR theory with more mathematical details below. Here we will note that in a mean-field picture the internal field will cancel the external field. As a first approximation to the half-filling problem, we will find that the ground state in the quasiparticle representation is simply a Slater-determinant of free waves that are filling a Fermi sphere in the inverse space in two dimensions, i.e. it represents a gas of fermionic quasiparticles. (The amplitude part of the Laughlin–Jastrow factor can be recovered in the field-theoretical approach by the random phase approximation (RPA) treatment of the density harmonic fluctuations.)

Therefore, in the Zhang's quasiparticle construction to each electron at position w is attached the following phase factor:

$$\prod_i \frac{|z_i - w|^m}{(z_i - w)^m}, \quad (13)$$

a flux tube. The ensuing quasiparticle sees two gauge fields: external and internal — it is a quasiparticle that possesses charge, and the density of quasiparticles is equal to the density of electrons.

On the other hand in the Read's construction²³ of quasiparticles, we start with the notion of fluxes (flux quanta or vortices) that can be introduced by external field in the system, and can be described by the following construction,

$$\prod_i (z_i - w)^m, \quad (14)$$

i.e. by insertion of m Laughlin quasiholes. We can make this object neutral by adding a unit of charge, more precisely an electron, to it, and in this way define the Read's quasiparticles as neutral objects, number of which is proportional to the number of external field flux quanta piercing the system. This view is in a way a dual approach (equivalent description of the same theory from a different

point of view) that was initially applied to bosonic systems where the description in terms of elementary particles — bosons was traded for the description in terms of excitations — vortices.²⁴

In any case both approaches take into account the precise commensuration between the number of electrons and the number of flux quanta in a system at a fixed filling factor, in our case 1/2.

The CS approach at 1/2, based on the Zhang's construction of quasiparticles, begins with the following Lagrangian (density),

$$\mathcal{L} = \Psi_{\text{cf}}^*(i\partial_t - A_0 - a_0)\Psi_{\text{cf}} - \frac{\Psi_{\text{cf}}^*(\mathbf{p} - \mathbf{A} - \mathbf{a})^2\Psi_{\text{cf}}}{2m} - \frac{1}{2} \frac{1}{4\pi} a\partial a. \quad (15)$$

In (15), Ψ_{cf} represents a fermionic (Grassmann quasiparticle) field, and the CS term is defined by $a\partial a \equiv \epsilon^{\mu\nu\lambda} a_\mu \partial_\nu a_\lambda$, $\mu, \nu, \lambda = 0, 1, 2$ (denote one time and two spatial coordinates), the summation over repeated indices is understood, and $a_\mu = (a_0, \mathbf{a})$ is a three-vector. The cf stands for composite fermions, a general name for underlying quasiparticles.

Considering the classical equations of motion, from $\frac{\delta\mathcal{L}}{\delta a_0} = 0$, we get

$$-\Psi_{\text{cf}}^*\Psi_{\text{cf}} - \frac{1}{2} \frac{\nabla \times \mathbf{a}}{2\pi} = 0. \quad (16)$$

(Above $\nabla \times \mathbf{a}$ denotes the z component of the vector, and can be considered as a scalar in this two-dimensional theory.) In the mean-field, when we assume that the density of quasiparticles is uniform, the internal field, $\frac{\nabla \times \mathbf{a}}{2\pi}$, exactly cancels the uniform external field at half-filling,

$$\frac{\nabla \times \mathbf{A}}{2\pi} = 2\overline{\Psi_e^*\Psi_e} = 2\overline{\Psi_{\text{cf}}^*\Psi_{\text{cf}}}, \quad (17)$$

where $\overline{\Psi_e^*\Psi_e}$ stands for the uniform electron density.

The Lagrangian in (15) is the basis or starting point for the HLR theory, which describes the physics at 1/2 as a FLL state of (fermionic) quasiparticles. We may notice, from the form of the Lagrangian, that the electron density-current vector is equal to the one of quasiparticles,

$$-\frac{\delta\mathcal{L}}{\delta A^\mu} = j_e^\mu = j_{\text{cf}}^\mu. \quad (18)$$

2.2.2. Dirac quasiparticle description of half-filled LL and at half-filling

In this section, we will first review the Dirac theory for a half-filled LL proposed in Ref. 7 and then consider its extension in the presence of a mass term that is relevant for the general case (with LL mixing) at half-filling.

We start with an isolated LL (of classical electrons) that is half-filled. It has the PH symmetry — the symmetry under exchange of electrons and holes. The low-energy physics of a zeroth LL of Dirac electrons in the weak coupling limit should correspond to the low-energy physics of isolated LL (of classical electrons).⁷

Thus we consider the Dirac problem in an external (magnetic) field, which is a background field (no dynamics):

$$\mathcal{L}_D = i\bar{\Psi}\gamma^\mu D_\mu^A\Psi + \text{interactions} = i\bar{\Psi}(\gamma^0 D_t + \boldsymbol{\gamma} \cdot \mathbf{D})\Psi + \text{interactions} \quad (19)$$

where $D_t = \frac{\partial}{\partial t} + iA_0$ and $\mathbf{D} = \boldsymbol{\nabla} - i\mathbf{A}$, and γ^μ , $\mu = 0, 1, 2$ are 2×2 gamma matrices for the Dirac description in two spacial dimensions, and Ψ is a two-component Grassmann field.

The Dirac system is a neutral system and there is no Hall conductance. To make up for this, i.e. to continue to discuss an isolated LL (of classical electrons), which has $1/(4\pi)$ of the units (e^2/\hbar) of Hall conductance, we consider

$$\mathcal{L}_A = i\bar{\Psi}\gamma^\mu D_\mu^A\Psi - \frac{A\partial A}{8\pi} + \text{interactions}. \quad (20)$$

If we define the density-current of electrons as

$$j_{\text{el}}^\mu = -\frac{\delta\mathcal{L}}{\delta A^\mu}, \quad (21)$$

it follows that for densities,

$$\rho_{\text{el}} = \rho_D + \frac{\boldsymbol{\nabla} \times \mathbf{A}}{4\pi}. \quad (22)$$

Because, $\bar{\rho}_D$ (average density of the Dirac system) = 0, we have a non-zero density of electrons

$$\frac{\bar{\rho}_{\text{el}}}{B} = \frac{1}{2}, \quad (23)$$

where $B = \frac{\boldsymbol{\nabla} \times \mathbf{A}}{2\pi}$ is the uniform external magnetic field. Also

$$\mathbf{j}_{\text{el}} = \mathbf{j}_D + \hat{\epsilon} \frac{\mathbf{E}}{4\pi}, \quad (24)$$

where $\hat{\epsilon}$ is a 2×2 matrix, $\epsilon_{xy} = -\epsilon_{yx} = 1$, $\epsilon_{xx} = \epsilon_{yy} = 0$. Thus, with $\bar{\rho}_D = 0$ and $\mathbf{j}_D = 0$, we are at half-filling, and the Hall conductance is equal to $\frac{1}{4\pi}(\frac{e^2}{\hbar})$.

Following Ref. 7, in a dual picture, we postulate a new Lagrangian, \mathcal{L} , with new dual Dirac field χ :

$$\mathcal{L} = i\bar{\chi}\gamma^\mu D_\mu^a\chi + a\frac{\partial A}{4\pi} - \frac{A\partial A}{8\pi} + \dots \quad (25)$$

where \dots denotes higher order terms. (We will ignore these higher order terms below and consider classical equations of motion in the framework of the linear response theory.) Why would we expect this Lagrangian in a dual picture? We provide an analysis with more details below, but here we may note that the Dirac (two-component) formalism is expected also in a dual picture, because it makes possible that the PH symmetry is manifestly included as demonstrated in Ref. 7. Also note that the dual fermion is not directly coupled to the external field, and, as we show below, the Lagrangian describes a Dirac system at a finite density, in agreement with our expectation that the system is in a FLL state of quasiparticles. For further details on the dual approach see Refs. 25 and 26.

- (i) It seems that χ 's represent Read's quasiparticles. Indeed, if we consider the following equation of motion,

$$0 = \frac{\delta \mathcal{L}}{\delta a_0} = -\rho_\chi + \frac{\nabla \times \mathbf{A}}{4\pi}, \quad (26)$$

we can conclude that the density of χ depends on the number of flux quanta. On the other hand,

$$\rho_{\text{el}} = -\frac{\delta \mathcal{L}}{\delta A_0} = -\frac{\nabla \times \mathbf{a}}{4\pi} + \frac{\nabla \times \mathbf{A}}{4\pi}, \quad (27)$$

and, at half-filling, in the mean-field approximation, $\nabla \times \mathbf{a} = 0$. Thus, χ 's do not experience any uniform, non-zero gauge field, $b = \frac{\nabla \times \mathbf{a}}{2\pi}$, that couples χ 's indirectly to the external field. Therefore, χ 's are, in the first approximation, neutral objects, but with the Dirac's singularity in the inverse space at $\mathbf{k} = 0$. In this way, they have a non-analytical feature that we do not expect from a description that is based on Read's quasiparticles. We find that the effective theories based on the description with the Dirac's quasiparticle are very useful when considering the pairing physics, as they capture the time-reversal and parity breaking (that is essential for the pairing physics) as we will explain later in this section.

- (ii) We expect that the effective theory of a half-filled LL should describe a Fermi-liquid of quasiparticles (if we do not consider the BCS instability). Indeed, in the mean-field approximation, in the first approximation, the internal field (b) is zero, and the theory describes a Dirac Fermi-liquid.
- (iii) If we vary \mathbf{a} in \mathcal{L} we find

$$\mathbf{j}_D = \hat{\epsilon} \frac{\mathbf{E}}{4\pi}. \quad (28)$$

Also,

$$\mathbf{j}_{\text{el}} = -\frac{\delta \mathcal{L}}{\delta \mathbf{A}} = \hat{\epsilon} \frac{\mathbf{E} - \mathbf{e}}{4\pi}, \quad (29)$$

where \mathbf{e} is the electric field due to the potential a^μ . Next, we assume that even in the presence of disorder, the PH symmetry is respected, and in the linear response we have,

$$\mathbf{j}_D = \hat{\sigma}^D \mathbf{e}, \quad (30)$$

where $\sigma_{xx}^D = \sigma_{yy}^D \neq 0$ represents a longitudinal conductance, and $\sigma_{xy}^D = \sigma_{yx}^D = 0$ (the Hall conductance is zero). The zero Hall conductance is an expression of the PH symmetry and a property of Dirac fermions. These three equations, (28), (29), and (30), combined lead to the conclusion that the Hall conductance of electrons is $\frac{1}{2}(\frac{e^2}{h})$, which we expect to be the case in the theory of the system with classical electrons that respects the PH symmetry.²⁷

It is important to notice that $\sigma_{xy}^D = \sigma_{yx}^D = 0$ is not an only natural “choice” for the response of the non-interacting Dirac system (conus) to a perturbation due to a gauge (internal a^μ) field. To get the Hall conductance, we assume the presence of the mass term in the non-interacting Dirac description,

$$\mathcal{L}_D = i\bar{\chi}\gamma^\mu D_\mu^a \chi - m\bar{\chi}\chi. \quad (31)$$

The σ_{xy}^D can be found by integration of Berry curvature in the inverse (\mathbf{k}) space,^{27,28} by choosing a specific gauge for eigenstates, and integrating over occupied states. In this way, we can get contributions (in units e^2/h):

$$\text{sgn}(m) \frac{1}{4\pi} \left(1 - \frac{|m|}{\sqrt{k_F^2 + m^2}} \right), \quad (32)$$

from the positive-energy states that are filled for $0 \leq |\mathbf{k}| < k_F$, and

$$-\text{sgn}(m) \frac{1}{4\pi}, \quad (33)$$

from the negative-energy states. There are two natural ways to take into account these two contributions: (1) to add them,

$$\sigma_{xy}^D = -\frac{m}{\sqrt{k_F^2 + m^2}}, \quad (34)$$

i.e. adopt a “dimensional regularization,” or (2) to consider only the contribution from the positive energy solutions:

$$\sigma_{xy}^D = \text{sgn}(m) \frac{1}{4\pi} \left(1 - \frac{|m|}{\sqrt{k_F^2 + m^2}} \right), \quad (35)$$

i.e. adopt a “Pauli–Villars regularization.” It is obvious that in order to get an appropriate response in the Dirac theory (of the half-filled LL) we need to assume and apply the dimensional regularization in the field-theoretical treatment.

We can also conclude that by choosing an appropriate singular gauge (phase) transformation on the negative energy eigenstates, we can switch from the dimensional regularization to the Pauli–Villars regularization (and vice versa). This transformation can be understood as an adoption of a new quasiparticle picture and a new Lagrangian (here without higher order terms):

$$\mathcal{L} = i\bar{\chi}^{\text{qp}}\gamma^\mu D_\mu^a \chi^{\text{qp}} - \frac{a\partial a}{8\pi} + a \frac{\partial A}{4\pi} - \frac{A\partial A}{8\pi}. \quad (36)$$

To find the same response as before, we have to adopt Pauli–Villars regularization (when integrating out fermions and generating quadratic terms in a) with a positive mass to cancel the second term in \mathcal{L} . Physically we indeed switched to a new quasiparticle picture of Zhang’s type. To see that let’s consider the full theory with a positive ($m > 0$) mass term:

$$\mathcal{L} = i\bar{\chi}^{\text{qp}} D_a \chi^{\text{qp}} - m\bar{\chi}^{\text{qp}} \chi^{\text{qp}} - \frac{a\partial a}{8\pi} + a \frac{\partial A}{4\pi} - \frac{A\partial A}{8\pi}. \quad (37)$$

(i) From the equations of motion,

$$0 = \frac{\delta \mathcal{L}}{\delta a^\mu} = -j_\chi^{\text{qp},\mu} - \frac{\partial a}{4\pi} + \frac{\partial A}{4\pi}, \quad (38)$$

and

$$j_{\text{el}}^\mu = -\frac{\delta \mathcal{L}}{\delta A^\mu} = \frac{\partial A}{4\pi} - \frac{\partial a}{4\pi}, \quad (39)$$

it follows that, $j_{\text{el}}^\mu = j_\chi^{\text{qp},\mu}$, as usual in the CS theory, i.e. the theory directly relates to the Zhang's quasiparticle construction.

(ii) If we let $m \rightarrow \infty$ the effective Lagrangian becomes the HLR after the shift $a^\mu \rightarrow a^\mu + A^\mu$.²⁹

We can conclude that the Lagrangian in (37), with $m = 0$, describes the physics of an isolated (PH symmetric) LL using the Zhang's quasiparticle picture. The introduction of non-zero m represents LL mixing, i.e. a measure of the inclusion of other LLs, so that for large m we can recover the HLR theory that does not reduce the effective physics of the electron system to a single LL.

3. Pfaffian Paired States at Half-Integer Filling

In this section, we will adopt the Dirac quasiparticle picture that is given by the Lagrangian in (37) for a FQHE system at a half-integer filling factor. Thus, the starting Lagrangian is

$$\mathcal{L} = i\bar{\chi}\gamma^\mu D_\mu^a \chi - m\bar{\chi}\chi - \frac{m}{|m|} \frac{a\partial a}{8\pi} + a \frac{\partial A}{4\pi} - \frac{A\partial A}{8\pi}, \quad (40)$$

where for simplicity we omitted qp letters when writing χ fields with respect to (37), but we should be aware that for any probes (perturbative expansions) the Pauli–Villars regularization is understood. We generalized the Lagrangian in (37) for both signs of mass m (to cancel the additional contribution due to the assumed Pauli–Villars regularization, the first term in (35)). It follows that

$$j_\chi^\mu = -\frac{m}{|m|} \frac{\partial a}{4\pi} + \frac{\partial A}{4\pi}, \quad (41)$$

and

$$j_{\text{el}}^\mu = -\frac{\partial a}{4\pi} + \frac{\partial A}{4\pi}, \quad (42)$$

as a generalization of (38) and (39) to both signs of mass. Exactly at half-filling, i.e. when in a uniform, constant magnetic field we have on average one electron per two flux quanta, we may solve (41) in the Coulomb gauge, $\nabla \cdot \mathbf{a} = 0$. The solutions are²²

$$a_x(\mathbf{r}) = 2 \frac{m}{|m|} \int d\mathbf{r}' i \frac{y - y'}{|\mathbf{r} - \mathbf{r}'|^2} \delta\rho_\chi(\mathbf{r}'), \quad (43)$$

and

$$a_y(\mathbf{r}) = -2 \frac{m}{|m|} \int d\mathbf{r}' i \frac{x-x'}{|\mathbf{r}-\mathbf{r}'|^2} \delta\rho_\chi(\mathbf{r}'), \quad (44)$$

and $\delta\rho_\chi(\mathbf{r}') = \chi^\dagger(\mathbf{r}')\chi(\mathbf{r}') - \bar{\rho}$, where $\bar{\rho}$ is a constant (external flux density). We would like to analyze the effect on pairing of the interaction term,

$$V_{\text{int}} = -\mathbf{a}\bar{\chi}\gamma\chi. \quad (45)$$

In the following, representation of γ matrices,

$$\gamma^0 = \sigma_3, \quad \gamma^1 = i\sigma_2, \quad \gamma^2 = -i\sigma_1, \quad (46)$$

where $\sigma_i, i = 1, 2, 3$ are Pauli matrices, we have

$$V_{\text{int}} = -\mathbf{a}\chi^\dagger\boldsymbol{\sigma}\chi. \quad (47)$$

In this representation, we have the following expression for the interaction:

$$V_{\text{int}} = -i2 \frac{m}{|m|} \int d\mathbf{r}' \delta\rho_\chi(\mathbf{r}') \chi^\dagger(\mathbf{r}) \begin{bmatrix} 0 & \frac{\bar{z}-\bar{z}'}{|\mathbf{r}-\mathbf{r}'|^2} \\ -\frac{z-z'}{|\mathbf{r}-\mathbf{r}'|^2} & 0 \end{bmatrix} \chi(\mathbf{r}). \quad (48)$$

On the other hand, the presence of the mass term in the Dirac system leads to the following eigenproblem,

$$\begin{bmatrix} m - \epsilon & k_- \\ k_+ & -m - \epsilon \end{bmatrix} \chi(\mathbf{k}) = 0, \quad (49)$$

where $k_- = k_x - ik_y$ and $k_+ = k_x + ik_y$. The positive eigenvalue, $\epsilon = \sqrt{|\mathbf{k}|^2 + m^2} \equiv E_{\mathbf{k}}$, corresponds to the following eigenstate,

$$\chi_E = \begin{bmatrix} m + E_{\mathbf{k}} \\ k_+ \end{bmatrix} \frac{1}{\sqrt{2E_{\mathbf{k}}(E_{\mathbf{k}} + m)}}. \quad (50)$$

As we consider relevant only (positive energy) states around k_F , we will keep only these states in the expansion over \mathbf{k} -eigenstates of field $\chi(\mathbf{r})$, and, further, only consider the BCS pairing channel in V_{int} . Thus (in the second-quantized notation)

$$\chi(\mathbf{r}) = \frac{1}{\sqrt{2V}} \sum_{\mathbf{k}} \exp\{i\mathbf{k} \cdot \mathbf{r}\} \chi_E(\mathbf{k}) a_{\mathbf{k}} + \dots, \quad (51)$$

and

$$\begin{aligned} V_{\text{int}}^{\text{BCS}} &= \frac{m}{|m|} \frac{2\pi}{8V} \sum_{\mathbf{k}, \mathbf{p}} a_{\mathbf{k}}^\dagger a_{\mathbf{p}} a_{-\mathbf{k}}^\dagger a_{-\mathbf{p}} \times \frac{1}{E_{\mathbf{k}} E_{\mathbf{p}} (m + E_{\mathbf{k}}) (m + E_{\mathbf{p}})} \\ &\times \{(m + E_{\mathbf{k}})(m + E_{\mathbf{p}}) + k_- p_+\} \\ &\times [m + E_{\mathbf{k}}, \quad -k_-] \begin{bmatrix} 0 & \frac{1}{k_+ - p_+} \\ -\frac{1}{k_- - p_-} & 0 \end{bmatrix} \begin{bmatrix} m + E_{\mathbf{p}} \\ -p_+ \end{bmatrix}. \quad (52) \end{aligned}$$

We used: $\int d\mathbf{r} \frac{1}{z} \exp\{i\mathbf{k}\mathbf{r}\} = i \frac{2\pi}{k_+}$. We may rewrite this expression (taking into account the antisymmetry of the fermionic operators) as

$$V_{\text{int}}^{\text{BCS}} = \sum_{\mathbf{k}, \mathbf{p}} V_{\mathbf{k}\mathbf{p}} a_{\mathbf{k}}^\dagger a_{\mathbf{p}} a_{-\mathbf{k}}^\dagger a_{-\mathbf{p}}, \quad (53)$$

where

$$V_{\mathbf{k}\mathbf{p}} = \frac{2\pi}{8V} \frac{1}{E_k \cdot E_p} \times \left[-4|m|kp \frac{i \sin(\theta_p - \theta_k)}{|\mathbf{k} - \mathbf{p}|^2} - \frac{m}{|m|} (E_k + E_p + 2m)(E_k - m)(E_p - m) \times \frac{\exp\{i2(\theta_p - \theta_k)\} - 1}{|\mathbf{k} - \mathbf{p}|^2} \right]. \quad (54)$$

Now we will adopt the mean-field BCS approximation, in an expectation that the topological characterization of pairing instabilities, will stay unchanged under this approximation. In the following, we will review the relevant parts of the BCS mean-field theory. We will follow the notation of Ref. 30. The effective Hamiltonian is

$$K_{\text{eff}} = \sum_{\mathbf{k}} \left\{ \xi_k a_{\mathbf{k}}^\dagger a_{\mathbf{k}} + \frac{1}{2} (\Delta_{\mathbf{k}}^* a_{-\mathbf{k}} a_{\mathbf{k}} + \Delta_{\mathbf{k}} a_{\mathbf{k}}^\dagger a_{-\mathbf{k}}^\dagger) \right\}, \quad (55)$$

and in our case $\xi_k = E_k - \mu$, with $E_k = \sqrt{|\mathbf{k}|^2 + m^2}$. The Bogoliubov transformation is

$$\alpha_{\mathbf{k}} = u_{\mathbf{k}} a_{\mathbf{k}} - v_{\mathbf{k}} a_{-\mathbf{k}}^\dagger, \quad (56)$$

with

$$\frac{v_{\mathbf{k}}}{u_{\mathbf{k}}} = \frac{-(\mathcal{E}_k - \xi_k)}{\Delta_{\mathbf{k}}^*}, \quad |u_{\mathbf{k}}|^2 = \frac{1}{2} \left(1 + \frac{\xi_k}{\mathcal{E}_k} \right), \quad (57)$$

$$|v_{\mathbf{k}}|^2 = \frac{1}{2} \left(1 - \frac{\xi_k}{\mathcal{E}_k} \right),$$

and $\mathcal{E}_k = \sqrt{\xi_k^2 + |\Delta_{\mathbf{k}}|^2}$.

On the other hand, if we start with a Cooper channel interaction and do the BCS mean-field decomposition with $b_{\mathbf{k}}^\dagger = a_{\mathbf{k}}^\dagger a_{-\mathbf{k}}$

$$\sum_{\mathbf{k}, \mathbf{p}} V_{\mathbf{k}\mathbf{p}} b_{\mathbf{k}}^\dagger b_{\mathbf{p}} = \sum_{\mathbf{k}, \mathbf{p}} V_{\mathbf{k}\mathbf{p}} \langle b_{\mathbf{k}}^\dagger \rangle b_{\mathbf{p}} + \sum_{\mathbf{k}, \mathbf{p}} V_{\mathbf{k}\mathbf{p}} b_{\mathbf{k}}^\dagger \langle b_{\mathbf{p}} \rangle - \sum_{\mathbf{k}, \mathbf{p}} V_{\mathbf{k}\mathbf{p}} \langle b_{\mathbf{k}}^\dagger \rangle \langle b_{\mathbf{p}} \rangle, \quad (58)$$

and specify $u_{-\mathbf{k}} = u_{\mathbf{k}} = u_{\mathbf{k}}^*$ and $v_{-\mathbf{k}} = -v_{\mathbf{k}}$, then

$$\frac{\Delta_{\mathbf{p}}^*}{2} = \sum_{\mathbf{k}} V_{\mathbf{k}\mathbf{p}} \langle a_{\mathbf{k}}^\dagger a_{-\mathbf{k}} \rangle$$

$$= \sum_{\mathbf{k}} V_{\mathbf{k}\mathbf{p}} \langle (u_{\mathbf{k}} \alpha_{\mathbf{k}}^\dagger + v_{\mathbf{k}}^* \alpha_{-\mathbf{k}}) (-v_{\mathbf{k}}^* \alpha_{\mathbf{k}} + u_{\mathbf{k}} \alpha_{-\mathbf{k}}^\dagger) \rangle, \quad (59)$$

i.e.

$$\frac{\Delta_{\mathbf{p}}^*}{2} = \sum_{\mathbf{k}} V_{\mathbf{k}\mathbf{p}} v_{\mathbf{k}}^* u_{\mathbf{k}} = \sum_{\mathbf{k}} V_{\mathbf{k}\mathbf{p}}(-) \frac{\Delta_{\mathbf{k}}^*}{2 \mathcal{E}_{\mathbf{k}}}. \quad (60)$$

In our case $V_{\mathbf{k}\mathbf{p}}$ is given in (54). The numerical solutions of the BCS self-consistent equation, when the parameter k_F is kept fixed, but mass m is varied, for channels $l = 1, 3, -1$, with $\Delta_{\mathbf{k}}^* = |\Delta_{\mathbf{k}}| \exp\{il\theta_{\mathbf{k}}\}$ are described in Fig. 1. We find that $\Delta_{\mathbf{k}}^* = |\Delta_{\mathbf{k}}| \exp\{-il\theta_{\mathbf{k}}\}$, $l = 1, 3, -1$ are solutions if we switch gauge for the eigenstates of the Dirac equation, i.e. instead of (50) we take

$$\left[\begin{array}{c} l \\ \vdots \end{array} \right] \quad \rightarrow \quad \left[\begin{array}{c} -l \\ \vdots \end{array} \right]$$

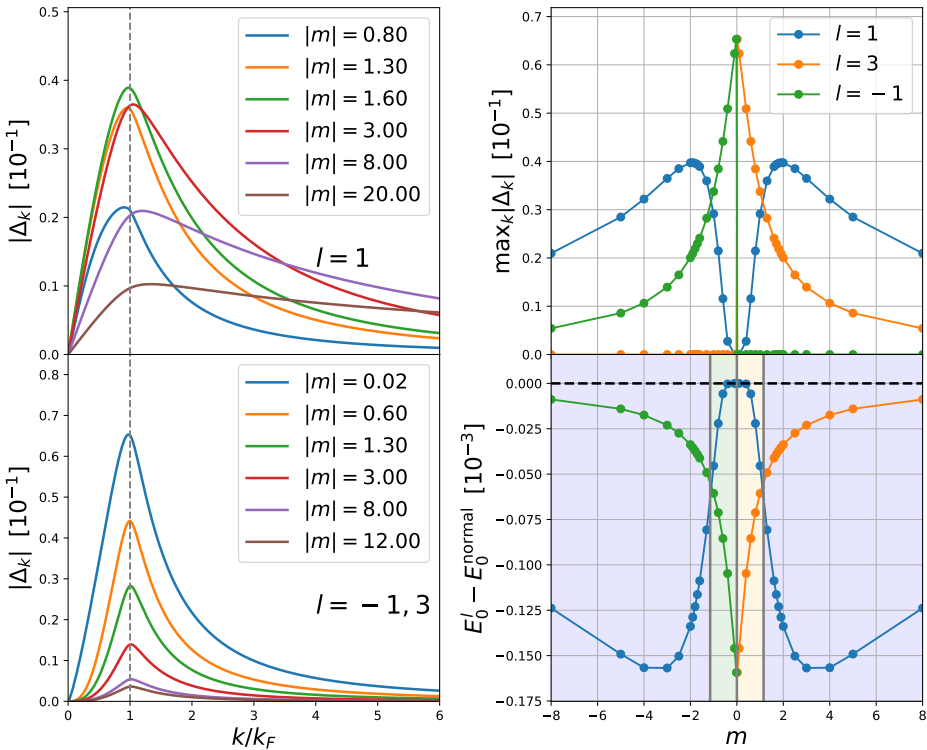


Fig. 1. (Color online) The solution of the self-consistent BCS problem. Left column: radial direction k -dependent pairing amplitude for various values of m . Channel $l = 1$ solution (PH Pfaffian) only depends on $|m|$, while $l = 3$ (anti-Pfaffian) and $l = -1$ (Pfaffian) channel solutions are symmetric with the sign-flip of m . Upper right panel: dependence of the maximum of the pairing amplitude on m (always found at the Fermi level k_F). Lower right panel: total energy of the different pairing solutions compared to the normal state energy. Gray vertical lines denote the transition between different channels. Color in the background corresponds to the energetically favorable channel at the given m : a measure of LL mixing. The color of lines: Pfaffian: green, anti-Pfaffian: orange, PH Pfaffian: blue. Reprinted with permission from Ref. 18 © the American Physical Society.

Thus we get two sets of solutions, because the effective theory does not possess the knowledge of the direction of the external magnetic field. Despite this, we have a clear prediction that for small m , LL mixing, depending on the sign of m we have Pfaffian or anti-Pfaffian, and for large m the PH Pfaffian solution is possible. Thus, in principle, the PH Pfaffian is possible in this effective theory of quasiparticle pairing. The nature of this state, whether it is gapped or gapless state of electrons, needs further investigations (though we see that the Bogoliubov quasiparticle spectrum is gapped).

These predictions on topological pairing, when the LL mixing (mass m) is small, are in accordance with numerical experiments (a) in the second LL, because for $m = 0$ there is a Schrodinger cat superposition of Pfaffian and anti-Pfaffian,^{31,32} and depending on the LL mixing (sign of PH breaking mass) we have Pfaffian or anti-Pfaffian, and (b) in the LLL, where a PH Pfaffian wave function has a large overlap with the composite fermion Fermi-liquid wave function,^{13,33} in accordance with Fig. 1 where the PH Pfaffian-like state is continuously connected to the excited composite fermion Fermi-liquid state at $m = 0$ and cannot represent a gapped state in an isolated LL.

The dimensionless m in the theory is a measure of the PH symmetry breaking and LL mixing, although the precise relation between m and

$$\kappa = \frac{e^2}{\hbar\omega_c} \frac{\epsilon_r l_B}{m_b c}, \quad (62)$$

i.e. the ratio between the characteristic interaction energy and cyclotron energy, known as a LL mixing coefficient, we do not know. In (62), ϵ_r is the dielectric constant of the background material, $\hbar\omega_c = \frac{\hbar e B}{m_b c}$, and m_b is the electron band mass. As we keep the density, $\rho = \frac{\nu}{2\pi l_B^2} = \frac{1}{2} \frac{1}{2\pi l_B^2}$, i.e. k_F fixed, from the mathematical limit of the PH symmetric case when $m = 0$, we reach various systems (experimental settings) by changing the interaction strength (dielectric constant ϵ_r). Thus m , in principle, can be connected with κ , which can be considerable in experiments. (According to Ref. 41 the parameter κ is given by $2.6/\sqrt{B}$, $14.6/\sqrt{B}$, $16.7/\sqrt{B}$, $22.5/\sqrt{B}$, in n-doped GaAs, p-doped GaAs, n-doped ZnO, and n-doped AlAs, with B measured in Tesla.)

4. Model Interactions for Pfaffian Paired States

It is important to know model interactions for model wave functions in order to probe their stability and nature. In the case of bosons, the Pfaffian state at filling factor 1 is

$$\begin{aligned} \Psi_{\text{Pf}}^b = & \sum_{\sigma} \text{sgn } \sigma \left\{ \frac{1}{(z_{\sigma(1)} - z_{\sigma(2)})} \cdots \frac{1}{(z_{\sigma(N_e-1)} - z_{\sigma(N_e)})} \right\} \\ & \times \prod_{k < l} (z_k - z_l). \end{aligned} \quad (63)$$

The model interaction for which this state is an exact, densest state of zero energy³⁴ is

$$H = v \sum_{\langle ijk \rangle} \delta^2(z_i - z_j) \delta^2(z_i - z_k), \quad (64)$$

where $v > 0$ and the sum is over all distinct triples of particles. Thus if three bosons meet (come as close as possible) this will cost repulsive energy. In the case of fermions at filling factor $1/2$, the Pfaffian model interaction is a generalization of the boson interaction to the one that, if three fermions come as close as possible, again, only this will cost energy. The lowest angular momentum wave function of three electrons in the LLL can be described as

$$\Psi(\mathbf{r}_1, \mathbf{r}_2, \mathbf{r}_3) \sim \sum_{\sigma} \text{sgn} \sigma z_{\sigma(1)}^2 z_{\sigma(2)}^1 z_{\sigma(3)}^0 \exp \left\{ -\frac{1}{4l_B} (|z_1|^2 + |z_2|^2 + |z_3|^2) \right\}. \quad (65)$$

We may conclude that if M (angular momentum) = 3 for three electrons this will cost interaction energy. Indeed, it can be argued, just as in the case of the Laughlin state and two-body PPs,³⁵ that in the case of Pfaffian we need to specify only a truncated series of three-body PPs with definite three-body angular momenta. At filling factor $1/2$, only non-zero three-body PP is the one for $M = 3$. (For bosons, at filling factor 1, the only non-zero three-body PP is for $M = 0$.)

These model interactions are highly artificial if we want to model and probe real physical systems. In the FQHE, we can always specify the base LL from which most of correlations originate, but should also consider the effects of LL mixing. Beside the Coulomb (two-body) interaction at a half-integer filling factor, we may take into account perturbatively the effects of LL mixing, by considering special three-body interactions.³⁷⁻⁴¹ In this way we may find a characteristic series of three-body PPs for Pfaffian state, when considering the specific problem of the second LL and associated LL mixing contribution. A PP is a certain characteristic energy, V_M , associated with a three-body state at total angular momentum M . (The dimension of the subspace of a fixed angular momentum for three particles may be larger than one for higher M , and V_M may be a matrix.) In the case of Pfaffian, the dominant, first three values of three-body PPs, for $M = 3, 5, 6$ are negative and $\frac{V_{M=5}}{V_{M=3}} \sim 0.4$ and $\frac{V_{M=6}}{V_{M=3}} \sim 0.7$.⁴¹ We may ask what would be a characteristic series for PH Pfaffian, if we assume that the PH Pfaffian state or phase exists, and expect that some kind of three-body interaction will be relevant also in this case.

To answer this question we may consider again the CS formalism, not directly connected with considerations in Sec. 3. We will recall³⁴ the effective derivation of the Pfaffian physics, by a part of the kinetic term in the non-relativistic CS description. (Thus these considerations will not relate to the solution in Sec. 3, in the large m limit, when we take into account the complete kinetic term.) We will use this formal derivation to propose a method for recovering model interactions for Pfaffian and PH Pfaffian. (By using the PH exchange we can reach a model interaction also for anti-Pfaffian.)

To get (formally) the Pfaffian pairing solution we may consider the kinetic energy part of the (non-relativistic) CS approach in (15), i.e. the part of the Hamiltonian given by

$$\mathcal{H} = \frac{\Psi_{\text{cf}}^+(\mathbf{p} - \mathbf{A} - \mathbf{a})^2 \Psi_{\text{cf}}}{2m}, \quad (66)$$

with $\mathbf{B} = B\mathbf{z}$, with $A_x = -(B/2)y$ and $A_y = (B/2)x$, as before, and

$$a_x(\mathbf{r}) = 2 \int d\mathbf{r}' i \frac{y - y'}{|\mathbf{r} - \mathbf{r}'|^2} \delta\rho_{\text{cf}}(\mathbf{r}'), \quad (67)$$

and

$$a_y(\mathbf{r}) = -2 \int d\mathbf{r}' i \frac{x - x'}{|\mathbf{r} - \mathbf{r}'|^2} \delta\rho_{\text{cf}}(\mathbf{r}'), \quad (68)$$

as before, in the Coulomb gauge $\nabla \cdot \mathbf{a} = 0$, and $\delta\rho_{\text{cf}} = \Psi_{\text{cf}}^+ \Psi_{\text{cf}} - \bar{\rho}$, where $\bar{\rho}$ is the average density. We consider the following part of the implied interaction,

$$V_a = -\mathbf{a}\mathbf{j}_{\text{cf}}, \quad (69)$$

with

$$\mathbf{j}_{\text{cf}} = \frac{1}{2m} [\Psi_{\text{cf}}^+(\mathbf{p}\Psi_{\text{cf}}) - (\mathbf{p}\Psi_{\text{cf}}^+) \Psi_{\text{cf}}], \quad (70)$$

more specifically its Cooper channel part.

After simple steps,¹⁹ we arrive at the Cooper channel part,

$$V_{\text{int}}^{\text{C}} = \frac{4\pi}{m} \frac{1}{V} \sum_{\mathbf{k}, \mathbf{p}} |\mathbf{k}||\mathbf{p}| \frac{i \sin(\theta_k - \theta_p)}{|\mathbf{p} - \mathbf{k}|^2} a_{\mathbf{k}}^\dagger a_{\mathbf{p}} a_{-\mathbf{k}}^\dagger a_{-\mathbf{p}}. \quad (71)$$

Note that in this case (following the mean-field equations and derivation in Ref. 30, or in Ref. 19) we find that the Cooper pair wave function behaves as,

$$\lim_{|\mathbf{r}| \rightarrow \infty} g(\mathbf{r}) \sim \frac{1}{z}. \quad (72)$$

This implies the Pfaffian construction (after the unitary CS transformation into the electron representation), if we recall that the choice of \mathbf{A} in (66) implies a holomorphic Laughlin–Jastrow factor (more precisely a phase factor after the unitary CS transformation) that is associated with the usual description of the Pfaffian state in (5). If we had an extra minus sign in (71), this would lead to the antiholomorphic pairing, i.e. the PH Pfaffian pairing.

To derive the model interactions for Pfaffian and PH Pfaffian, we assume that we can use an effective non-relativistic CS description to describe the pairing of underlying quasiparticles (composite fermions). On the basis of the previous consideration ((69) and (71)), we consider an effective Hamiltonian,

$$H_{\text{BCS}}^{\text{ef}} = \frac{1}{2m} \Psi_{\text{cf}}^\dagger(\mathbf{p})^2 \Psi_{\text{cf}} + \lambda \delta \mathbf{a}\mathbf{j}_{\text{cf}}, \quad (73)$$

where $\delta \mathbf{a} = \mathbf{A} + \mathbf{a}$, and the coupling λ is negative in the Pfaffian case and positive in the PH Pfaffian case. Thus we assumed that a complete (non-relativistic) CS

description that includes all effects of interactions can be reduced to the effective form if a pairing occurs. By using the non-relativistic CS description we take into account PH symmetry breaking necessary to stabilize these pairing states.

If we apply the CS transformation in reverse,¹⁹ going from the composite fermion representation to an electron one, we arrive at the following effective Hamiltonian for electrons,

$$H_{\text{BCS}}^{\text{el}} = \frac{1}{2m} \Psi^\dagger (\mathbf{p} - \mathbf{A})^2 \Psi - \frac{1}{2m} (\delta \mathbf{a})^2 \Psi^\dagger \Psi + (1 + \lambda) \delta \mathbf{a} \mathbf{J}_{\text{el}} + (1 + \lambda) \frac{1}{m} (\delta \mathbf{a})^2 \Psi^\dagger \Psi, \quad (74)$$

where

$$\mathbf{J}_{\text{el}} = \frac{-i}{2m} \Psi^\dagger (\nabla + i\mathbf{A}) \Psi - [(\nabla + i\mathbf{A}) \Psi]^\dagger \Psi, \quad (75)$$

is the (gauge invariant) electron current.

We concentrate on the effective three-body (electron) interaction that is present in the Hamiltonian,

$$V_{\text{BCS}}^3(\lambda) = (1/2 + \lambda) \frac{1}{m} : (\mathbf{a})^2 \Psi^\dagger \Psi : . \quad (76)$$

The three-body interaction in coordinate representation is

$$V(\mathbf{r}_1, \mathbf{r}_2, \mathbf{r}_3) = (1/2 + \lambda) \frac{4}{m} \frac{(\mathbf{r}_3 - \mathbf{r}_1)(\mathbf{r}_3 - \mathbf{r}_2)}{|\mathbf{r}_3 - \mathbf{r}_1|^2 |\mathbf{r}_3 - \mathbf{r}_2|^2}. \quad (77)$$

To describe the relevant matrix elements for LL(s), we will choose our base LL to be the LLL, which is the most natural choice when we consider a CS description; the very CS transformation is based on the Laughlin–Jastrow correlations in the LLL. Thus, for example, we will relate the effective PPs that we know for the Pfaffian state, based on the perturbation theory, in the second LL, with here calculated PPs, based on the CS description, in the LLL.

To describe relevant three-body PPs (V_M) in the LLL, we introduce rescaled matrix elements, $\Delta_{M=2k+3l}$,

$$V_M = \int d\mathbf{r}_1 \int d\mathbf{r}_2 \int d\mathbf{r}_3 V(\mathbf{r}_1, \mathbf{r}_2, \mathbf{r}_3) |\Psi_{k,l}(\mathbf{r}_1, \mathbf{r}_2, \mathbf{r}_3)|^2 = (1/2 + \lambda) \cdot 4/m \cdot \Delta_{M=2k+3l},$$

where $\Psi_{k,l}$ are normalized, fully antisymmetric wave functions for three electrons,⁴² classified by integers $k \geq 0; l \geq 1$, and the total angular momentum of the state is $M = (2k + 3l)$. The calculated Δ_M are shown in the Table 1.

The matrix elements are illustrated by their rescaled values $\frac{m}{4} V_M = (1/2 + \lambda) \cdot \Delta_{M=2k+3l}$, in the cases when $\lambda = -1$ and $\lambda = 0$ in Fig. 2. What is remarkable is that according to the Table 1, $\frac{V_{M=5}}{V_{M=3}} = 0.5$, and $\frac{V_{M=6}}{V_{M=3}} = 0.7$, and are quite close to the ratios of the relevant matrix elements from the perturbation theory in the second LL, ~ 0.4 , and ~ 0.7 , respectively, that favor the Pfaffian physics.⁴³

Thus the CS description is able to capture the sign — a negative one of necessary PPs when $\lambda < -1/2$, and their relative magnitude for relevant, those first three PPs in the Pfaffian case. Therefore, we are encouraged to probe the PH Pfaffian case

Table 1. Matrix elements in the LLL. Reprinted with permission from Ref. 19 © the American Physical Society.

M	3	5	6	7	8	9	
Δ_M	1/24	1/48	7/240	1/80	2/105	$\frac{221/10080}{1/(240\sqrt{21})}$	$\frac{1/(240\sqrt{21})}{1/120}$
$\frac{\Delta_M}{\Delta_{M=3}}$	1	0.5	0.7	0.3	~ 0.475	~ 0.526 ~ 0.022	~ 0.022 0.2

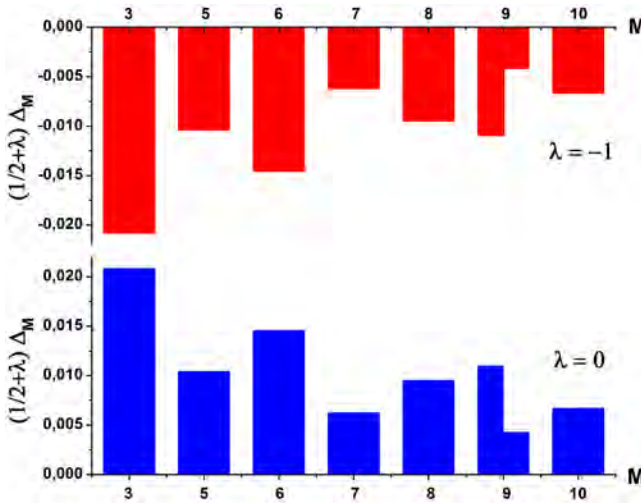


Fig. 2. (Color online) Matrix elements of three body PPs in the LLL for $\lambda = -1$ (above) and $\lambda = 0$ (bottom). (We plotted two values, diagonal matrix elements in the two-dimensional subspace, in the case when $M = 9$.) Reprinted with permission from Ref. 19 © the American Physical Society.

for certainly $\lambda > 0$. (We can identify the $\lambda = 0$ case with composite fermion Fermi liquid case.) But we have to be aware that in the effective description by H_{BCS}^{el} , the estimate that we can make for LL mixing parameter (in general the ratio of characteristic interaction energy and cyclotron energy) is $|\lambda + 1/2|$, and that for any considerable $\lambda \gtrsim 1/2$ for which PH Pfaffian correlations are relevant, we have to include higher LL(s) (i.e. not only the base LL — the LLL in the CS description). Thus in the PH Pfaffian case, we have to include (three-body) PPs for at least one more LL. The calculated PPs (more precisely their rescaled $(m/4)V_M$ values) for two LLs when $\lambda = 1$ are illustrated in Fig. 3. While calculating these PPs, we had to include the natural cut-off l_B in the field-theoretical description, to suppress divergences in the second LL. We can conclude from Fig. 3 that in the case of PH Pfaffian, there is an abrupt decrease in the positive values of three-body PPs at $M = 7$ in the base (LLL) level and also at $M = 5$, when two of three electrons are in the higher (second) LL. This can be compared with the usual (truncated) model for Pfaffian with only non-zero, positive potential $V_{M=3}$; there is no three fermion state

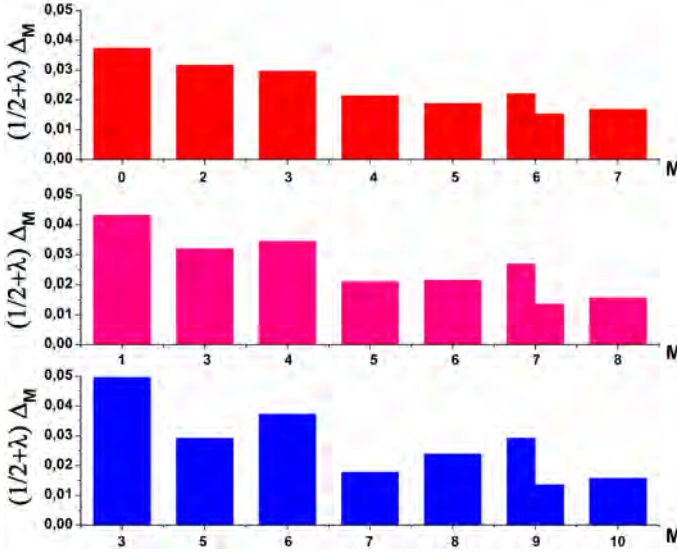


Fig. 3. (Color online) Three-body PP matrix elements for $\lambda = 1$ (PH Pfaffian case) in the second LL (top), for states with two particles in the second LL and one in the LLL (middle), and (all three) in the LLL (bottom). Reprinted with permission from Ref. 19 © the American Physical Society.

with $M = 4$, and the V_5 PP that is connected with the characteristic three-body angular momentum for Pfaffian in the LLL, $M = 5$, is zero.³⁶ In the case of the PH Pfaffian, the characteristic angular momentum is $M = 7$ in the LLL, and thus the abrupt decrease(s) in the values of three-body PPs that we may associate with the PH Pfaffian pairing correlations. The (almost) monotonic decrease of PPs when all three particles are in the second LL suggests that the space of two LLs may be necessary, but also sufficient for the realization of the PH Pfaffian correlations. The important question, which needs further investigation, is whether these correlations are associated with a gapped state. The most recent suggestion for the realization of PH Pfaffian is in Ref. 44.

5. Conclusions and Outlook

In this review, we have demonstrated that the CS field-theoretical approach can be useful and informative in the description of Pfaffian and anti-Pfaffian states — well-established candidate states for the explanation of gapped states at half-integer filling factors in the FQHE. It can capture the pairing nature of these states, when the basic gauge-field constraints are taken into account in a generalized Dirac effective description of the problem. The effective Dirac description originates from the physics inside a base LL, which, when isolated (in the case of the Coulomb problem) possesses PH symmetry. To stabilize Pfaffian or anti-Pfaffian, we have to break this symmetry by a mass (of definite sign) term in the Dirac theory.

The physics of an isolated base LL in the Dirac effective description suggests a possible existence of a PH symmetric Pfaffian state.⁷ We find that this solution is relevant only when a significant PH breaking (mass) is included in the Dirac description. Considering a non-relativistic limit of the description we find that interaction parameters that describe the influence from the higher (second) LL must be non-perturbatively included in a model interaction for PH Pfaffian (beside the ones from the base (lowest) LL). This may be helpful in the effort to stabilize and detect PH Pfaffian correlations in numerical experiments.

Acknowledgments

This research was supported by the Ministry of Education, Science, and Technological Development of the Republic of Serbia under Project ON171017, and by the Ministry of Science of Montenegro under Project SFS013454.

References

1. D. C. Tsui, H. L. Stormer and A. C. Gossard, *Phys. Rev. Lett.* **59** (1987) 1776.
2. R. Willett, J. P. Eisenstein, H. L. Stormer, D. C. Tsui, A. C. Gossard and J. H. English, *Phys. Rev. Lett.* **59** (1987) 1776.
3. G. Moore and N. Read, *Nucl. Phys. B* **360** (1991) 362.
4. S. H. Simon, in *Composite Fermions*, ed. O. Heinonen (World Scientific, Singapore, 1998), p. 91.
5. R. L. Willett, R. R. Ruel, K. W. West and L. N. Pfeiffer, *Phys. Rev. Lett.* **71** (1993) 3846.
6. B. I. Halperin, P. A. Lee and N. Read, *Phys. Rev. B* **47** (1993) 7312.
7. D. T. Son, *Phys. Rev. X* **5** (2015) 031027.
8. S.-S. Lee, S. Ryu, C. Nayak and M. P. A. Fisher, *Phys. Rev. Lett.* **99** (2007) 236807.
9. M. Levin, B. I. Halperin and B. Rosenow, *Phys. Rev. Lett.* **99** (2007) 236806.
10. T. Jolicoeur, *Phys. Rev. Lett.* **99** (2007) 036805.
11. P. T. Zucker and D. E. Feldman, *Phys. Rev. Lett.* **117** (2016) 096802.
12. E. H. Rezayi, *Phys. Rev. Lett.* **119** (2017) 026801.
13. R. V. Mishmash, D. F. Mross, J. Alicea and O. I. Motrunich, *Phys. Rev. B* **98** (2018) 081107(R).
14. M. Banerjee, M. Heiblum, V. Umansky, D. E. Feldman, Y. Oreg and A. Stern, *Nature* **559** (2018) 205.
15. K. K. W. Ma and D. E. Feldman, *Phys. Rev. B* **100** (2019) 035302.
16. D. F. Mross, Y. Oreg, A. Stern, G. Margalit and M. Heiblum, *Phys. Rev. Lett.* **121** (2018) 026801.
17. C. Wang, A. Vishwanath and B. I. Halperin, *Phys. Rev. B* **98** (2018) 045112.
18. L. AntoniĆ, J. Vućičević and M. V. Milovanović, *Phys. Rev. B* **98** (2018) 115107.
19. S. Djurdjević and M. V. Milovanović, *Phys. Rev. B* **100** (2019) 195303.
20. R. B. Laughlin, *Phys. Rev. Lett.* **50** (1983) 1395.
21. E. H. Rezayi and F. D. M. Haldane, *Phys. Rev. Lett.* **84** (2000) 4685.
22. S.-C. Zhang, *Int. J. Mod. Phys. B* **6** (1992) 25.
23. N. Read, *Semicond. Sci. Technol.* **9** (1994) 1859; N. Read, *Surf. Sci.* **361** (1996) 7.
24. D. H. Lee and M. P. A. Fisher, *Phys. Rev. Lett.* **63** (1989) 903.
25. N. Seiberg, T. Senthil, C. Wang and E. Witten, *Ann. Phys.* **374** (2016) 395.

26. T. Senthil, D.T. Son, C. Wang and C. Xu, *Phys. Rep.* **827** (2019) 1.
27. A. C. Potter, M. Serbyn and A. Vishwanath, *Phys. Rev. X* **6** (2016) 031026.
28. D. Xiao, M.-C. Chang and Q. Niu, *Rev. Mod. Phys.* **82** (2010) 1959.
29. C. Wang, N. R. Cooper, B. I. Halperin and A. Stern, *Phys. Rev. X* **7** (2017) 031029.
30. N. Read and D. Green, *Phys. Rev. B* **61** (2000) 10267.
31. M. R. Peterson, K. Park and S. Das Sarma, *Phys. Rev. Lett.* **101** (2008) 156803.
32. H. Wang, D. N. Sheng and F. D. M. Haldane, *Phys. Rev. B* **80** (2004) 241311(R).
33. A. C. Balram, M. Barkeshli and M. S. Rudner, *Phys. Rev. B* **98** (2018) 035127.
34. M. Greiter, X. G. Wen and F. Wilczek, *Nucl. Phys. B* **374** (1982) 567.
35. F. D. Haldane, in *The Quantum Hall Effect*, eds. R. Prange and S. M. Girvin (Springer-Verlag, New York, 1987), p. 303; F. D. M. Haldane, *Phys. Rev. Lett.* **51** (1983) 605.
36. S. H. Simon, E. H. Rezayi and N. R. Cooper, *Phys. Rev. B* **75** (2007) 195306.
37. W. Bishara and C. Nayak, *Phys. Rev. B* **80** (2009) 121302(R).
38. M. R. Peterson and C. Nayak, *Phys. Rev. B* **87** (2013) 245129.
39. S. H. Simon and E. H. Rezayi, *Phys. Rev. B* **87** (2013) 155426.
40. R. E. Wooten, J. H. Macek and J. J. Quinn, *Phys. Rev. B* **88** (2013) 155421.
41. I. Sodemann and A. H. MacDonald, *Phys. Rev. B* **87** (2013) 245425.
42. R. B. Laughlin, *Phys. Rev. B* **27** (1983) 3383.
43. K. Pakrouski, M. R. Peterson, T. Jolicoeur, V. W. Scarola, C. Nayak and M. Troyer, *Phys. Rev.* **X5** (2015) 021004.
44. C. Sun, K. K. W. Ma and D. Feldman, arXiv:2003.14227 (2020).